Development of Ultrabright Electron Sources and Time-Resolved Low-Energy Electron Diffractometer (LEED)

Dissertation with the aim of achieving a doctoral degree

at the Faculty of Mathematics, Informatics and Natural Sciences

Department of Chemistry

of Universität Hamburg

Submitted by Chiwon Lee

2019 in Hamburg

Acknowledgement

I would have not been able to finish my phd study without helps from people in the Miller group at MPSD. These people should be mentioned in this section, and special thanks must be given to them.

First of all, I would like to express my deepest gratitude to Prof. R.J. Dwayne Miller, my phd supervisor. Even though it is still a mystery about how I attracted his mind in the Skype interview when I applied to his group in Seoul, I am convinced myself that the last five and half years of my phd study was absolutely precious training times for me to strengthen the basis on the way to be an independent scientist. From Dwayne's enthusiasm about science and ability to collaborate, I have earned a way out of the difficulties that most of phd candidates, including myself, go through during their research. Besides, his unceasing support and encouraging words were always sufficient to remind me of my goal to do great science.

I greatly appreciate Dr. Soichiro Tsujino at PSI for his sincere support at the time when I spent the first year of my phd study. In hindsight, it was a quite brave decision for me to change my major from chemical engineering to ultrafast science. I should admit that Soichiro's guidance and patience whenever I made mistakes in his lab enabled me to smoothly enter to this new field of science.

I would like to specially thank Dr. Günther Kassier for spending his time and effort on transferring knowledge about electronics. Especially, the state-of-the-art streak camera technology that he developed in South Africa has become an indispensable part of my setup. Also, I appreciate for his spending time on discussions whenever I have troubleshooting on my setup and for budget planning in our subgroup in the limited resources every year.

Besides of these people, I have met the most talented scientists and engineers at CFEL, who deserve to be acknowledged. I thank Dr. Khalid Siddiqui for sharing the general concept of pump-probe experiment; Dr. Alexander Marks for his help on diffraction data interpretation; Dr. Friedjof Tellkamp for the assistance on LabView programming; Mr. Hendrik Schikora for the CAD modelling on my setup; Dr. Martin Kollewe for constructing high voltage pulser system and PCB design for the steak camera; Dr. Miriam Barthelmess for training me on how to use e-beam evaporator; Dr. Robert Bücker, Dr. Stuart Hayes, and Mr. Gopal Singh for the inspiring conversations and interactions.

Words cannot express my deepest thankfulness to my parents. Without their continuing love and prayer for my future, I could have never completed this thesis. This thesis is yours.

Declaration of Oath

I hereby declare on oath, that I have written the present dissertation by my own and have not used other than the acknowledged resources and aids. The submitted written version corresponds to the version on the electronic storage medium. I hereby declare that I have not previously applied or pursued for a doctorate (PhD studies)

Abstract

Low-energy electron diffraction (LEED) is capable of determining the surface structure of matter with few- to monolayer sensitivity and atomic spatial resolution. This surface-sensitive technique, with appropriate introduction of femtosecond pump-probe protocols, is capable of imaging a surface chemical reaction accompanying atomic and molecular structural changes at the surface on an ultrafast timescale. In this thesis, a transmission-mode time-resolved LEED is demonstrated for the expressed purpose by exploiting the state-of-the-art streak camera technology with the aim of the realization of subpicosecond temporal resolution for a high density low-energy electron bunch ($>10^4$ number of electrons per bunch). For a low density low-energy electron bunch ($<10^2$ number of electrons per bunch), active control of the bunch duration is demonstrated by an optical fiber-based low-energy electron gun, important to determine the observable time-window of dynamics in streaking experiments. In addition, an on-chip double-gated nanotip field emitter is developed for the purpose of making an ultrabright electron source that can generate a highly coherent and collimated electron beam with large beam current. The time-resolved measurement data are analyzed separately for a direct and diffracted beam in order to separate artificial kinetics caused by the transient electric field effect from the structural change-driven one of prime interest.

Zusammenfassung

Niederenergetische Elektronenbeugung ('Low Energy Electron Diffraction', LEED) ist in der Lage, die Oberflächenstruktur von Materie mit bis zu einschichtiger Empfindlichkeit und atomarer räumlicher Auflösung zu bestimmen. Mit dieser oberflächensensitiven Technik kann bei entsprechender Einführung von Femtosekunden-Pump-Probe-Protokollen eine chemische Reaktion der Oberfläche, die atomare und molekulare Strukturänderungen an der Oberfläche begleitet, in einem ultraschnellen Zeitmaßstab abgebildet werden. In dieser Arbeit wird eine zeitaufgelöste LEED Technik für den angegebenen Zweck demonstriert, indem die neueste 'streak camera' Technologie mit dem Ziel genutzt wird, eine zeitliche Auflösung von weniger als einer Pikosekunde für ein Elektronenbündel mit niedriger Energiedichte zu realisieren (Elektronenanzahl $> 10^4$ pro Puls). Für einen energiearmen Elektronenpuls mit niedriger Dichte ($< 10^2$ Elektronen pro Puls) wird die aktive Steuerung der Pulsdauer durch eine auf Lichtwellenleitern basierende, niederenergetische Elektronenquelle demonstriert. Eine solche Steuerung ist die für die Bestimmung des beobachtbaren Zeitfensters der Dynamik in 'streak camera' Experimenten von Bedeutung. Darüber hinaus wurde ein On-Chip Nanospitzen Feldemitter mit zwei integrierten Elektroden entwickelt, um eine ultrahelle Elektronenquelle herzustellen, die einen hochkohärenten und gebündelten Elektronenstrahl mit großem Strahlstrom erzeugen kann. Die zeitaufgelösten Messdaten werden getrennt für einen direkten als auch einen gebeugten Strahl analysiert. Somit können Artefakte, die durch kurzlebige elektrische Felder verursacht werden, von den eigentlich interessanten strukturveränderungsgetriebenen Phänomenen getrennt werden.

List of Figures

List of Tables

TABLE OF CONTENTS

1. Introduction

A surface and an interface define a boundary between a condensed phase (*i.e.* solid and liquid) and its surrounding environment [1]. At the molecular level, atoms at the two-dimensional space possess fewer nearest neighbors than those in the three-dimensional bulk phase. Whenever chemical and physical interactions occur at this boundary, the structurally broken symmetry induces drastically different interaction mechanisms from those in the bulk. This exotic aspect of surface science has *not only* attracted the curiosity of scientists from the fundamental point of view *but also* accelerated interest from industries paying attention to the tremendous economic impact made by the relevant technologies. The fact that approximately 35% of the world's GDP (Gross Domestic Product) is directly and indirectly contributed by catalysis [2], a representative example of surface chemistry, indeed reflects the importance of its role in our daily lives.

To understand surface interaction mechanisms, it is indispensable to investigate the microscopic structure of a given surface at the atomic level. Historically, this demand has resulted in the development of in-situ surface-sensitive measurement techniques, including GISAXS (Grazing-Incidence Small-Angle X-ray Scattering), AFM (Atomic Force Microscopy), STM (Scanning Tunneling Microscopy), LEED (Low-Energy Electron Diffraction), and etc. These currently available techniques provide few- to monolayer sensitivity and excellent spatial resolution, enabling one to grasp a static picture of surface atomic structures. From the Chemist's point of view, however, the world is dynamic. Chemistry is essentially a "race against time" [3], meaning that those static measurement tools are not suitable for capturing surface atomic motions in real time - the very essence of Chemistry.

The required temporal resolution to observe surface chemical reactions depends on the reaction mechanisms. Nonetheless, an approximate time scale can be estimated by taking an example of bond breaking: for a thermally fluctuating molecular system with the speed of sound (10^3 m/sec) and a bond length of 1 Å (= 10^{-10} m), the relevant time scale of the bond breaking is on the order of 100 fs (= 10^{-13} sec). This femtosecond time window has been only achievable with the development of ultrashort laser technology that opened the field of so-called femtochemistry [4]. In this regard, one can conceive a picture of combining the ultrashort laser technology with one of the above mentioned surface-sensitive techniques for the realization of making a surface molecular movie with the relevant spatial and temporal resolution.

To attain this objective, LEED is selected in this thesis work as the low-energy electrons possess unique properties suited for the time-resolved study of surface reactions. First of all, the short

inelastic-mean-free-path of this structural probe allows few to sub-monolayer sensitivity. Second, the extremely high elastic scattering cross-section of low-energy electrons makes this probe the most sensitive possible one for studying surface reaction and interfacial dynamics. Third, low-energy electron beams have a de-Broglie wavelength in the range of the angstrom to sub-angstrom, depending on their kinetic energy, providing sufficient atomic spatial resolution. Fourth, compared to atom-by-atom scanning techniques such as STM and AFM, LEED is more suitable in capturing long-range molecular motions relevant to chemistry. Fifth, compared to X-ray techniques, table top construction of the apparatus is possible, saving time, and cost.

Challenges also exist. The charged nature of electrons leads to Coulombic repulsion in an electron bunch such that, especially for a low-energy electron bunch with a high charge density, leading to rapid temporal broadening, making sufficiently short electron bunch lengths and the resultant high temporal resolution difficult to be achieved. Although there are several demonstrated methods (*e.g.*, rebunching [5] by exploiting the linear chirp [6]) to solve this space charge issue in high-energy electron diffraction, implementing the same technologies into a LEED apparatus is challenging due to other constrains that will be described in the following Chapters. The other challenge lies in the electron source brightness. As the bunch length goes shorter, the number of electrons in the bunch goes smaller, deteriorating SNR (signal-to-noise-ratio) and spatial resolution of a recorded image.   For a given electron density in a bunch, the way to obtain a higher brightness is to increase the transverse spatial coherence of the beam, demanding the development of a new class of electron sources. In this thesis, efforts to overcome these challenges are described.

The framework of this thesis consists of two main parts, namely the ultrabright electron source development (Chapter 2 and 3) and the time-resolved LEED setup development (Chapter 4, 5, 6, and 7). In Chapter 2, some essential properties of free-electron bunchs are introduced, which will help in understanding the contents of the following Chapters. In Chapter 3, the development of two types of novel electron sources and the characterization results are presented. Before moving to the LEED setup development, a brief introduction about properties of low-energy electrons is provided in Chapter 4. Subsequently, a detailed explanation about the anatomy of the time-resolved LEED setup and basic setup characterization results are given in Chapter 5. In Chapter 6, a potential artifact related to thermionic and photoemission from the sample (*i.e.* transient electric field effect) that may lead to wrong interpretation of time-resolved diffraction data is deeply discussed. In Chapter 7, a new methodology to realize a single-shot LEED (*i.e.* streaking) and preliminary results are presented. The thesis is completed with a short outlook and several ideas worthwhile to be tried in the future in Chapter 8.

Seeing is believing. If one can watch reaction dynamics at the atomic level, chemistry and

physics governing the reaction mechanism can be understood. Once one can understand the underlying principle, there is a chance to control it with new levels of precision - one of the über goals of science.

2. Properties of Free-Electron Bunchs

2.1. Electron beam parameters

In Chapter 1, the required temporal resolution for the imaging of chemical reactions was discussed. The canonical time window for watching the molecule's atomic motions such as bending, stretching, and rotation, or formation and breaking of bonds is estimated approximately 100 fs. It is however possible for faster reactions to be present even for complex biological systems [7]. Through the advance of methods including electron bunch compression [8], temporal filtering [9] or use of relativistic electron bunches [10] to mitigate space charge induced temporal bunch broadening, sub-100 fs time resolved UED experiments employing highly charged electron bunches are now within reach. With the additional constraint of single or few- electron pulses emitted from optically triggered field emission sources, it is even possible to reach the attosecond time domain [11,12]. This remarkable progress means that the camera shutter speed for recording molecular movies is now truly fast enough to capture atomic motions of the target molecules. However, as in most of scientific problems, while the ultrashort electron bunch solves the temporal resolution issue on one hand, it also gives rise to another very fundamental issue on the other hand. For a given molecular system, the total number of electrons required to record a single electron diffraction image with sufficient signal-to-noise ratio (SNR) and image contrast is determined by the system itself and the spatial property (i.e. transverse coherence) of the electron beam *but not by* its temporal property. As the electron bunch length becomes shorter and shorter, the number of electrons that constitutes the bunch becomes smaller and smaller, and as a result, the required number of pump shots initiating chemical reactions becomes larger and larger. If the characteristics of the system of interest is completely reversible, which means the system can be reversed back to the ground state from an excited state during unlimited times of pumping cycles, the large required number of pump shots would not be a problem; unfortunately, scientists' curiosity does not stay on this sort of simple reversible systems but also is heading toward more complex chemical systems that cannot survive during such a multiple times of pumping cycles. The solution lies in the electron source. If the source can generate an electron beam bright enough to light up the atomic structure in a given ultrafast time frame in an ideally single shot manner, the problem is solved at least in terms of the pump-probe imaging scheme (the raster scanning of the sample to exchange the exposed area is an another technical challenge though [13]). Conventional photocathodes used in time-resolved electron diffraction does not meet the demand of the high brightness beam, and therefore, development of an ultrabright cathode is an indispensable step not only to improve the spatial and temporal resolution of the time-resolved electron diffraction but also to expand the applicability of this technique to a chemical species, which have important

fundamental questions that have not been possible to address due to its structural complexity. Then, the remaining task is to know what physical factors affect the beam brightness and make a strategy to develop the ultrabright cathode by exploiting this information, which will be explained in the following subsections of this chapter.

2.1.1. Beam brightness

Brightness B of a particle beam is defined by the beam current density J per unit solid angle Ω as [14],

$$B = \frac{J}{\Omega} \tag{2.1}$$

From equation (2.1) it can be intuitively conceived that the number of electrons is not only the matter but also how the beam is propagating in space is an important factor in determining the brightness. A more useful formula to investigate the beam brightness is to write equation (2.1) in terms of the emittance [15]:

$$B = \frac{J}{\Omega} \approx \frac{I}{\pi^2 \varepsilon_x \varepsilon_y} \tag{2.2}$$

Here, I is the beam current, and ε_x and ε_y are the root mean square (rms) transverse normalized emittance in the x- and y-directions, respectively (here, the z-axis is defined by the beam propagation direction). Assuming a symmetric beam where $\varepsilon_x = \varepsilon_y$, the brightness is inversely proportional to the square of the transverse normalized emittance, implying that beam brightness increases rapidly with decreasing ε_x or ε_y. B is the fundamental quantity determining the quality of the beam, and in general, it is limited by space charge and energy spread of the cathode, which will be discussed in Chapter 2.2.

2.1.2. Transverse emittance

Emittance is the property of a particle beam that indicates the spatial quality of the beam [16]. It is defined as the volume occupied by the particles in 6-dimensional phase space (x, p_x, y, p_y, z, p_z), the latter fully describing the state of the particle ensemble. Here, p_x, p_y, and p_z are defined by the particle momentum in x-, y-, and z-direction. By solving the Hamiltonian equation, the path of individual particles as a function of time in the phase space is determined, and the particle path does not intersect each other according to Liouville's theorem [17] unless any external or focusing forces are applied.

This statement implies that the density of particles in the phase space is constant, leading to an invariant phase space volume, no matter how the particle distribution evolves as the beam propagates, except the case that nonlinear forces such as lens aberrations or space charge are involved.

Under the assumption of no coupling between the longitudinal (z, p_z) and transverse components (x, p_x, y, p_y), it is useful to separate the transverse and longitudinal planes. Here, we define the longitudinal axis as the beam propagation direction. Analogous to the 6-dimensional case, the area in the 2-dimensional transverse phase space is also a conserved quantity, even though the particle distribution changes as the beam propagates. The transverse emittance is defined by the conserved phase space area as illustrated in Figure 2.1..
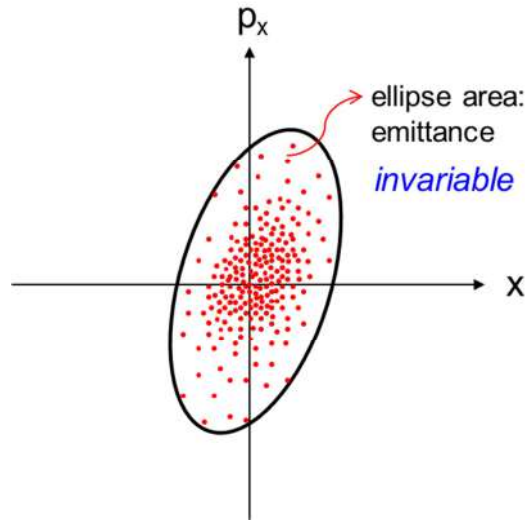
{Figure 2.1. Illustration of transverse emittance in position-momentum space}

The transverse rms normalized emittance ε_x is expressed by the following equation [18]:

$$\varepsilon_x = \frac{1}{m_0 c}\sqrt{<\sigma_x^2><\sigma_{p_x}^2> - <\sigma_x \sigma_{p_x}>^2}$$

(2.3)

where, m_0, c, σ_x, and σ_{p_x} are the electron mass, speed of light, transverse rms electron beam size, and transverse rms momentum spread, respectively. Here, the "normalized" means that the emittance is scaled according to the beam energy to conserve the invariant property of the beam emittance. The angle brackets $<...>$ indicate an ensemble average of electrons in the bunch, which can be mathematically expressed as the 2nd order moments of a distribution of N number of electrons

At a beam waist, it is assumed that no linear correlation between the position and momentum of electrons is present, yielding $<\sigma_x \sigma_{p_x}> = 0$ in equation (2.3). The emittance formula is then

simplified as follows:

$$\varepsilon_x = \frac{1}{m_0 c} \sigma_x \sigma_{p_x}$$

(2.4)

The ε_x of an electron beam is also a function of electron temperature, T. For the nonrelativistic case, the σ_{p_x} is described by $m_0 \langle v_x^2 \rangle$, where $< v_x^2 >$ indicates the mean squared transverse velocity assumed to follow a Maxwell-Boltzmann velocity distribution:

$$\langle v_x^2 \rangle = \frac{\int_0^\infty v_x^2 e^{-\frac{m_0 v_x^2}{2k_B T}} dv_x}{\int_0^\infty e^{-\frac{m_0 v_x^2}{2k_B T}} dv_x} = \frac{k_B T}{m_0}$$

(2.5)

where, k_B refers to the Boltzmann constant. Then, σ_{p_x} can be expressed by a function of T, consequently giving rise to the following relationship between ε_x and T:

$$\varepsilon_x = \sigma_x \sqrt{\frac{k_B T}{m_0 c^2}}$$

(2.6)

Due to the conservation of transverse normalized emittance, the brightness is determined by the electron source. Thus, the transverse normalized emittance in a beamline is determined exclusively by the electron source, provided that only linear phase space transformations take place.

Which quantities determine the transverse emittance at the source? As shown in equations (2.6) and (2.7), a smaller electron emission area σ_x and lower temperature T of the generated electrons, results in a smaller ε_x. These two parameters, σ_x and T, are dictated by the geometry of the electron source and emission mechanism, respectively, as will be discussed in Chapter 2.2.

2.1.3. Transverse coherence

The rms transverse spatial coherence length σ_c is related to the rms transverse normalized emittance ε_x and the transverse rms beam size σ_x through the following formula [19]:

$$\sigma_c = \frac{\hbar}{m_0 c} \frac{\sigma_x}{\varepsilon_x} \tag{2.7}$$

Combining equation (2.4) and (2.7) yields an inversely proportional relationship between σ_c and σ_{p_x}:

$$\sigma_c = \frac{\hbar}{\sigma_{p_x}} \tag{2.8}$$

Here, $\hbar$ is the reduced plank constant, defined by $h/2\pi$. The uncorrelated angular beam spread, σ_θ, is defined as the ratio between σ_{p_x} and p_z, where p_z is the longitudinal component of the electron beam momentum.

$$\sigma_\theta = \frac{\sigma_{p_x}}{p_z} \tag{2.9}$$

Combining equation (2.9) and equation (2.8) generates the following equation:

$$\sigma_c = \frac{\hbar}{\sigma_\theta p_z} \tag{2.10}$$

Equation (2.10) indicates that, for a given electron beam energy, the smaller σ_θ, the larger σ_c.

The idea of the transverse spatial coherence length is conceived by the transverse distance over which propagating wave maintains the same phase difference among each wavelet at any given instant. The degree of the phase difference should be conserved as the beam propagates, unless external energy is applied to change the phase of each wavelet. Therefore, along a beamline, coherence is larger in regions where the beam size is large, and vice versa. This extensive property of the transverse coherence length can be understood from the wave optics point of view as illustrated in Figure 2.2.

In contrast σ_c, the global coherence G is a conserved quantity regardless of the electron beam size and defined by the ratio of σ_c to σ_x [20, 21]. G is a useful quantity that enables one to calculate σ_c for any given beam size. In coherent diffractive imaging (CDI) applications for example, which also requires highly coherent electron or X-ray beams, G is required to be more than 50 %. [22]

8

x-axis, transverse

Point
Source

transverse coherence length

transverse beam size

z-axis, longitudinal
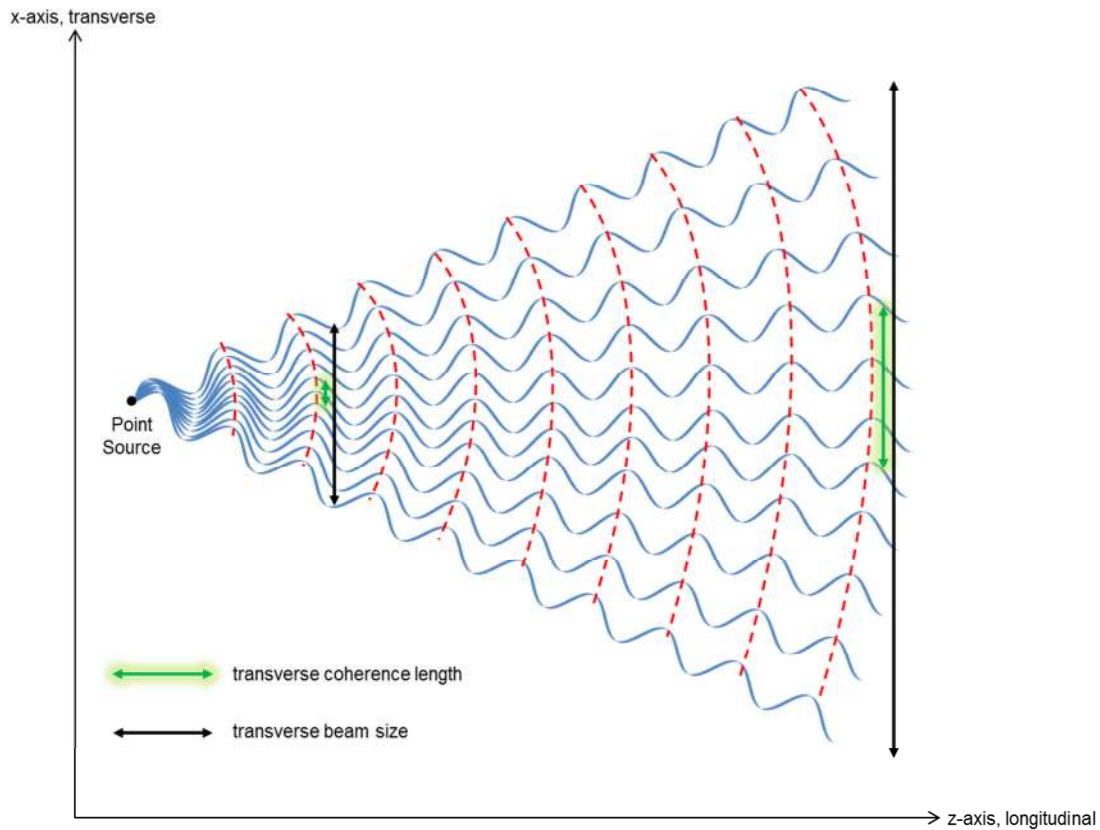
{Figure 2.2. Illustration of transverse coherence length. As the wave consisting of many wavelets propagate in the longitudinal direction from the point source, the transverse distance from one end to the other end of the wave (indicated by the black arrow) at a particular longitudinal location, increases because of the diverging property of the beam. Concomitantly, the distance maintaining the same degree of phase difference among each wavelet in transverse direction (indicated by the green arrow) increases, as the wave propagates.}

2.2. Electron emission mechanisms

2.2.1. Field emission

Unlike thermionic emission or photoemission processes which require emitted electrons to have energy greater than the work function of the cathode material, field emission allow for electron energy that is lower than the potential barrier at the vacuum/metal interface. Field emission is governed by the quantum mechanical tunneling effect, and the tunneling probability becomes larger with increasing applied electric field strength by reducing the tunneling depth. This unique electron emission mechanism allows for the field emitted electrons to have attractive physical properties, compared to those generated from other emission mechanisms. In field emission, conduction band electrons tunnel through the vacuum/metal interface potential barrier, and consequently the electron

temperature is significantly lower as compared to thermionic or photoemission, both of which are characterized by the "over-the-barrier" concept in classical mechanics. The Maxwell-Boltzmann distribution describing the particle distribution probability as a function of electron kinetic energy indicates that a distribution with lower mean temperature has a narrower kinetic energy spread ΔE_k [23]. In this regards, the field emitted electrons have a smaller ΔE_k compared to that of thermionic electrons or photoelectrons. As pointed out in equation (2.6), the transverse emittance of an electron beam is proportional to the square root of the electron temperature, indicating that the relatively cold electron beam resulting from field emission has a smaller transverse emittance as compared with beams generated by the other two emission mechanisms. In addition, owing to the required high field strength (>1 GV/m) to onset the field emission, the field emission cathode has the physical size typically less than 1 micrometer whereas thermionic cathode and photocathode have much larger source size. This small source size of the filed emitter provides a small emission spot area that can generate an electron beam with the small transverse beam size, leading to small transverse emittance.

Table 2.1 [24]. shows a comparison of electron emission parameters for different commonly used electron sources.

Parameters of Electron Source	Thermionic	Thermionic	Schottky Field Emitter	Cold Field Emitter
Cathode Material	W	LaB_6	ZrO/W (100)	W (310)
Operating Temperature (K)	2800	1900	1800	300
Normalized Brightness, ($A \cdot cm^{-2} \cdot sr^{-1} \cdot kV$)	1×10^4	1×10^5	1×10^7	2×10^7
Cathode Radius (nm)	60,000	10,000	<1,000	<100
Effective Source Radius (nm)	15,000	5,000	15*	2.5*
Energy Spread (eV)	0.59	0.40	0.31	0.26
Total Current (μA)	200	80	200	5
Operating Vacuum Conditions (mbar)	$<1 \times 10^{-5}$	$<1 \times 10^{-6}$	$<1 \times 10^{-9}$	$<1 \times 10^{-10}$
Typical Cathode Life (h)	100	>1000	>5000	>2000
Cathode Regeneration	Not required	Not required	Not required	Every 6 to 8 hours

{Table 2.1. Typical Electron Source Performance Comparison}

2.2.2. Fowler-Nordheim (FN) description of field emission and experimental data fitting

The quantitative description of the field emission process is given by the Fowler-Nordheim (FN) theory [24]. It is based on the following main assumptions [25]:

(i)   The cathode metal has a free-electron band structure obeying the Sommerfeld free electron model with Fermi-Direct statics.

(ii)   The cathode metal has a uniform work function ϕ independent of the external field.

(iii)   The calculation is considered only for a one-dimensional problem and performed for metal surface at T = 0 K.

(iv)   Outside the metal, the potential barrier is regarded as entirely due to the image force (= $e^2/16\pi\epsilon_0 x$), where, e, ϵ_0, and x denote elementary charge, vacuum dielectric constant, and the distance from the metal surface to the vacuum side.

Under these assumptions, the potential barrier is given by:

$$U(x) = \phi - eFx - e^2/16\pi\varepsilon_0 x \qquad (2.11)$$

where F is the applied electric field. The second term on the right hand side of the above equation indicates the Schottky lowering effect that bends the vacuum/metal interface potential with applied external field, and the third term is the image potential term makes a rounding effect of the lowered potential owing to its hyperbolic curved nature. It can be shown from the FN theory that the field emission current is given by [25, 26, 27]

$$I = Aa\phi^{-1}F^2\exp(-b\phi^{3/2}/F) \qquad (2.12)$$

where, $a\ (\cong 1.541\,434 \times 10^{-6}AeVV^{-2})$ and $b\ (\cong 6.830\,890\ eV^{-3/2}Vnm^{-1})$ are the so-called first and second FN constants, and A denotes the emission area. The above equation can be rewritten as follows, reflecting the relationship between the cathode biasing voltage (V) and the applied potential (F), $F = \beta V$, where β is the field factor:

$$I = (Aa\phi^{-1}\beta^2)V^2\exp(\frac{-b\phi^{3/2}}{\beta}\cdot\frac{1}{V}) \qquad (2.13)$$

This relation provides a clear description of the distinct *I-V* characteristic of field emission over

thermionic emission or photoemission. Plotting $\ln(\frac{I}{V^2})$ versus $\ln(\frac{1}{V})$ results in a straight line on a double logarithmic graph, which indicates that experimentally measured *I-V* data should follow a linear behavior if it is due to field emission. In practice, the experimental *I-V* data measured with a field emitter-to-gate bias voltage, V_{ge}, is fitted to the following approximation:

$$I = A_{FN} \left(\frac{V_{ge}}{B_{FN}}\right)^2 \exp\left(-\frac{B_{FN}}{V_{ge}}\right) \qquad (2.14)$$

where A_{FN} and B_{FN} are fitting parameters. These can be related to the field emission area *A* and the electric field at the tip apex, $F_{apx} = \beta V$ as follows [28]:

$$A \propto A_{FN} \qquad (2.15)$$

$$F_{apx} = b\phi^{3/2} B_{FN} / V_{ge} \qquad (2.16)$$

Measured *I-V* data is be fitted to equation (2.14), allowing the extraction of B_{FN}. Then, F_{apx} can be obtained from equation (2.16), and the field enhancement factor β can calculated. Overall, the fitting parameters A_{FN} and B_{FN} provide qualitative and quantitative comparison among field emitter devices.
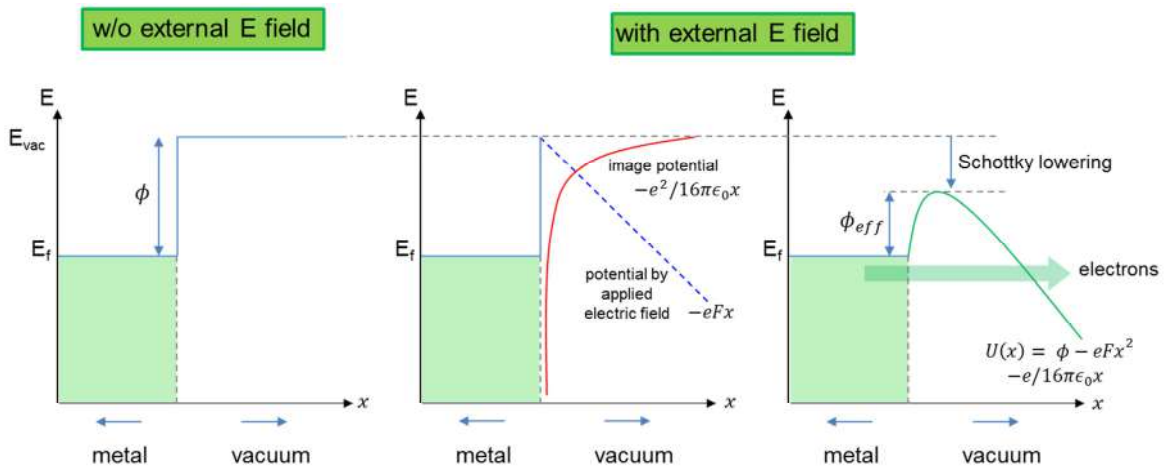
{Figure 2.3. Schematic illustration of field emission based on the Fowler-Nordheim (FN) theory. E_f, E_{vac}, ϕ_{eff}, ϕ, ε_0, and F denote Fermi energy of the emitter, vacuum potential, effective work function, work function, vacuum dielectric constant, and applied field strength, respectively.}

2.2.3. Photoemission

Unlike the field emission mechanism, photoelectron emission requires electrons with energy high enough to escape the potential energy barrier, as illustrated in Figure 2.4. Before the photoexcitation happens, no electrons can be liberated from a metal cathode because their energy is lower than ϕ_{eff}. Once photons with photon energy $\hbar\omega$, where ω denotes the light frequency, impinge on the metal, the energy distribution of conduction electrons changes such that conduction electrons gaining excess energy above ϕ_{eff} can escape from the metal surface.

The photoemission process from a metal cathode is described by the well-known Three-Step Model proposed by W.E. Spicer [29]. According to this model, photoemission is composed of three distinct processes: 1) photon absorption by the free electron inside the cathode bulk, 2) electron transport to the cathode surface, and 3) escape through the barrier [23]. The detailed theoretical description for this model is beyond the scope of this thesis, the focus here being a discussion of factors relevant to the quality of the photoemitted electron.

Given the fact that electrons must travel through the cathode surface according to the Three-Step model, the longitudinal momentum p_z of the electrons needs to satisfy the following relationship:

$$\frac{p_z^2}{2m_0} > E_F + \phi_{eff} \tag{2.17}$$

p_z is related to the total momentum p_{tot}, the internal energy of the electrons (before excitation) E, and σ_θ, through equation (2.18).

$$p_z = p_{tot}\cos\sigma_\theta = \sqrt{2m_e(E+\hbar\omega)}\cos\sigma_\theta \tag{2.18}$$

Combining equations (2.17) and (2.18) yields

$$\cos\sigma_\theta \geq \sqrt{\frac{E_F + \phi_{eff}}{E + \hbar\omega}} \tag{2.19}$$

Equation (2.19) clearly indicates that, for a given ϕ_{eff}, σ_θ is inversely proportional to the photon energy $\hbar\omega$, and therefore to the emittance as well.
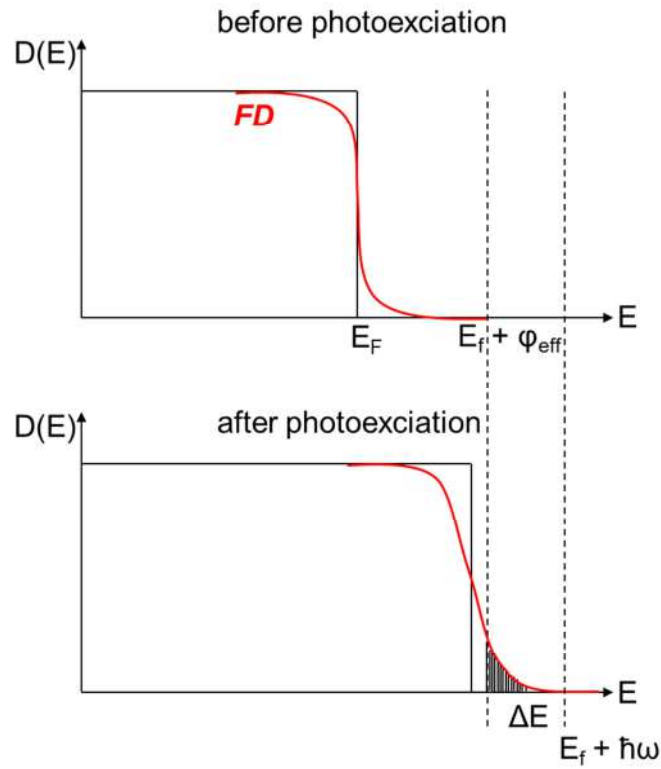
{Figure 2.4. Energy distribution (D) of electrons inside a metal cathode before and after photoexcitation. FD denotes Fermi-Dirac distribution curve. The shaded area indicates the photoelectrons emitted with finite ΔE_k.}
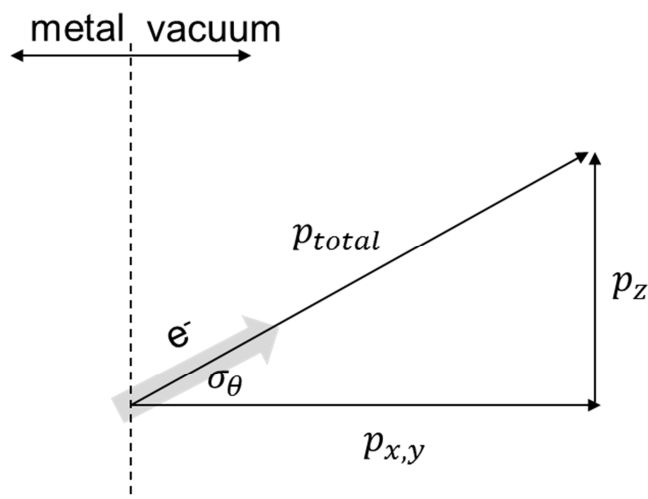
{Figure 2.5. Definition of σ_θ and p_z}

The quantum efficiency of a cathode material is defined as the number of electrons that are generated for a given number of impinging photons. Momentum phase space shown in Figure 2.6.

provides a graphical aid to understanding of the relation between photon energy and quantum efficiency. The blue circle defines the momentum of conduction electrons of a metal cathode before photoexcitation, and horizontal dotted line indicates the longitudinal momentum cut. The red circle indicates the momentum of the electrons after gaining excess energy after photoexcitation. Because of the large value of ω, the radius of the red circle for the higher photon energy case is larger. The shaded gray area defined by the momentum cut and the red circle indicates the number of the electrons that can escape from the cathode. The half of the central angle subtended by the arc of the red circle and momentum cut represents the σ_θ. From this Figure, it is clearly visible that both the quantum efficiency and emittance increases as photons with higher photon energy impinge on the cathode.
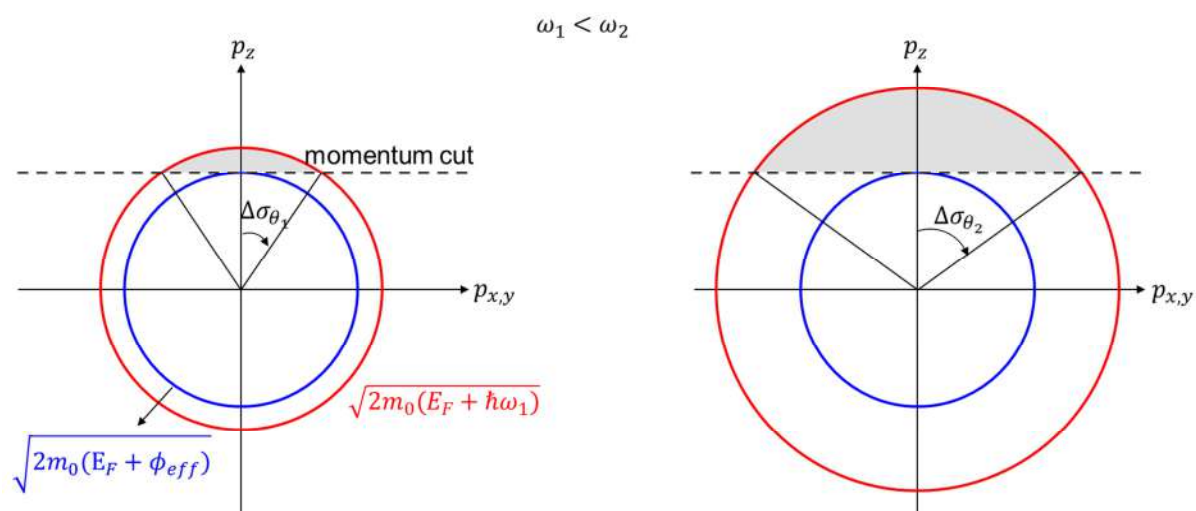
{Figure 2.6. Two-dimensional momentum phase space for two different photon energy case.]

2.3. Electron bunch length in time

In typical time-resolved ultrafast electron diffraction (UED) experiments, electrons are generated by irradiating a photocathode with ultrashort (in the order of few tens to hundreds of femtoseconds) laser pulses. The generated electrons are accelerated toward the anode, and then traverse a drift space until they reach the diffraction sample, as described in Figure 2.7. The temporal electron bunch length of interest in UED experiments is the one at the sample plane in that it is a limiting factor for the temporal resolution in the pump-probe type UED experiment.

The initial electron bunch length near the cathode is comparable to that of the laser triggering pulse length itself. As discussed in section 2.2.3, the photoemitted electrons have a finite kinetic

energy distribution ΔE. In contrast to photons propagating the free space with the speed of light, electrons travels the drift region with a different speed, depending on their kinetic energy: vacuum is dispersive for electrons ($v_z = \sqrt{2E_{kin}/m_0}$ for nonrelativistic electrons, where v_z is the electron velocity, m_0 is the electron mass, and E_{kin} is the electron kinetic energy). As a result, faster electrons with higher kinetic energy move towards the front of the bunch, while the slower (lower energy) electrons fall behind, leading to temporal broadening of the electron bunch during its propagation ({Figure 2.).
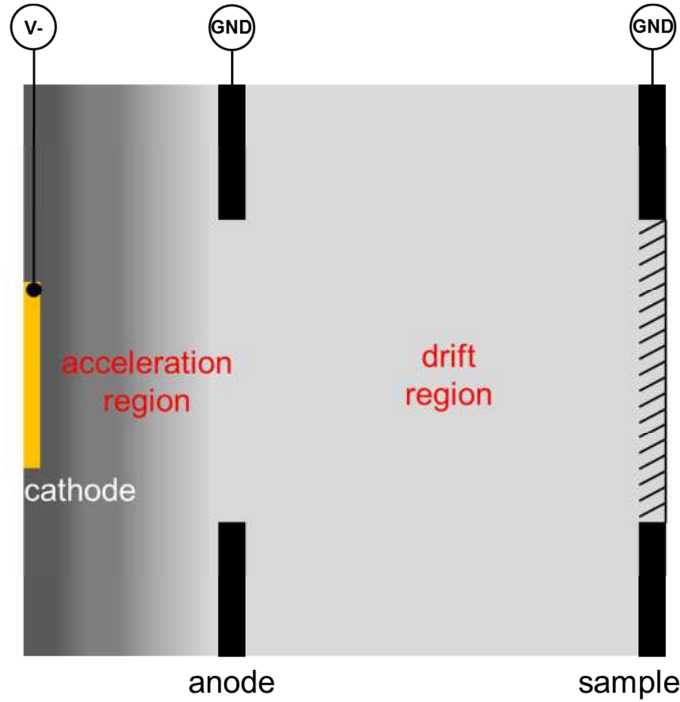
{Figure 2.7. Illustration of acceleration and drift region in UED setup.}

The dispersive broadening τ_d of an electron bunch with a disc-like bunch shape is given by [69]:

$$\tau_d \approx \sqrt{2m_0} \frac{(\sqrt{E_{kin,0} + \Delta E/2} - \sqrt{E_{kin,0} - \Delta E/2})}{eE_{acc}} \tag{2.1}$$

where, $E_{kin,0}$ is the mean electron kinetic energy immediately after photoemission and E_{acc} is the acceleration field applied between the cathode and anode. As implied from the above equation, for a given electron kinetic energy, the way to reduce the dispersive broadening is either by reducing the energy spread or by increasing the acceleration field. Given the fact that ΔE is determined by the difference bewteen the work function of the cathode material and the triggering laser photon energy,

optimization of these two variables will certainly lead to a small value of τ_d. In contrast, the other parameter E_{acc} is limited by the vacuum breakdown issue. For a DC electron gun, typical threshold before the breakdown is 15-20 MV/m while 100 MV/m can be achievable for RF gun case.
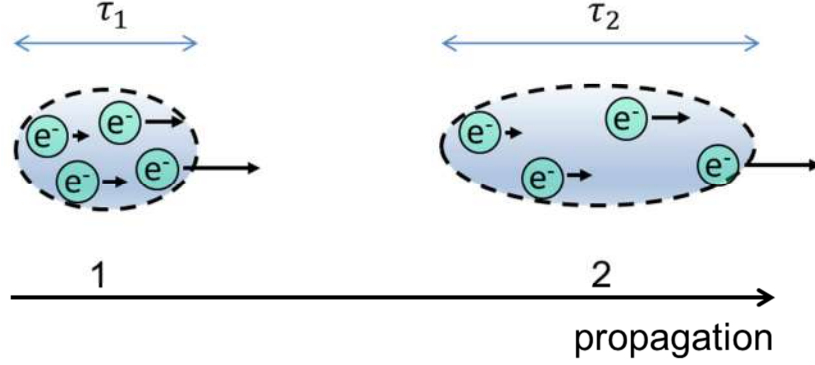
{Figure 2.8. Schematic illustration of the dispersive broadening of the electron bunch. τ_1 and τ_2 indicate temporal bunch length at point 1 and point 2, respectively. As the electron bunch at point 1 propagates toward to point 2, the bunch length is broadened due to the Coulomb repulsion.}

In addition to the electron kinetic energy spread, space charge effect also plays a decisive role in the temporal bunch broadening. Because of the charged nature of electrons, individual electrons inside the bunch repel each other (*i.e.*, Coulomb repulsion), leading to temporal broadening of the bunch as it travels in vacuum.

Considering that temporal resolution in UED is mostly determined by the electron bunch duration, it is important to calculate the expected bunch duration at the diffraction sample plane for a given setup design and electron beam parameters. For this calculation, ideally, one has to solve equation of motion for every electron in the bunch in a given electromagnetic field affected by the self-field generated by the charge distribution itself. Solving the closed-loop algorithm in which the electron distribution changes the field and the field changes the electron distribution, for the mutually interacting $10^4 - 10^5$ electrons (typical number of electrons per bunch in UED experiment), in a self-consistent way, yields a high computational cost, and therefore is intractable. Instead, the mean field approach where the particle-to-particle interaction is approximated by an averaged effect provides useful simulation results on the particle tracking [6]. In this way, the many-body problem can be simplified into a one-body problem, reducing the computation requirements.

Lastly, quantitative results regarding the electron bunch broadening on its propagation are shown in {Figure 2.. As a collective contribution of the kinetic energy spread and space charge effect, it is clear that the bunch starts to broaden in length (equally in time) rapidly even in the 100 μm long

propagation distance in the acceleration region. For the high charge and low energy electron bunch simulated in this case, the bunch broadening is expected to be more significant than low charge and relativistic electrons. In the drift space (normally the sample-to-anode distance), this bunch broadening effect is more significant. Another important feature of the electron bunch propagation dynamics (nonrelativistic case) is that a linear velocity chirp develops as it propagates, resulting from the electron redistribution inside the bunch as discussed in the above. This highly linear chirp of the electron bunch provides a valuable insight that linear dispersive elements can be exploited to compress the electron bunch, analogues to the prism in optics, and based on this knowledge, rebunching technique using RF field compression technique has been used for nonrelativistic [5] electron bunches to achieve temporal bunch length as short as less than 100 fs with 10^5-10^6 electrons.
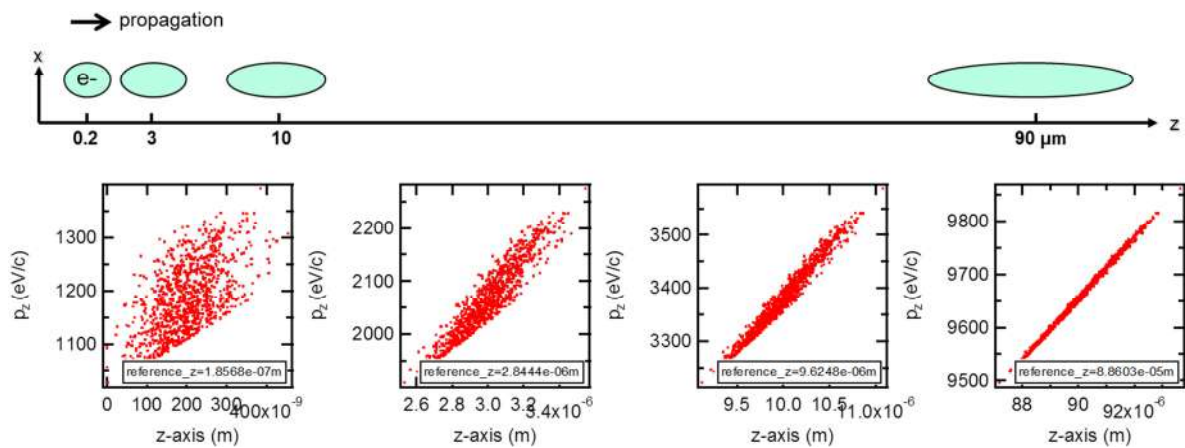
{Figure 2.9. ASTRA particle tracking simulation result for 1 keV electrons. It is assumed that 2×10^4 electrons per bunch propagate in a static electric field of 1 MV/m (in longitudinal z-axis direction) after 100 fs laser triggering on a gold photocathode}

3. Electron Source Development and Characterization

3.1. Nanofabricated all-metal double-gate single nanotip field emitter

3.1.1. Motivation

As explained in Chapter 2, electron beam brightness is determined by the electron source properties and emission mechanism, unless cooling or heating forces are applied during the beam propagation. Given that brightness is a function of beam current (i.e. number of electrons per unit time) and transverse emittance, optimizing these two factors are the ultimate goal for the development of ultrabright cathode. In other words, a cathode generating large beam current with small transverse emittance can be targeted as an ideal electron source.

What quantities determine the transverse emittance? Since the position-momentum space area that defines the transverse emittance is an invariant, this quantity is conserved on the beam propagation, and therefore, it is determined from the electron source. At the source where electrons are generated at the very beginning, the linear correlation between the position and momentum of the electrons assumed to be zero, yielding proportional relationship between the transverse emittance and the emission area or transverse momentum spread. A single atom cathode could provide ideally the smallest emission area as demonstrated in [30], however, it suffers from the low beam current (even less than one electrons per pulse), impractical to be used in the time-resolved electron diffraction for irreversible systems requiring at least more than 10^6 accumulated electrons to record a good quality single diffraction image. Metal nanotip cathodes [31-33] featuring few nanometer-sized tip apex can produce larger beam current due to the relatively larger emission area and high density of conduction band electrons [24] of about 10^{22} - 10^{23} cm^{-3}. In addition, the nanometer sized tip apex enhances electric field strength (*i.e.* field enhancement with the typical number of in the order of 10) when DC or AC (with optical field, antenna effect) electric field are applied, therefore possibly serving as a point-like source with a well-defined very small electron emission geometry. These physical features of the metal nanotip source consequently give rise to small transverse emittance, leading to a promising candidate in the development of an ultrabright cathode.

It is very important to discuss about the transverse coherence length in electron diffraction in investigating atomic structures of large unit cell systems (for example, protein crystals). A conventional method to attain a required large transverse coherence length in electron microscopes (for example, transmission electron microscope) is to limit the source size, by magnifying and clipping the beam by an aperture, as depicted in Figure 3.1. In this way, a region composed of highly

coherent wavelets is selected, achieving large global transverse coherence length (defined by the ratio of the local transverse coherence length to the beam size, see in section 2.1.3). However, this method indispensably gives rise to the significant sacrifice of beam flux and the total number of electrons comprising the electron beam or bunch, limiting either spatial or temporal resolution in time-resolved electron diffraction. This fundamental challenge motivates the development of a new class of cathode generating highly coherent electron beams from the source with sufficiently large beam current, *i.e.* the development of ultrabright cathodes.
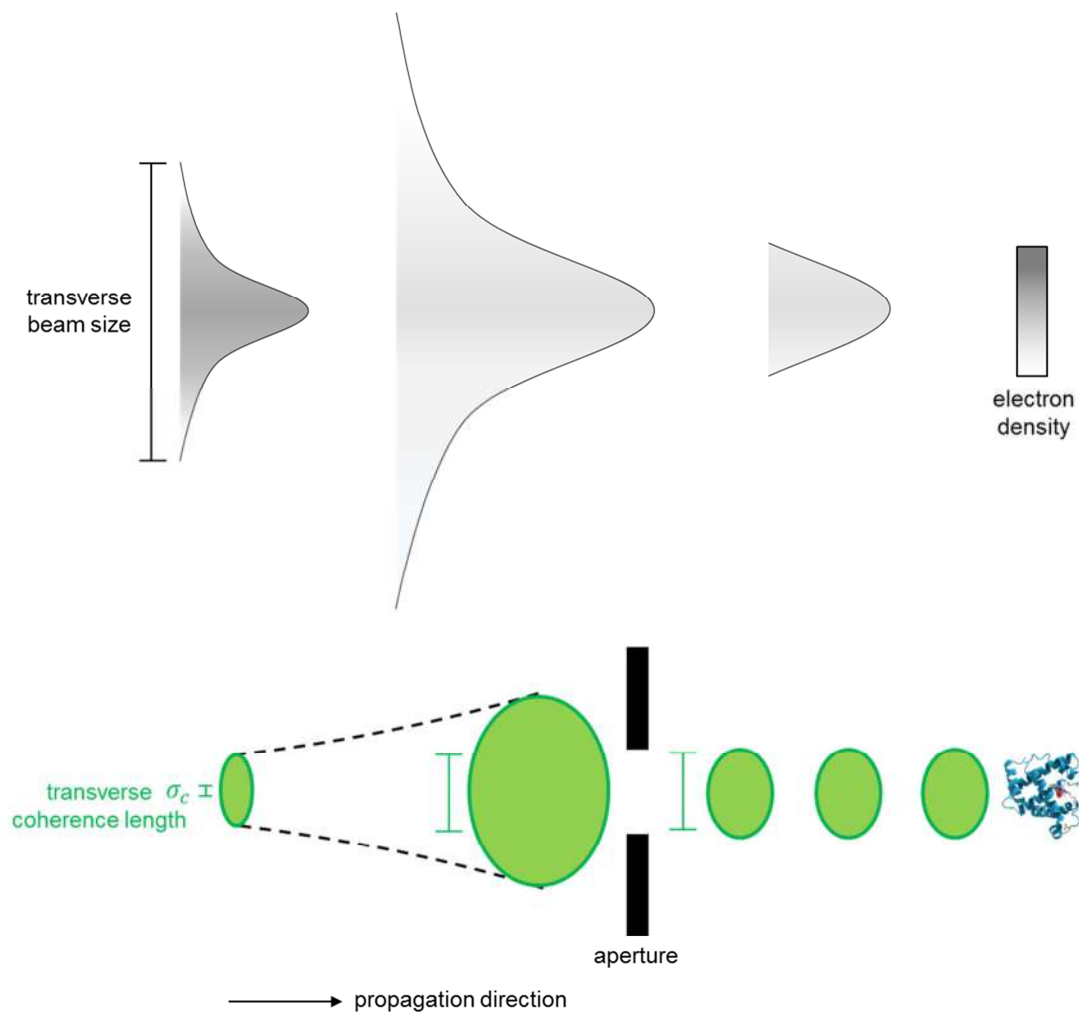
{Figure 3.1. Illustration of the conventional method to attain large coherence beam in electron microscopy}

Fabrication method of metal nanotip cathodes has been well-established [34]. The simple chemical etching technique is used to shape a few nanometer sized cathode geometry out of a bulk metal structure. However, the beam current still remains in the order of nA even though the highest

beam brightness has been reported [35] from this type of cathode. In addition, implementation of the etched needle-shaped nanotip cathodes in electron microscope or diffraction apparatus, requires additional electron optical elements [36] in that this type of sources should be under a high acceleration electric field, on the order of 10–100MV/m, i.e., the maximum extraction field conditions for minimum space charge broadening to conserve the beam brightness with the highest bunch density possible [28]. In this regard, it is advantageous to come up with a gated structure of nanotip cathode that can shield the acceleration field, and the fabrication method of such device has been well established [37,38 39] in a form of field emitter array, called Spindt type cathode [40], following the first inventor of this device.

The double-gated nanotip field emitter is a more advanced device. Integrated with electron extraction and collimation gate in a stacked manner on top of the nanotip field emitter as shown in Figure 3.2, this device can generate a field emission beam in the on/off manner with the application of a gate potential on the order of 100V independently from the acceleration field. Moreover, owing to the collimation gate, the generated electron beam can be highly collimated from the source, eliminating the need to implement a lens system in electron diffraction [41].
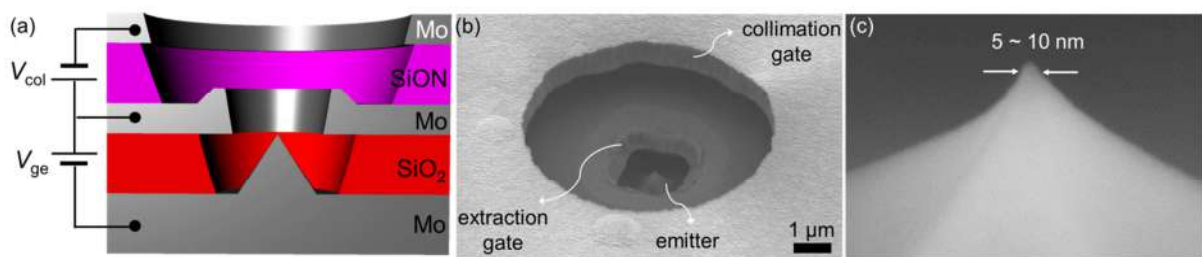
{Figure 3.2. (a) Schematic illustration of the cross-sectional view of the double-gate nanotip field emitter. V_{ge} and V_{col} indicate the gate-emitter voltage and collimation gate voltage, respectively. (b) perspective view of the scanning electron microscope (SEM) image of the double-gate emitter and (c) zoomed view focusing on the nanotip apex}

Fabrication of double-gate metal nanotip array devices based has been developed by Dr. Soichiro's group at PSI with unique micro- and nanofabrication methods. This method is replicated in this thesis work to the single nanotip case.

3.1.2. Device fabrication

Fabrication of the double-gate single nanotip field emitter device exploits various nano- and microfabrication techniques well established in semiconductor industries. The total number of steps included in the entire fabrication process is over 30, which takes approximately 3-4 weeks to reach the

final chip dicing step starting from a bare silicon wafer, provided that there is minimal time loss from machine breakdown, overbooking, and a delay from technicians' side. The single nanotip fabrication steps are basically the same to those of the nanotip array device except the point that some parameters in electron beam lithography and mask types in photolithography are different. The detailed fabrication method for the array device is published by E. Kirk *et al*. [42] and P. Helfenstein *et al*. [43]. In the present Chapter, key steps focusing on the single nanotip fabrication process are introduced. Frequent checking of the fabricated structures by optical microscopy and scanning electron microscopy (SEM) and measurement of the film quality and thickness in every step can avoid a possible defective that might be found in the last step, resulting in a waste of the entire labor effort and time. Also, using a dummy wafer is a good choice to calibrate etching or deposition rate.

The device fabrication steps are largely categorized in three parts: 1) preparation of the mold by molding technique, 2) first gate (extraction gate) fabrication by self-alignment process, and 3) second gate (collimation gate) fabrication by electron-beam lithography.
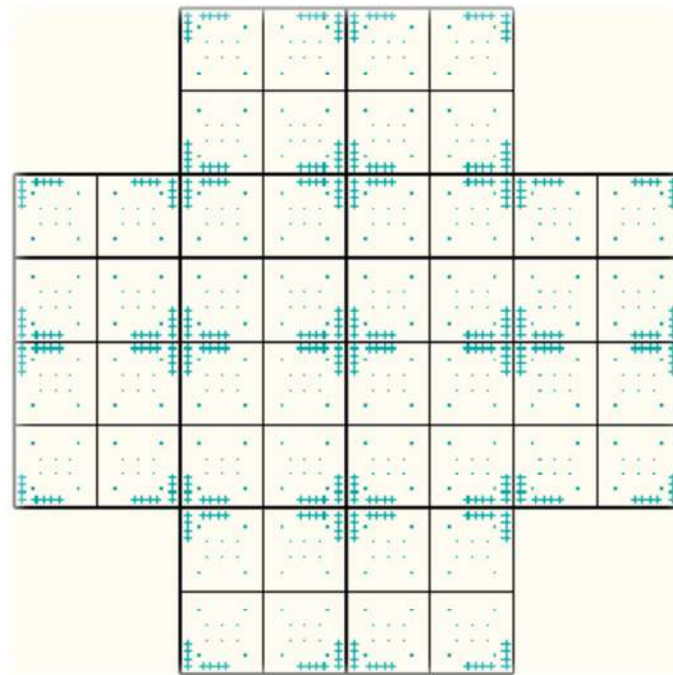
{Figure 3.3. Photolithography mask design for patterning the mold}

22

To fabricate the single nanotip field emitter, a 4-inch bare silicon wafer (100) with thickness of 380 µm is used. As the very first step, a 100 nm thick thermal oxide film is deposited on one side of the wafer, where spin-coating of photoresist and subsequent photolithography are conducted to pattern the nanotip locations and alignment markers (Figure 3.3) needed during gate fabrication steps. The patterned wafer is dry-etched by a reactive-ion etcher (RIE, Oxford RIE 100) such that the oxide layer is removed only on the patterned and exposed area. After removal of the residual photoresist by acetone and isopropanol, the dry-etched wafer is immersed in a hot potassium hydroxide (KOH) bath. In this step, the remained oxide layer plays a role as a hard mask such that only the patterned region is etched away by the KOH solution. Because of the different etch rate along the [100] and [111] plane of the silicon wafer for the KOH etchant, a V-shaped groove with a few tens of nm sized-joint is formed at every nanotip location, Figure 3.4. The size of the joint is further reduced by depositing a second thermal silicon oxide layer after removing the first layer by buffer-oxide etching (BOE), as seen in Figure 3.5 (a). After then, the groove is entirely filled with a Mo layer by magnetron sputtering in an argon environment (Nordiko), as seen in Figure 3.5 (b). The argon base pressure and the film thickness deposited affect the stress of the metal film, which cracked sometimes, resulting from wrong deposition conditions. The metalized silicon wafer is subsequently back plated by electroplating of Ni after depositing adhesion layers (Ti and Pd). The schematic illustration of the molding technique is depicted in Figure 3.6.
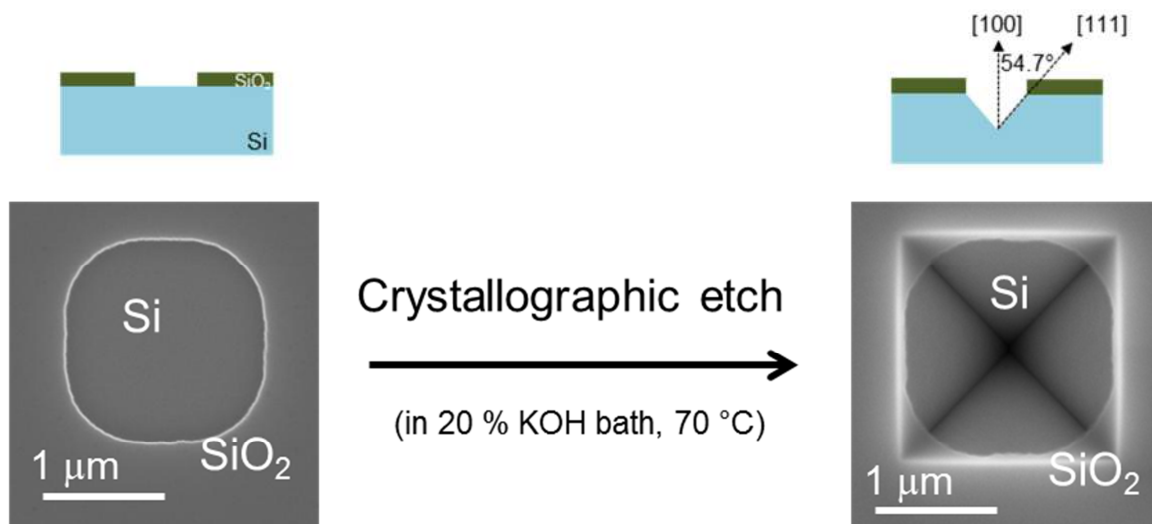
{Figure 3.4. Schematic illustration of the crystallographic etch of the (100) silicon wafer}
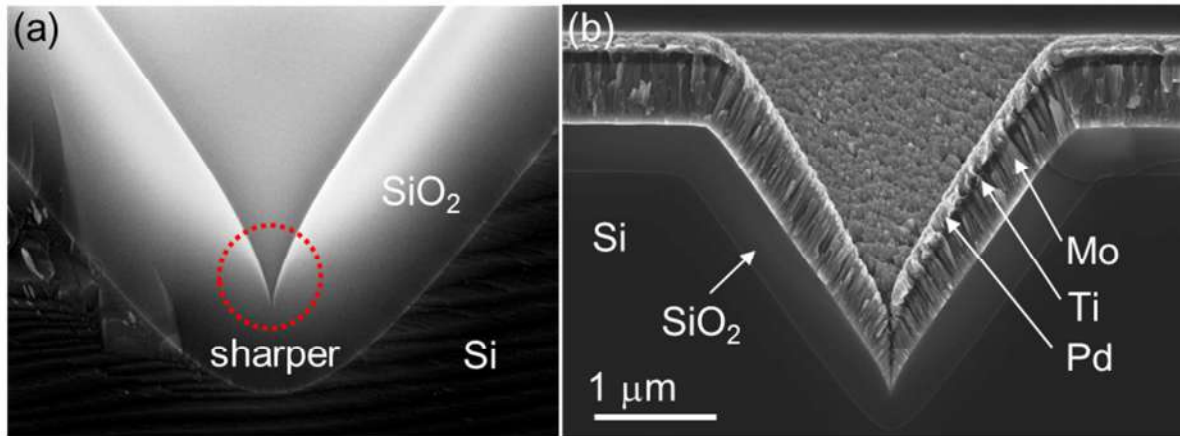
{Figure 3.5. Cross-sectional view of the SEM image for the mold at the nanotip location before (a) and (b) after filling}
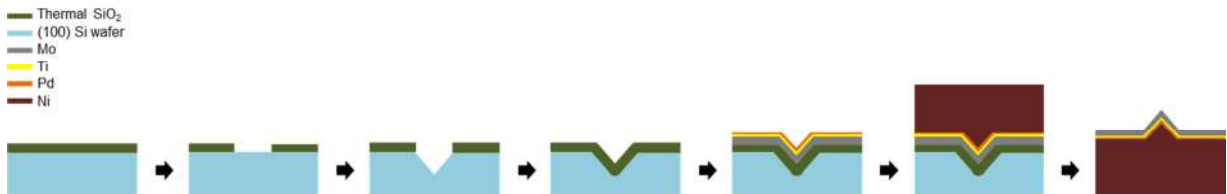
{Figure 3.6. Schematic illustration of the molding technique}

After the electroplating step, the silicon wafer and the thermal oxide layer are completely removed by KOH etching. This step is called demolding. The fabricated structure has a pyramidal shaped emitter typically with 5-10 nm emitter tip apex size as shown in Figure 3.2 (c). The Ni substrate with Mo single nanotips (called "mold") are diced into several chips to be used in the further gate fabrication process.
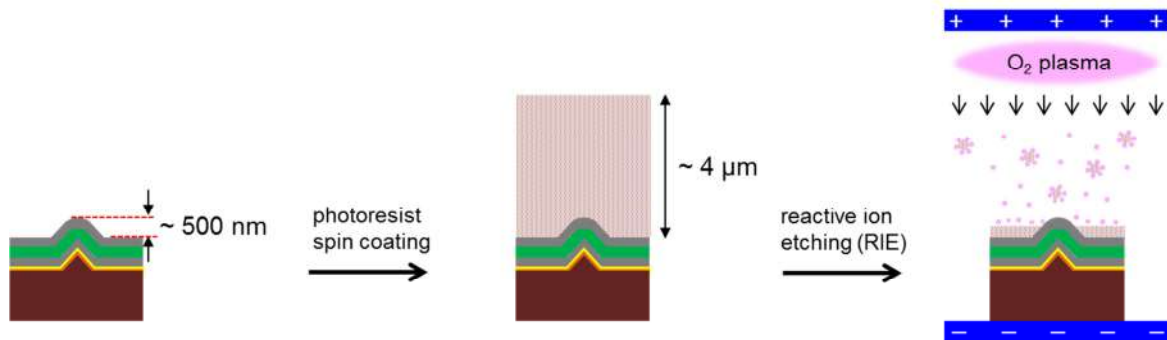
{Figure 3.7. Schematic illustration of the self-alignment process}

The next fabrication process is the so-called "self-alignment" process for extraction gate fabrication. As a first step for this process, approximately 1.2 µm thick plasma-enhanced chemical vapor deposition (PECVD) silicon oxide and 500 nm thick sputtered Mo layer are deposited sequentially on the diced chip (on the side where nanotip emitters are located). The SiO_2 and Mo layer play a role as an insulating and extraction gate layer, respectively. After then, the chip is flattened by spin-coating with a 4 µm thick photoresist. The spin-coated photoresist is uniformly thinned down from the top of the resist by RIE etching as illustrated in Figure 3.7. Once the RIE etching is stopped at a particular time point, only a small area of the structure can be exposed as shown in Figure 3.8 (a). The quasi-spherically exposed structure shown in Figure 3.8 (a) is the extraction gate layer, and the others are remaining photoresist. Then, this exposed area is etched away by a metal etchant, resulting in a "self-aligned" extraction gate aperture hole on the nanotip emitter, shown in Figure 3.8 (b). The aperture hole size is controllable by changing the RIE etching time so that from smaller to larger aperture can be fabricated. The typical size of the extraction gate aperture is approximately 1.5 µm. The extraction gate pad for electrical biasing is patterned on the fabricated chip by photolithography. The schematic illustration of the entire process for the extraction gate fabrication is depicted in Figure 3.9.
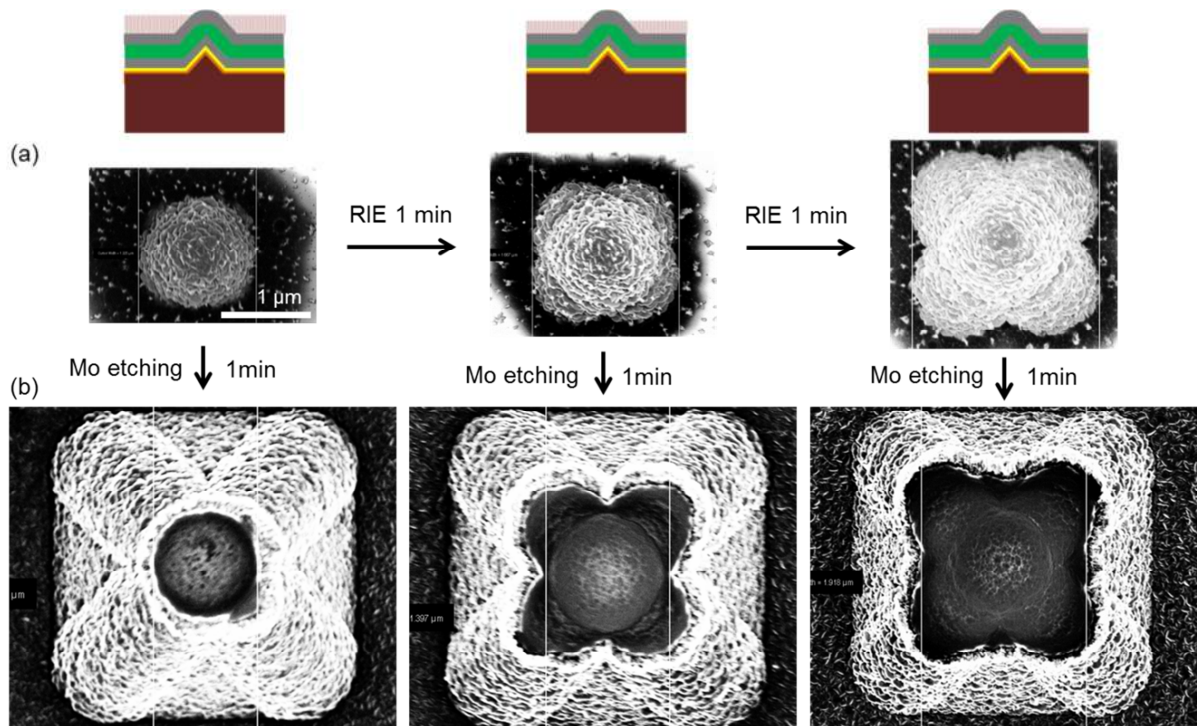
{Figure 3.8. SEM images after (a) resist-thinning step and (b) extraction gate aperture opening step}

25

{Figure 3.9. Schematic illustration of the extraction gate fabrication process}
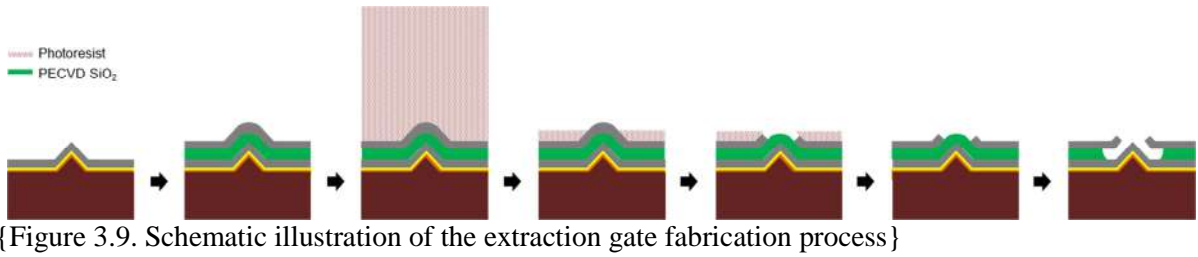
The collimation gate fabrication starts with the deposition of a 1.2 µm thick PECVD SiON layer and a 500 nm thick sputtered Mo layer, sequentially, on the as-fabricated chip prepared from the previous step. The SiON and Mo layer play a role as an insulating and collimation gate layer, respectively. Subsequently, 600 nm thick electron beam resist is spin-coated on the collimation gate layer, and then electron beam is exposed to the gate aperture position. In the electron beam lithography step, topological markers simultaneously fabricated in the molding steps are exploited to align the electron beam exposure position with respect to the gate aperture position, as shown in Figure 3.10. After development, only the exposed area is opened and the resist remains on the rest of the chip. Using the remained resist as a soft mask, the collimation gate aperture is opened by either wet-etching or dry-etching. The typical size of the collimation gate aperture is approximately 6 µm (Figure 3.11). The collimation gate pad for electrical biasing and the biasing hole for the extraction gate are patterned by photolithography. The schematic illustration of the entire process for the collimation gate fabrication is depicted in Figure 3.12.
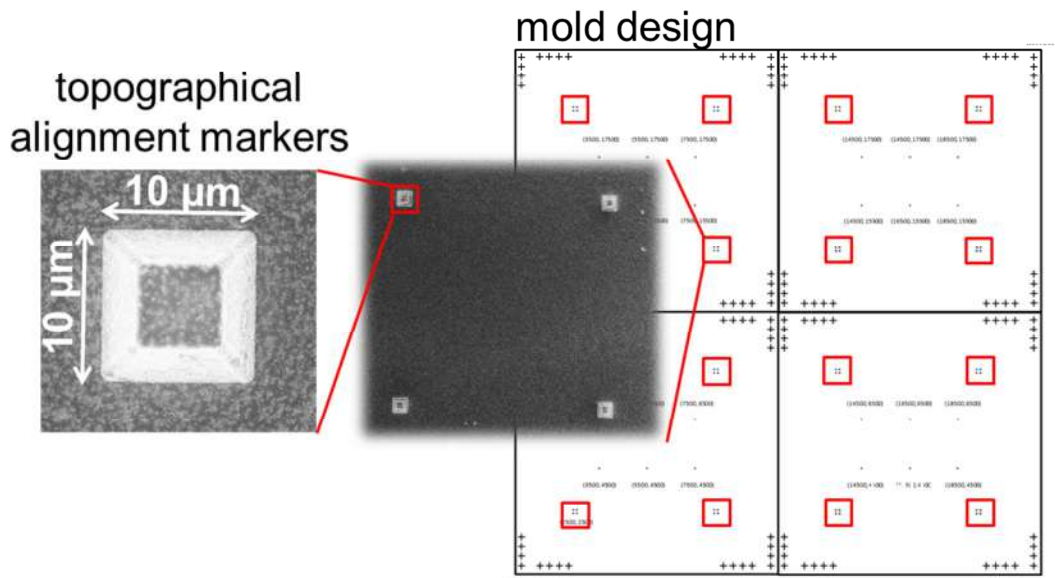
{Figure 3.10. Topographical alignment markers used in the electron-beam lithography process}
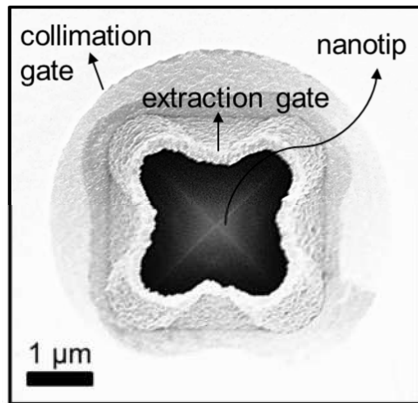
{Figure 3.11. SEM image after etching of the collimation gate aperture and the remained protected layers (SiO$_2$ and SiON)}
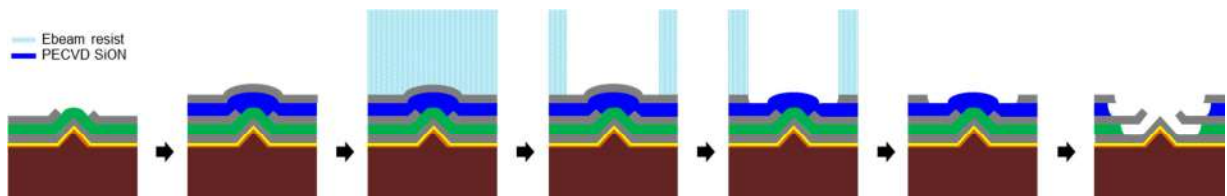
[Figure 3.12. Schematic illustration of the collimation gate fabrication process]

The fabricated chip is diced into 7 mm by 7 mm pieces, where totally six double-gate single nanotip emitters are located. Each diced piece is BOE etched to remove the remaining SiO$_2$ and SiON layers near the nanoips. Before measurement, the device is wire-bonded with 200 um thin Al wires for totally 12 electrical contact points including 6 extraction and 6 collimation gates (Figure 3.13).
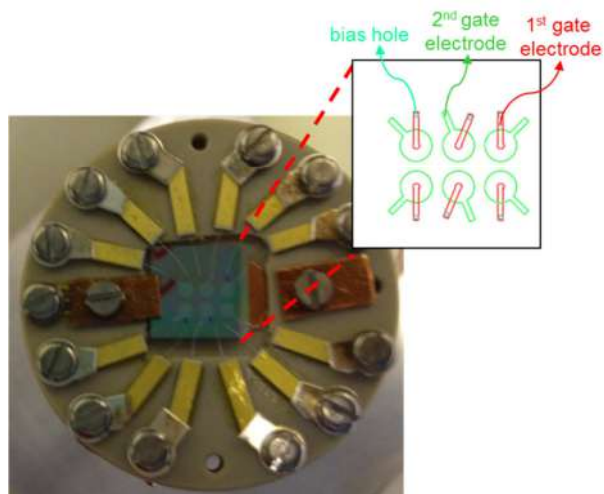
{Figure 3.13. The final diced chip mounted on a chip holder after wire-bonding}

3.1.3. Device characterization[†]

This section describes the first characterization of field emission and beam collimation properties of the double-gate single nanotip field emitter. In this work, two nanotip emitters with different geometrical features are compared in terms of *I-V* characteristic, beam current conservation characteristics upon beam collimation, and space charge-induced-beam brightness degradation. The main messages of this work are summarized as follows:

1) Maximum 4.04 µA of field emission current generated from the double-gate single nanotip device is observed, a phenomenally high value from about a 10 nm sized electron source.

2) A maximum collimation condition reduces the beam size about a factor of 10, leading to the enhancement of the beam current density approximately about one order of magnitude.

3) An optimized gate structure provides an excellent beam current conservation property on the beam collimation: about 70 % of the beam current is conserved by the electrostatic shielding effect due to a tall collar structure surrounding the extraction gate aperture.

4) Upon the maximum collimation condition, a space charge dominated beam with microamp beam current is observed, resulting in an obvious beam size expansion compared to the case of the nanoamp current beam. Higher acceleration field (10-100 MV/m) could solve the issue by quickly increasing longitudinal velocity of the electron beam before the space charge induced beam expansion occurs.

[†]adapted from C. Lee et al., J. VAC. SCI. TECHNOL. B **33**, 03C111 (2015)

3.1.3.1.   Abstract

Field-emission and beam collimation characteristics of single metal nanotip devices with double-gate electrodes are studied. Applying a previously developed method to fabricate all-metal double-gate nanotip arrays with a stacked on-chip extraction G_{ext} and collimation G_{col} gate electrodes with the large G_{col} apertures, we produced single double-gate nanotip devices and measured their beam characteristics. Excellent beam collimation capability with minimal reduction of the emission current and the enhancements of the current density up to a factor of ~7 was observed. The results indicate that these single nanotip devices are highly promising for electron beam applications that require extremely high brilliance and coherence.

3.1.3.2.   Introduction

Ultrabright cathodes are critical elements in a broad range of applications such as cathodes for X-ray free electron lasers as well as time-resolved electron microscopy and diffraction experiments that aim at resolving the dynamics of materials and molecules on the atomic length and time scales. One of the core requirements for such cathodes is the generation of a low emittance electron beam with high current to ensure the delivery of sufficient current to the target. For such applications, metal nanotip field emitters [31-33,43-47] are attracting considerable interest recently as high brilliance cathodes that may outperform state-of-the-art photocathodes. This is because metal nanotips allow high emission current with narrow energy spread *via* quantum tunnelling of electrons through the surface barrier at the nanometer scale emitter tip apexes. One can also generate ultrafast electron pulses by exciting the metal nanotips with ultrafast laser pulses. [31-33,44-47] So far, etched-wire needle-shaped field emitters prepared by electrochemical etching and in-situ thermal treatment have been the most widely studied. [31,32,44-46] However, for high charge, high beam brilliance applications, the cathode must be used under a high acceleration electric field, on the order of 10-100 MV/m, i.e., the maximum extraction field conditions for minimum space-charge broadening to conserve the beam brilliance with the highest bunch density possible. This makes the nanofabricated metal nanotip emitters with on-chip gate electrodes attractive for many applications since the electron emission can be switched with the application of a low gate potential on the order of 100 V independently from the acceleration field. [9,10] In fact, integration of the single-gate field emission array (FEA) into a combined diode-RF cavity electron gun and stable sub-nanosecond pulsed field emission operation under the acceleration field up to 30 MV/m has been reported recently. [48]

Further, highly collimated electron beams can be generated from double-gate FEAs by adding a collimation gate electrode on top of the electron extraction gate electrode and individually collimating the field emission beamlet [43,49]. We note that this is crucial to generate the high

intrinsic brilliance FEA beam. [17, 18] The intrinsic transverse beam emittance of a single beamlet, given by the rms radius R_{tip} of the emitter tip apex and the angular divergence equal to ~30°, is in the order of 10^{-3} mm-mrad. This extremely small value is a consequence of the small R_{tip} in the nanometer range. In the case of single-gate FEAs with the large target current of several amperes, the transverse beam emittance is in the order of 1 mm-mrad. However, the transverse emittance can be much reduced with double-gate FEAs. By decreasing the angular beam divergence of the individual beamlet by an order of magnitude, [43,49] the double-gate FEA beam can potentially achieve an intrinsic emittance lower than that of state-of-the-art high brilliance photocathode (equal to ~0.2 mm-mrad with the cathode radius of 0.5 mm).

The excellent beam collimation capability of double-gate FEAs with a large collimation gate aperture was experimentally demonstrated recently. [8] An order of magnitude enhanced beam intensity was observed from a 4×10^4 tip double-gate FEA at the maximally collimated condition. Together with the compatibility with high acceleration electric field extraction and the possibility to generate ultrafast electron pulses using near infrared ultrafast laser excitation, these FEAs are highly promising as ultrabright electron sources that may open up new applications in femtosecond time resolved applications. [47]

In this work, we study the field emission and beam collimation properties of single nanotip double-gate emitters to investigate the characteristics of the individual nanotips that were only inferred in the previous experiments on arrays. Such investigation is important on one hand to further improve the beam collimation properties and beam uniformity for scaling to arrays, and on the other hand, to explore the applicability of such metal nanotips for high brilliance beam applications.

3.1.3.3. Sample and Experiment

Two double-gate single nanotip devices (FE1 and FE2), see Figure 3.14. and Table 3.1, studied in this work were fabricated by adapting the fabrication method for arrays of double-gate emitters. [43,50] It starts with the preparation of molybdenum nanotips by the molding method using the oxidized Si wafer where pyramidal pits are patterned on its surface. [51] The emitters are pyramidal shape with ~1.5 µm base size and with the emitter tip apex radius of curvature in the range of 5-10 nm, see Figure 3.14 (c) inset. On top of the emitter substrate the extraction gate electrode G_{ext} and the collimation gate electrode G_{col} were fabricated. The gate electrodes were patterned from 0.5 µm-thick molybdenum layers. The emitter substrate and G_{ext} are separated by a ~1.2 µm-thick SiO_2 layer, and G_{ext} and G_{col} are separated by a ~1.2 µm-thick SiON layer. The G_{ext} apertures were patterned by the self-aligned process. A collar structure surrounds the G_{ext} aperture edge, which is height-controllable by adjusting mask-etching and wet-etching duration of the self-aligned G_{ext} aperture patterning step. The G_{col} apertures with 3-5 times larger aperture diameter than that of G_{ext} were patterned by electron

beam lithography. On a 7 mm-square chip, 6 such double-gate single nanotips were fabricated. For the experiment, each chip was mounted on a sample holder, wire-bonded for the gate contacts with Al-wires with the diameter of 20 µm, and loaded into a measurement chamber equipped with a phosphor screen and a retractable Faraday cup (FC) with a back ground pressure of $(0.5\text{-}1.5)\times10^{-8}$ mbar.
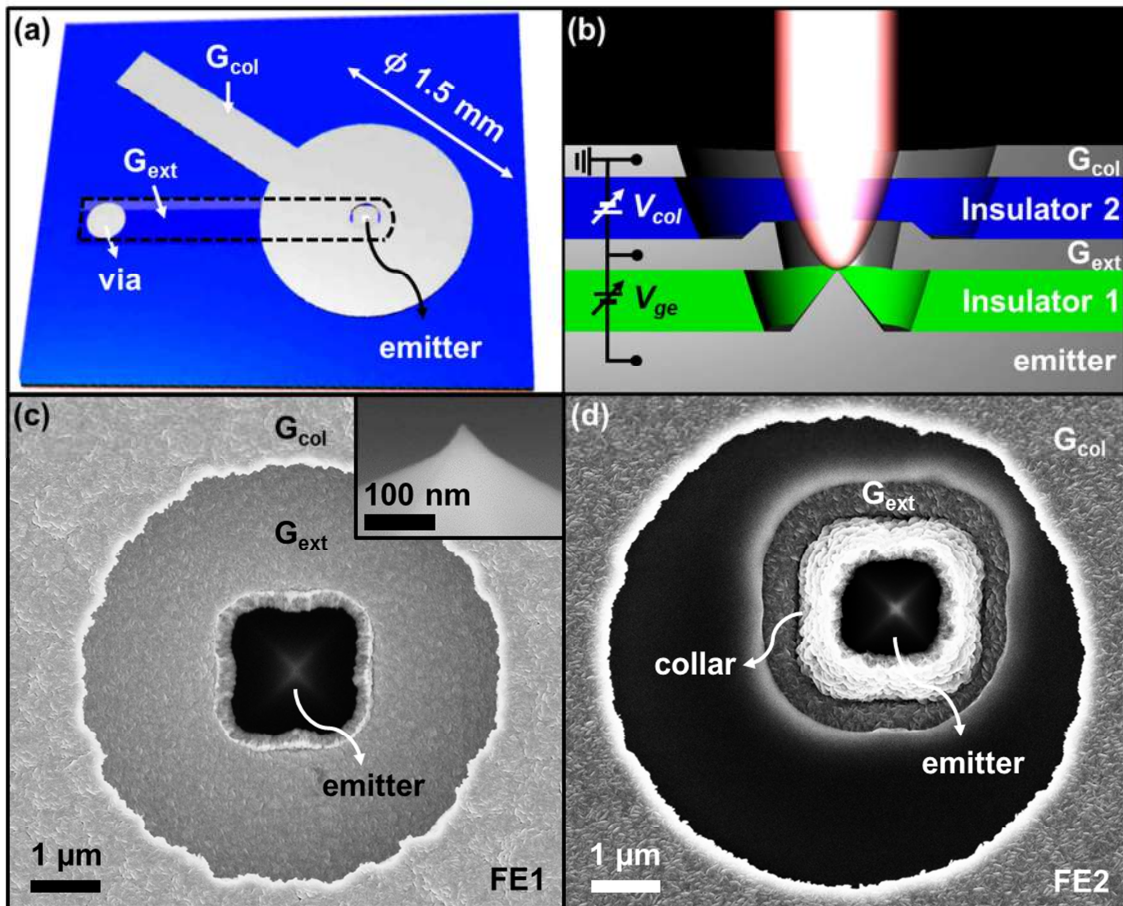
{Figure 3.14. (a) Top-view and (b) cross-sectional-view schematic diagram of the double-gate single nanotip emitter device. In (a), the dotted line indicates the G_{ext} electrode buried underneath the insulator 2. The electrical contact to G_{ext} is provided through via hole through the insulator 2. The G_{col} electrode is a 1.5 mm-diameter circular shape with a rectangular contact pad. In (b), the schematic trajectory (envelope) of the maximally collimated beam with V_{col} equal to $\sim(-V_{ge})$ is shown. (c) and (d) show the SEM image of FE1 and FE2, respectively. Inset of (c) shows the high magnification SEM image of emitter tip apex of FE1 observed with the viewing angle of 47°.}

	FE1	FE2
G_{ext} aperture diameter (µm)	1.69	1.43
G_{ext} collar thickness (µm)	0.25	0.56
G_{col} aperture diameter (µm)	5.97	6.85
Aperture diameter ratio	3.5	4.8
Emitter lateral offset (µm)	0	0.8

{Table 3.1. Structural parameters of FE1 and FE2. The lateral offset of the emitter is measured from the center of G_{col} aperture.}

The field emission beam was measured as a function of the electron extraction potential V_{ge} and the beam collimation potential V_{col} under DC or pulsed conditions. When a negative collimation potential V_{col} is applied between G_{col} and G_{ext} while generating the field emission beam by applying a positive electron extraction potential V_{ge} between G_{ext} and emitter, see Figure 3.14 (b), the angular divergence of the beam is substantially reduced. In the case of the DC measurements, we connected G_{ext} to ground potential and applied $-V_{ge}$ to the emitter substrate and V_{col} (<0) to G_{col}. The DC gate potentials were applied using source-measure units (Keithley 2400) and scanning the voltages with 20 ms steps. For the pulse measurement, we connected G_{col} to ground and applied $-V_{col}$ to G_{ext} and $(-V_{ge}+|V_{col}|)$ to the emitter substrate. The pulsed potential, with a typical duration of 200 µs, was generated using a custom-built double-pulser. [52] The field emission current was measured either directly by inserting the FC in front of the device with a separation of 10 mm or from the integrated beam intensity of the beam images observed on the phosphor screen (calibrated by the current measured with the FC). The beam image was measured with the phosphor screen at the screen potential of 2.5 kV when the device was placed 50 mm from the screen. For the beam measurements, we captured the phosphor screen image generated by pulsed field emission using a synchronously triggered CCD camera with an effective resolution of 16-bit. Care was taken to avoid saturation of all pixel values to be able to evaluate the relative field emission current of the beam as well as the root-mean-square (rms) radius denoted by dashed white circle in the images in Figure 3.16 and Figure 3.17. The emission current and beam image data presented below were recorded after several hours of

32

conditioning that was done by scanning V_{ge} between 0 V and 100 V until the field emission current-voltage characteristics became stable.

3.1.3.4.   Results and Discussion

Figure 3.15(a) shows the relation between the field emission current I and V_{ge} at zero V_{col} for FE1 and FE2. The observed I-V_{ge} characteristics of the devices above the noise level (~0.5 nA for the FE1 measurement and ~0.2 nA for the FE2 measurement) were described well by the equation,

$$I = A_{FN}(V_{ge}/B_{FN})^2 \exp(-B_{FN}/V_{ge}) \tag{3.1}$$

as shown by the curves in Figure 3.15(a). The fitting parameters A_{FN} and B_{FN} were equal to 1.6×10^{-4} A and 1000 V for FE1, and 2.95 A and 997 V for FE2, respectively. The same B_{FN} values of the two emitters (within ~10% of the estimated uncertainty) indicate the stability of the tip fabrication process since B_{FN} is largely determined by the tip apex radius of curvature R_{tip}; from the comparison of the observed B_{FN} value and the calculated emission characteristic as a function of R_{tip}, [42] we found that the estimated R_{tip} are equal to ~10 nm for both devices that is consistent with the high-resolution SEM image of the emitter tip apex (Figure 3.14. (c) inset).

In Figure 3.15(b), we show the field emission current at finite V_{col}. V_{ge} was fixed at 130 V for FE1 (open triangles). For FE2, two sets of measurements with V_{ge} of 90 V (open squares) and 110 V (open circles) are displayed. In Figure 3.15(b), we denote V_{col} by the ratio k_{col} defined as,

$$k_{col} \equiv -V_{col}/V_{ge} \tag{3.2}$$

In the case of FE1, the emission beam current was diminished to 18 % of the uncollimated beam current ($k_{col} = 0$) already when k_{col} was equal to 0.3, implying that much of the electric field at the emitter tip apex applied via V_{ge} is relaxed by V_{col}. Increasing k_{col} to 0.94 resulted in the emission current equal to 4.7 % of the uncollimated beam current. Further increase of k_{col} to 0.96 results in the decrease of the emission current by several orders of magnitude. In contrast, in the case of FE2, more than 70 % of the uncollimated beam current was maintained at k_{col} of 0.94. At the same value, the peak current density was maximum as shown below (see Figure 3.18). We ascribe the improved current conservation characteristic of FE2 to the structural features of gate apertures of the device; compared to those of FE1, the ~400 nm-taller-collar in height, surrounding G_{ext} aperture, together with the ~1 µm-larger-G_{col} aperture diameter provide additional electro-static shielding of the emitter tip apex by preventing direct line-of-sight from the tip apex from G_{col} aperture, [43,49] and reducing the influence of V_{col} on the emission current.
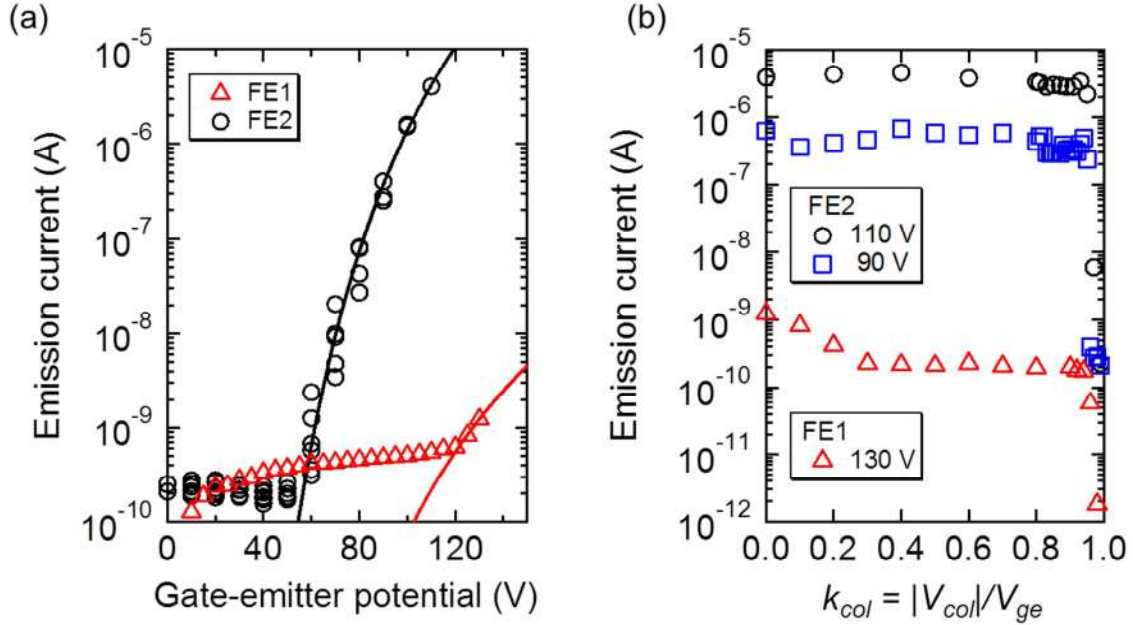
{Figure 3.15. Field emission characteristics of double-gate single nanotip emitters. (a) The relations between the field emission current and V_{ge} at zero collimation potential for FE1 (triangles) and FE2 (circles). Curves are the fitted result of the data above the noise level with the Fowler-Nordheim function. (b) The relations between the field emission current and the collimation potential ratio k_{col}.}

Figure 3.16 presents the selected field emission beam images of FE1 for k_{col} between 0 and 0.98 when V_{ge} was equal to 143 V. The uncollimated beam with zero k_{col} showed two separated spots with different beam intensities. Interestingly, as we increased k_{col}, the two spots converged as indicated by the shrinking beam envelopes denoted by the broken circles toward point C, given by the crossing of the horizontal and vertical broken lines. This suggests that only a part of the emitter apex within the radius of R_{tip} is active, but G_{col} can collimate the beam emitted from the whole apex. When k_{col} was equal to 0.96, the two spots became indistinguishable at point C and the peak beam intensity was enhanced by a factor of ~7 from the uncollimated beam with k_{col} of 0. Further increase of k_{col} to 0.98 substantially reduced the emission current and beam intensity. The comparison of the two beams with k_{col} equal to 0.96 and 0.98 suggests the over-focusing of the beam at k_{col} of 0.98.

Figure 3.17 shows the field emission beam of FE2 at various k_{col} for V_{ge} equal to 90 V. Differently from FE1, the zero k_{col} field emission beam of FE2 spreads more uniformly over the area with the diameter of ~5 mm, thereby indicating that much larger fraction of the emitter tip apex within R_{tip} contributes to the field emission. When we increased k_{col} from 0 to 0.8, the beam size reduced only gradually by ~25 %. Then further increase of k_{col} to 0.94 resulted in the steep reduction of the beam by a factor of 10 with the simultaneous increase of the peak beam intensity by a factor of ~6, see Figure 3.18. A similar beam collimation was also observed with the high current beam at V_{ge} of

110 V. These observations demonstrate the excellent beam collimation characteristic of these double-gate single nanotip emitters. [53]
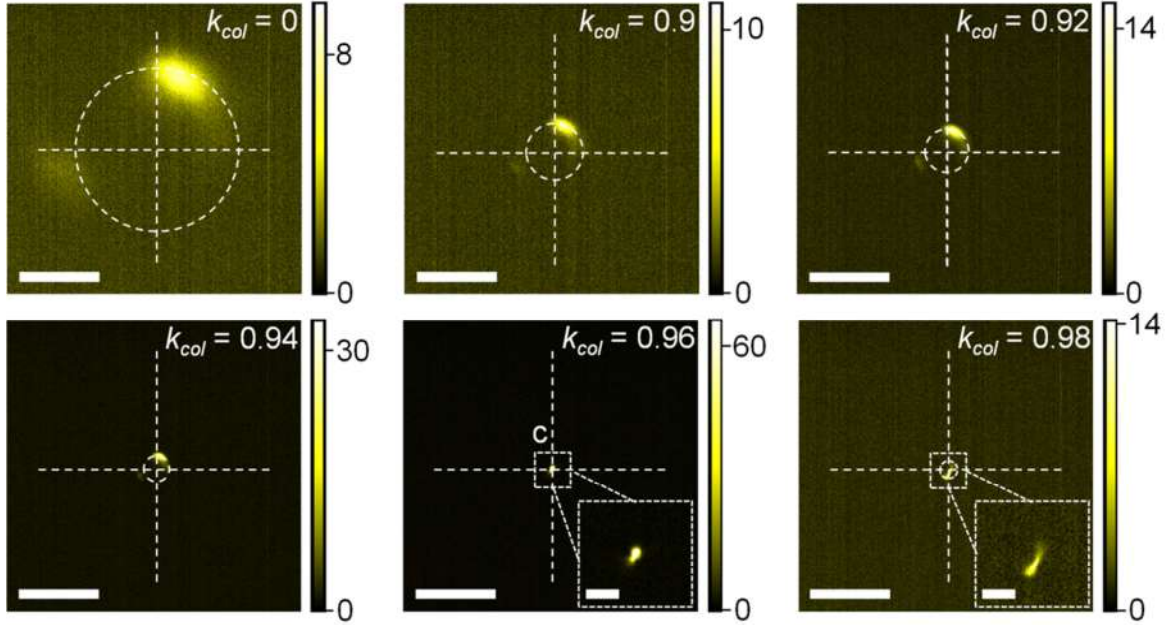
{Figure 3.16. Variation of the field emission beam of FE1 with the increase of k_{col} from 0 to 0.98 for V_{ge} of 143 V. The scale bar of the images is 5 mm. The inset images are enlarged to highlight the small beam spot (the scale bar is 1 mm.)}

In Figure 3.19, we summarized the relation between the beam radius and k_{col}. From the rms beam radius R, we evaluated the rms transverse velocity u_t with the assumption of free propagation of the electrons in the transverse direction while they are accelerated along the beam axis, see Ref. [43]. In short, u_t is equal to $\sim R/T$, where T is the propagation time of the electron from the emitter to the screen. T is approximately equal to $2L/u_{scr}$, where L is the emitter-screen distance equal to 50 mm and u_{scr} is the velocity equal to $\sqrt{2eV_{scr}/m_e}$ (V_{scr} is the screen potential equal to 2.5 kV, e is the electron charge, and m_e is the electron rest mass). Figure 3.19 shows an order of magnitude reduction of u_t with the increase of k_{col} from zero to 0.94 (FE1 case) or 0.95 (FE2 case) with the smallest value compatible with the array beam experiment. [43,52]

35
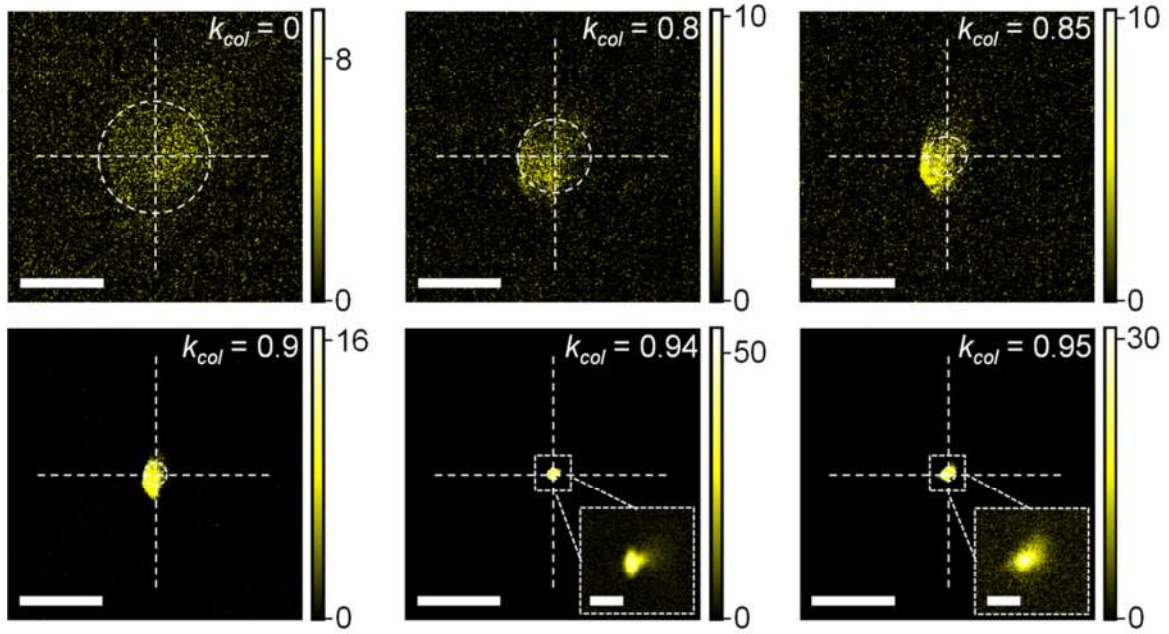
{Figure 3.17. Variation of the field emission beam of FE2 with the increase of k_{col} from 0 to 0.95 for V_{ge} of 90 V. The scale bar of the images is 5 mm. The inset images are enlarged to highlight the small beam spot (the scale bar is 1 mm.)}

As the beam images in Figure 3.19 show, we found that R and u_t of FE2 beam at k_{col} of 0.94 increased by a factor 3 when V_{ge} was increased from 90 V to 110 V with the concomitant increase of the emission current from ~50 nA to ~0.5 µA. This effect is likely caused by the Coulomb repulsion of the electrons. In the case of the uncollimated beam, the large beam divergence at the source (in the order of 30°) quickly dilutes the density of electrons as they propagate to the anode (screen), and the beam radius on the screen is unchanged within 20% as the current increases from ~100 nA to ~4 µA. However, such a dilution does not occur in the case of the highly collimated beam with k_{col} of ~1 because of the order of magnitude smaller initial angular spread. Therefore, the initial diameter of the beam (equal to at most the diameter of the G_{col} aperture) at a few micron above the G_{col} plane can be maintained on the screen only when the beam current density is small or when the acceleration field is sufficiently large so that the longitudinal velocity is increased quickly before the space-charge expansion of the beam increases u_t and degrades the beam brilliance. In fact, previous simulation showed that the acceleration field of 10-100 MV/m (typically used for electron guns) is sufficient to maintain the low emittance of field emission beamlet with the tip current of 1-10 µA. [54] In contrast, the acceleration field of the present experiment was ~50 kV/m and not sufficient to maintain the small initial emittance of the space-charge dominated beam, resulting in a larger beam size as observed in Figure 3.19. We do not consider that the expanded beam radius at the higher V_{ge} is due to the nonlinearity of the focusing characteristic of G_{col} at higher V_{ge}. In fact, observation that the FE1 beam

36

at V_{ge} of 143 V (with ~0.1 nA emission current) shown in Figure 3.19 is even smaller than the FE2 beam with V_{ge} of 90 V indicates that such nonlinearity of the G_{col} can be small. Nevertheless, u_t of the FE2 beam at V_{ge} of 110 V and at k_{col} of 0.94 was small; the value equal to ~0.7×10^{-3} c (c is the light velocity in vacuum) is smaller than the state-of-the-art photocathodes (with intrinsic beam emittance of 0.2 mm-mrad for a 1 mm-diameter cathode) currently in use. [55] We also note that the emitter position of FE2 is shifted from the G_{col} center by ~0.8 µm caused by misalignment during the electron beam lithography process. Therefore, improved single nanotip emitter performance is expected with a smaller offset of the emitter position to realize a further reduction of the minimum beam size and further enhancement of beam current density.
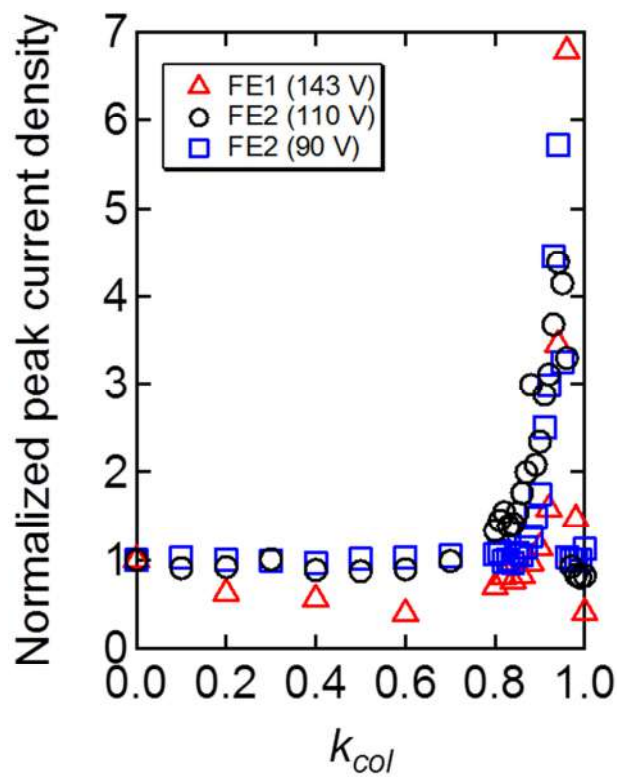
{Figure 3.18. Peak current density of the field emission beams as a function of k_{col}. The current density values were normalized by the zero k_{col} value of each scan.}
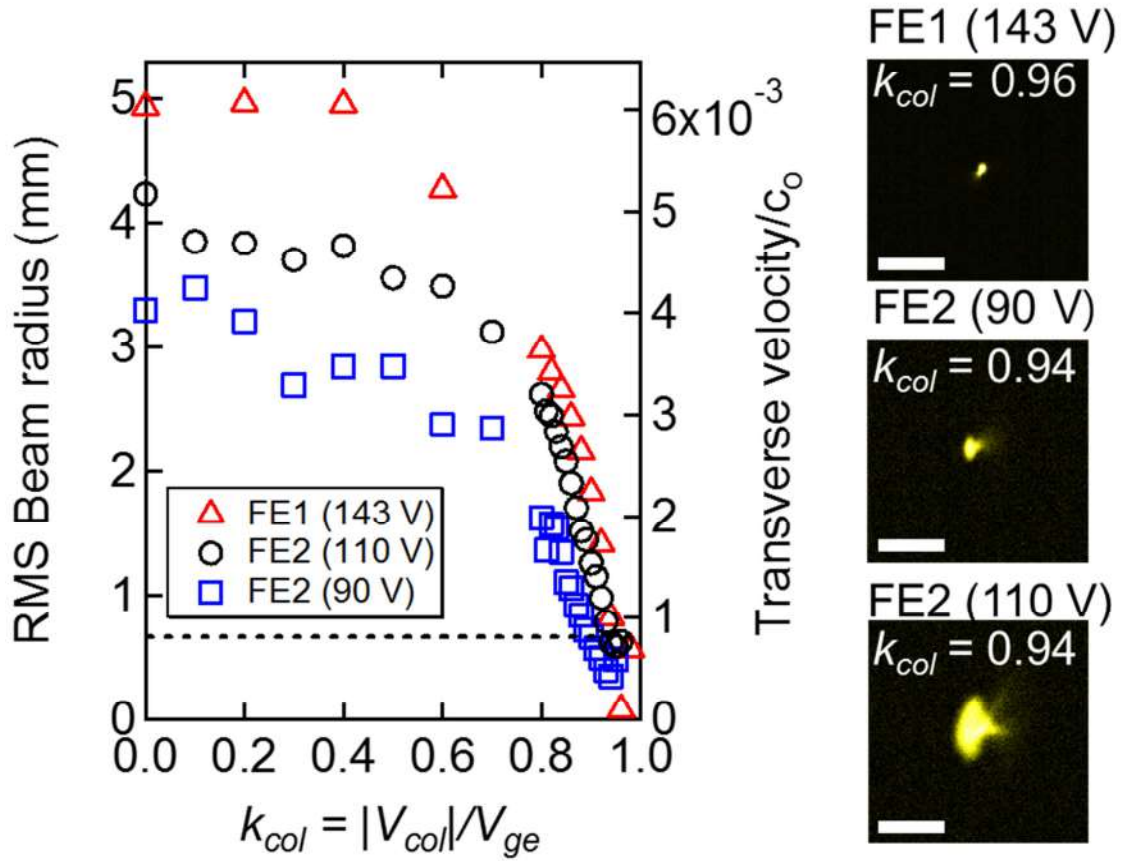
{Figure 3.19. Variation of the rms radius of the beam envelope and transverse velocity u_t normalized by the light velocity in vacuum c_0 with the increase of k_{col} from 0 to ~1. For each scan, V_{col} was varied while V_{ge} was fixed at certain value; for FE1 V_{ge} was equal to 143 V (red triangle), and for FE2, V_{ge} was equal to 90 V (blue squares) and 110 V (black circles). The broken line shows the transverse velocity equal to $8\times10^{-4}\,c_0$, corresponding to the performance of the state-of-the-art photocathode with intrinsic beam emittance of 0.2 mm-mrad for a 1mm-diameter cathode currently in use. The maximally collimated beams of each scans are also shown. The scale bar of the images corresponds to 2 mm.}

Finally we discuss the difference of the field emission current of the two emitters at zero k_{col} (*i.e.* 1.24 nA for FE1 at V_{ge} of 130 V and 4.04 μA for FE2 at V_{ge} of 110 V). Considering the fact that B_{FN} of the two devices are approximately the same, the lower current and lower A_{FN} value of FE1 than those of FE2 is most likely ascribed to the difference of the effective emitting area S. From the Fowler-Nordheim equation, we can relate the value of A_{FN} with S using the following approximate relationship (see Ref. [40]),

$$A_{FN} \approx Sab^2\phi^2 \exp(bc^2 / \phi^{0.5})$$

(3.3)

where the constants a, b, and c are given by $a = 1.541434 \times 10^{-6}$ A eV V^{-2}, $b = 6.830890$ eV$^{-3/2}$ V nm^{-1}, and $c = 1.199985$ eV V$^{-1/2}$ nm$^{1/2}$, and ϕ is the work function of Mo equal to 4.5 eV. [21,22,32 ,40] Substituting πR_{tip}^2 for S, A_{FN} takes the value equal to 0.2-20 A for R_{tip} in the range of 1-10 nm. This is in good agreement with A_{FN} (=2.95 A) of FE2, obtained from the fitting of the *I-V*, Figure 3.15. Accordingly, the small A_{FN} of FE1 indicates that the emission area of the FE1 beam is much smaller than the emitter tip apex. This interpretation is compatible with the highly non-uniform beam image of FE1 (Figure 3.16) with the indication that the active emission part of FE1 is limited to two separate small spots, perhaps occupying a small fraction of $\sim10^{-2}$ or lower at the tip apex. The numerical disagreement of the actual emission area and the value estimated form the Fowler-Nordheim fitting has been discussed previously. [21,25] However, further quantitative comparison will require atomically resolved beam image measurement, resolving the work function non-uniformity as well as more involved theory that takes into account the precise expression of the field emission current density, [22,40] therefore it is out of the scope of the present manuscript.

3.1.3.5. Summary and Conclusion

In summary, we have studied the field emission beam characteristics of double-gate single metal nanotips with G_{ext} and G_{col} electrodes. A possibility to produce highly collimated electron beamlet with the proposed double-gate structure, which was shown previously by array emitters, was demonstrated with single tip emitter in this work. The importance of the electro-static shielding of the tip apex from the collimation potential, previously discussed with the array experiment was confirmed using well defined single tip operation. We conclude that an excellent collimation capability with minimal current loss can be attained with double-gate single nanotip emitters, optimized in terms of the G_{ext} aperture shape and the alignment of G_{col} aperture. In addition, the single-tip experiment here showed that one can produce the highly collimated beamlet with the emission current on the order of 1 μA, which suggests that one can produce highly collimated field emission beam from double-gate FEA with the emission current in the order of tens of milliamperes with the intrinsic emittance below ~0.1 mm-mrad and that nanotips are highly promising for high brilliance applications such as time resolved electron diffraction studies to provide atomic views of structural dynamics.

3.1.4. Determination of the lower estimate spatial coherence length[†]

In this Chapter, the transverse coherence length of the electron beam generated from the double-gate nanotip field emitter is estimated by transmission low-energy electron diffraction (LEED) experiment in a sub-millisecond electrical pulsed mode. By analyzing Bragg electron diffraction pattern of suspended monolayer graphene with a Gaussan- and axial-wave model for the approximation of electron wavefunctions, a lower estimate of the transverse coherence length of the collimated electron beam is extracted. The detailed results are published by C. Lee *et*. *al*. [41], and the main messages of this work are summarized as follows:

1) Shape and pattern of the electron diffraction spots are dependent both on the angular divergence and size of the electron beam, controlled by the on-chip collimator of the double-gate nanotip device.

2) The estimated transverse coherence length is about 1 nm, a significantly shorter than an expected value of few tens of nm. In the present work, the sample area irradiated by the electron beam is much smaller than the beam size itself, and in this case, the diffraction pattern analysis could only provide *a lower estimate* of the transverse coherence.

3) The observed sharper satellite spots near the main 6-fold symmetric Bragg spots of monolayer graphene indicate a longer transverse coherence length of the incident electron beam.

4) Electron diffraction experiment by using only the cathode device without additional optics is demonstrated, advantageous touu time-resolved electron diffraction requiring a short electron travel distance toward samples to minimize temporal broadening especially in time-resolved LEED.

3.1.4.1.   Abstract

We explore the spatial coherence of double-gate nanotip single field emitters by low-energy electron diffraction experiments in transmission mode. By producing collimated field emission pulses from the single nanotip cathode and irradiating a suspended monolayer graphene film, without additional optics, we observed sharper and higher resolution Bragg diffraction spots than a previous experiment using a nanotip array cathode. In particular, we found complete conservation of the size and the shape of the diffraction spots with those of the incident beam on the sample. The result indicates that the transverse coherence of such a nanofabricated double-gate single-tip emitter is much larger than a few nanometers as determined by the apparent diffraction spot size and overall spatial resolution based the observed diffraction pattern.

3.1.4.2.   Introduction

The large scattering cross section of electrons makes electron diffraction experiments advantageous in determining atomic structures of small crystal samples that are difficult with X-rays [56]. However, to provide the needed resolution, the transverse coherence length of the electron beam should exceed tens or hundreds of angstroms to analyze large-unit-cell organic or biological crystal samples [3,19,57]. High-resolution electron microscopy can routinely achieve sub-angstrom resolution in small solid particles or near-atomic-resolution single-particle imaging for biological specimens [58,59], but only through the sacrifice of electron flux by magnifying and clipping the beam with an aperture. The development of ultrabright electron sources using cathodes based on a metal nanotip emitter [20,31,32] has been motivated by the desire to overcome the limit of the spatial and temporal resolution for time-resolved studies that are compromised or untenable with low flux sources [3,57]. The attainment of high field emission current densities of 10^6-10^7 A/cm^2 within the desired narrow intrinsic energy spread of ~0.2 eV produced from a few nanometer nanotip apex (with even smaller virtual source size) is exceedingly hard to achieve with thermionic emitters or UV-excited photocathode [25,60-62].

In the literature, electron guns using etched-wire needle-shaped field emitters have been reported [36,63-65]. However, these sources suffer from the large geometrical divergence of the field emission beam because of the curved emitter surface, but *not* due to the intrinsic transverse velocity spread. For efficient use of the bunch charge and to utilize the beam with the intrinsic brightness, dedicated optics is normally required. In addition, the requirement of a high acceleration field to suppress the space-charge degradation of the beam brightness and coherence is often compromised when the acceleration field is coupled to the electron emission from nanotip sources. In contrast, irradiating samples with collimated field emission pulses without additional optics under the required

high acceleration field is feasible with the double-gate nanotip emitter structure because of the on-chip-integrated beam collimator and the electrostatic shielding of the nanotip from the external field [43,66,67].

In this Letter, we study the low-energy electron diffraction from suspended graphene to explore the transverse coherence property of double-gate field emitters. Comparing to our recent experiment using a 10^4-nanotip array (or field emitter array, FEA) double-gate emitter [61], we were able to achieve diffraction with improved spatial resolution and signal quality. We found a clear influence of the beam shape and the sample size on the Bragg diffraction spots from graphene. This indicates that the transverse coherence length of our single nanotip source is much larger than the value evaluated from the apparent Bragg spot size. In addition, close inspection of the Bragg diffraction intensity shows that the on-chip beam collimation not only reduces the beam divergence but significantly improve the wave front flatness.

3.1.4.3.   Results and Discussion

We prepared the double-gate single-nanotip emitter (Figure 3.20(a) and (b)) with the same design and fabrication procedure reported previously [28,42,68]; the emitter was a pyramidal shape molybdenum with the tip apex diameter of 10 - 20 nm. The electron extraction gate G_{ext} and beam collimation gate G_{col} layers, respectively 500 nm- and 300 nm-thick, were stacked on top of the emitter 1.2-µm-thick insulating layers (Figure 3.20(b)). The diameter of the G_{ext} and G_{col} apertures were equal to 1.8 µm and 5.5 µm, respectively, as measured by SEM (Figure 3.20(a)). To measure the transmission through and the Bragg diffraction from a suspended monolayer graphene sample, we loaded the emitter into the setup depicted in Figure 3.21(a). The monolayer graphene sample was supported on a copper TEM grid (PELCO®).

After we evacuated the experimental chamber down to $(1-1.4)\times10^{-8}$ mbar, we first conditioned the emitter by repeatedly applying the electron extraction potential V_{ge} to G_{ext} with respect to the emitter substrate from 0 V to a certain value with the zero V_{col}, where we define the collimation potential V_{col} as the potential applied to G_{col} with respect to G_{ext}. G_{ext} was connected to the ground potential in this and following measurements. The field emission current was measured by using the sample holder as the anode biased at 30 V. We continued the conditioning for 30 min until the current-voltage characteristics (*I-V*) became stable as shown in Figure 3.20(c) by filled circles (the empty circles show the initial *I-V*). After the conditioning, the emission current was equal to 4.86 µA at V_{ge} = 155 V. The leak current through the gate electrodes was several orders below that value. The *I-V* fits well to a relation, $I = A_{FN}(V_{ge}/B_{FN})^2 \exp(-B_{FN}/V_{ge})$, with the fitting parameter $A_{FN} = 20$ and B_{FN}

= 1600. Using this fitting parameters (in particular from B_{FN}), we estimated the electric field at the emitter tip apex F_{tip} was equal to 6.31 V/nm at V_{ge} = 155 V with the assumed value of the work function $\phi \cong 4.5\,eV$ (for molybdenum). [25]

(a)

(b)

(c)

(d)
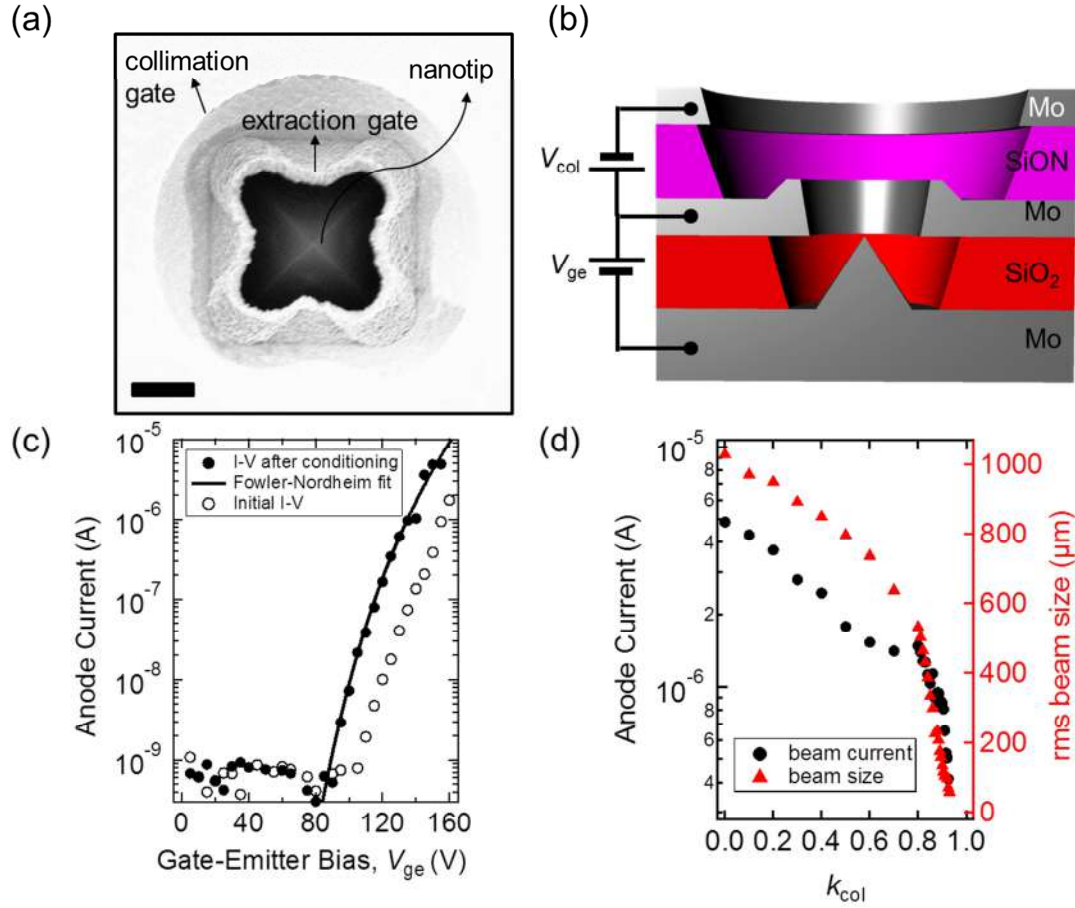
{Figure 3.20. (a) SEM image of the double gate field nanoemitter device (top view). Scale bar is 1 μm. (b) Schematic illustration of the field emitter, cutout of the side view. Emitter base plate and collimation gate layer are electrically biased at negative potential with respect to the extraction gate biased at ground. V_{ge} and V_{col} refer to (extraction) gate-to-emitter voltage and collimation voltage, respectively. (c) I-V characteristics of the device. Empty circles show the initial I-V, and the filled circles show the I-V after 30 min of conditioning. The line superposed to the latter show the fitting of the I-V by the Fowler-Nordheim equation as described in the main text. (d) Beam current and the rms beam size variation depending on collimation voltage. k_{col} refers to the ratio V_{col} to V_{ge}.}

For the electron transmission and diffraction experiments, we fixed V_{ge} = 90 V with the zero-collimation potential emission current of 530 pA. To produce collimated field emission pulses, we applied the V_{ge} pulse and the V_{col} pulse synchronously. We applied 800 V to the sample. The field emission electron pulses were then accelerated at the acceleration field of ~0.4 MV/m in the gap

between the cathode and the sample holder with the separation of ~2 mm, propagated through the 2 mm-diameter-hole of the 3 mm-thick sample holder, and irradiated the sample that was mounted on the electron detector side of the sample holder. The transmitted direct beam and the Bragg diffracted beams propagated approximately 20 mm to the electron detector. We applied 500 V at the entrance plane of the electron detector, 100 V to the MCP for the amplification, and 4.5 kV to the phosphor screen for the electron detection. The beam images were subsequently captured by a CCD camera triggered synchronously with the gate pulses. To image the direct transmission beam, we applied 10-µs-long gate pulses. The beam size on the sample was evaluated by using the shadow of the TEM grid with the grid spacing of 85 µm as the scale as function of V_{col} (Figure 3.20(d)), in which V_{col} was specified by $k_{col} = |V_{col}/V_{ge}|$. The relationship between the emission current k_{col} estimated from the integrated image intensity is also shown in Figure 3.20(d). We note that, due to the increased fraction of the TEM grid area as the beam spot size was reduced at larger k_{col}, this method systematically underestimates the current of the collimated beam. Nevertheless, the observation that the emission current was about 10% of the zero-k_{col} value was consistent to previous experiments [28,68]. At $k_{col} =$ 0.925, the rms (root mean square) beam size reached 59 µm. This was a factor of 17 smaller than that of zero k_{col} beam. Beyond this k_{col} value, the emission current was quickly quenched.

To study the electron diffraction from the graphene sample, we applied 900-µs-long gate pulses at $V_{ge} = 90$ V. As shown in Figure 3.21(b), we were able to observe the hexagonally arranged clear 1st and the 2nd order diffraction spots from the graphene by irradiating a single collimated field emission pulse with ~50 pA current amplitude and $k_{col} = 0.92$ (at $V_{ge} = 90$ V) with ~3×10^5 electrons in the pulse. The signal from the direct beam was saturated on the camera at this measurement condition.
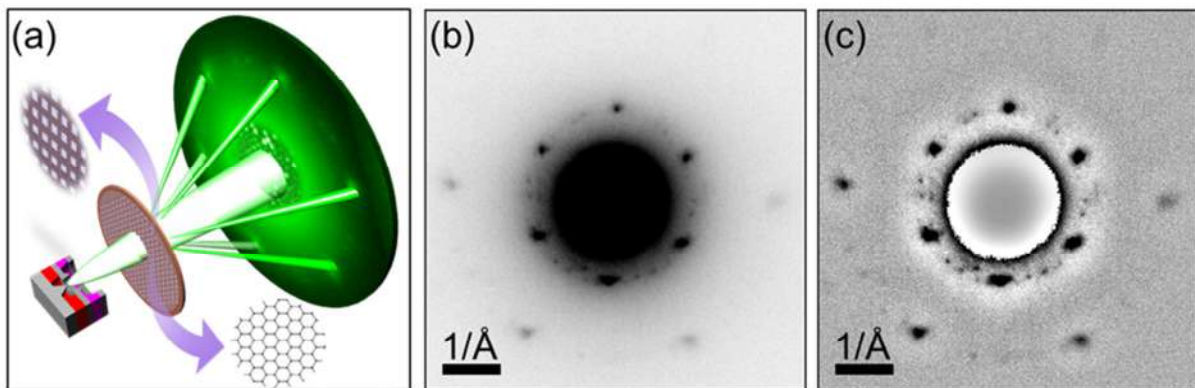
{Figure 3.21. (a) Experimental schematic for transmission low-energy electron diffraction from a suspended monolayer of graphene. Beam size at the sample position is estimated by the projected shadow image of the TEM grid on which single graphene layer is covered with lacy carbon sheet. (b) Observed electron transmission image through a suspended monolayer of graphene for which the

collimation potential of the double-gate single-nanotip field emitter was set at the maximally collimation condition ($k_{col} = 0.92$) with $V_{ge} = 80$ V. The hexagonal 1st order and the 2nd order Bragg reflection peaks are clearly observed. With the given electron beam wavelength at 900 eV and the c-c bond length of graphene, the Bragg angle and the camera length are calculated to 8.26° and 19.2 mm, respectively. (c) High frequency filtered image of Figure 3.21(b) to highlight the satellite Bragg diffraction spots closed to the 1st order spots.}

To analyze the diffraction spots at high signal-to-noise ratio, we have digitally averaged 20 images repeatedly captured at the same condition and subtracted the background. In Figure 3.22(a), we show the evolution of the direct beam (left panel) and diffraction spots (right panel) when k_{col} was increased from 0.8 to 0.925. The direct beams showed randomly distributed bright spots in addition to the shadow of the grid. We ascribe these bright spots that were not observed in the separate beam imaging experiment without the sample to the non-uniformity of the sample. Figure 3.22(a) shows that, when k_{col} was increased from 0.8 to 0.925 and the beam spot size was reduced from 0.5 mm to 59 µm (Figure 3.20(d)), the probed area of the sample was reduced from ~15 grid to within approximately one grid zone. The center of the beam shifted upwards by a small amount at the same time, perhaps due to the non-uniformity of the beam acceleration or residual magnetic field. When k_{col} was increased to 0.84 and the beam spot size was reduced by one third of the zero k_{col} case (Figure 3.20(d)), the hexagonal Bragg reflection spots became visible. Each diffraction spot emerged as a group of spots mainly on the six-fold symmetric position. With the further increase of k_{col} and the decrease of the beam spot (Figure 3.20(d)), the Bragg reflection spots including the satellite spots became clearer and their overall rms radius, σ_{diff}, became smaller (Figure 3.22(b)). This is similar to that observed previously with field emitter array (FEA) beams [61], but the present result obtained by using the single nanotip emitter exhibits higher spatial resolution. This is also indicated by the factor of ~2 larger R/σ_{diff} ratio (Figure 3.22(b)) observed here than the FEA experiment, where R is the distance between the center of the direct beam to the center of the diffraction spots. The satellite spots with the same R reflect the contribution of multiple graphene lattice domains at the large beam size.

When we analyze the main Bragg spot size by a Gaussian- and axial-wave model with a full consideration of the diffraction angle dependent electron elastic scattering cross section, we obtained the *lower estimate* transverse coherence length [65] of ~1 nm, which is a few times smaller than the radius of the curvature of the nanotip apex. However, we consider that the spatial coherence length is much larger than this value. This is on one hand because of the similarity of the Bragg diffraction spots with the direct beam shape (see below), and on the other hand, because of the observation of the

45

satellite Bragg diffraction spots that are an order of magnitude smaller than the main diffraction spots (Figure 3.21(c)] hence indicating a transverse coherence length of tens of nanometers.
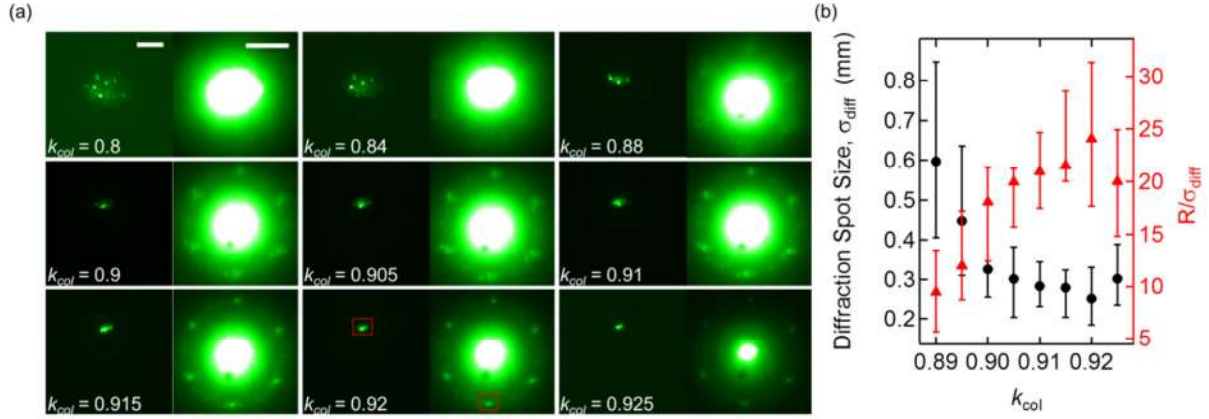
{Figure 3.22. (a) Selected image display of the direct (left panel) and the diffracted beam (right panel). Scale bar is 500 µm and 5 mm on the respective beam image. For some k_{col}-value images, a view of some parts of the images (the direct beam and one of the diffraction spots) are indicated in the image of $k_{col} = 0.92$ by the red box to highlight the beam quality for the diffracted beam relative to input beam. The magnified views are summarized in Figure 3.23(a). (b) Variation of the rms diffraction spot size (σ_{diff}) and the ratio between beam center-to-diffraction spot distance and σ_{diff} as a function of k_{col}.}

When the spot size of the incident beam is small and the sample is uniform over the irradiated spot, the R/σ_{diff} ratio can be a quantitative measure of the transverse coherence length of the incident beam [65]. However, when the beam size is finite and the sample is not uniform, σ_{diff} is rather determined by the beam size and the non-uniformity of the sample instead of the spatial coherence length and the R/σ_{diff} ratio merely gives the lower estimate of the coherence length. From the comparison of the direct beam and the diffraction spots, we consider this applies to the present experiment: in Figure 3.23(a), we show the magnified images of the direct beam and one of the 1st order diffraction spots (in the 6 o'clock direction). These were taken from the region indicated by the red boxes in Figure 3.22(a) (see $k_{col} = 0.92$ image). The strong similarity of the Bragg reflection spots and the direct beam shape is apparent.

Because of the highly coherent nature of the field emission beam [66], the transverse spread of the wave function of the field emission electron beam is much smaller than the incoherent beam case. The acceleration of the beam along the beam axis as in the present geometry should also have an effect in making the transverse spread of the wave function upon propagation narrower than the free space propagation. However, for a field emitter with the apex radius of curvature of 5 nm, the expected transverse spread is several microns even under the finite acceleration [67]. This is consistent with our present conclusion that the transverse coherence length of the single nanotip double gate emitter is much larger than the value determined by the apparent Bragg diffraction spot size that might be larger than tens of nanometers as the small satellite Bragg diffraction spot size indicates. Further experimental characterization of the transverse coherence length of our nanotip emitters is of particular practical relevance, requiring experiments with large unit cell systems for calibration and determination of the upper limit to the coherence most relevant to spatial resolving power of atomic structures.
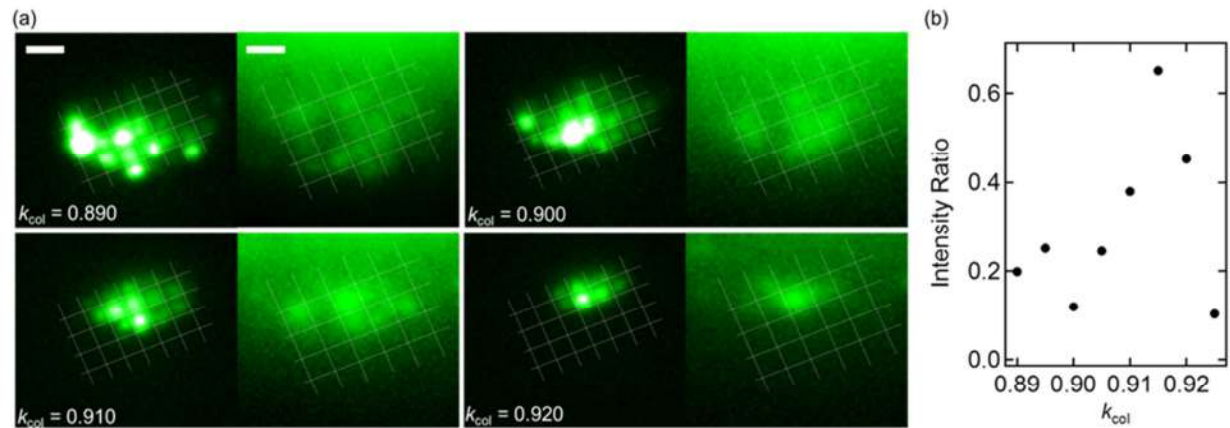
{Figure 3.23. (a) Magnified comparison of the direct beam spot and the diffraction spot at various k_{col}. Cropped and magnified region (indicated by red box in Figure 3.22(a)) of the shadow image (left panel) and the diffraction spot at the 6 o'clock position in the diffraction patterns shown in Figure 3.22 (right panel). The grid spacing is 85 µm on the actual sample surface. The scale bars denoted on the images are 500 μm indicating the size of the beam on the phosphor screen. (b) Variation of the brightness of the Bragg reflection spot to that of the direct beam with the increase of k_{col} from 0.89 and 0.925.}

We finally note the influence of the increased k_{col} on the brightness of the diffraction spots observed in Figure 3.23(a). In Figure 3.23(b), the ratio of the brightness of the diffraction spot on that of the direct beam was summarized. When k_{col} was increased, the diffraction spot size decreased because of the decrease of the direct beam spot size, thereby increasing the spatial resolution of the electron probe. However, the increase of the brightness of the diffraction spot is governed by a

separate effect. We ascribe this to the fact that the increasing k_{col} is not only collimating the otherwise diverging electron trajectories emitted from the nanotip apex but also flattening the electron wave front, hence substantially reducing the beam-front-dependent angular dispersion of the Bragg diffraction direction. Figure 3.23(b) shows that the wave front was most flat when k_{col} was 0.915-0.920, and its curvature increased at higher k_{col} due to over focusing, even though the beam spot was the smallest at $k_{col} = 0.925$. This highlights the unique characteristic of our double-gate nanotip emitter that allowed for detecting sharp diffraction images without external optics.

3.1.4.4. Summary

In summary, we demonstrated that the double-gate single nanotip emitter is capable of producing sharp Bragg diffraction from a suspended monolayer graphene sample. By using the on-chip beam collimator, we were able to generate electron pulses that are not only collimated but also spatially coherent with coherence lengths greater than 1 nm, allowing for the low-energy transmission diffraction experiment using a minimal experimental setup without additional electron optical elements. Analysis of the recorded diffraction and direct beam images and the observation of small satellite diffraction spots clearly showed that shape and pattern of the diffraction spots are dependent both on the angular divergence and size of the electron beam that are controlled by the on-chip collimator of our device.

3.1.4.5. Supplementary Materials

See Appendix A for the entire collection of the direct and diffracted beam images and Appendix B for the derivation of transverse coherence length of collimated electron beam.

3.1.5. Outlook and challenge

Aiming at single-shot pump-probe experiments, the achievable temporal resolution mostly determined by the electron bunch length in time can be conceived given by experimentally measured beam current of the maximum 4 µA generated from the double-gate single nanotip field emitter. As shown in Figure 3.15, this beam current corresponds to a range from 10^5 electrons for 10 nsec bunch to 10^{10} electrons for 1 millisecond bunch. This parameter range covers the required number of electrons recording a single diffraction image, depending on structural complexity and thickness of samples, with an acceptable signal-to-noise ratio (SNR) [69], assuming a DC electron gun concept. This time scale seems far from the desired temporal resolution (~100 fs) in capturing barrier-crossing dynamics of a chemical reaction [3], discussed in Chapter 1 and 2, but it is still a useful time window to investigate structure changes of biological macromolecules, occurring in millisecond [70], microsecond [71], and nanosecond time scale [72], in a single-shot manner.

Bunch length in time	Number of electrons per bunch
10 nanosecond	2.5×10^5
100 nanosecond	2.5×10^6
1 microsecond	2.5×10^7
10 microsecond	2.5×10^8
100 microsecond	2.5×10^9
1 millisecond	2.5×10^{10}

{Table 3.2. Number of electrons comprising electron bunches with 4 µA beam current at different bunch length from 10 nsec to 100 µsec.}

Although a lower-limit of transverse coherence length of the electron beam generated from this device is only estimated in the present thesis, a larger value is expected in reality, based an experimentally measured value with a similarly shaped nanotip [20]; according to this reference, the global coherence of photoemitted electron beam is measured as 0.36. Given that the required transverse coherence length for protein crystallography is in the order of 10 nm, protein crystals as small as 100 nm can be possibly studied without loss of the beam current and current density by

matching the size of the probe beam and the single crystal, assuming no beam quality deterioration due to such tight electron beam focusing with the high current density.

The method of electron beam generation is another important point to discuss. In case of double-gate nanotip arrays, the picosecond bipolar current pulse switching has been successfully tried [73], indicating that this electrical switching method can also apply to the single nanotip case. Also, laser-triggering method with near infrared laser (via single-photon photofield emission mechanism) has been proved for single-gate arrays [74]. However, application of this direct laser triggering method to the double-gate single nanotip device emerges several issues. First of all, irradiating a focused laser beam to the emitter location with a good overlap out of mm scale device with micrometer resolution (gate aperture size) is technically challenging. Second, there is inherent multiphoton-induced electron emission coming from the collimation gate made of Molybdenum when the triggering laser hits the device. This byproduct should be distinguished from the photofield emitted electrons. Third, micrometer tight optical focusing requires a short focal length lens, indicating its placement in close proximity to the device and a concomitant increase of the sample-to-source distance affecting temporal resolution in time-resolved electron diffraction. An alternative way to do the laser triggering of the double-gate single nanotip device is to use a semiconductor photoswitch [75] attached to the emitter base plate such that emitter biasing voltage is applied only when femtosecond laser hits the switch.

A stability test of the field emission beam with microampere current and transverse coherence or emittance measurement are also important steps in completing the device characterization toward the development of ultrabright cathode.

3.2. Optical fiber-based photocathode

3.2.1. Motivation

Conventional photocathodes used in time-resolved electron diffraction is prepared by coating electron emitting layers on one side of an inch-sized large area optical window [76]. In case of the back-illumination scheme for electron generation (Figure 3.24), femtosecond optical laser pulses are injected from the backside of the window and focused on the emitting layer with few hundreds of micrometer focal spot size. Given the fact that typical femtosecond laser systems have a finite degree of the instability of beam pointing and the average power, it is required to shape the probe electron bunch by using an aperture in order to maintain bunch parameters such as number of electrons per bunch, bunch size, position, profile and etc., for the entire course of the data collection, which otherwise, could affect the high signal-to-noise ratio (SNR) of differential images (pumped image subtracted from unpumped image) processed in the data analysis step [77]. This instability issue becomes more significant if a few micrometer tight laser focusing is aimed on the large photocathode substrate for achieving small source size and transverse emittance (in other words, for maximizing beam brightness).
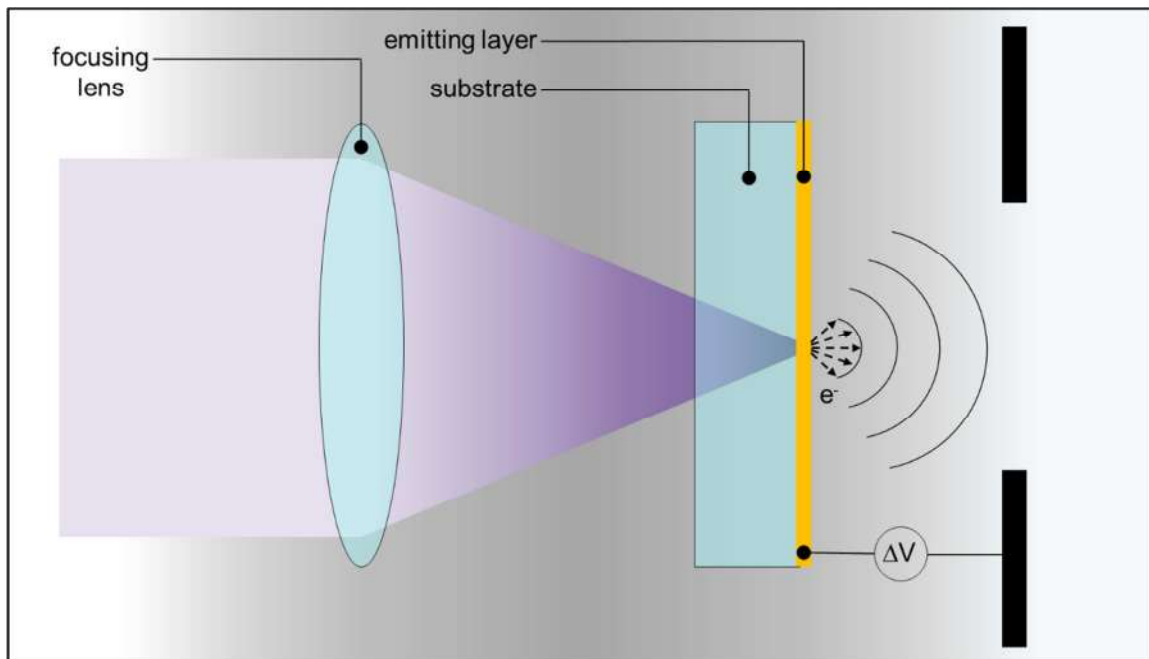
{Figure 3.24. Conventional photoelectron generation scheme in time-resolved electron diffraction}

Instead of the flat optical window, using an optical fiber as a photocathode substrate can eliminate the need of the electron beam shaping, therefore allowing for the construction of a compact setup with many advantages in time-resolved electron diffraction. Fed by femtosecond optical laser pulses at one end of the fiber, while the other end is coated with thin metal layers acting as an electron

emitting surface, this cathode provides self-alignment between the electron source and the wave-guided photoinjection pulses (Figure 3.25). As a result, it can generate electron bunches with a well-defined beam size and profile by optimizing geometrical parameters of the fiber (for example, the fiber core/cladding size and shape) without electron beam shaping.
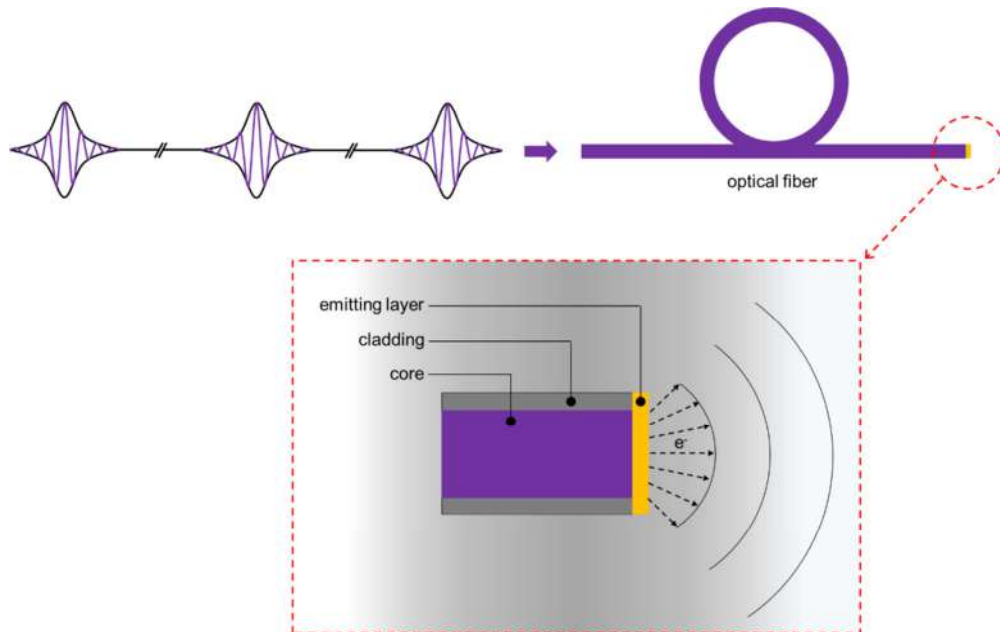
{Figure 3.25. Photoelectron generation scheme with optical fiber}

In addition to the advantage in controlling spatial properties of electron bunches, the optical fiber-based photocathode also enables the control of temporal properties of the electron bunch. On propagating inside the waveguide, optical pulses experience temporal stretching owing to the various types of dispersion effects dictated by geometrical parameters of the fiber and it's coupling condition to the laser beam: the initial few hundreds of femtosecond laser pulses at one end of the fiber are stretched to few or tens of picosecond pulses at the other end after propagation, which generates electron bunches with the same order of the temporal bunch length. The picosecond long electron bunch is useful in ultrafast streak electron diffraction, which will be explained in Chapter 4, in that the observable time window for the entire transient dynamics is determined by the temporal electron bunch length. Compared to other methods such as RF field induced bunch broadening [78,79] or THz streaking [80] to generate the picosecond long electron bunches, this innovative electron source concept is relatively simple and robust and combines all these features in a single fiber optic based device without needing to invoke space charge effects, which could affect the beam quality.

3.2.2. Optical fiber-based electron gun[†]

In this section, the first demonstration of the optical fiber-based low-energy electron gun for time-resolved electron diffraction and characterization of the temporal property of the low-energy electron bunch are described. Because of the highly diverging characteristics of the low-energy electron beam, an electrostatic Einzel lens system is integrated with the optical fiber-based photocathode. Ultrafast streak camera, which will be discussed in Chapter 7 in detail, is implemented not only for the electron bunch profile characterization, but also for the feasibility test of the time-resolved low-energy streak diffraction that have many advantageous over conventional pump-probe experiment in ultrafast low-energy electron diffraction. The detailed results and device fabrication method are published by C. Lee et al. [81], and the main messages of this work are summarized as follows:

1) Because of dispersion, the femtosecond photoinjection optical pulse is stretched on propagation inside the fiber, resulting in few picosecond duration of the pulse arriving at the emitting layer. This stretched photoinjection pulse indicates the initial electron bunch length of few picosecond as it is generated.

2) For the low-density (200 electrons per bunch) few picosecond low-energy electron bunch studied in this work, the space charge and initial kinetic energy spread induced bunch broadening turns out to be minimal, as expected. This result is confirmed both experimentally by using a streak camera and computationally by a particle tracking simulation, leading to a conclusion that the stretched photoinjection pulse duration governs the electron bunch duration at the diffraction sample plane.

3) Given that dispersion is dictated by geometrical parameters of the fiber (for example, fiber length or free space-to-fiber coupling condition), the result 1) and 2) imply that electron bunch can be actively controlled by tailoring fiber parameters.

4) The implemented Einzel lens system well focalize the electron beam on the detector in order to obtain diffraction images at different electron energies, ranging from $1.0 - 2.0$ keV, without space charge induced beam emittance degradation.

3.2.2.1. Abstract

Here, we present an optical fiber-based electron gun designed for the ultrafast streaking of low-energy electron bunches. The temporal profile of the few tens of picosecond long electron bunch composed of 200 electrons is well characterized by a customized streak camera. Detailed analysis reveals that the stretched optical trigger pulse owing to the dispersion effects inside the waveguide dominantly determines the temporal length of the low density electron bunch. This result illustrates the capability to control the observable time-window in the streak diffraction experiment by tailoring geometrical parameters of the fiber source and its coupling condition. With the electrostatic Einzel lens system integrated on the fiber-based cathode, we also demonstrate spatial focusing of the electron beam with the RMS spot size of 98 μm and imaging of static low-energy electron diffraction (LEED) pattern of monolayer graphene in the range of 1.0 – 2.0 keV electron kinetic energy.

3.2.2.2. Introduction

The ultrafast electron diffraction (UED) technique is a powerful tool that enables the investigation of dynamical structure-function relationships of molecular species on the relevant time scale of their atomic motions [3,57]. The clear demonstration of this technique was achieved through the development of high energy, high brightness electron guns that can deliver electron pulses containing on the order of 10^4 - 10^5 electrons per bunch while maintaining on-target pulse durations in the low 100 fs regime, thus allowing direct observation of a large class of ultrafast structural dynamical phenomena [82-88]. These bunch parameters have been achieved by compact direct DC guns on the one hand, and RF compressor approaches on the other, such that current table-top UED setups routinely operate with < 200 femtosecond temporal resolution at 100 keV electron energy [5,21,88-90].

While high energy UED probes are best suited to probing bulk material dynamics of samples in the order of 100 nm thickness, low-energy electrons in the order of 1 keV or less are more suited to study atomic motions involved in surface-activated systems [12,64,65,91] such as photocatalysis [92]. Given the importance of surface mediated catalysis, from water splitting to CH bond activation, there is ample justification for pursuing time resolved low-energy electron diffraction (LEED) techniques; unfortunately, achieving the femtosecond bunch length is significantly more difficult as temporal dispersive effects due to the initial energy spread and space charge are exacerbated at low beam energies [65,63]. Motivated by the design of high-energy UED setups, several attempts with low-energy electrons have tried to shorten the source-to-sample distance down to sub-millimeter range by using miniaturized electron guns composed of a nanometer sized electron source [64,65,12,36] Although this approach is interesting and has achieved few picoseconds temporal resolution in transmission [64] and reflection [12] geometries, the achievement of sub-picosecond pulse durations

remained elusive due to limitations in the attainable extraction electric field. In addition, construction of such a miniature gun is not trivial, possibly hindering its more widespread proliferation. An alternative strategy for the realization of sub-picosecond resolution in the time-resolved LEED experiment is to use the ultrafast streaking technique [79,91,94]. In contrast to the conventional stroboscopic pump-probe scheme using hundreds of short electron bunches to sample each time point of the delay in recording the entire dynamics, the ultrafast streaking technique exploits, ideally, a single long (typically few picoseconds) electron probe in which time-varying structure information is encoded after photo-excitation of the sample being probed by electron diffraction. The long electron bunch acts as an observable time-window of the dynamics from which different temporal components are separated in space under a transient electric field generated inside the streak camera75. The resultant streaked diffraction patterns are imaged on the detector screen, and in this case, the temporal resolution is determined by the angular streak velocity of the streak camera. Previous work has demonstrated 400 fs temporal resolution with an electronically triggered RF-cavity based streak camera and MeV electrons [79] and 550 fs with a phototriggered streak camera and 30 keV electrons [94]. These results provide the impetus for the development of ultrafast streak cameras for time-resolved LEED experiments.

In this Letter, we present an optical fiber-based ultrafast low-energy electron gun that has several advantages over nanotip-based or conventional planar optical window-based electron gun in ultrafast streaking. As demonstrated by our previous work [95], the fiber-based electron source is prepared by coating of the electron emitting layer directly to the fiber end and back-illuminated by the photoinjection beam. This work takes explicit advantage of the functionality of tailoring geometrical parameters of the fiber and its coupling to the photoinjection beam. In this manner, this simple fiber based source can generate electron bunches with tunable pulse duration that defines the observable time-window of the dynamics in ultrafast streaking. In addition, the fiber-based source allows one to easily control the well-defined electron beam size and profile without beam shaping typically needed for UED setups. Lastly, the optical fiber-based cathode design provides a self-alignment between the cathode and photoinjection beam, opening the possibility to construct a portable time-resolved LEED system.

3.2.2.3. Experimental

Solarization-resistant multimode optical fiber with a mode field diameter of 100 μm was chosen to prepare the fiber-based electron source, since this large core fiber allowed for relatively efficient coupling of the free space laser pulse to the fiber compared to the single mode variant. The fiber was connected to the photoinjection beam with a standard fiber plug on one end, and a metallic

fiber ferrule on the other, wherupon both sides were polished. The metallic ferrule end was coated with a 30 nm thick gold layer by using the electron beam evaporation method, thereby forming a back-illuminated photocathode (Figure 3.26(a), (b), (c)). The other end of the fiber was connected to a commercial fiber vacuum feedthrough in the experimental chamber. The gold-coated fiber ferrule was then mounted to a holder (Figure 3.26(d)) in which an electrostatic Einzel lens system was integrated for the purpose of electron beam focusing (Figure 3.26(e), (f)). As shown in Figure 3.26(g), this lens system was composed of an extractor, lens, and ground plate, which are assembled in a stacked manner together with three isolation plates. Based on the actual geometry of each lens element and electron source properties characterized by our previous study [95], the electron beam trajectory was simulated using a particle tracking solver (CST, computer simulation technology, particle studio [96]), (Figure 3.26(h)).

The assembled electron gun was loaded into the UHV chamber with a base pressure of 3×10^{-8} mbar. The triggering laser pulses (257 nm, ~180 fs, 10 kHz) were coupled to the fiber vacuum feedthrough via a connector to an intermediate fiber of identical type, thereby allowing measurement of the in-coupled average laser power with known coupling losses at the fiber feedthrough prior to carrying out the experiments. The total length of the first (in-vacuum) and second (in-air) fiber used in the present study was approximately 1 m. Before using the prepared fiber, we carried out a fiber conditioning process until we see no significant power change as a function of the exposure time to the photoinjection UV pulse due to the fiber solarization (*i.e.* photodegradation) effect that can reduces the transmission of the input power. After the conditioning step is completed, we measured the output power reduced to approximately 10 % of the input power on the total length of the fiber including the fiber feedthrough at 257 nm wavelength. Before imaging experiments, we measured electron beam current as a function input laser power and confirmed a linear relation, indicating single-photon photoemission as an electron emission mechanism of this fiber-based source. During imaging experiments, an input power of 20 μW corresponding to 200 electrons per bunch was maintained. Beam spots were imaged with a chevron type microchannel plate (MCP)-phosphor screen assembly and captured by a lens- coupled scientific grade CCD camera. The distance between the source and the screen was approximately 40 mm.
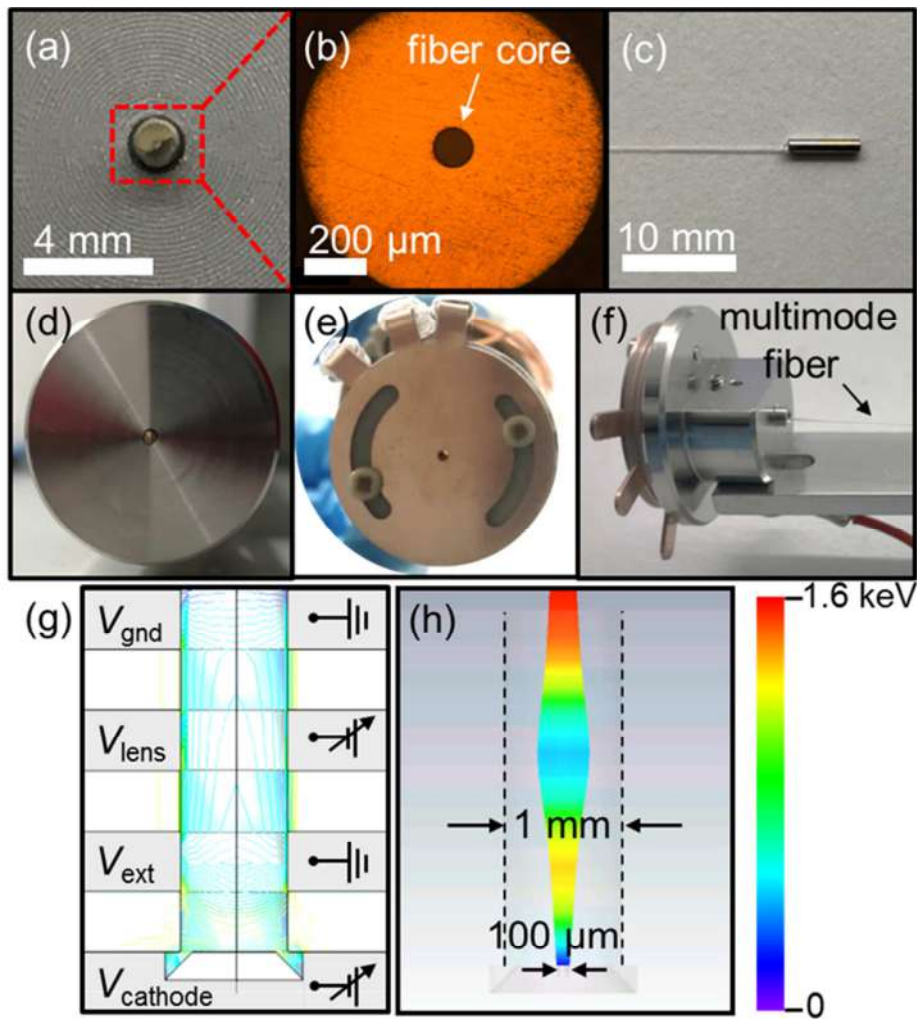
{Figure 3.26. View of the optical fiber-based electron gun. (a) gold coated fiber ferrule, (b) optical microscope image of the magnified view of the selected region in (a), (c) fiber ferrule connecterized with the fiber, (d) ferrule holder before the assembly of Einzel lens plates, (e) Einzel lens plates, (f) the entire gun assembly. (g) Cross-section view of the simulation model of the lens system in a particle tracking solver. Solid cyan color indicates the equipotential line in the maximum focusing case. (h) Simulated electron beam trajectory at V_{lens} of -1.2 kV with the fixed $V_{cathode}$ of -1.6 kV. The range of the electron kinetic energy is scaled by the false color. The Einzel lens aperture and electron source size are set to 1 mm and 0.1 mm, respectively.}

We first tested the focusing ability of the Einzel lens system by varying the lens voltage V_{lens}, at a fixed cathode voltage $V_{cathode}$ = -1.6 kV. As shown in Figure 3.27(a), the beam size is gradually reduced with the increase of V_{lens} from -0.8 kV to -1.22 kV, expanding again in the -1.22 kV to -1.3 kV range, indicating over-focusing of the beam. In case of the maximum focusing condition (V_{lens} of -1.22 kV), the rms beam spot size recorded at the screen was more than a factor of two smaller than is the case for V_{lens} = -0.8 kV (Figure 3.27(b)). For the maximum focusing condition, we analyzed the

57

electron beam profile by using a knife-edge method conducted at approximately 5 mm far from the gun. The rms beam spot size measured at this position is 98 ± 5.6 µm. As shown in Figure 3.27(c), the spatial profile is an asymmetric bell shape, while that of the beam spot recorded on the screen (i.e. 1.2 kV image in Figure 3.27(a)) is well fitted by a Gaussian distribution (Figure 3.28) which indicates minimal spherical aberration of the Einzel lens system. We ascribe this profile inconsistency to a minor measurement error on the knife-edge scanning.
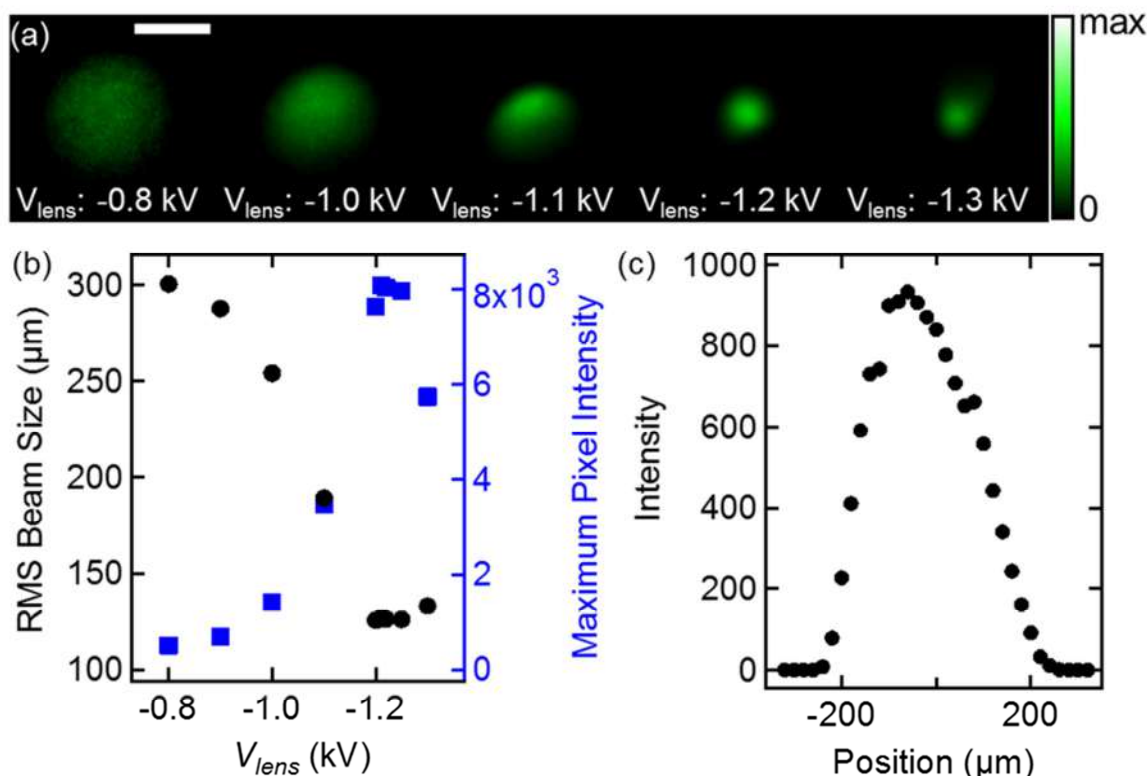
{Figure 3.27. Characterization of the electrostatic Einzel lens system. (a) Electron beam spot experimentally recorded at V_{lens} of -0.8 kV, -1.0 kV, -1.1 kV, -1.2 kV, and -1.3 kV with the fixed $V_{cathode}$ of -1.6 kV. Scale bar indicates 1 mm. The maximum intensity set in each image is 2000, 5000, 10000, 20000 and 20000 for -0.8 kV, -1.0 keV, -1.1 keV, -1.2 keV, and -1.3 keV image, respectively. (b) Summary of the RMS beam spot size and the maximum pixel intensity as a function of V_{lens}. (c) Intensity profile of the maximum focused electron beam. The camera integration time is 1 sec.}

Next, we carried out static electron diffraction experiments using a freestanding monolayer of graphene. We recorded diffraction images by changing the kinetic energy of the electron beam E_{kin} from 1.0 to 2.0 keV with a fixed $V_{lens}/V_{cathode}$ ratio of the maximum focusing condition obtained from the lens experiments. The sample was placed in the same distance from the source, where the beam size is measured. As displayed in Figure 3.29(a), diffraction spots up to 2nd order are clearly visible for the entire range of E_{kin}. Moreover, with the increase of E_{kin}, the diffraction spots become sharper and

brighter. This observation can be explained by the relation between the beam spot size, σ_x, and E_{kin}, $\sigma_x \sim 1/\sqrt{E_{kin}}$. We measured the size of the first order diffraction spots, σ_{diff}, for the respective images, showing an inversely proportional fit to the root mean square of E_{kin} (Figure 3.29(b)), consistent with this known relation.
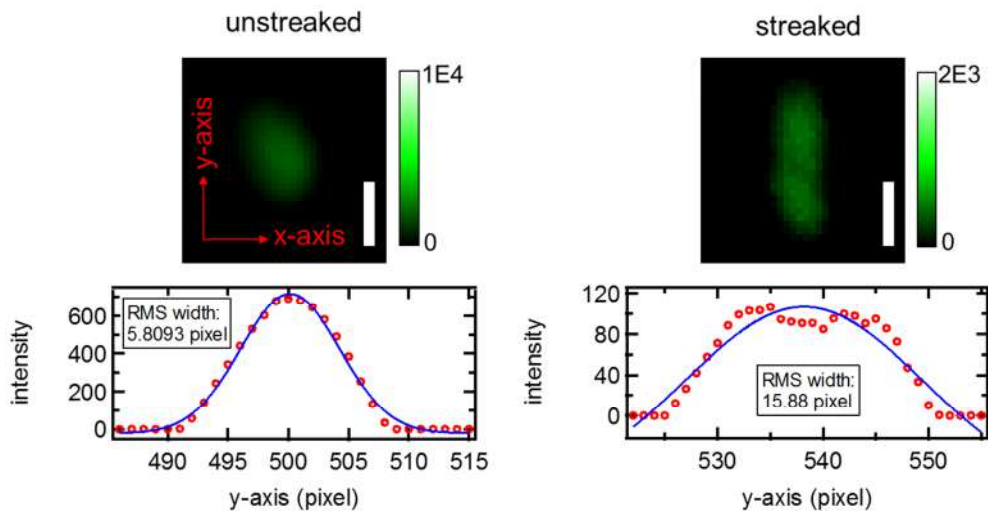
{Figure 3.28. Line profile of the beam spot in y-axis direction after binning pixels in x-direction.}

From the diffraction images, the transverse coherence length of the electron beam, σ_c, can be estimated from the relation [64,97],

$$\sigma_c = a \times \frac{R}{\sigma_{diff}} \tag{3.4}$$

where, a and R represent the lattice constant of the diffraction sample and the beam center-to-first order diffraction spot distance, respectively. In the case for diffraction images recorded at 1.6 keV electron energy, we calculated σ_c to be 5.22 ± 1.22 nm. With σ_c and the measured value of σ_x using the knife-edge technique, we were able to obtain the normalized transverse beam emittance, $\varepsilon_{n,x}$, of 20 ± 4.7 π nm from the following relation [95],

$$\varepsilon_{n,x} = \frac{\hbar}{mc} \times \frac{\sigma_x}{\sigma_c} \tag{3.5}$$

where, *m* and *c* indicate the electron mass and speed of light. The inferred value is comparable with the reported one (= 16 π nm) from our previous emittance measurement of this fiber-based source [95], reflecting that space-charge induced emittance degradation caused by beam focusing is negligible for experimental conditions relevant for diffraction.
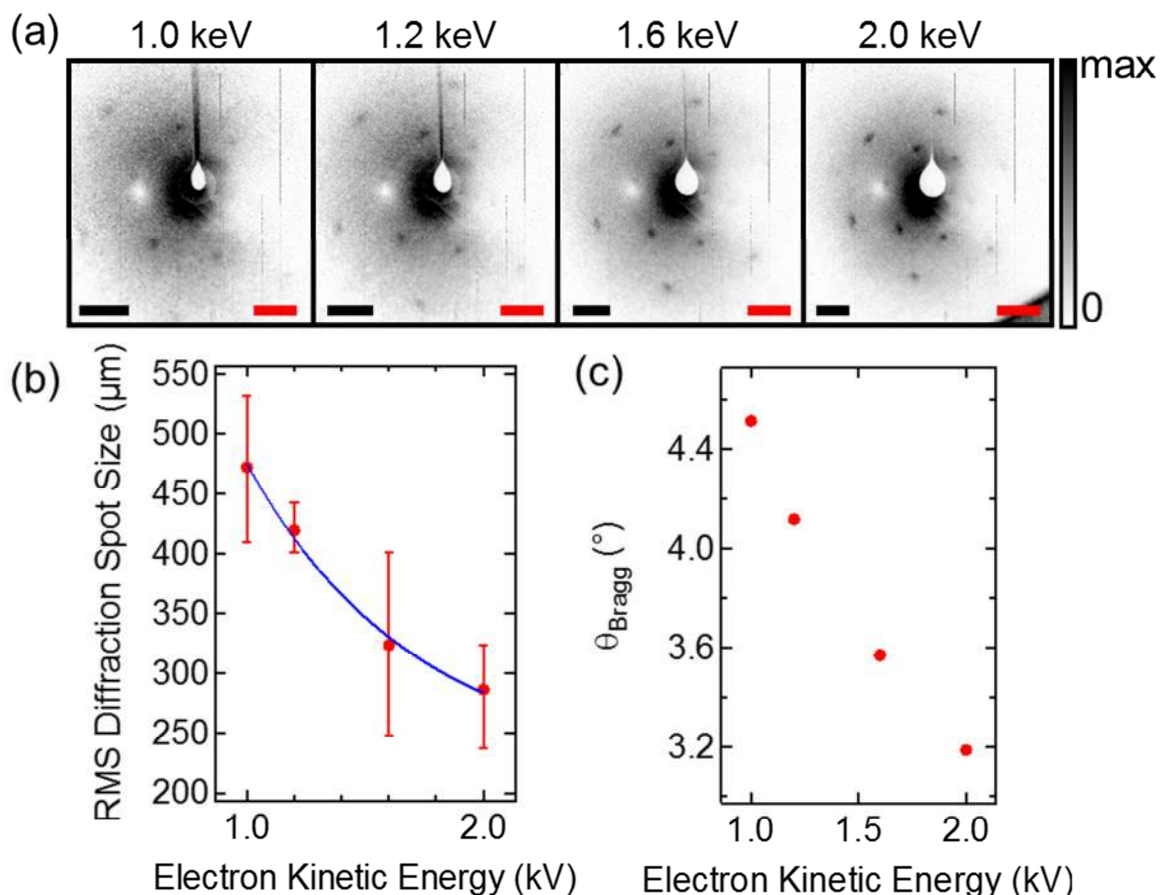
{Figure 3.29. (a) Static electron diffraction pattern of the freestanding graphene, recorded at the maximum focusing condition with different kinetic energies for the incoming electron beam. The maximum intensity set in each image is 700, 800, 1300, and 1300 for 1.0 keV, 1.2 keV, 1.6 keV, and 2.0 keV image, respectively. The black and red scale bar indicate 1/Å and 5 mm, respectively. (b) RMS diffraction spot size of the 1st order Bragg peaks as a function of electron kinetic energy. (c) Calculated Bragg diffraction angle as a function of electron kinetic energy. The camera integration time is 100 sec.}

We then characterized the temporal length of the electron bunch by using a home-built laser-triggered streak camera previously demonstrated in [75]. The detailed synchronization scheme of the streak camera triggering pulse with respect to the electron bunch entrance timing is explained in section 3.2.2.7. The streak camera is composed of a GaAs photoswitch and two streak plates aligned

parallel to each other in which transient electric field is generated in the orthogonal direction with respect to the electron beam propagation direction upon hitting the photoswitch with an optical trigger (180 fs FWHM, 515 nm) as illustrated in Figure 3.30 (a). The resultant angular deflection of the electron bunch gives rise to a streaked electron beam image at the screen (Figure 3.30 (c)), and by comparing it with the unstreaked one (Figure 3.30 (b)), the temporal profile of the electron bunch is extracted (Figure 3.30 (d)). By placing the center of the two streak plates at the position where the diffraction sample would be placed, we ensure minimal deviation of the bunch length between the characterized one and the actual one used in the diffraction experiment. The measured FWHM bunch length is 14 ± 2 ps in the maximum focusing condition with the fixed $V_{cathode}$ of -1.6 kV.
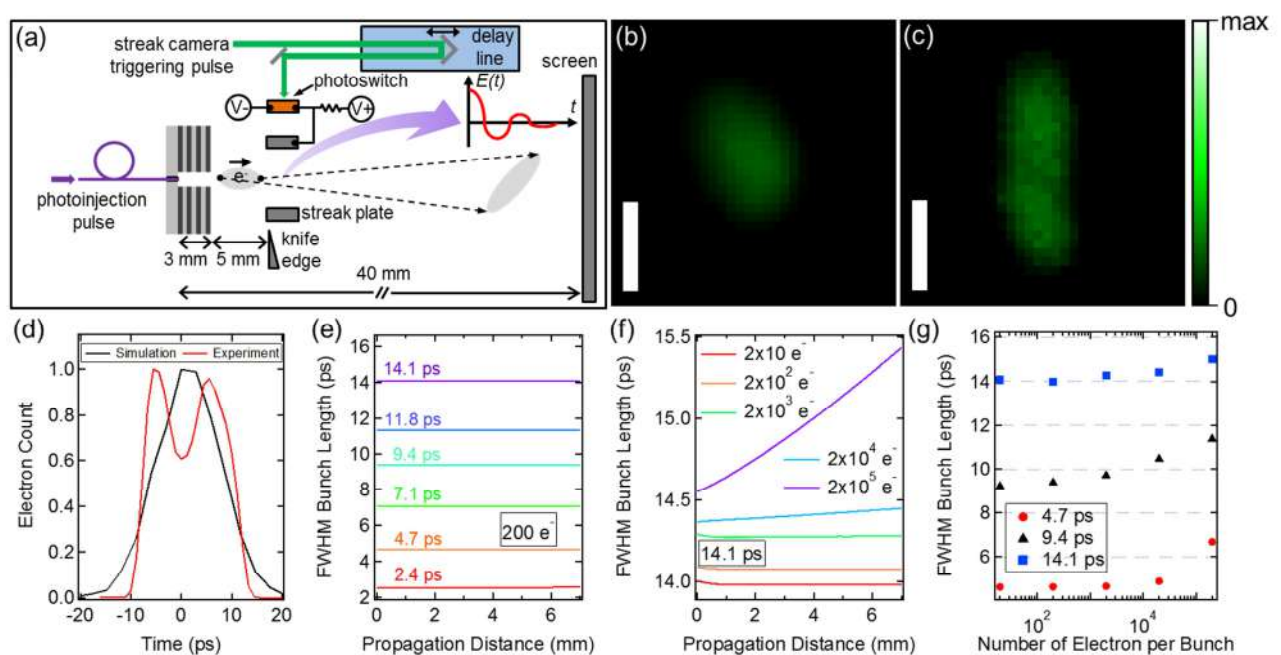
{Figure 3.30. Temporal characteristics of the electron bunch. For the experiment and simulation, the electron energy was set to 1.6 keV. (a) Schematic illustration of the streak camera operation. The maximum streak velocity of the streak camera is found by changing the relative time delay of the streak camera triggering pulse with respect to the fixed arrival time of the photoinjection pulse. (b) Unstreaked and (c) streaked electron beam image. The scale bar indicates 10 pixels. The maximum intensity is 10000 and 2000 for unstreaked and streaked image, respectively. The intensity profile of these two images are binned horizontally and deconvolved each other with Tikhonov regularization parameter of 2.4 to generate the temporal profile of the electron bunch shown in (d). In Figure 3.30(d), black and red curve indicate data extracted from ASTRA simulation and streak camera measurement, respectively. (e) Calculated FWHM length of the bunch as a function of the trigger pulse width (with 200 electrons), and (f) the number of electrons per bunch (with 14.1 ps trigger pulse) (g) Calculated FWHM length of the bunch measured at the diffraction sample position (5 mm far from the electron

gun). The camera integration time is 1 sec.}

When the laser trigger pulse for the electron emission travels through a waveguide, the temporal pulse width stretches owing to dispersion effects. Given the geometrical parameters, and the coupling condition, the FWHM temporal width of the stretched pulse along the travel length of 1 m inside the fiber is estimated as 13.69 ps (section 3.2.2.5). We note that this estimated triggering pulse width is close to the measured electron bunch length, leading us to conclude that space-charge or initial electron kinetic energy spread induced bunch broadening is negligible for the electron bunch generated in the fiber-based cathode upon its propagation.

In order to verify our scenario, we simulated the temporal electron bunch length using the ASTRA[98] code capable of tracking space charge fields by varying the pulse width of the stretched photoinjection pulse at the end of the fiber and the number of electrons per bunch. The detailed simulation method and parameters are described in section 3.2.2.6. As shown in Figure 3.30(e), no perceptible temporal broadening is calculated for the bunch composed of 200 electrons, indicating that the space charge effect is negligible for the temporal property of the non-dense electron bunch triggered by the stretched pulse in the range of the FWHM pulse width from 2.4 ps to 14.1 ps. In contrast, for bunches with more than 10^4 electrons, the bunch length starts to broaden upon propagation even in the case of maximally stretched pulses in the simulation (Figure 3.30(f)). As summarized in Figure 3.30(g), this bunch broadening tendency is significant as the number of electrons per bunch becomes larger and when the pulse width of the trigger is shorter. These results are expected. The calculations are important to determine the acceptable parameter space and to compare to experimental characterization of the beam to ensure stray field and space charge effects are not deteriorating the beam quality for diffraction. In this respect, this simulation result well supports our experimental data that the trigger pulse width is the most critical factor in determining the time window of the observable dynamics in ultrafast streak diffraction experiment in the case in which the number of electrons is sufficiently small. The calculations allow one to properly optimized electron number and density for various applications of interest. In general, the number of electrons per pulse for given beam, focusing conditions, and sample limitations needs to be maximized within the required spatial resolution to improve the signal to noise for a particular application. This approach allows one to optimize the electron pulse profile by controlling the input pulse and stretch factors to maximize the diffraction image quality and associated space-time resolution to recording atomic motions.

3.2.2.4. Summary

In summary, we have demonstrated an optical fiber-driven low-energy electron gun developed for the purpose of ultrafast low-energy streak diffraction that can overcome the temporal resolution limits of current time-resolved LEED and the resulting difficulties in the design of the setup. By using the implemented electrostatic Einzel lens system on the fiber-based photocathode, the electron beams are focused to the detector, and with the well-focused beam, static electron diffraction images were obtained in a wide range of electron energies. Temporal characteristics of the generated electron bunch and simulation results indicate that the temporal length of the sparse electron bunch triggered by few picosecond laser pulse stretched inside the fiber is minimally affected by space charge effects. Finally we expect that compared to the electron bunches triggered by the pre-stretched picosecond pulses as in the present work, electron bunches generated by femtosecond pulses and subsequently broadened to picosecond range by the space charge effect are more challenging in delivering large number of electrons per bunch into the sample without beam brightness degradation.

Lastly, considering a possible higher streak velocity generated from an improved streak camera design, we expect the ultimate temporal resolution of our optical fiber-driven gun combined with the ultrafast streaking technique can reach to a subpicosecond regime in the time-resolved LEED experiment. Also, as demonstrated in the static electron diffraction of monolayer graphene, the spatial resolving power of the low-energy electron bunch is 1.23 Å. Therefore, this simple fiber optic approach, explicitly exploiting dispersion, can be used to tailor the electron bunch to fully optimize image quality in combination with streaking to maintain high space-time resolution for the study of structural dynamics at surfaces, including irreversible surface reaction dynamics.

3.2.2.5. Estimation of the temporal broadening of the triggering pulse

We discuss four kinds of dispersion that can affect stretching of the laser pulse width during propagation inside a fiber [99].

1) Modal dispersion, σ_m

Each mode propagating inside the large core multimode fiber has different group velocities. The rms pulse width owing to the modal dispersion inside the fiber, σ_m, is a function of the fibre length, L, and numerical aperture of the fiber (NA), and refractive index of the core (n_1).

$$\sigma_m = \frac{L \cdot NA^2}{4 \cdot c_0 \cdot n_1} \tag{3.6}$$

The NA of the fiber used in the present experiment is 0.228127, L = 1 m, n_1 =1.46, thereby yielding

σ_t = 31.19 ps. This value is the theoretical maximum of the modal dispersion-induced pulse stretching, assuming that the incoming free space beam is coupled to the fiber with the same *NA* as the nominal *NA* value of the fibre.

The effective numerical aperture due to the actual coupling condition, $NA_{effective}$, is different from the nominal *NA* of the fiber, and has to be taken into account to estimate the actual value of σ_m during the experiment [100], and can be written as

$$NA_{effective} = n \cdot \sin \theta \tag{3.7}$$

where, *n* is the refractive index of the free space medium (=1 for air), and θ is the half-angle of the cone of the converging light from the lens into the fiber.
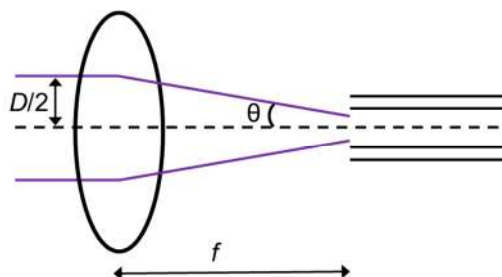
{Figure 3.31. Illustration of free space-to-fiber coupling}

In the experiment, we used a focusing lens with a focal length of 40 mm for the purpose of free space beam-to-fiber coupling, and the rms beam size (*D/2*) of the free space beam was 525 μm. From these values, $NA_{effective}$ is calculated as 0.01312, approximately a factor of 17 smaller than the nominal *NA* of the fiber. The actual σ_m is then estimated as 98 fs.

2) Material dispersion, σ_{mat}

When the free space laser pulse composed of a spectrum of different wavelengths is coupled to the fiber, each wavelength component travels with a different group velocity inside the fiber core. As a result, the initial temporal pulse width in the free space spreads after propagating a distance. The pulse stretching caused by this material dispersion, σ_{mat}, is described as follows:

$$\sigma_{mat} = D_{mat} \cdot \sigma_\lambda \cdot L \tag{3.8}$$

where D_{mat} and σ_λ are the material dispersion coefficient and the spectral width of the free space laser, respectively. D_{mat} is 5174 ps/km-nm, as specified by the fiber supplier. σ_λ is measured as 1.09 nm (RMS) at the central wavelength of 257 nm. Thus, σ_{mat} = 5.64 ps.
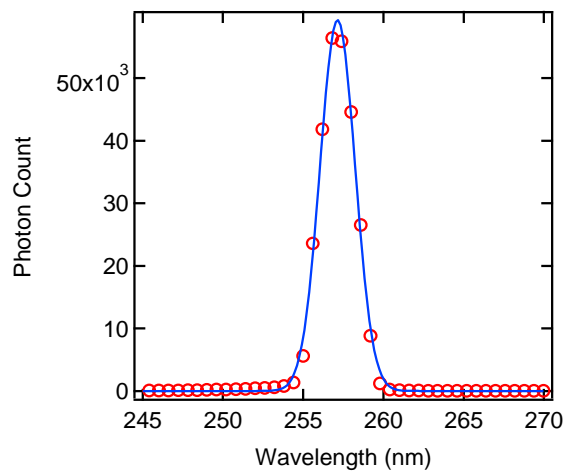
{Figure 3.32. Wavelength spectrum of the trigger laser pulse}

3) Waveguide dispersion, σ_w

Waveguide dispersion arises owing to the different phase velocities in the core and cladding when the pulse travels inside the fiber. It is significant in single mode fibers, but not in large core multimode fibers in which the field distribution ratio between the core and the cladding is large. The pulse stretching owing to the waveguide dispersion is described as

$$\sigma_w = D_w \cdot L \cdot \sigma_\lambda \tag{3.9}$$

where, D_w is the waveguide dispersion coefficient, expressed by the following relation:

$$D_w(ps \cdot nm^{-1} \cdot km^{-1}) \approx -\frac{83.76 \cdot \lambda(\mu m)}{[a(\mu m)^2 n_2]} \tag{3.10}$$

Here a and n_2 are the fiber core diameter and refractive index of the cladding, respectively. Given the 100 μm core size of the present fiber, we neglect the effect of the waveguide dispersion in considering the pulse stretching.

4) Nonlinear dispersion, σ_n

Due to the relatively low power of the incoming light and the large size of the core, we neglect any nonlinear dispersion effect in the pulse stretching.

65

Finally, based on the above discussion, modal and material dispersion effects contribute to the overall temporal stretching of the laser pulse, leading us to conclude that the estimated rms temporal width of the laser pulse, σ_{total}, after propagation of 1 m of the fibre is 5.81 ps

($\sum \sigma_{total}^2 = \sum \sigma_m^2 + \sum \sigma_{mat}^2 + \sum \sigma_{initial\_RMS\_pulse\_width}^2$). With an assumption of Gaussian temporal profile, this value is equal to the FWHM width of 13.69 ps.

3.2.2.6. Description of the ASTRA code simulation

ASTRA is a space charge tracking solver based a mean-field approach.

1) The longitudinal electric field component on the longitudinal position on the radial-symmetry axis is calculated in the case of maximum focusing condition corresponding to V_{lens} of 1.22 kV at $V_{cathode}$ of 1.6 kV with a commercial software package (CST particle studio), and is exported to the ASTRA particle tracking code for defining the actual electrostatic fields nearby the electron beam propagation. The radial and magnetic field components are deduced from the derivative of the longitudinal field with respect to the longitudinal position, automatically from ASTRA.

2) To simulate photoelectron generation on our optical fiber-based cathode in ASTRA, we set 1000 particles generated from a circular spot with 100 um rms diameter. The actual number of electrons per bunch is reflected by adjusting the bunch charge parameter. In the emission spot, the transverse and longitudinal spatial distributions of the electrons are assumed to have a Gaussian profile. The effective work function of the gold layer is assumed to 4.3 eV and the photon energy is set to 4.824 eV corresponding to the 257 nm wavelength of the triggering laser pulse. The initial momentum distribution of the electrons in the transverse and longitudinal axis is assumed to have a Fermi-Direc distribution at 300 K. Given those assumptions, ASTRA simulator calculates the rms electron kinetic energy spread, σ_{Ekin}, by the following formula [98]:

$$\sigma_{Ekin} = \frac{1}{3\sqrt{2}}(E_{phot} - \phi_{eff}) \qquad (3.11)$$

The calculated rms energy spread is equal to 0.12 eV (= 0.28 eV FWHM), which is in good agreement with the reported value of a photocathode made of the thin gold film on a sapphire substrate [101]. This calculated value is taken into account during the entire particle tracking simulation. We also note that the measured rms spectral width (0.02 eV equal to 1.09 nm, as shown in Figure 3.32) of the photo injection trigger beam is only approximately 17 % of the energy spread

caused by the photoemission process. Therefore, we expect the effect of the broadened spectra of the trigger beam is negligible to the simulated electron bunch length.

3) In ASTRA, the space charge field is calculated on a cylindrical coordinate based volume. We sectioned this space charge field volume into 5 rings in the radial direction and 8 slices in the longitudinal direction, indicating that on average 25 particles are contained in each sectioned grid in the simulation.

3.2.2.7. Synchronization scheme of the streak camera triggering pulse with respect to the electron bunch entrance timing

As illustrated in Figure 3.30(a), we vary the travel distance of the streak camera triggering pulse by moving the mirror placed on the delay line stage. The travel distance of the photoinjection pulse is fixed. In this way, we are able to control the arrival time of the streak camera triggering pulse with respect to that of the photoinjection pulse.

In order to find the maximum streak velocity region (typically in the first zero-crossing where the linear field ramp-up or –down appears), we image the electron beam spot on the screen and compare the streaked beam spot positions to that of the unstreaked one, as shown in Figure 3.33.
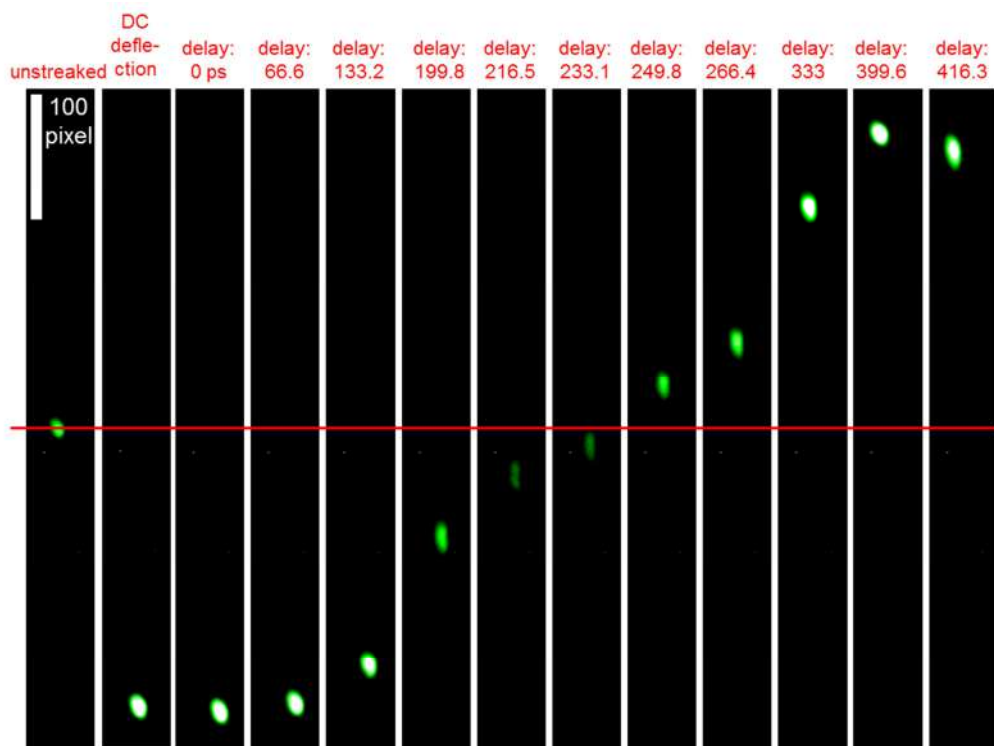
{Figure 3.33. Change of the electron beam spot position as a function of relative delay between the streak camera triggering beam and the electron bunch entrance timing.}

67

4. Theoretical Background of Transmission-Mode Time-Resolved Low-Energy Electron Diffraction (LEED)

4.1. Kinematic approach on electron diffraction

In this Chapter, electron diffraction phenomenon is briefly discussed based on the kinematical scattering theory with following assumptions:

1) The incident electron beam is monochromatic coherent plane wave.

2) All atoms of the diffraction sample scatter the electron wave one time. No multiple scattering.

3) There is no absorption from the diffraction sample.

4.1.1. Coherent elastic electron scattering

When a coherent incident electron beam is irradiated to a diffraction sample (thin enough for the incident electron to penetrate through), as depicted in Figure 4.1, a part of the beam interacts with the sample (specifically atoms of the sample), experiencing an angular deviation on its pathway, while the rest of it does not. The undeviated electron beam resulted from no incident electron-to-sample interaction is referred to "direct beam". The deviated beam is a consequence of the electron scattering with matter, categorized into elastic and inelastic scattering process. As its definition indicates, the elastic scattering conserves the wave energy before and after the scattering process and gives rise to relatively higher scattering angle (1-10°) whereas the inelastic scattering process results in smaller scattering angle ($<1^{o}$) without energy conservation. In the electron-matter interaction, what can be a useful probe to extract the atomic structural information is the elastically scattered electron in that wavelength and amplitude of the scattered electrons from all the atoms of the sample are same, and only the phase of them are different (see the section 4.1.2.).
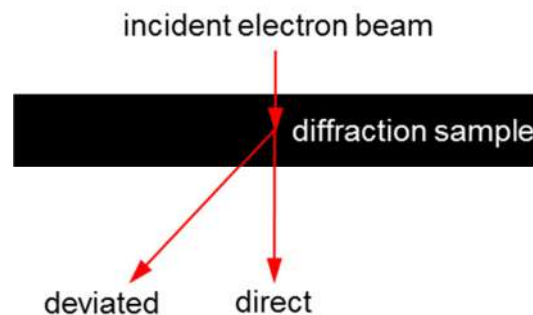
{Figure 4.1. Illustration of the incident electron beam irradiation on the diffraction sample}

What is the origin of the elastic electron scattering from matter? Electron is a charged particle. As illustrated in Figure 4.2, when this charged particle penetrates into the electron cloud of an atom, it is attracted by the positive potential of the nucleus. The closer the incident electron comes to the nucleus, the larger the Coulombic force is applied, resulting in a large angle deflection. In the extreme case, even complete backscattering (180°) can occur with a three magnitude lower probability [102]. The incident electron is elastically scattered not only by the nucleus but also by the electron cloud of an atom, however, the comparison of the electron elastic scattering cross-section by nucleus and that of the electron cloud indicates that the electron-electron induced elastic scattering event is negligible compared to the electron-nucleus interacted one, especially for high atomic number atoms (Appendix C).
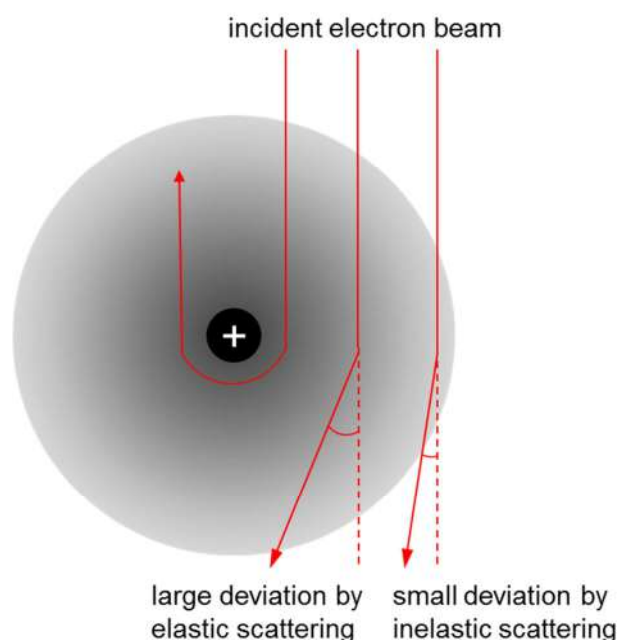
{Figure 4.2. Illustration of the incident electron-atom interaction. The central '+' sign indicates the positive charge of the nucleus. The surrounding electron cloud is depicted as the gradation color.}

The wavelength (10 – 100 pm) of the hard X-ray (12 – 120 keV) implies its capability to use as an atomic structural probe, as like electrons, however, the information provided by the X-ray is different from that by the electron probe, which originates from its scattering mechanism with matter. Therefore, it is informative to compare the elastic scattering mechanism by the incident electron and atom to that by X-ray and atom. X-ray is a form of electromagnetic radiation. When the X-ray is incident to an atom, the bound electrons of the atom oscillates with the period of the applied X-ray electromagnetic field. These accelerated charged particles then radiate a copied electromagnetic field (*i.e.* electric dipole radiation as pictured by a classical ball-string model), identical in wavelength and phase to the incoming X-ray. In this regard, X-rays probe the nuclear position indirectly via the

diffuse electron density of the atom by field-to-field exchange mechanism, while electrons probe the nuclear position directly by Columbic interaction. As a result, the elastic scattering cross-section of electron with matter is much larger (10^6 – 10^7) than that of X-rays with matter [56]. This large elastic cross section of electrons alleviates the difficulty in the structural study of radiation damage sensitive samples (for example, proteins) compared to X-ray probes in that more useful events (elastic scattering) occurs for a given number of incident probe particles.

4.1.2. Bragg diffraction

As a result of the electron elastic scattering from a diffraction sample composed of many atoms, diffraction spots or rings for crystalline samples are imaged at the detector plane. As shown in Figure 4.3, as one coherent ray is incident on an atom on a crystal plane with an incident angle, θ, the atom plays a role as a mirror such that one elastically scattered ray propagates with the same amount of angle, θ, from the crystal plane. A second ray performs the same thing for another atom on a next crystal plane separated from the first plane by d, generating the second elastically scattered ray. The diffraction spots are formed at the screen only when the two scattered rays constructively interfere with each other. The constructive interference can be generalized to other atoms on other crystal planes of the diffraction crystal, and a simple mathematical description on this phenomenon was first introduced by Sir W. L. Bragg with reflected X-rays from a crystalline solid in 1913 [103]. The end result is the famous Bragg law, $\lambda = 2d_{hkl} \sin\theta_{hkl}$, where λ, d_{hkl}, and θ_{hkl} refer to the wavelength of the incident ray, spacing distance between (hkl) planes, and corresponding Bragg reflection angle, respectively. The Bragg law can also be applied to the case of coherent incident electrons, considering the wave-particle property of electron.
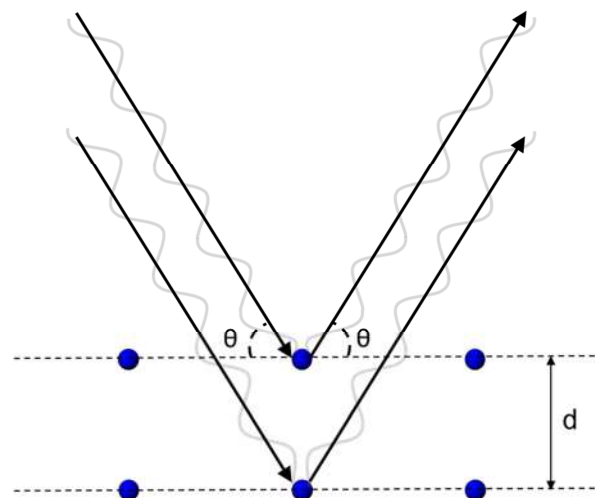
{Figure 4.3. Illustration of the Bragg diffraction}

70

4.1.3. Fourier analysis on diffraction

A crystal is composed of periodically repeated bases in which atoms are arranged. The basis, called a unit cell, thus represents the distinct atomic structure of the system, the target that has to be revealed by diffraction. The periodicity is characterized by the concept of a lattice, $\mathcal{L}(\mathbf{r})$, where $\mathbf{r}$ denotes the lattice vector in the three-dimensional real space. Given the fact that the atomic structure is copied over the entire lattice, the crystal can be mathematically conceived by the convolution, $\otimes$, of the atomic structure of the unit cell over the lattice, as illustrated in Figure 4.4. Therefore, the mathematical expression of the crystal is given by equation (4.1).

$$crystal\ structure\ in\ real\ space = unit\ cell\ \ structure\ in\ real\ space \otimes \mathcal{L}(\mathbf{r})$$

(4.1)

Taking Fourier Transform (*FT*) of equation (4.1) yields a new equation (4.2).

$$FT(crystal\ structure\ in\ real\ space) = FT(unit\ cell\ \ structure\ in\ real\ space) \times FT\big(\mathcal{L}(\mathbf{r})\big)$$

(4.2)

The term $FT(\mathcal{L}(\mathbf{r}))$ is equivalent to the reciprocal lattice, $\mathcal{R}(\mathbf{r})$. The term $FT(unit\ cell\ \ structure\ in\ real\ space)$ is the one that contains the atomic structure of the unit cell, and is called the structure factor. With these implications, equation (4.2) can be rewritten as:

$$FT(crystal\ structure\ in\ real\ space) = Structure\ Factor \times \mathcal{R}(\mathbf{r})$$

(4.3)
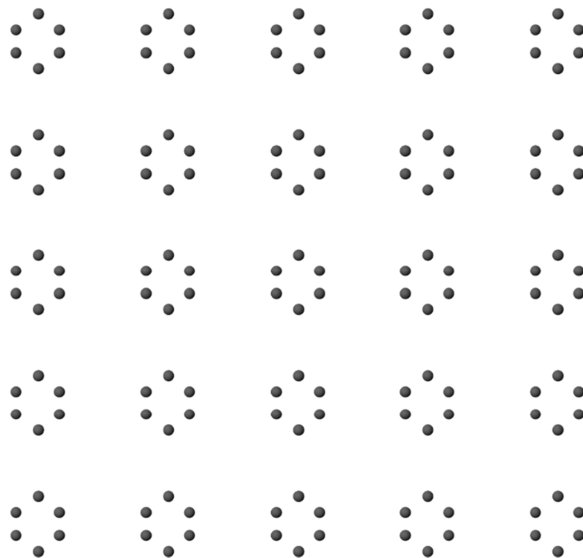
{Figure 4.4. Conceptual illustration of crystal formation as a convolution of basis and real space lattice}

72

4.1.4. Structure Factor

As mentioned in the above, atomic structural details of the unit cell are encoded in the structure factor term. Given that it is nothing but a Fourier Transform of the mathematical expression of the unit cell, it is intuitive to take Inverse Fourier transform of the structure factor to retrieve the atomic structure of the unit cell. Unfortunately, this statement is not completely true due to the notorious phase problem, which will be explained in the following.

What does the structure factor mean physically in terms of kinematical scattering theory? The illustration in Figure 4.5 describes a general situation of the coherent elastic electron scattering from two atoms separated by a distance $\mathbf{r}$.
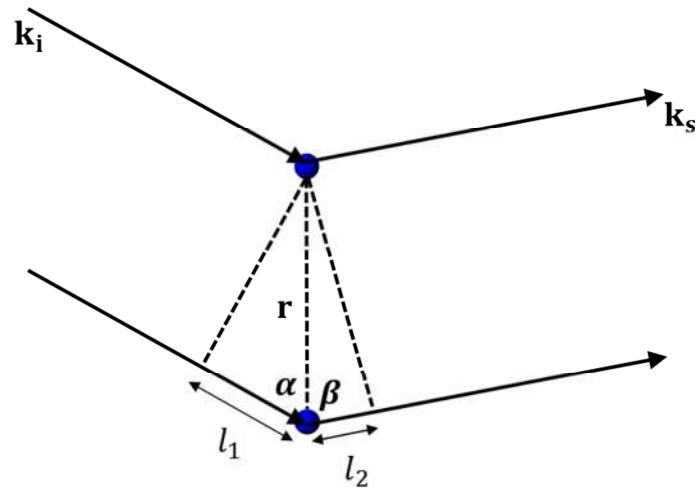
{Figure 4.5. Illustration of the scattering rays from two atoms, which leads to the path length difference}

In this case, the angle of the incident ray with wave vector $\mathbf{k_i}$ does not have to necessarily be same as the angle of the scattered ray with the wave vector $\mathbf{k_s}$: the specular reflection assumed in Bragg diffraction (section 4.1.2) is not considered. The two incoming rays are incident on the upper and bottom atom, respectively, with the same incident angle, α, leading to the path length difference, l_1, and concomitant phase difference, $\mathbf{k_i r}$. The scattered rays with the scattered angle, β, from the two atoms also give rise to the phase difference, $-\mathbf{k_s r}$, owing to the path length difference, l_2. Those two contributions from the incoming and scattered rays make the total phase difference, $(\mathbf{k_i} - \mathbf{k_s})\mathbf{r}$. Here, the change of the wave vector, $(\mathbf{k_i} - \mathbf{k_s})$, is defined by $\mathbf{Q}$, called the scattering vector or the momentum transfer, as depicted in Figure 4.6.
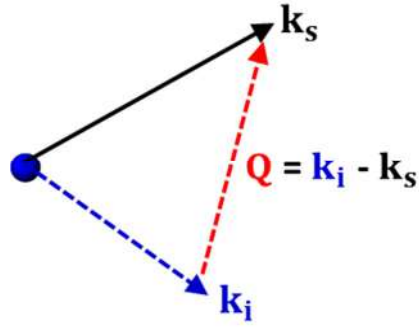
{Figure 4.6. Scattering vector, **Q**]

The scattering vector is a useful quantity in that the overall phase change not depends on either $\mathbf{k_i}$ or $\mathbf{k_s}$, separately, but only on **Q**. By taking the position of the first atom to be the origin, the wave equation of the scattered ray by the first atom can be expressed as:

$$\psi_{first\ atom}(\mathbf{x}) = exp(i\mathbf{k_s}\mathbf{x}) \tag{4.4}$$

where, **x** denotes the propagation direction of the scattered ray. The scattered ray from the second atom is out of phase by the total phase difference **Qr**, and its wave equation is expressed as:

$$\psi_{second\ atom}(\mathbf{x}) = exp(i\mathbf{k_s}\mathbf{x})exp(i\mathbf{Qr}) \tag{4.5}$$

Then, the total scattering is expressed as:

$$\psi_{first\ atom}(\mathbf{x}) + \psi_{second\ atom}(\mathbf{x}) = exp(i\mathbf{k_s}\mathbf{x})(1 + exp(i\mathbf{Qr})) \tag{4.6}$$

The comparison of equation (4.4) and (4.6) indicates that the amplitude of the scattered beam is modified by the phase factor:

$$F(\boldsymbol{Q}) = 1 + exp(i\mathbf{Qr}) \tag{4.7}$$

The electron scattering from two atoms can be extended to a situation of the electron scattering from many atoms, by defining the positions of each atom with respect to the origin (the first atom position) as $\mathbf{r_j}$. Then, the amplitude of the scattered rays from n atoms can be expressed as:

$$F(\boldsymbol{Q}) = \sum_j^n exp(i\mathbf{Qr_j}) \tag{4.8}$$

Given that each atom scatters the incoming rays by a different amount due to its different atomic number, a weighting factor has to be taken into account for the amplitude of the total scattered rays. This factor is denoted by f_j, and called scattering factor or atomic form factor. With f_j, equation (4.8) is modified to:

$$F(\boldsymbol{Q}) = \sum_{j}^{n} f_j \, exp\big(i\mathbf{Qr_j}\big) \tag{4.9}$$

The intensity of the diffraction spot is square of the amplitude of the scattered rays in that diffraction is a result of the constructive interference.

$$I = |F(\boldsymbol{Q})|^2 = \left|\sum_{j}^{n} f_j \, exp\big(i\mathbf{Qr_j}\big)\right|^2 \tag{4.10}$$

Equation (4.10) clearly points out two important aspects of diffraction. First, the information about the relative position of each atom with respect to the origin defined by the first atom position is contained in the measured diffraction spot or ring intensity. Second, unfortunately, this information cannot be directly extracted from diffraction because of the feature of the square multiplication of the phase term. This issue is called the phase problem in the determination of the crystal structure by diffraction.

As introduced in section 4.1.1, the information extracted from the electron elastic scattering with an atom is the electrostatic potential of nucleus of the atom, denoted by ϕ_j. A group of atoms has their relative position, $\mathbf{r_j}$, in the unit cell, and the position of each atom can be represented by a Dirac delta function, $\delta(\mathbf{r} - \mathbf{r_j})$, as shown in Figure 4.7.
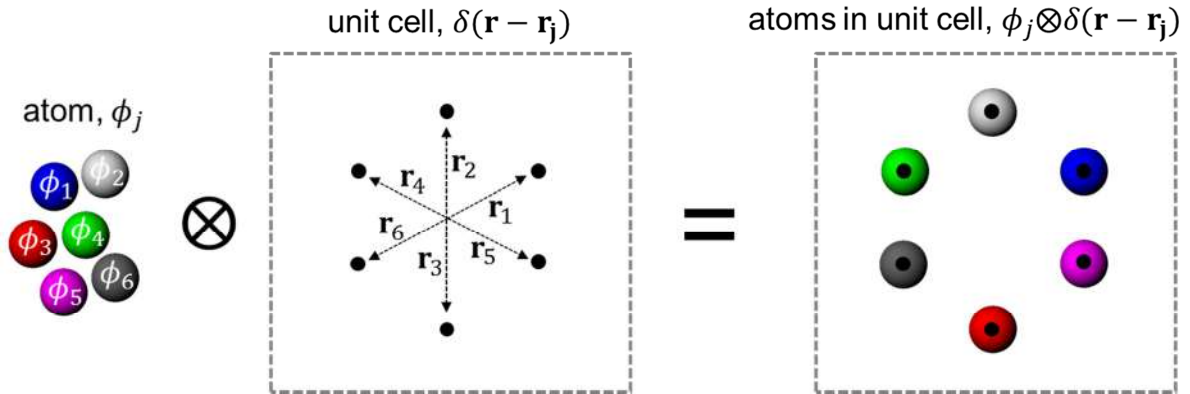
[Figure 4.7. Illustration of individual atom positions in the unit cell]

In this regard, analogous to the mathematical expression of the crystal in section 4.1.3, the electrostatic potential associated with the atomic position in the unit cell, can be written as:

$$individual\ atoms\ in\ unit\ cell = \sum_{j}^{n} \phi_j \otimes \delta(\mathbf{r} - \mathbf{r_j}) \tag{4.11}$$

Taking Fourier Transform on the left and right hand side of the equation (4.11) yields a new equation:

$$FT(individual\ atoms\ in\ unit\ cell) = \sum_{j}^{n} FT(\phi_j) \, exp\big(i\mathbf{Qr_j}\big) \tag{4.12}$$

Given that ϕ_j reflects the scattering strength of each atom, the term $FT(\phi_j)$ can be considered as equivalent as the scattering factor, f_j. Then, equation (4.12) can be rewritten as:

$$FT(individual\ atoms\ in\ unit\ cell) = \sum_j^n f_j\, exp(i\mathbf{Qr_j}) \qquad (4.13)$$

Comparison of equation (4.9) and (4.13) leads to the conclusion of this chapter: the physical meaning of the Fourier Transform of the individual atoms in unit cell, the *structure factor*, is the amplitude of the elastically scattered electron rays.

4.1.5. Debye-Waller factor

An atom in a crystal has its thermal motion even at absolute zero temperature. The instantaneous position of the atom in the crystal, therefore, is far from a regular periodic position defined by the delta function, $\delta(\mathbf{r} - \mathbf{r_j})$, which affects diffraction. A new term about this thermal or temperature effect on the atomic position needs to be added in the structure factor for the proper structural retrieval from diffraction data:

$$\mathrm{F}(\mathbf{Q}) = \sum_j^n f_j\, exp(i\mathbf{Qr_j})\mathbf{T}_j(\mathbf{Q}) \qquad (4.14)$$

where, the term, $\mathbf{T}_j(\mathbf{Q})$, is called the Debye-Waller factor.

The thermal motion of a single atom can be described by the classical harmonic oscillator model with characteristic parameters, $<\mathbf{u}(t)^2>$, m, and ω, denoting the mean square time-dependent displacement of the atom, atomic mass, and frequency of the oscillator, respectively. The end result in deriving the diffraction intensity based on the harmonic oscillator model including crystal temperature parameter is shown as:

$$\ln\left\{\frac{I(hkl)}{I_0(hkl)}\right\} = -\frac{1}{3}\langle u^2\rangle\mathbf{Q}^2 \qquad (4.15)$$

where, $I_0(hkl)$ and $I(hkl)$ refer to the spot intensity of the Bragg diffracted beam corresponding to (hkl) plane without and with the thermal motion, respectively. Equation (4.15) implies two points. First, as the crystal temperature increases, the diffraction spot or ring intensity decreases, but the spot size or the angular width of the ring do not change. Second, the larger the reciprocal lattice (equivalently stated as the higher of the diffraction order), the weaker the diffraction at high temperature.

4.1.6. Ewald sphere

In view of reciprocal space, diffraction occurs only when the scattering vector, **Q**, introduced in section 4.1.4, coincides with a reciprocal lattice point of a diffraction crystal as illustrated in Figure 4.8 (a). For a fixed orientation of the crystal with respect to the incident electron beam, the diffraction event can happen at one of these points, as denoted by the pink colored dot. If the crystal rotates with respect to the incident beam, effectively equivalent to an angle change of the incident beam, the meeting point is changed accordingly as shown in Figure 4.8 (b). Given by the fact that the complete diffraction involves all crystal orientations, the complete set of **Q**s will construct a surface of a sphere with the radius of $|\mathbf{k_i}|$ ($=2\pi/\lambda$) in three-dimensional reciprocal space. This geometrical construct is called the Ewald sphere [104], showing all possible sets of crystal planes that can fulfill the diffraction condition. A two-dimensional representation of the Ewald sphere, sketched over the reciprocal lattice, is depicted in Figure 4.8 (c).
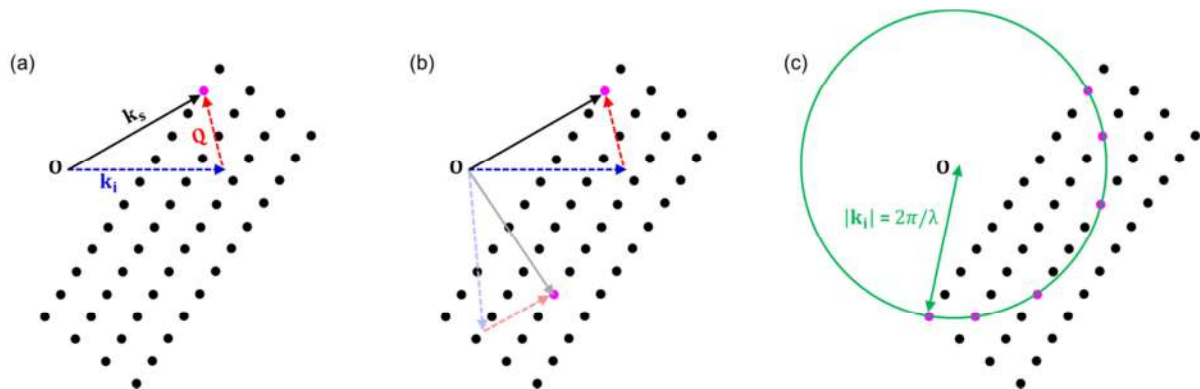
{Figure 4.8. Illustration of two-dimensional section of reciprocal lattice and Ewald sphere.}

Compared to the wavelength of X-ray beams, electron beams (even for 2 keV electrons studied in this thesis) have shorter wavelengths, and thus, the radius of the Ewald sphere is longer. This specific condition of the electron beam makes the curvature of the Ewald sphere shallow. Furthermore, a finite lattice system owing to the finite size of the crystal (especially for electron diffraction, the typical thickness of crystals is ranged in few to few tens of nanometer) is mathematically represented by the multiplication of a three-dimensional slit function to an infinite lattice system. Fourier transforming of the finite lattice system results in the elongation of the reciprocal lattice points due to convolution of the reciprocal lattice with a sinc function. Lastly, the incident electron beam always has a certain amount of energy spread, as described in Chapter 2, indicating that the surface of the Ewald sphere is a line with a finite thickness. Overall, all these distinct features of electron diffraction make the Ewald sphere intersected by many reciprocal lattice points for a given relative angle between the incident beam and crystal orientation, as illustrated in Figure 4.9., allowing to avoid rotation of the crystal in the diffraction measurement.
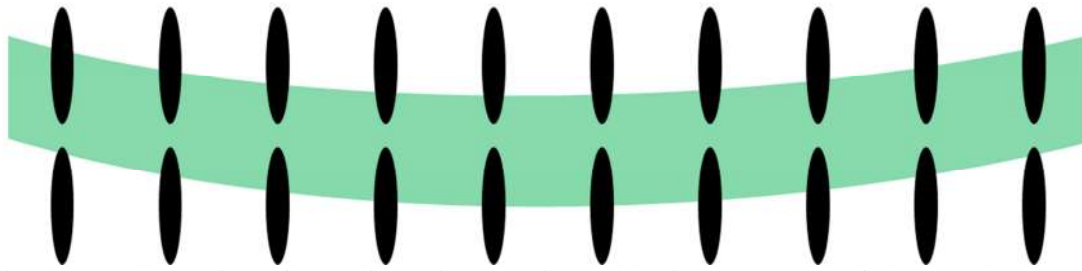
{Figure 4.9. Illustration of two-dimensional reciprocal lattice composed of elongated rods caused by thin thickness of the electron diffraction sample. The reciprocal points are cut by Ewald sphere with a large radius and a certain thickness due to finite electron beam energy spread.}

4.2. Characteristics of low-energy electrons

4.2.1. Wavelength and speed

In this thesis the low-energy electrons is defined by the one with the electron kinetic energy, E_{kin}, ranging from 0 – 2 keV. Because the speed of this electron, v_z, is below a tenth of the speed of light in vacuum (c = 2.99×10^8 m/sec), these electrons can be considered as nonrelativistic electrons, and the Newtonian kinetic energy formula ($E_{kin} = \dfrac{1}{2}m_0 v_z^{\,2}$, where m_0 is the electron rest mass) can be applicable in calculating v_z. The deBroglie wavelength equation ($\lambda = \dfrac{h}{p}$, where h and p denote the Planck constant and electron momentum, respectively) provides the relationship between the electron wavelength, λ, and v_z. The λ and v_z of low-energy electrons as a function of E_{kin} are listed in Table 4.1.

E_{kin} (kV)	λ (Å)	v_z (m/sec)	v_z/c
0.05	1.734	4193521	0.013988081
0.1	1.226	5930099	0.019780682
0.2	0.867	8385196	0.027970005
0.5	0.548	13252328	0.044205008
1	0.388	18727896	0.06246954
1.5	0.317	22920117	0.076453282

2	0.274	26446534	0.088216142

{Table 4.1. Low-Energy Electron Parameters. λ, v_z, and v_z/c as a function of E_{kin}}

4.2.2. Inelastic mean free path

When an electron beam is incident to the surface of a solid sample, the intensity of the beam is damped as it travels through the sample because of the strong electron-matter interaction as discussed in section 4.1.1. The electron inelastic mean free path (IMFP) is defined by the travel distance before the intensity of the incident beam decays to $1/e$ (where, e (=2.71828) is the base of the natural logarithm) of the initial inensity. The IMFP varies as a function of E_{kin} and also depends on the atomic components of the sample. In particular, IMFP for low-energy electron regime is well characterized by a so called "universal curve" calculated by empirical functions based on experimentally measured data [105], shown in Figure 4.10. The empirical function shown in Figure 4.10 legend is based on equation (5) in Ref. [105]. The IMFP of low-energy electron ranges from few angstroms to nanometers, depending on E_{kin}. This short IMFP for low-energy electron indicates that elastic scattering of electrons is very surface sensitive.
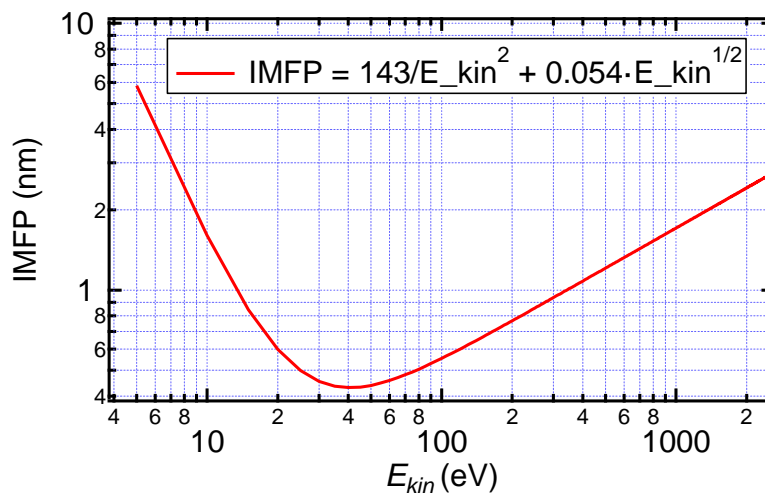
{Figure 4.10. Universal curve presenting IMFP as a function E_{kin}.}

4.2.3. Scattering angle

Unlike the photon-matter interaction featured by isotropic scattering, electrons exhibits anisotropic scattering [66]. As shown in Figure 4.11, the elastic scattering cross section (for carbon atom) ranges widely from 0° to 180° for 50 eV electrons, while 10 keV electron scatters in the forward direction

within a few degrees. The idea of the reflection-mode low-energy diffraction indeed takes advantage of the large angle scattering capability, and the intensity of the elastically backscattered electron diffraction is known to be approximately 0.1% of the incoming intensity [106].
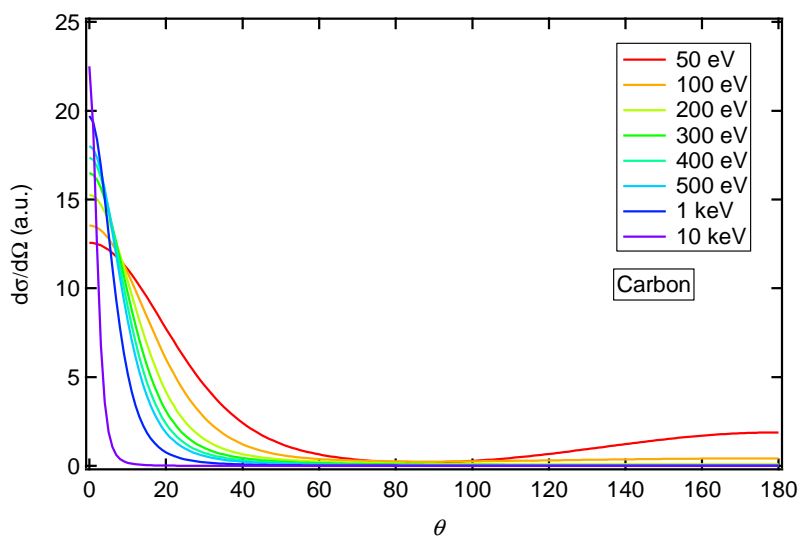
{Figure 4.11. Differential electron elastic-scattering cross section, $d\sigma/d\Omega$, of the carbon atom as a function of polar scattering angle, θ, for different electron kinetic energy. The values were provided from the NIST library [https://srdata.nist.gov/SRD64/Home/Intro].}

4.2.4. Bunch broadening

As introduced in detail in Chapter 2, an electron bunch generated from a cathode has an inherent kinetic energy spread that causes the temporal bunch broadening as the bunch travels in vacuum. In addition, the space charge effect puts additional broadening on the bunch such that the initial bunch duration at the proximity of the cathode is hardly maintained during its delivery to the sample. In particular, the low-energy electron is extremely susceptible to this bunch duration broadening, as shown in Figure 4.12, such that the electron source-to-sample distance should be in the order of few tens to hundreds of micrometer to achieve the femtosecond bunch duration at the sample plane.
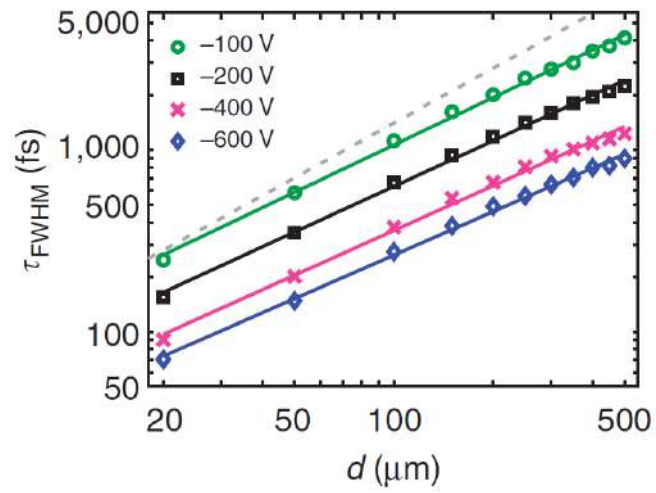
{Figure 4.12. The simulated electron pulse duration as a function of cathode-to-sample distance d for different cathode voltage from -100 V to -600 V. In this simulation, single electron wave packet is considered neglecting space charge effect. Reproduced from [65]. Copyright 2014 Nature Publishing Group.}

5. Development and Characterization of Time-Resolved LEED Setup

5.1. Low-energy electron gun

The low-energy electron gun consists of a typical large area photocathode and an electrostatic Einzel lens system.

5.1.1. Photocathode

The photocathode is prepared by electron beam-assisted thin film deposition of 3 nm of Cr and 30 nm of Au layers, consecutively, on one surface of a double side-polished and half-inch-sized UV-fused silica optical window with 92.5 % transmission for UV wavelength range as shown in Figure 5.1. (a). The prepared cathode is placed inside a half-inch groove on a cathode holder made of stainless steel. Electrical contact is made by gluing a small amount of silver paste along the edge of the cathode. At the center of the backside of the holder, a 1 mm sized aperture hole is drilled, where the UV light is injected. This design of the photocathode and holder allows for a back illumination scheme.
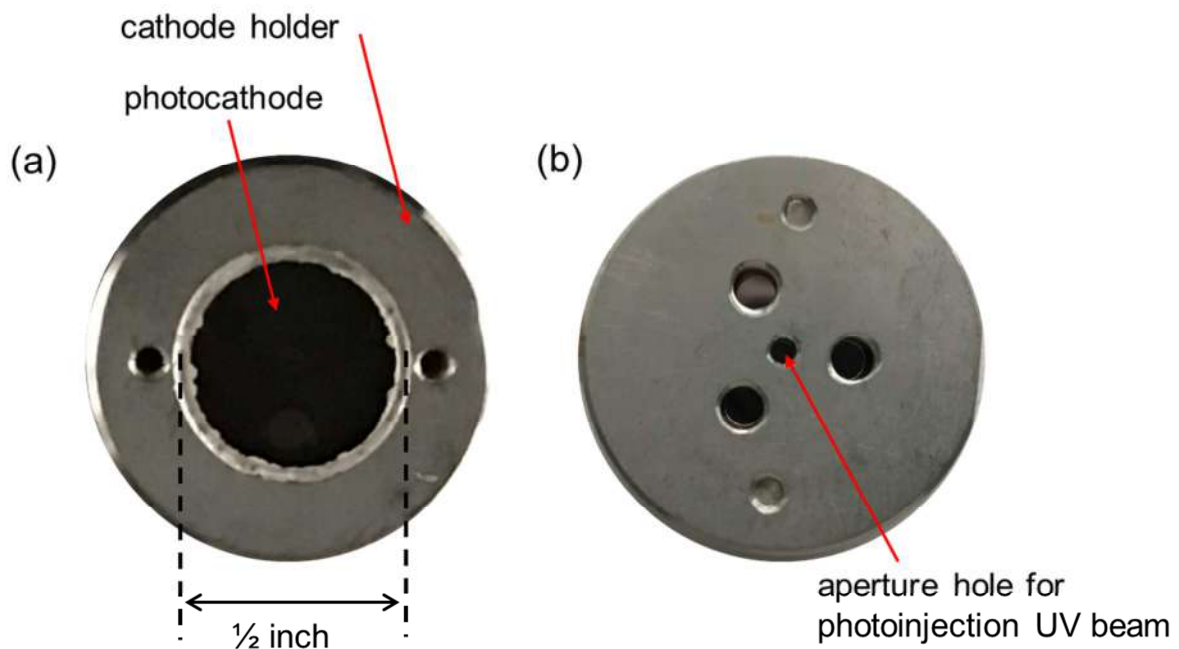
{Figure 5.1. (a) front and (b) back side of the photocathode and cathode holder.}

How many numbers of electrons per bunch can be generated with this cathode? In order to answer this question, the beam current at an anode placed approximately 30 mm far from the cathode

82

is measured as a function of the average input power of the UV photoinjection beam. The anode area (~ 40 mm) is large enough to collect almost all the photoelectrons. 257 nm (4.8 eV) light with 1 kHz repeation rate and ~180 fs pulse length (FWHM) is used for the photoinjection beam. Figure 5.2. displays the measurement result for three different cathode voltages of 0.5 kV, 1.0 kV, and 1.5 kV. All three cases clearly show the linear dependency of the beam current on the input power, indicating a single photon induced photoemission regime. In the input power range from 10 μW to 80 μW, the maximum photoelectron current is measured as 50 pA with the input power of 80 μW, corresponding to approximately 3×10^5 electrons per bunch. The quantum efficiency (electrons per photons), η, is calculated as approximately 3×10^{-6}, in accordance with the reported range of $10^{-5} - 10^{-7}$ for metal photocathodes with UV light [107]. The η slightly increases with the increase of the biasing voltage on the cathode, which can be understood by the Schottky lowering effect explained in Chapter 2.2.
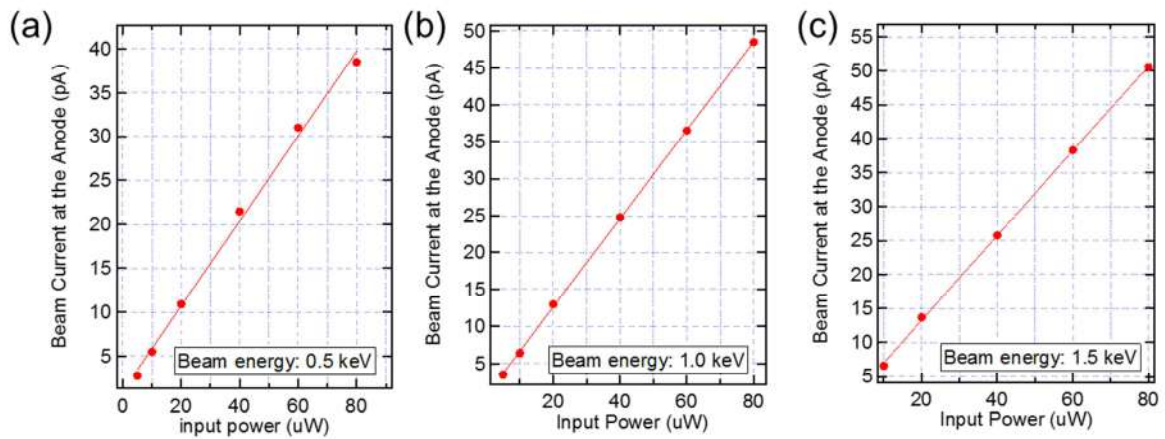
{Figure 5.2. Beam current as a function of photoinjection input power in case when the cathode is biased at (a) 0.5 kV, (b) 1.0 kV, and (c) 1.5 kV}

5.1.2. Electrostatic Einzel lens

For a typical high energy (for example, 100 keV) ultrafast electron diffraction setup, a magnetic lens is placed in between the diffraction sample plane and the screen in order to focus the scattered electron beam from the sample, which otherwise, is imaged as a diffused spot at the screen. Magnetic lens is quite effective than electrostatic Einzel lens for electron beam focusing in that the radial motion of electron has quadratic dependence on the magnetic field while it has linear dependence on the electric field, based on the first-order paraxial approximation of the electron trajectory. However, for ultrafast low-energy electron diffraction setup, the required short sample-to-screen distance owing to the large Bragg scattering angle and finite screen size (40 mm in the present setup case) restricts the use of the magnetic lens in the beam line. Because of this reason, an electrostatic Einzel lens is

integrated directly to the photocathode. In this case, the focal point of the lens is at the screen, not at the diffraction sample, such that the minimum electron beam size is achieved at the screen.

A typical electrostatic Einzel lens system is composed of electron extraction plate acting as an anode biased with ground voltage (V_{ext}) with respect to the negatively biased cathode voltage ($V_{cathode}$), lens plate biased with lens voltage (V_{lens}), and ground plate biased with ground voltage (V_{gnd}). These three plates are made of a conducting material, and in the present setup, 500 μm thick CuBe sheet (200 mm by 200 mm) is laser-cut, producing three identical round discs with 18 mm diameter. At the center of the plates, a 1 mm sized aperture hole is laser-cut as shown in Figure 5.3. Between each of these plates, an insulating plate made of MACOR® ceramic is placed for electrical isolation. The thickness of the insulating plate is set to 750 μm, yielding the field strength of 2.67 MV/m when $V_{cathode}$ is -2 kV.
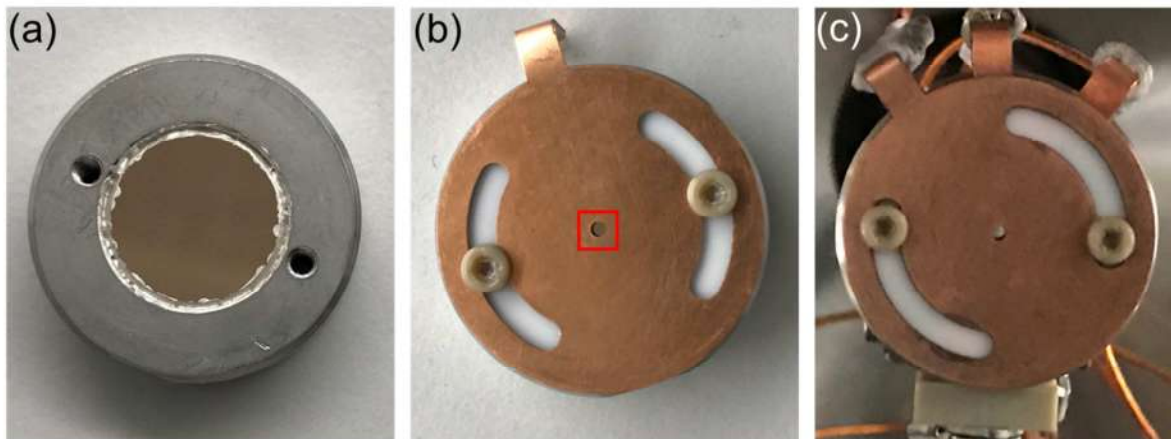
{Figure 5.3. Einzel lens assembly. (a) photocathode mounted in a holder. (b) Extraction plate assembled into the photocathode. An aperture hole with 1 mm diameter indicated by the red box is visible. (c) The entirely assembled Einzel lens system. Two PEEK screws are used to fix the three metal and three isolation plates. Those six plates should be well aligned each other for the generation of symmetric electrostatic field inside the aperture. Asymmetric field by misalignment results in spherical aberration.}

Because the geometrical details of each plate affect the beam focusing ability, a particle tracking solver (CST PARTICLE STUDIO®) is used to simulate and check the electron beam trajectory with this Einzel lens configuration. As shown in Figure 5.4, the actual dimensions of each lens plate, the electron gun-to-screen distance (=~35 mm), and screen diameter (= 40 mm) are reflected in the simulator model. Also, electron beam parameters (for example, emission area assumed to be identical with the photoinjection beam size (=~100 μm FWHM) and intrinsic kinetic energy spread (= 0.28 eV FWHM) for a gold photocathode) are taken into account for the simulation. The

particle trajectory and distribution in transvers direction are monitored by varying V_{lens} with a fixed $V_{cathode}$ of -2 kV. As shown in the simulation results in Figure 5.5 and Figure 5.6, the beam size decreases with the increase of V_{lens} from 0 kV to -1.6 kV. Also, the beam size at V_{lens} = -1.7 kV is larger than the one at V_{lens} = -1.6 kV, indicating that the best focusing condition can be achieved at V_{lens} in between -1.6 kV and -1.7 kV.
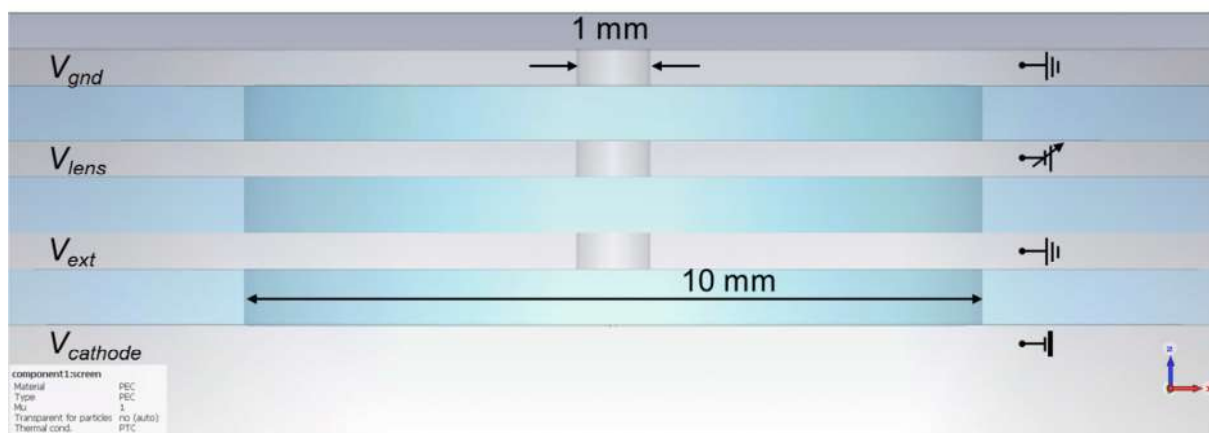
{Figure 5.4. Cross-section view of the CST simulation model for Einzel lens system. Three cyan colored layers indicate insulating plates. The three ground, lens, extraction plates and cathode plate, indicated by grey colors, are defined by a perfect electric conductor.}
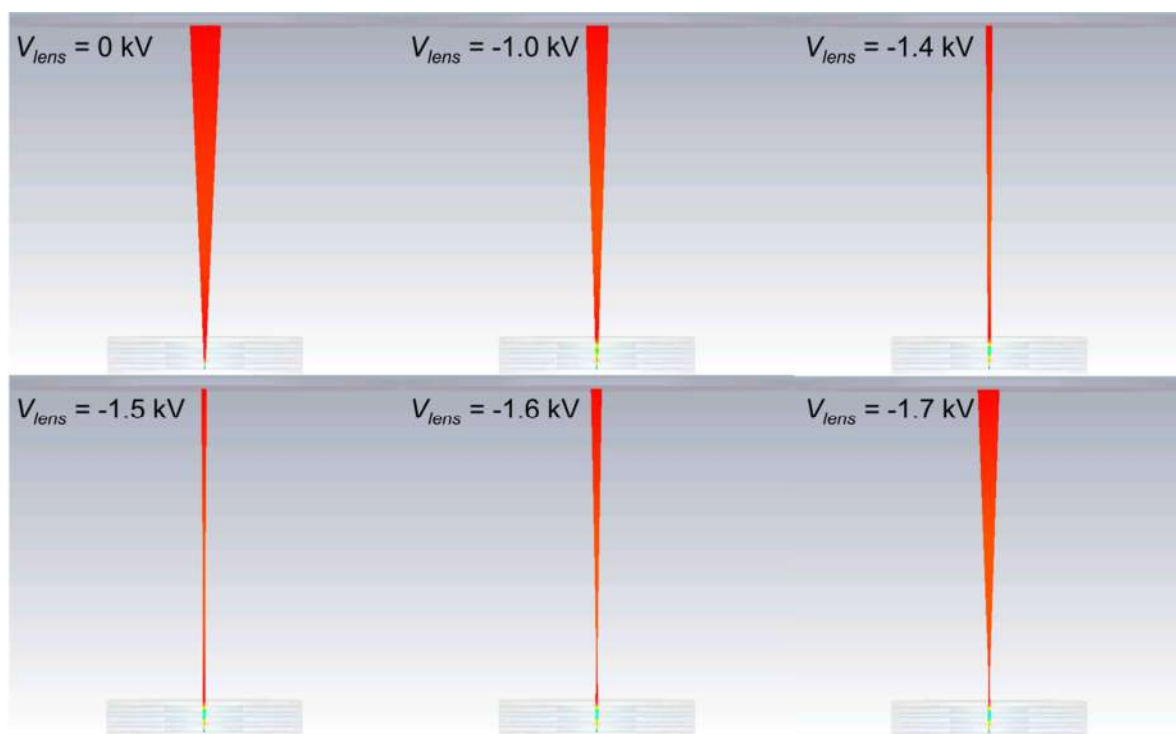
{Figure 5.5. Simulated electron beam trajectory as a function of V_{lens} with the fixed $V_{cathode}$ of -2.0 kV.}

85
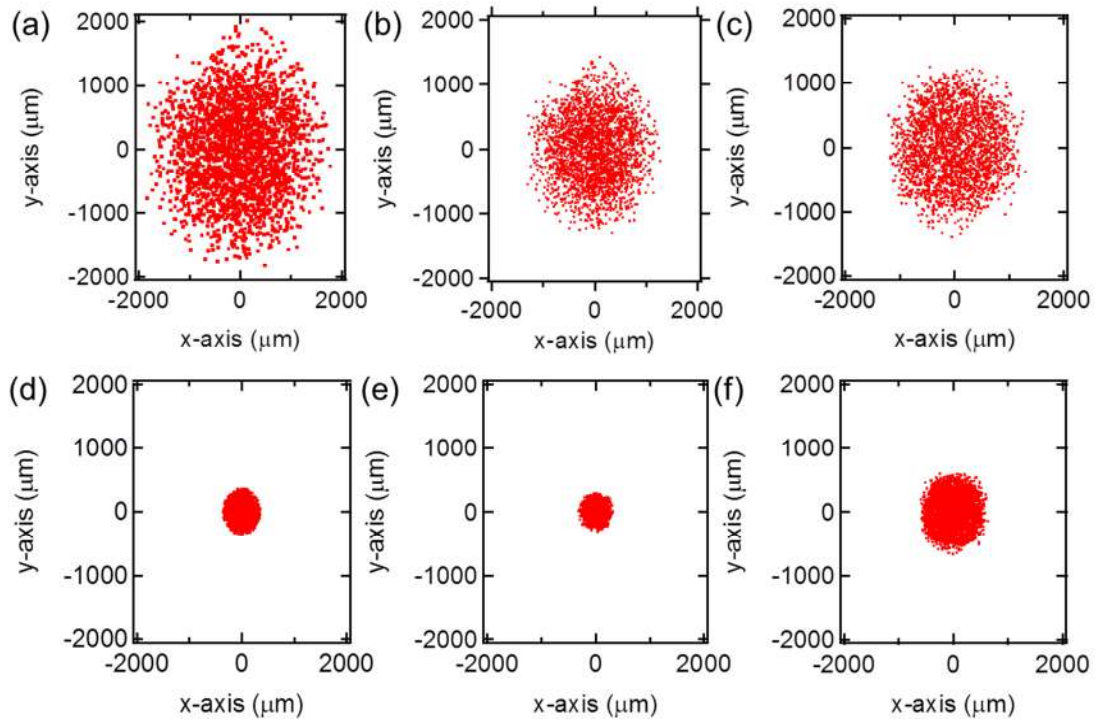
{Figure 5.6. Simulated particle distribution in transverse direction, captured at the screen. (a) V_{lens} = 0 kV, (b) V_{lens} = -1.0 kV, (c) V_{lens} = -1.4 kV, (d) V_{lens} = -1.5 kV, (e) V_{lens} = -1.6 kV, (e) V_{lens} = -1.7 kV}

5.2. Spatial characteristic of electron beam

5.2.1. Beam focusing with Einzel lens

The next task is to experimentally characterize the electron gun. Figure 5.7 shows images recording the electron beam spot at the screen position as a function of V_{lens} at the fixed $V_{cathode}$ of -2.0 kV. It is clearly visible that the beam shrinks as V_{lens} changes from -1.0 kV to -1.67 kV. The quantitative analysis shown in . indicates that the RMS spot size at the maximum focusing condition of V_{lens} of -1.67 kV is 22 % of that of the condition at V_{lens} of -1.0 kV. The decrease of the beam size concomitantly gives rise to the increase of the maximum pixel intensity by approximately one order of magnitude in the case of maximum focusing condition, compared to the condition at V_{lens} of -1.0 kV. After the maximum focusing condition, the beam size starts to increase, and the maximum pixel intensity decreases, as expected from the particle simulation result (overfocusing).
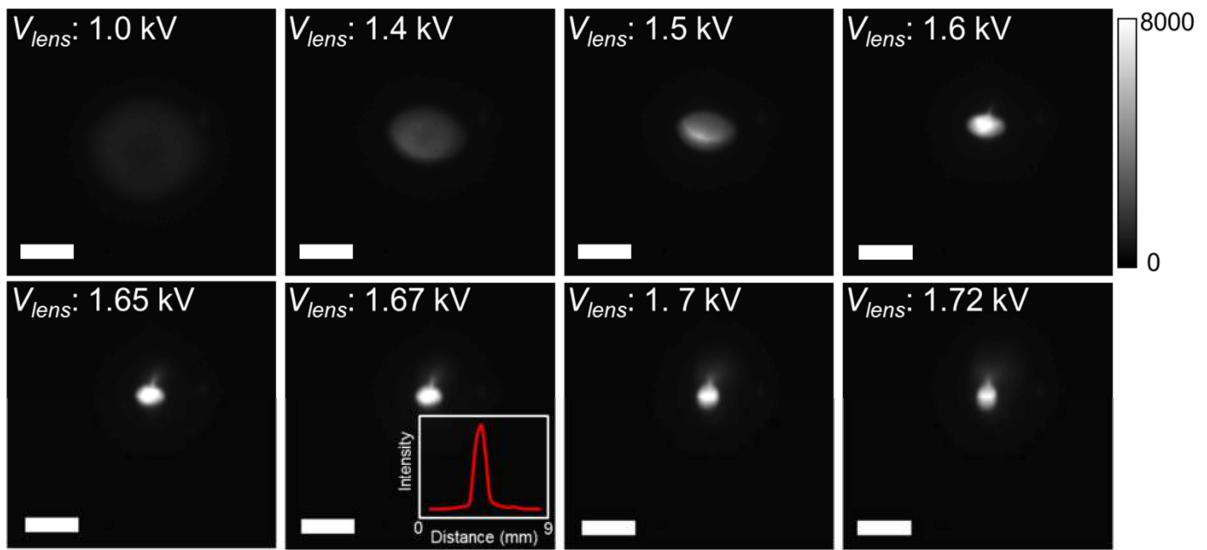
{Figure 5.7. V_{lens} dependent electron beam size. In this measurement, $V_{cathode}$ is fixed to 2.0 kV. Scale bar is 2 mm. Inset: intensity profile of the beam spot}

5.2.2. Transverse beam size at the sample location

For the pump-probe measurment, it is assumed that the sample area probed by the electron beam is homogeneously excited by the pump beam, which shows an identical structure feature at a given pump beam fluence. Considering the Gaussain intensity profile of the pump beam and the possible beam walking during the delay stage scanning (on the probe beam line), it is safe to make the pump beam size larger than the probe beam size by two to three factor. The transverse size of the electron beam at the sample location provides the information regarding what size of the pump beam is required.
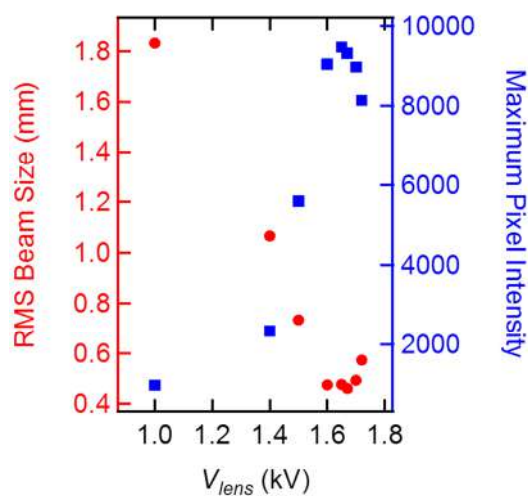
{Figure 5.8. Variation of the RMS size and maximum pixel intensity of the electron beam spot recorded at the screen as a function of V_{lens}}

To measure the electron beam size at the maximum focusing condition, the knife-edge technique is exploited, assuming a Gaussian charge density of the electron bunch in transverse direction, based on the intensity profile of the beam spot image shown in Figure 5.7. The knife-edge structure is made of a 2 mm by 4 mm silicon wafer where one side is coated with 25 nm PECVD SiN thin film that shows blue-green color to maximize the reflection of the pump beam (515 nm) and the other side is coated with 30 nm Au thin film to avoid the charging effect. The knife-edge structure is attached to the edge of the sample holder, as shown in Figure 5.9, such that 2 mm by 2mm square feature is protruded from the edge. While the electron beam is scanned both in x- (horizontal) and y-direction (vertical) by the knife-edge, the pixel intensity in the region-of-interest (ROI) containing the beam spot recorded in the image is integrated as a function of knife-edge position. The knife-edge scanning yields a curve representing the measured beam spot intensity-versus-position of the knife-edge as shown in Figure 5.10, and the curve is fitted to an error function with the fitting parameter that defines the root-mean-square (RMS) width of the Gaussian profile. The measured transverse FWHM beam size is 97.7 µm and 93.0 µm, in x- and y-direction, respectively.

{Figure 5.9. Knife-Edge structure attached on the sample holder}
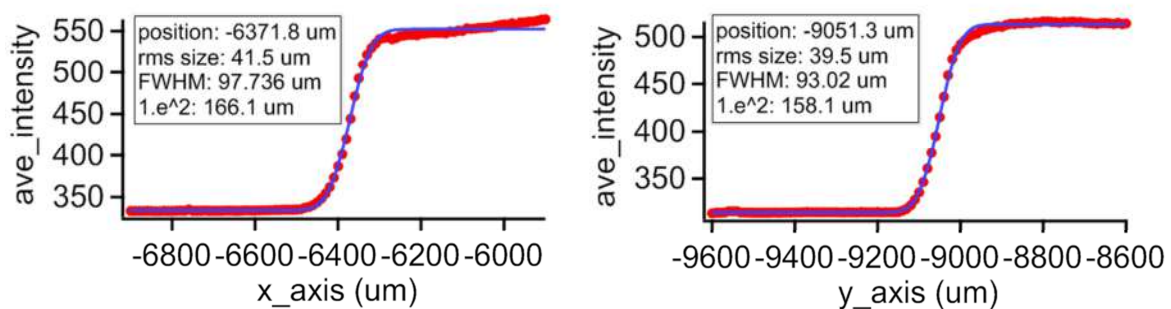
{Figure 5.10. Transverse electron beam size measured at the maximum focusing condition. The x- and y-axis of the graphs indicate knife-edge position and the averaged pixel intensity of the beam spot.}

5.2.3. Estimation of transverse coherence

As stated in section 2.1.2., the electron source emittance is the key parameter that governs the diffraction image quality. Indeed, equation (2.4) indicates that the small transverse emittance leads the transverse momentum spread to be small for a given virtual electron source size. In the opposite case, for a given transverse momentum spread by photoemission mechanism with a fixed light wavelength and cathode work function, the source size is the parameter that dictates the emittance. The effect of the source emittance on the diffraction image is clearly visible in Figure 5.11: sharper diffraction spots are imaged at the screen by the electron source with smaller size (approximately 100 μm). The source size defined by the photoinjection beam size at the cathode can be selected by adjusting the distance from the cathode to the focal lens.

The lower estimate of the transverse coherence, σ_c, can be deduced from the diffraction image with the following equation:

$$\sigma_c = a \times \frac{R}{\sigma_{diff}} \qquad (5.1)$$

where, a, R, and σ_{diff} denote the lattice constant of the diffraction sample, the beam center-to-first order diffraction spot distance, and first order diffraction spot size, respectively. The calculated lower estimate of σ_c is 5.6 nm.

1. Source size	> 300 μm	~ 100 μm
2. Accumulated number of electrons per image	5×10^8	5.7×10^8
3. Electron kinetic energy	2 keV	2 keV
5. Static diffraction image	1 Å⁻¹ 2nd order spot	1 Å⁻¹
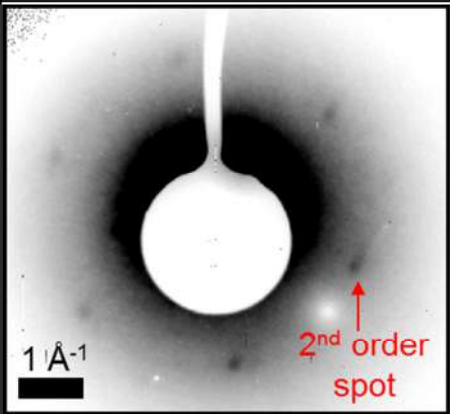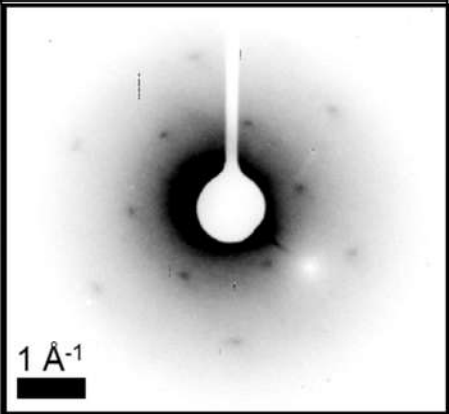
{Figure 5.11. Comparison of the electron diffraction image obtained with different electron source size. Here, the source size refers the virtual source size defined by the laser-cathode interaction region, not by the physical cathode size. The diffraction sample is monolayer graphene.}

5.3. Temporal characteristic of electron beam

The temporal electron bunch length and profile are determined by the streaking method introduced in Chapter 7.

5.3.1. Streak velocity determination

The first task to extract the temporal electron bunch profile from a streak electron beam image is to determine the streak velocity v_s of the streak camera. As explained in Chapter 7.5, v_s essentially refers to the sweep speed of the oscillating electric field (in time) inside the streak plates. It is determined at the proximity of the first zero crossing point that has the steepest slope of the sinusoidal curve because the bunch profile streaked by the field in this region can be retrieved with the best possible temporal resolution of the streak camera used in the experiment. In this regard, the required experimental data to determine the streak velocity is a measured electric field in the streaking direction as a function of time. In practice, the position of the electron beam spot imaged at the screen is recorded as a function of the delay time of the streak camera triggering pulse with respect to the electron bunch entrance timing to the streak plates or vice versa. Since the stronger the field the more deflected the electron beam in the streaking direction, this method provides the information about the beam spot position (indicative of the field strength and direction)-versus-time. Therefore, the unit of v_s is [pixel/time].

A typical experimental data showing the beam spot position change as a function of the delay time and the extracted pixel intensity profile are displayed in Figure 5.12 (a) and (b). The beam spots are the one imaged with the direct beam when the streak plate voltage is biased to 800 V. It is clearly visible that the beam spot moves up as the delay time changes from the statically deflected beam position (0 ps) before the transient field starts. At around the delay time of 116 ps, the streaked electron beam spot position is close to the unstreaked beam position (indicated by the red line in Figure 5.12 (a)), implying that the zero-crossing point is located closely in this delay time region. The extracted intensity profile from the streak at this delay time also shows the largely elongated line width and the decreased peak pixel value, compared to the static deflection case, as expected at the zero-crossing.
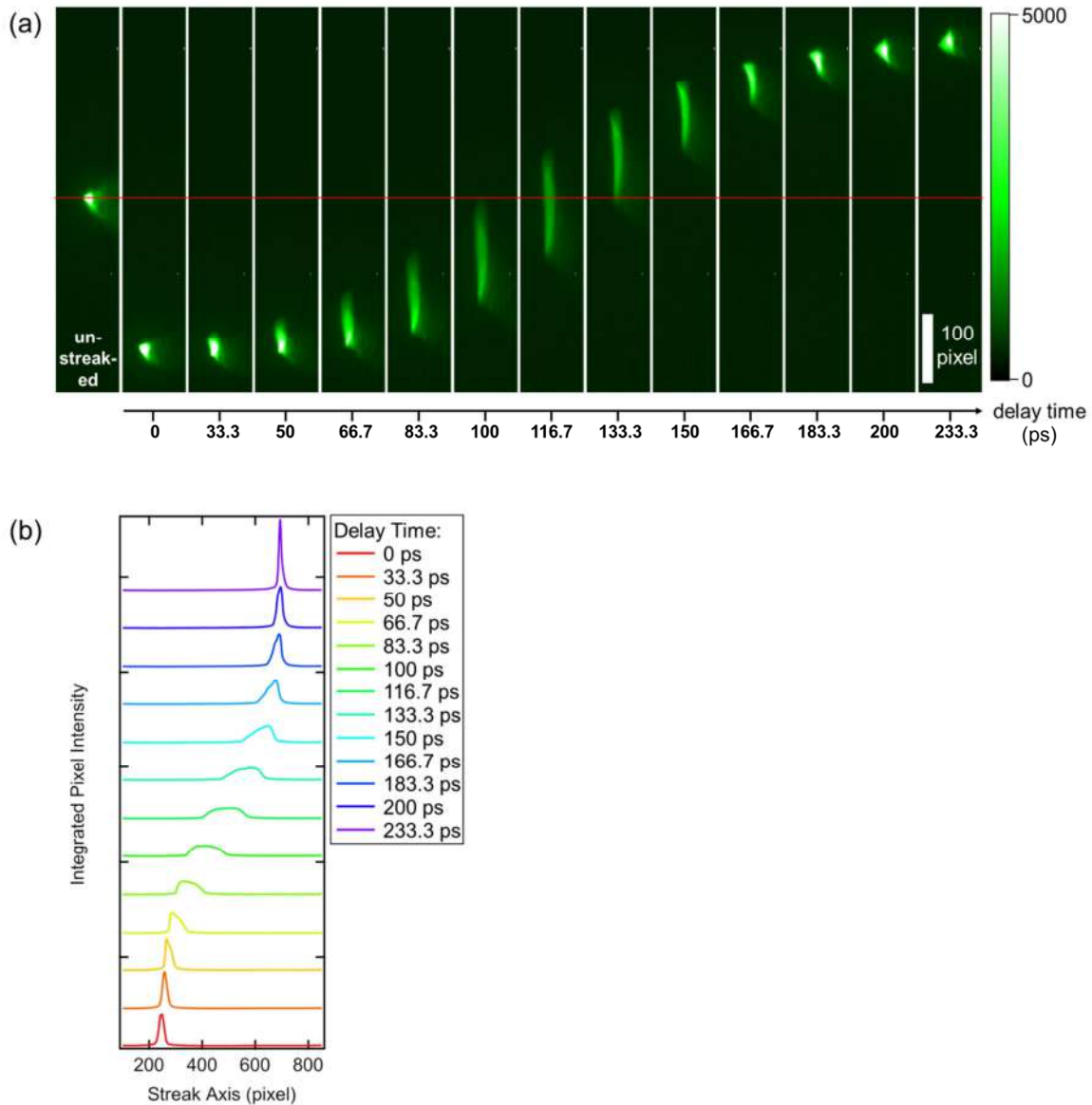
{Figure 5.12. (a) Beam spot images of the direct electron beam, obtained by changing the relative delay of the streak camera triggering bean with respect to the t electron bunch entrance timing into the streak plates. (b) Pixel intensity profiles of the beam spot in vertical direction (streak axis) as a function the delay time. The pixels of each beam spot are binned in horizontal direction (normal to the streak axis) before extracting the line profile.}

To make the beam spot position-versus-time curve from the data shown in Figure 5.12, the extracted intensity profiles are fitted to Gaussian profiles, and the pixel location corresponding to the maximum pixel value of the fits are plotted as a function of the delay time as shown in Figure 5.13. The v_s is determined by the slope of the linear fit by taking three points (100, 116.7, 133.3 ps) close to the zero crossing point. The v_s is extracted from streak images obtained with various streak plate

voltage conditions ranging from 100 to 800 V, showing a pseudo-linear dependence on the plate voltage (Table 5.1). This trend is expected given by the fact that the field strength is proportional to the plate voltage. Other useful information obtained from this graph is that the half oscillation period of the transient field is approximately 200 ps, determined by the LC time of the streak camera (see in section 7.5).
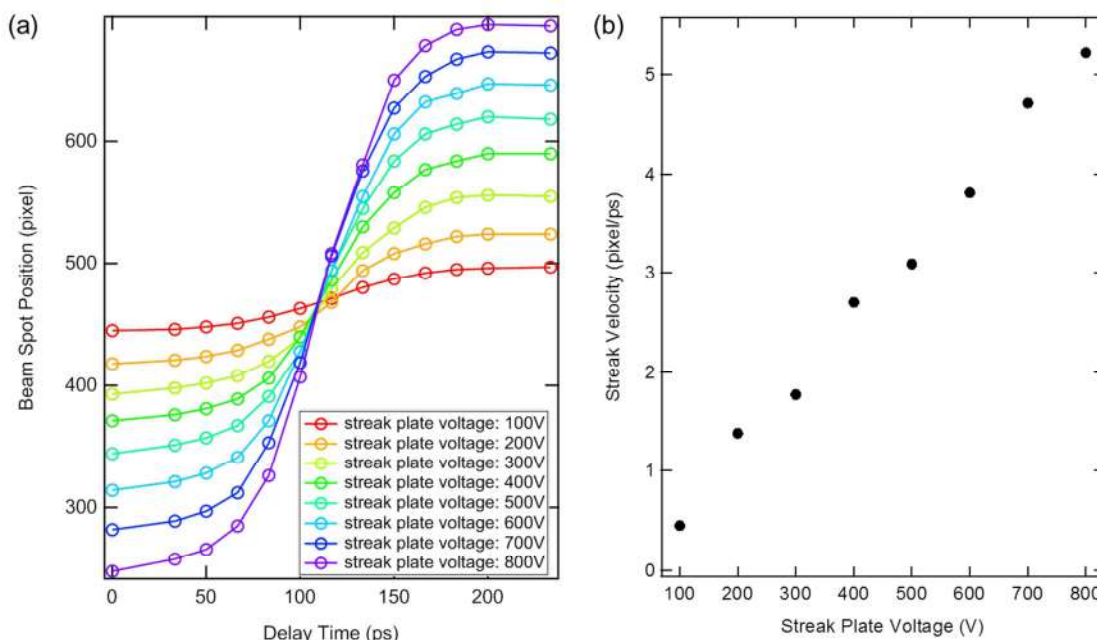
{Figure 5.13. Characterization of streak velocity, v_s (a) change of the beam spot position as a function of the delay-time (b) dependence of v_s on the streak plate voltage}

Streak plate voltage (V)	100	200	300	400	500	600	700	800
Streak velocity, v_s (pixel/ps)	0.45	1.38	1.77	2.70	3.09	3.81	4.71	5.22

{Table 5.1. v_s to be used for temporal bunch length calculation}

5.3.2. Temporal bunch profile

The underlying principle of the streak image analysis is explained in section 7.5, and the calculated results with experimental data are discussed in this Chapter. For the extraction of the bunch profile

with the best temporal resolution achievable in the present streak camera configuration, the maximally streaked spot (that is, the one imaged at the delay time of 116 ps and streak plate voltage of 800 V) presented in Figure 5.12 is selected.
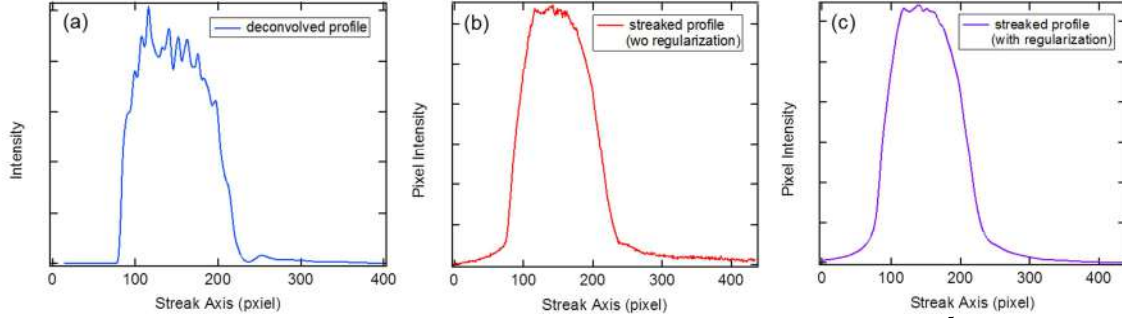
{Figure 5.14. (a) Deconvolved profile when the regularization parameter, γ, is 5×10^5 in solving the ill-posed problem. (b) The unregularized ($\gamma = 0$) and (c) regularized ($\gamma = 5 \times 10^5$) streak profile.}

Shown in Figure 5.14 (a) is the deconvolution result of the streak profile with the unstreaked one, and Figure 5.14 (b) and Figure 5.14 (c) display the streak profile without and with regularization, respectively. The regularization parameter, γ, is chosen as 5×10^5 such that the rms deviation (= 1.24 %) of the regularized streak profile from the unregularized one is higher than the expected uncertainty (= 1.0 %) of the profile, extracted from ten measured streak spot images at the same experimental condition. The large wiggles on the deconvolved profile are a result of the amplification of the noisy feature of the unregularized streak profile, meaning that the deconvolution operator acts as a high-pass filter. The wiggling feature is expected to originate either from the true nature of the charge density profile of the electron bunch or simply from the inhomogeneous detector efficiency that could be corrected by a flat-field calibration.

The effect of regularization on the streak profile is well described in Figure 5.15. As the more regularized of the profile, the more smoothened of the profile at the expense of intensity deviation from the unregularized one. The increase of γ also leads to the increase of the line width of the impulse response function of the streak camera, as shown in Figure 5.16, which can be considered as a computational error and therefore affects the temporal resolution in determining the temporal bunch length. To obtain the temporal bunch profile, the streak axis of the deconvolved profile in Figure 5.14 (a) is replaced with the time axis by using the determined v_s in the previous chapter. The extracted bunch profile is shown Figure 5.17. The calculated bunch length τ deconvolution error, and impulse response of the streak camera $\Delta\tau_{imp}$ as a function of γ, are summarized in Table 5.2. In case of γ equal to 5×10^5, τ is 18.2 ps, and the temporal resolution, $\Delta\tau$, calculated according to equation (7.12) ($\Delta\tau_{imp} = 0.85$ ps, $\tau_{max} = 18.2$ ps, $\tau_0 = 18.0$ ps, $\Delta\tau_{jitt} \leq 0.1$ ps), is below 1.2 ps.

93
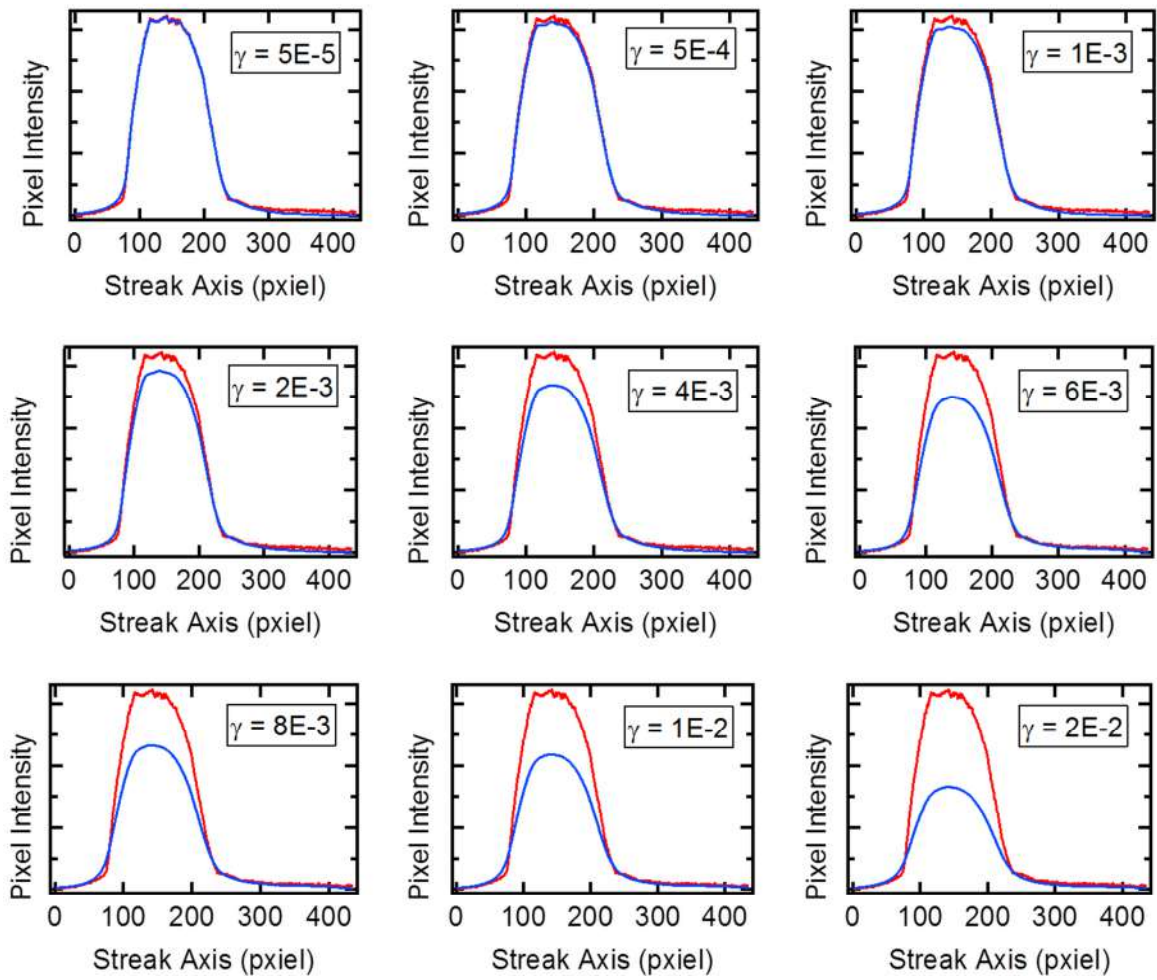
{Figure 5.15. The effect of regularization on the streak profile. The red and blue curves correspond to the unregularized and regularized one, respectively.}
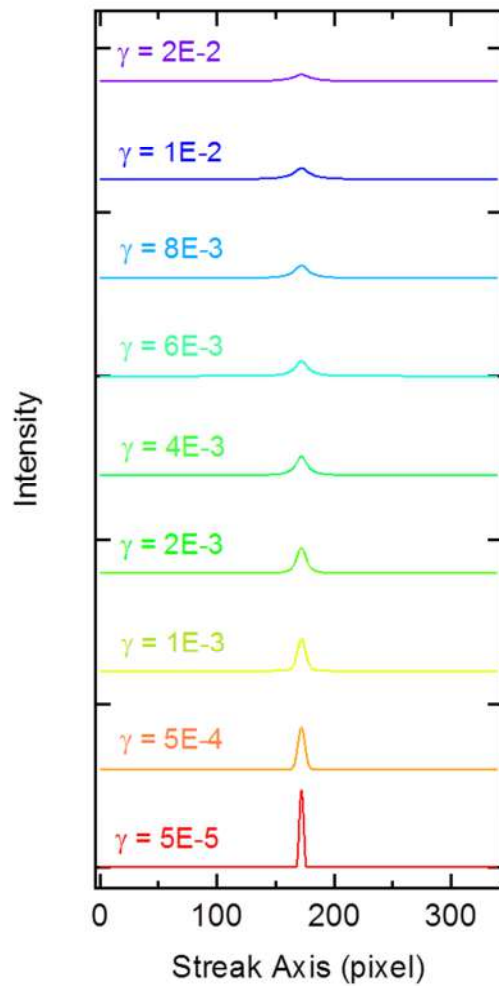
{Figure 5.16. The effect of regularization on the impulse response function of the streak camera.}
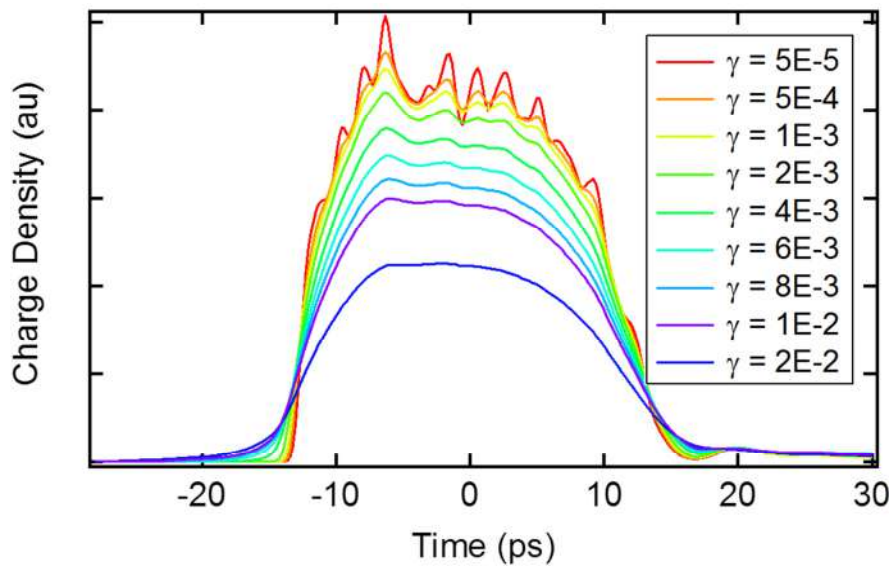
{Figure 5.17. Extracted temporal electron bunch profile.}

γ	RMS deconvolution error, streaked image (%)	FWHM bunch length, τ (ps)	RMS deconvolution error, unstreaked image (%)	FWHM impulse response, τ_{imp} (ps)
5E-5	1.24	18.2	1.07	0.85
1E-4	1.24	18.4	1.48	0.98
5E-4	1.69	18.6	3.59	1.90
1E-3	2.66	18.2	5.50	2.75
2E-3	4.72	19.1	8.59	4.27
3E-3	7.02	17	11.3	5.05
4E-3	9.11	19.5	13.8	5.73
5E-3	11.3	20	16.2	6.16
6E-3	13.5	22.6	18.5	6.92
8E-3	17.9	23	23.1	7.72
1E-2	22.3	24	27.5	8.38
2E-2	44.1	24.6	49.2	10.4

{Table 5.2. Summary of the calculated electron bunch length, impulse response, and deconvolution error, as a function of regularization parameter, γ.}

5.4. Setup requirements and previous studies

As discussed in the previous chapter, the pulsed low-energy electron bunches are broadened quickly in time: even if the initial bunch duration is on the order of few hundreds of femtosecond just after emission, they are broadened to more than one picosecond in few hundreds of micrometer. With the aim of achieving femtosecond resolution, therefore, the first requirement of constructing time-resolved ultrafast low-energy electron diffraction setup is to make source-to-sample distance short as much as possible. This requirement implies that the smaller the electron gun size the more the possibility to achieve short temporal resolution in view of the conventional stroboscopic pump-probe scheme. The second requirement is to make sample-to-screen distance (i.e. camera length) short. Low-energy electrons scatter with relatively large angle, and therefore, not to miss the high order diffracted beams at the screen, the compact size of the setup is absolute. In addition, low-energy electrons diverge quickly in transverse direction due to their slow propagation speed. This feature requires the use of lensing system to avoid the diffused diffraction spot at the screen. However, the second requirement implies that post-lensing system typically used in high-energy ultrafast electron diffraction setup is difficult to be implemented for the low-energy electron diffraction setup. Instead, a compact electron gun composed of a lensing system directly integrated to the cathode is a better choice.

The most successful try to date to meet these requirements is the use of a nanotip based-electron source. Inherent small physical size of this source has enabled to design a millimeter- or even micrometer-sized electron gun [36]. In fact, this kind of miniaturized electron source has been widely used in TEM communities especially as a DC field emission source, but exploiting it with light has not been conceived until irradiation of femtosecond laser pulses directly to the nanotip source has tried [31]. With those tries, understanding of the interaction between the light and nanotip source has become clear, opening an avenue to use it as a femtosecond electron source via new kinds of nonlinear free electron generation methods including photo-field (single photon in the weak field regime), optical field (single photon in strong field regime), and multiphoton emission (without field). The achieved temporal resolution with this source technology is in the order of 1 ps.

5.5. Setup characterization

5.5.1. Setup overview

The transmission-mode time-resolved low-energy electron diffraction (LEED) experiment is carried out under the ultrahigh vacuum (UHV) condition ($<10^{-8}$ mbar). This UHV requirement is associated not only with technical reasons to operate the electron gun (i.e. photoemission) and detector (MCP-phosphor combination) but also with the issue regarding the diffraction sample contamination by gas residuals inside the setup chamber. For low-energy electron diffraction, the electron probe is capable of sensing a few layers of contaminant on the sample surface owing to its short inelastic scattering mean free path (see Chapter 4.2.2). It is well known in the field of surface science that the time for a complete monolayer contamination coverage on a 1 cm^2 solid surface composed of 10^{15} atoms (typically in the case of a metal) is calculated as 4000 sec in 10^{-10} torr (1 torr = 1.333 mbar) pressure based on the adsorption kinetic theory. This calculation can be equally stated that 40 sec is the transit time from an uncontaminated to a contaminated state in case of the 10^{-8} mbar environmental pressure. The expected temperature of the hot monolayer graphene, the first target sample of this setup, is above 1000 K under the femtosecond irradiation with high enough pump laser fluence, which is in the typical annealing temperature range for sample cleaning in the surface science community. The repetition rate of the femtosecond laser pulse in the LEED experiment is set to 1 kHz, implying that the irradiated area by the pump pulse can be assumed to be cleaned repeatedly at every 1 ms. The camera readout time is approximately 1 sec, well below the restricted time of 40 sec.

The LEED setup is constructed on the optical table where a mode-locked femtosecond laser facility is installed. This femtosecond laser is PHAROS (Light Conversion®), featuring tunable repetition rate (1 – 50 kHz), pulse duration (170 fs – 10 ps), and maximum pulse energy upto 1. mJ. The central wavelength of the laser is 1030 nm. The overview of the laser beam line for the LEED setup is shown in Figure 5.18. The fundamental of the PHAROS is frequency-doubled by a nonlinear crystal (ß-BaB$_2$O$_4$, Type I, θ = 23.4°), and the 2nd harmonic (515 nm) one is separated from the residual by a harmonic beam splitter (HBS). The green light is divided into two arms by a beam splitter (BS), and the one arm is frequency-doubled to generate a UV beam with 257 nm wavelength by a nonlinear crystal (ß-BaB$_2$O$_4$, Type I, θ = 50°). The UV beam is separated from the green residual and tightly focused at the cathode by a lens. The other arm of the 2nd harmonic is divided again into two arms to use for the sample excitation and for the streak camera triggering. While the excitation beam is focused to the sample to achieve a laser fluence high enough to initiate a structural change, the streak camera trigger is not in order to ensure the full coverage of the laser spot on the photoswitch for its well-functioning. On each beam line, a translational stage is installed to make a

time-delay with respect to the fixed timing of the electron bunch, the reference.
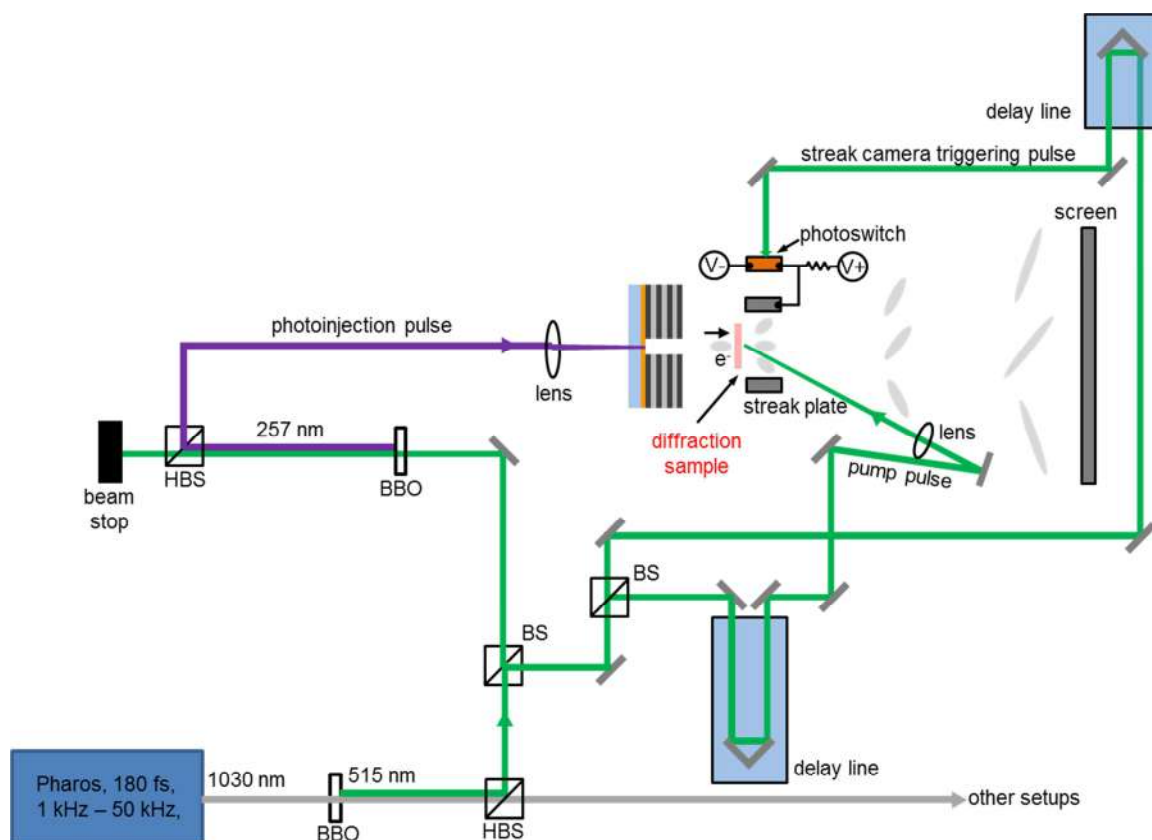
{Figure 5.18. The overview of the laser beam line for LEED setup. HBS: harmonic beam splitter; BS: beam splitter, BBO: ß-BaB$_2$O$_4$ nonlinear crystal}

As stated in the section 5.4, the size of the LEED setup has to be compact due the physical requirements. In case of the present thesis, the standard CF100 sized cube piping component made of stainless steel (https://www.pfeiffer-vacuum.com) is chosen as a main experimental chamber, and the inside is decorated with required optics and electronics as shown in Figure 5.19. The main included items are a sample holder equipped with a knife-edge structure, a three-dimensional in-vacuum stage to hold diffraction samples, a home-built streak camera, a beam block, pump beam guiding mirrors, and the electron gun. On each side of the cube chamber, optical and electrical feedthroughs, viewports, turbo molecular pump, pressure gauge, mechanical manipulators and electron detector are attached.

The diffracted electron signals after the sample are captured and amplified by chevron-type multichannel plates (MCPs) combined with a phosphor screen. The pore size of single MCP is 12 μm. Considering the two MCPs stacked each other and the further expanding of the secondary electrons

from the exit of the back MCP to the phosphor screen (with approximately 1 mm separation distance), electron detector resolution can be estimated approximately as 50 μm. A lens-coupled scientific graded CCD camera (MicroMAX, Princeton Instrument®) is used finally to record the image formed on the screen. The pixel size of the CCD is 13 μm. The screen size defined by the phosphor screen and the screen pixel size are approximately 40 mm and 40 μm (1024 pixel-by-1024 pixel), respectively.
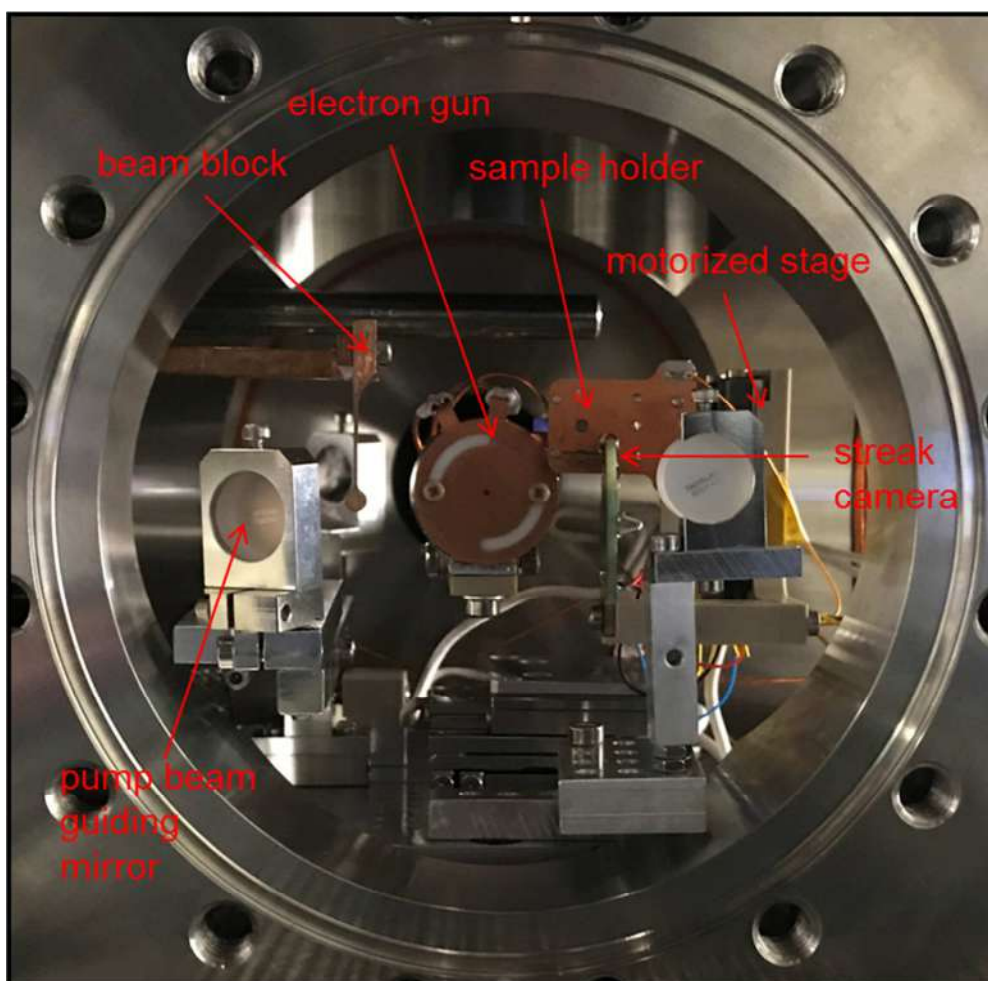
{Figure 5.19. Photograph image showing the inside of the main LEED experimental chamber.}

5.5.2. Synchronization

For the time-resolved ultrafast electron diffraction the timing of the electron probe bunch and excitation pulse should be well-controlled in that the measurement time points to track the structural evolution are defined by the delay-time points between these signals. A practical way to achieve synchronization between these signals is well described in section 5.5.3. Further to the conventional stroboscopic pump-probe electron diffraction, streak camera operation in the time-resolved streak diffraction adds complexity to the synchronization scheme. Essentially, a third femtosecond laser

trigger (more than the pump and probe laser triggers) is required to make the GaAs photoswitch of the streak camera become conductive, initiating the transient electric field inside the streak plates. The timing of the third optical trigger therefore needs to be synchronized with the electron bunch. Moreover, on the operation of the steak camera, two high voltage power supplies are used for the streak plate biasing, controlled by a few hundred of nanosecond electric pulse (TTL) from a digital delay generator. The reason for this is to prevent high voltage breakdown of the photoswitch, already observed at DC voltage of a few hundred volts, depending on the size of the switch. Overall, the synchronization scheme among the three optical triggers as well as two high voltage electric pulses is summarized in Figure 5.20.
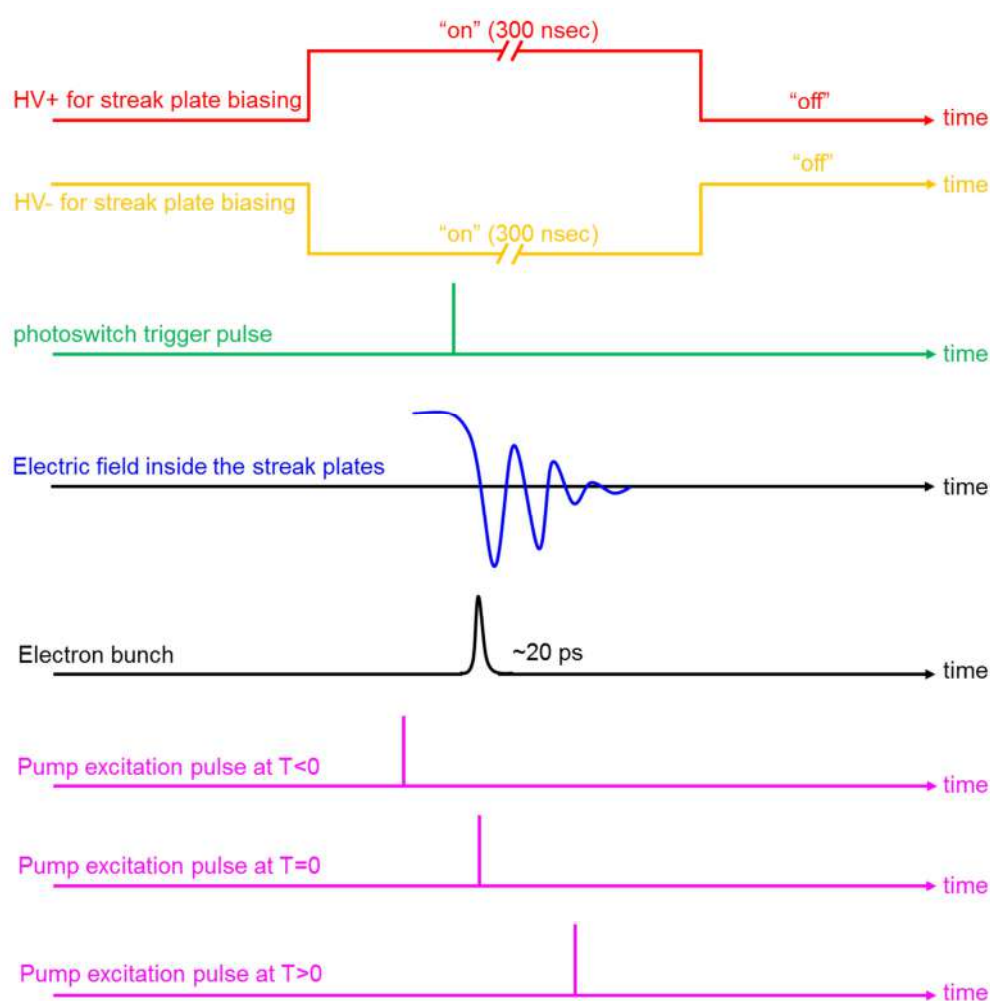
{Figure 5.20. Synchronization scheme of time-resolved LEED with streaking}

The electron beam is dispersive in vacuum so that the speed of electron is energy-dependent, whereas the light travels in vacuum with the speed of 3×10^8 m/sec regardless of its photon energy, as discussed in Chapter 2.. The travel time difference resulted from the two different propagation speed

101

of the beams, therefore, should be taken into account when the three optical beam lines are designed. For example, for 2 keV electron beam propagating the travel distance of 1 cm in the drift space toward the sample, the travel time is calculated as 379 ps. This time corresponds to the light travel length of 11.38 cm, which has to be added to the sample excitation and streak camera triggering beam line distances to compensate the travel time difference. Table 5.3 shows the relation between the electron beam propagation distance and corresponding light travel distance for 2 keV electron beam.

Propagation distance (cm)	Speed of 2 keV electron in vacuum (m/sec)	Travel time (ps)	Corresponding light travel distance (cm)
0.5	2.64×10^7	190	5.70
1	2.64×10^7	379	11.38
1.5	2.64×10^7	569	17.07
2	2.64×10^7	758	22.76

{Table 5.3. Summary of the travel time of 2 keV electron beam in vacuum and corresponding light travel distance}

5.5.3. Spatial and temporal overlap between electron and pump

How one can ensure that the probe and pump beams are well-overlapped in space and time in a UED experiment to expect the observation of a structural change as deduced from diffraction? In high-energy UED setup with the front illumination geometry of the pump and probe, shown in Figure 5.20, the method to find good overlap is quite standardized. First, good spatial overlap is found by using a standard knife-edge or aperture scanning technique. The probe and pump beams are scanned by knife-edge or aperture structures placed at the sample plane, and by this way, the center of each beam can be found. The position of one of the guiding mirrors for the pump beam is iteratively adjusted until the centers of the two beams are well matched. After the spatial overlap is guaranteed, a standard sample (Au or Al thin film), proven to exhibit ultrafast structural changes [83], is typically used to check the temporal overlap (delay time = 0). Unfortunately, this standard method is not available for the transmission LEED setup because of the back illumination geometry of the pump beam (see Figure 5.21), required for a minimum source-to-sample distance, as well as the lack of a standard sample thin

enough to be tested with low-energy electrons. This section deals with a practical way to achieve the same goal (good spatial and temporal overlap) suited particularly for low-energy electrons.
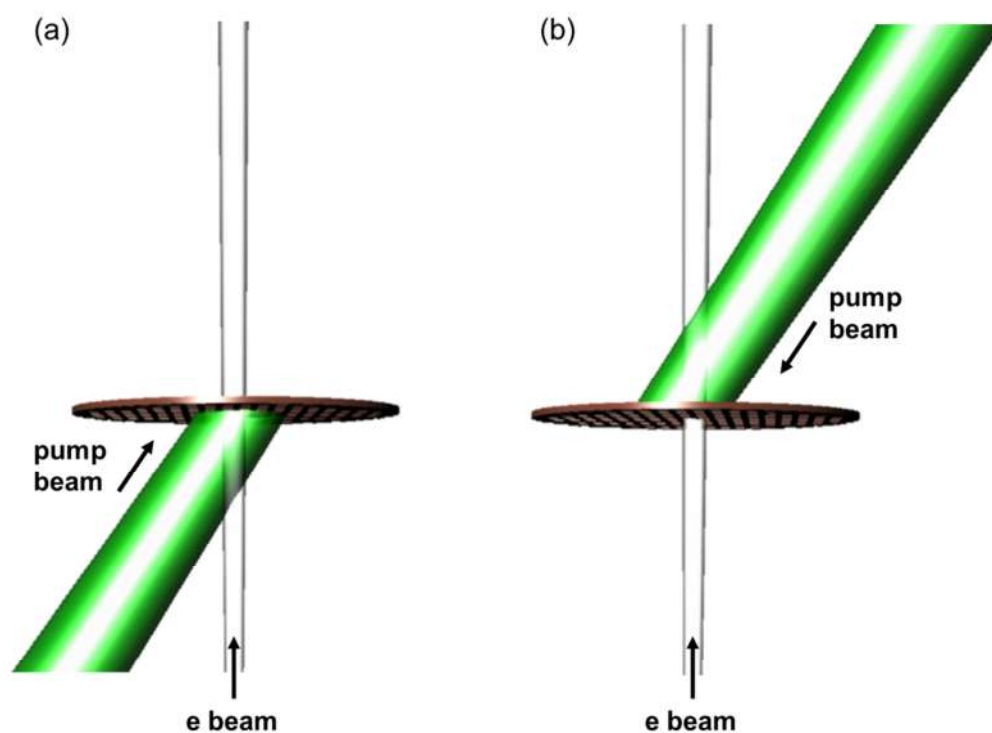
{Figure 5.21. Sample illumination scheme (a) front illumination (b) back illumination}

The effective method in finding the spatial and temporal overlap between low-energy electrons and the pump pulse is to use the transient electric field (TEF) effect [33]. The detailed description about this effect is in Chapter 6. Briefly, the TEF effect is a result of the interaction between the probe electrons and the electron plasma generated at the sample and the sample substrate. Because of the electric field generated between the negatively charged electron cloud and positively charged substrate, the charged electron beam is spatially deflected when it passes through the field region. As a result, either the spot position or the intensity of the electron beam reaching the detector screen is expected to change, the indication of the spatial and temporal overlap. In practice, a defocused electron beam is used to make an electron shadow (projection) image at the screen, as shown in the inset image in Figure 5.22. A bare TEM (transmission electron microscope) grid made of copper (PELCO®, Hole Width 54 µm, Bar Width 31 µm) is chosen as the object. The advantage of using the defocused beam is based on the fact that relatively large area of the grid can be imaged, which increases the probability to observe the TEF effect with a minimal alignment effort. Once a static shadow image is obtained, the grid is irradiated by the pump pulse, and the time-dependent shadow images are recorded by varying the delay-time. The integrated pixel intensity on the selected area of the shadow images is tracked as a function of the delay-time. The typical time-trace of the

pixel intensity is shown in Figure 5.22. A rapid intensity drop is observed near the T = 0 point, indicating the initiation of the TFE captured by the low-energy electrons. The gradual recovery of the intensity, observed after approximately 20 ps, is also a distinctive feature of the TEF effect: charge recombination (detailed given in Chapter 6. The calculated instrument response from an error function fit to the transient intensity change is 16.5 ± 1.2 ps, in good agreement with the measured electron bunch length independently by the streak camera (section 5.3).
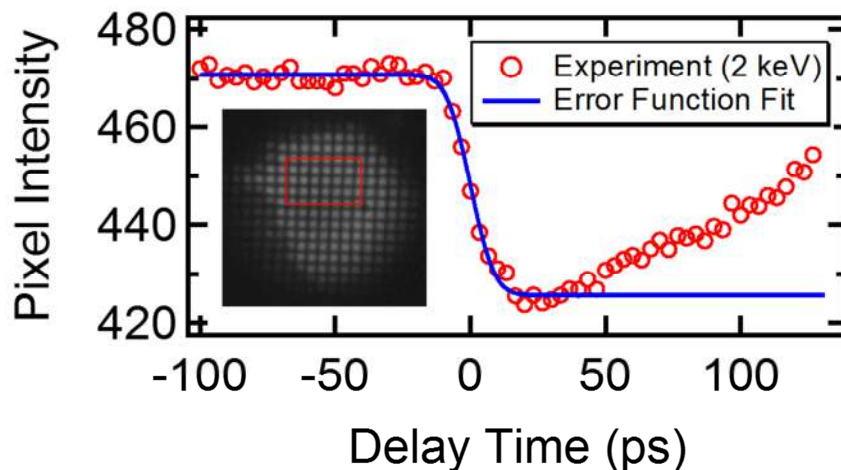
{Figure 5.22. Delay-time dependent pixel intensity change of the region-of-interest (indicated by red box) in the electron shadow image. The object is a bare TEM grid. The inset image is obtained at $V_{cathode}$ of 2.0 kV and V_{lens} of 0.5 kV. }

The defocused beam allows only a course spatial alignment with respect to the pump beam position in that the pump beam size should be 2 – 3 times larger than the probe beam size to ensure the homogeneous excitation on the sample. Thus, for a good spatial overlap, the next step is to do the fine alignment by using a focused electron beam used in the actual diffraction experimental condition. The fine alignment can be achieved by comparing the beam spot of a shadow image captured at a negative delay time point, as a reference, with that of the one captured at a time point showing TEF most significantly (for example, ~ 20 ps in Figure 5.22). If a clear distinction (*i.e.*, pixel intensity or spot position) is observed from the comparison of these two beam spots for a certain defocused beam, V_{lens} increase by a small step to decrease the beam size a bit, and the measurement is repeated. If this is not the case, one of the pump beam guiding mirror is iteratively adjusted until TEF is well observed. Once V_{lens} reaches a maximum focusing condition, the good spatial overlap is guaranteed. The typical example of this procedure is shown in displayed in Figure 5.23.
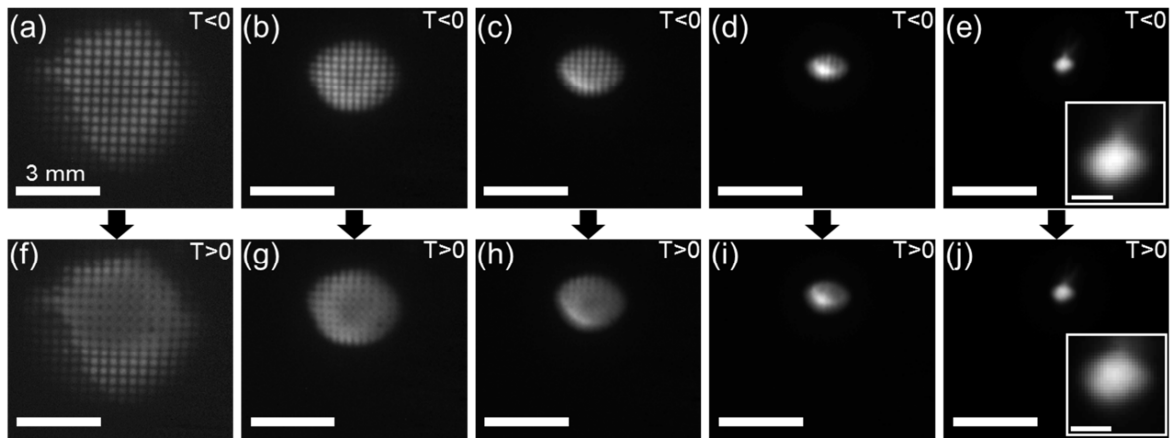
{Figure 5.23. Electron shadow images recorded before ((a) – (e)) and after ((f) – (j)) T = 0. The images are obtained at the fixed electron kinetic energy of 2 keV, but at different lens voltage, V_{lens}. The images (a) and (f), (b) and (g), (c) and (h), (d) and (i), and (e) and (j) are obtained with V_{lens} of 0.5, 1.3, 1.4, 1.5, 1.6 kV, respectively. The inset images in (e) and (j) are the magnified ones to highlight the beam spot, and the scale bar indicates 0.5 mm, used for a measure of the beam size at the screen.}

5.5.4. Static low-energy electron diffraction
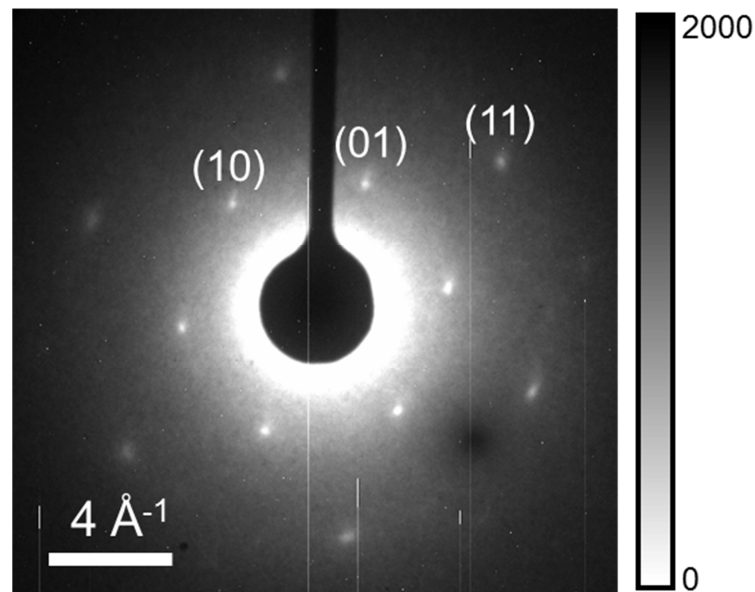
{Figure 5.24. Electron diffraction of monolayer freestanding graphene. The electron kinetic energy is 2 keV. }

The low-energy electron diffraction image of the freestanding graphene sample is shown in Figure 5.24 The six-fold symmetry of the 1st and 2nd order diffraction spots represents the honeycomb structure of graphene. Also visible is a faint diffraction ring on the 1st and 2nd spots, implying that the electron-probed region is composed of a small portion of multiple domains. The intensity of the 1st

order diffraction spot is higher than that of the 2nd order one, an indication of the monolayer structure [108]. The static image is obtained with photoelectrons generated by femotosecond pulsed laser at the repetition rate of 1 kHz. The number of electrons per generated electron bunch is approximately 7.5×10^4, and the camera integration time is 8 sec. The accumulated number of electrons to record the single image is calculated as 6×10^8.

From the static electron diffraction image and the graphene sample with known atomic structure, the camera length, L, is calibrated, required for the purpose of indexing of samples with unknown structures. The L is defined by the distance between the diffraction sample and the detector screen, as illustrated in Figure 5.25. In this diffraction geometry, r_{hkl} and θ_{hkl} refer to the beam center-to-diffraction spot distance at the screen and Bragg diffraction angle, respectively. Then, the geometric relationship among L, r_{hkl}, and θ_{hkl} is established as follows:

$$\frac{r_{hkl}}{L} = \tan(2\theta_{hkl}) \tag{5.2}$$

Combined with the Bragg's law introduced in section 4.1.2, equation (5.2) is transformed into:

$$L = \frac{r_{hkl}}{\tan 2(\sin^{-1}(\frac{\lambda}{2d_{hkl}}))} \tag{5.3}$$

where, d_{hkl} refer to the spacing distance between (hkl) planes. In case of two-dimensional hexagonal crystal system (*e.g.*, graphene), d_{hkl} is expressed as follows:

$$d_{hk} = \frac{\sqrt{3}}{2} \frac{a}{\sqrt{h^2 + hk + k^2}} \tag{5.4}$$

where, a is the lattice constant. For (10) plane of the graphene, the d_{10} is 0.213 nm. With all, the calculated L is 36.2 mm.
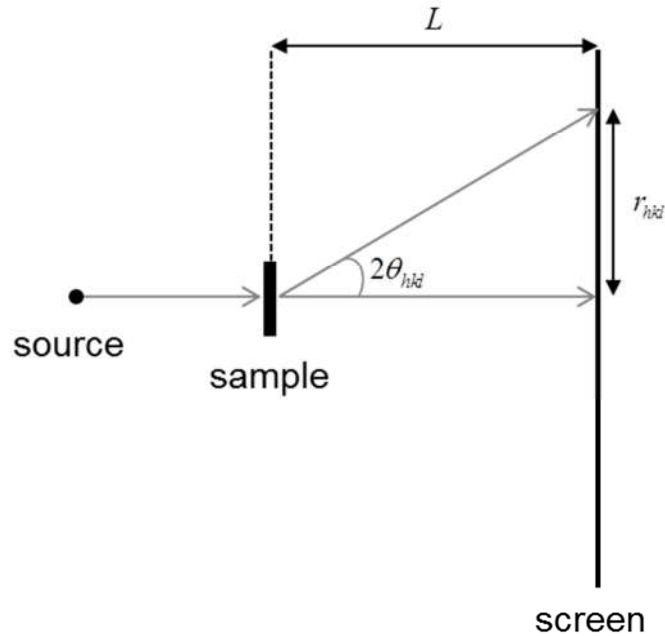
{Figure 5.25. The definition of camera length, L, in the transmission reflection geometry. }

5.5.5. Target system

A freestanding monolayer graphene has several advantages to use as a test case for time-resolved transmission-mode LEED:

1) It is commercially available.

2) It has single atom thickness. The concern about the penetration depth of the low energy electrons in transmission-mode setup can be avoided.

3) It has a small lattice constant. Thus, the issue about the overlap between streak diffraction spots can be minimized.

4) The large size of the single crystal domain is obtainable, suitable for streaking.

5) The ultrafast structure change on the freestanding monolayer graphene has been reported recently [109] by high-energy electrons. Thus, it is a good model system to compare the diffraction data by the conventional pump-probe method with the one by streaking of low-energy electron.

Graphene is a honeycomb lattice consisting of a single layer of carbon atoms as shown in Figure 5.26

(a). The carbon atoms are held together by three covalent sigma bonds of overlapping sp^2 hybrid orbitals. The remaining p_z orbital, perpendicular to the carbon plane, forms a delocalized π-bond with the p_z orbital from the adjacent carbon atoms, as similarity as benzene molecule, which endows the material with exceptional electrical and thermal properties. The carbon-carbon covalent bond length is 1.42 Å, which leads to the lattice constant of 2.46 Å (= $\sqrt{3} \times 1.42$ Å). It is the first two-dimensional material, successfully obtained with the mechanical exfoliation method [110].

The target system chosen for the proof-of-principle experiment of the time-resolved LEED is the ultrafast in-plane acoustic phonon dynamics of graphene by optical excitation. Graphene has a bandgap less feature (Figure 5.26 (b)), and thus, can absorb any wavelength of light (including 515 nm one used in the present experiment) with 2.3 % efficiency per layer [111]. Once femtosecond laser pulses are absorbed on the material, valance band (VB) electrons of graphene are excited to the conduction band (CB) in less than one picosecond and these hot electrons are thermally equilibrated to lattices subsequently. As a result, the lattice temperature increases, leading to a larger random thermal motion of carbon atoms, associated with the superposition of acoustic phonon modes. This phenomenon can be directly captured by electron diffraction: the mean square time-dependent displacement of the atoms, $<\mathbf{u}(t)^2>$, increases owing to the high temperature, and concomitantly, the diffraction spot intensity decreases due to the statistically less ordered state. In transmission-mode electron diffraction, the scattering vector, $\mathbf{Q}$, introduced in section 4.1.4, lies in parallel to the graphene plane. In this regard, in-plane atomic displacements only contribute to the diffraction spot intensity. This temperature dependence on the diffraction spot intensity is called the Debye-Waller effect, as discussed previously.

The freestanding monolayer graphene used in the present experiment is supported on an ultra-fine mesh type copper TEM grid (www.tedpella.com). The grid itself has a pepper pot type structure where multiple circular holes with 6.5 μm diameter are located. The pitch size is 12.5 μm. This system will be discussed in detail in the following Chapter.
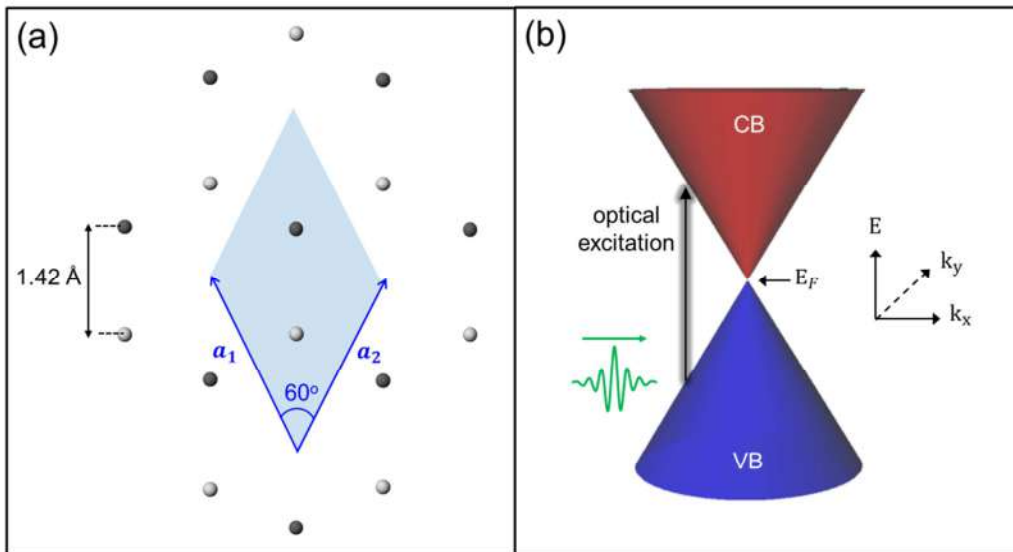
{Figure 5.26. (a) Schematic of the structure of graphene. Two inequivalent carbon atoms in the primitive unit cell indicated by the pale blue region are colored in black and grey. Lattice vectors $(\boldsymbol{a_1, a_2})$ are labelled with blue arrows. (b) Schematic of the band structure of graphene at K point in k-space. E_F denotes the Fermi energy at the Direct point where the valance band (VB) and conduction band (CB) meet.}

6. Effect of Transient Electric Field on Intensities of Direct and Diffracted Ultrafast Low-Energy Electron Beam

6.1. Transient electric field (TEF) effect.

In a UHV environment, visible-light pulsed laser excitation of a metal surface can lead to the electron emission via three distinct mechanisms [112]. The first mechanism is thermionic emission (TE) that allows for the thermalized hot free-electron gas near the Fermi energy to be emitted from the metal surface. The second mechanism is multiphoton photoemission (MPPE). For a high illumination intensity condition, two or three visible-light photons with the energy range from 1.8 eV to 3.1 eV are involved in the population of an intermediate state and a subsequent excitation above a typical metal work function ranging from 4.0 eV to 5.0 eV, essentially a quantum mechanical process. The third mechanism is the thermally-assisted (or thermally-enhanced) photoemission (TP) that combines TE and photoemission.

Which one of those three mechanisms dominates over the other in the visible-light excitation depends on the laser fluence and the pulse duration. Once the optical energy is transferred to the metal surface, the free-electron gas is thermalized in less than 100 fs, while the lattice is thermally uncoupled from the electrons for this time scale. The hot electrons are thermally equilibrated to the lattice in a few picoseconds, leading to the decrease of the electron temperature T_e and the simultaneous rise of the lattice temperature T_l. In this regard, for a given laser fluence, the highest T_e can be reached before the thermal equilibration starts, and the number of emitted electrons via thermally-dependent processes is maximized in the femtosecond time scale. On the other hand, in case of a pico- to nanosecond excitation, MPPE becomes dominant at low laser fluence, and the threshold fluence leading to TE or TP is higher than that of the femtosecond laser excitation case. For example, the threshold fluence is about 1.0 mJ/cm^2 for 100 femtosecond excitations [113-117,118], while it is about 40 – 100 mJ/cm^2 for nanosecond excitations [119,120]. For a few picosecond excitation case [121-123], no TE is observed since the damage threshold of most of metal surfaces is reached before thermionic current is observed. In this regime, MPPE dominates in the electron emission.

In the femtosecond visible-light excitation with sufficiently high laser fluence for TE, the hot electrons initially form a thin disk-like shaped electron cloud with a negative charge density $-\sigma_0$, parallel to the solid surface ionized with a positive charge density $+\sigma_0$ [124,125]. As a result, an electric field is generated in a subpicosecond time scale inside the two oppositely charged planes,

leading to a spatial deflection of charged particle beams when passing through this field, as illustrated in Figure 6.1. This transient electric field (TEF) effect is a well-known phenomenon in UED communities. Because the fluence of femtosecond laser excitation required for triggering a structural change is typically higher than the threshold fluence generating TEF, the two independent sources of altering the probe electron beam needs to be considered in the data interpretation in UED, especially for low-energy electron beams more vulnerable to TEF. This issue was firstly raised by H. Park *et al*. [125] in 2009 in which they demonstrated 0.001° deflection of a 30 keV ultrafast tangential electron beam (in grazing-incidence angle geometry) by TEF with the maximum field strength of 34 kV/m, created by 67.7 mJ/cm^2 ultrashort laser (130 fs, 800 nm) fluence. One year after, this work was disputed by S. Schaefer *et al*. [126] in which they have calculated the surface electric field by using a two-disc model and showed the structurally-induced Bragg spot dynamics of graphite, depending on the laser fluence and spot order, insisting the irrelevance to their previous works [127,128] on TEF.
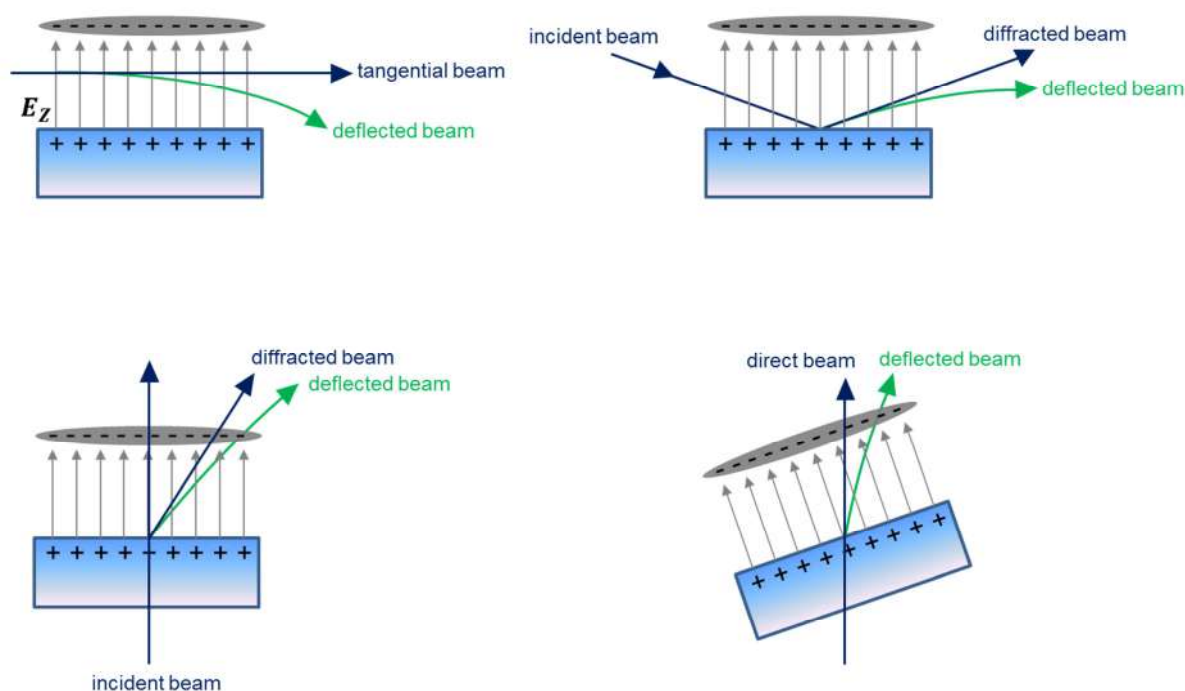
{Figure 6.1. Spatial deflection of probe electron beams by TEF.}

In this Section, the effect of TEF on direct and diffracted ultrafast low-energy (2 keV) electron beams is experimentally studied in transmission geometry by changing excitation laser fluence and pulse duration, and their behaviors are compared, providing a clue to find experimental conditions allowing for the separation of the structural change- and TEF-driven Bragg spot intensity changes.

6.2. A brief picture on the dynamics of hot electron cloud

As briefly mentioned earlier, the hot electrons escaped from the solid surface after femtosecond excitation create a thin disc like electron cloud. This charged cloud leaves the surface with an average speed of $v_0(t=0)$ and gradually decelerates until it reaches to the point where its average velocity $v_0(t_{max})$ becomes zero. t_{max} denotes the elapsed time of this electron could separation and ranges from 10 – 100 ps, depending on $v_0(t=0)$ and the number of emitted electrons. At the velocity turning point, 0 to 10 % of the electrons still continue to travel in the forward direction, and the rest of the electrons (90 – 100 %) start to travel in the backward direction and eventually recombines with the surface. A schematic illustration of the electron cloud dynamics is presented in Figure 6.2.
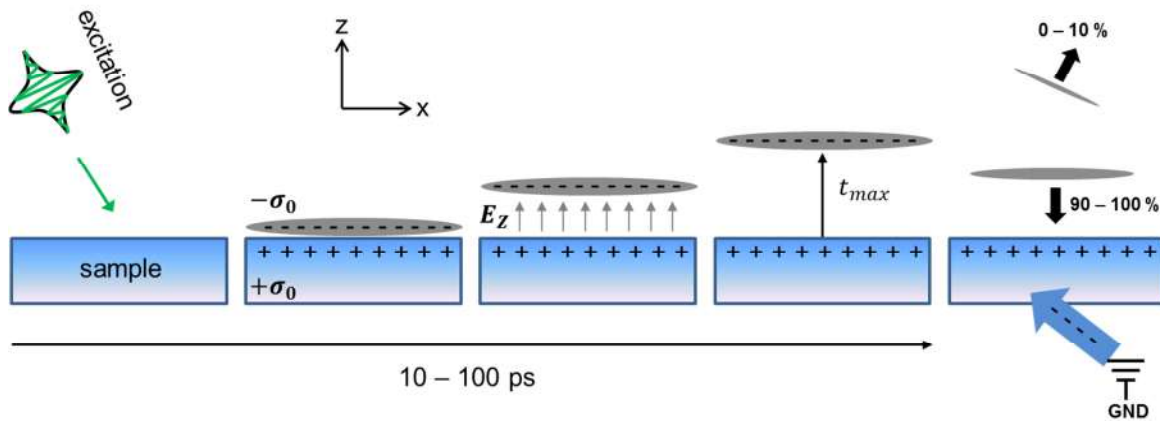
{Figure 6.2. Schematic illustration of the life of hot electron cloud.}

The experimentally determined parameters v_0, t_{max}, and the surface charge density σ_0, depending on the laser fluence, adapted from the literature [125], are summarized in Table 6.1. The table indicates that the higher the laser excitation fluence is the faster the electrons move and more hot electrons are generated, which more quickly reach the velocity turning point and recombine to the surface.

112

Laser fluence (mJ/cm^2)	v_0 (μm/ps)	t_{max} (ps)	σ_0 (×10^6 e/mm^2)
13.5	0.25	90	0.54
27.1	0.55	90	0.92
40.6	0.85	78	1.2
54.2	1.4	65	1.5
67.7	1.6	60	1.9

{Table 6.1. Dependence of of v_0, t_{max}, and σ_0 on the laser fluence. The definition of each parameter is described in the main text. The numbers on the table are adapted from [125]. }

6.3. Experimental scheme

The time-resolved transmission-mode LEED setup except the streak camera part, introduced in section 5.5 is used. The electron kinetic energy is set to 2 keV. In case of the direct beam study, a diverging beam generated from the Einzel-lens integrated LEED gun is used as a probe of the TEF effect, and for optical excitation, a green wavelength (515 nm) pulsed laser is used to irradiate a pepper pot type TEM (transmission electron microscope) mesh grid made of Cu (pitch: 12.5 μm, hole width: 6.5 μm, bar width: 6 μm). The projection image of the grid captured in the electron detector-CCD camera combination is monitored as a function of the delay time Δt between the excitation laser and the probe electron at various laser fluence and pulse duration conditions. In case of the diffracted beam study, a freestanding CVD-grown graphene monolayer supported on the same type of Cu mesh grid used in direct beam study is excited by the green laser, and a maximally focused electron beam is used. For both cases, the intensity change of the direct beam spot, the 1st and the 2nd order Bragg reflection spots in the difference map obtained by the subtraction of the unpumped from the pumped image, is time-traced. The electron bunch duration is approximately 16 ps FWHM.
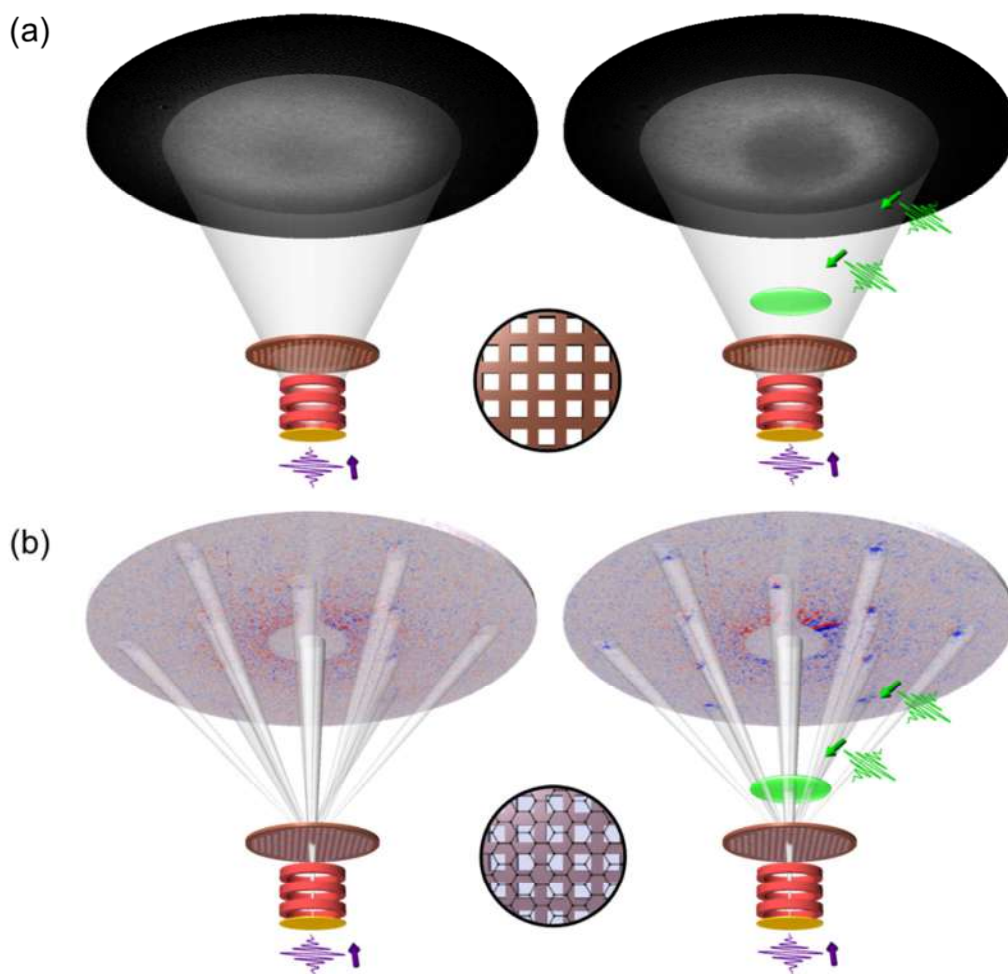
{Figure 6.3. Experimental layout. (a) A diverging photoelectron beam (2 keV) triggered by an ultrafast laser pulse (ultraviolet) forms a shadow image of a Cu TEM mesh grid at the screen. A sequence of ultrafast pump pulses (green) is irradiated to the mesh grid, giving rise to a TEF. The shadow image is recorded as a function of a delay time between the pump pulse and the diverging electron beam. (b) A focused photoelectron beam by an electrostatic Einzel lens is incident on a freestanding monolayer graphene suspended on the same type of the mesh grid. A differential diffraction image (unexcited – excited image) is monitored as a function of the delay time between the pump pulse and the focused electron pulse. }

6.4. The effect of TEF on direct beam

114

Figure 6.4 (a) shows the temporal behavior of the normalized intensity change $\Delta I(\Delta t)/I(\Delta t < 0)$ of the direct beam as a function of the excitation fluence at the fixed pulse duration of 180 fs (FWHM). For the fluence range of 4.5 - 27.3 mJ/cm^2, a sudden intensity drop is identified at around $\Delta t = 0$ point, marking the onset of TEF caused by hot electron clouds. Given that no clear intensity drop is observed below this fluence range, the threshold intensity for TEF at this excitation pulse duration is determined to be below 2.5×10^{10} W/cm^2. After a maximum intensity drop is reached at around few tens of picosecond, the recovery of the intensity drop starts, resulted from the charge recombination to the ionized Cu mesh grid.
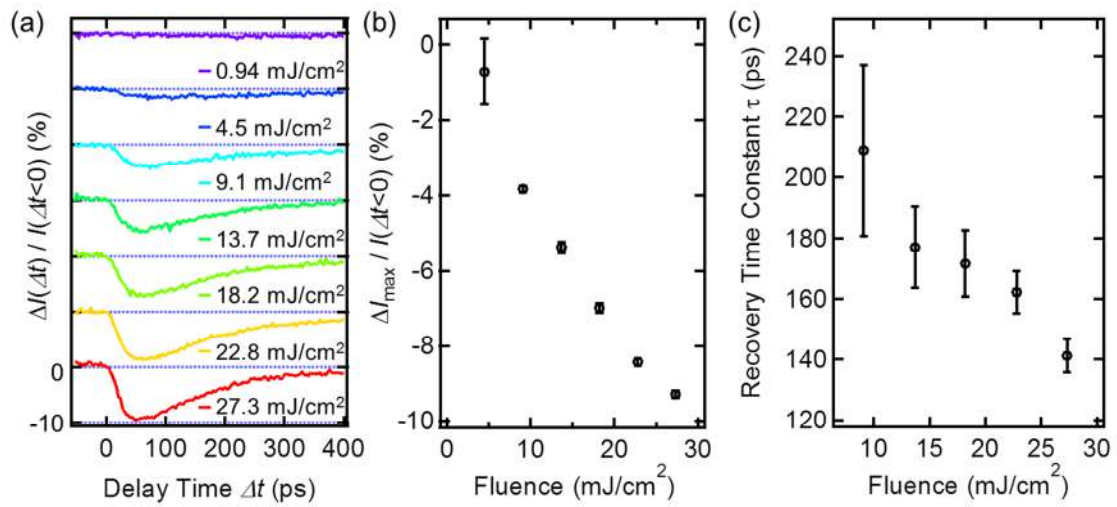
{Figure 6.4. Pump-probe kinetics of the direct beam at different excitation pulse fluences. (a) Temporal evolution of the direct beam intensity difference ($\Delta I(\Delta t) = I(\Delta t < 0) - I(\Delta t)$), normalized to the intensity at negative time delays $I(\Delta t < 0)$. Fluence dependence on (b) the maximum of the normalized intensity difference $\Delta I_{max}/I(t < 0)$ and (c) the recovery time constant τ. }

In order to evaluate the maximum magnitude of the normalized intensity change $\Delta I_{max}/I(t < 0)$ and the recovery time constant τ of the time trace, the measured data is fitted to a function:

$$y_0 + A_1 \cdot erf\left\{\frac{-(x-x_1)}{\sqrt{2} \cdot w}\right\} + A_2 \cdot \exp\left\{\frac{-(x-x_2)}{\tau}\right\} \tag{6.1}$$

where, the first two terms corresponds to an error function to evaluate the maximum intensity change, and the last single exponential term is used to fit the recovery feature of the time trace. $\Delta I_{max}/I$ is determined as $y_0 + A_1$, while τ is taken directly in the third term in the above fit function. The

115

evaluated $\Delta I_{max} / I$ and τ as a function of the excitation fluence are summarized in Figure 6.4 (b) and (c). As the fluence increases, $\Delta I_{max} / I$ increases, and τ decreases. These trends can be explained by a single parameter T_e. The increase of T_e with the increase of fluence results in the increase of σ_0, considering a proportional relation between T_e and the electron yield in the TE process. Because the magnitude of TEF ($= \sigma_0 / 2\varepsilon_0$, where ε_0 denotes the vacuum permittivity) is proportional to σ_0, the larger intensity drop is expected for a higher excitation fluence condition. In addition, the increase of σ_0 caused by the increase of T_e should provide higher acceleration field in the charge recombination process, which accounts for the decrease of τ with the increase of fluence.

The excitation pulse duration dependence of TEF on the direct beam is displayed in Figure 6.5. For this measurement, the fluence is fixed to 27.3 mJ/cm^2, the value high enough to generate TEF at the shortest pulse duration, confirmed in the previous fluence dependence study of TEF. As shown in Figure 6.5 (a), the temporal behavior of the start of the intensity drop at $\Delta t = 0$ and a subsequent gradual recovery on a few hundreds of picoseconds is observed in the entire range of the different pulse duration studied, similarly to that of the fluence dependence studies.

In the pulse duration variation range from a few hundreds of femtoseconds to a few picoseconds, T_e is expected to decrease with the increase of the pulse duration because of thermal coupling between hot electrons to phonons (in copper). The decrease of $\Delta I_{max} / I$ and the increase of τ with the increase of the pulse duration, shown in Figure (b) and (c), can be viewed as a result of the decreased T_e and the concomitant decrease of TEF effect on the direct beam.
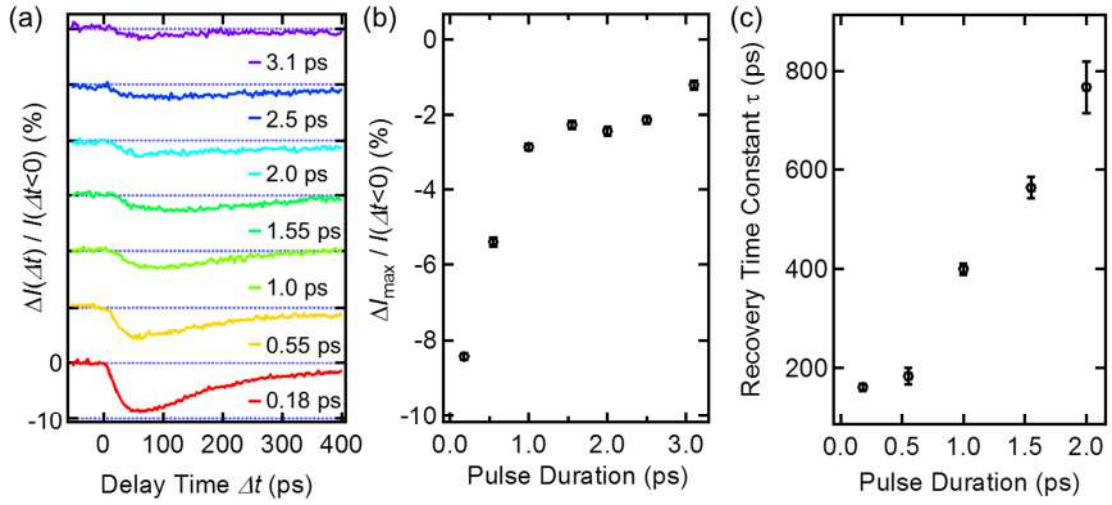
{Figure 6.5. Pump-probe kinetics of the direct beam at different excitation pulse durations. (a) Temporal evolution of the normalized intensity difference. Fluence dependence on (b) the maximum of the normalized intensity difference and (c) the recovery time constant τ. }

6.5. The effect of TEF on diffracted beam

The $\Delta I / I$ of the 1st and 2nd order Bragg diffraction spots of graphene as a function of Δt is shown in Figure 6.6 (a). For this measurement, the exaction pulse duration is fixed to 2.0 ps, In the excitation fluence range varied in this measurement, both of the [10] and [11] diffraction spots exhibits a similar temporal behavior compared with that of the direct beam case: a sudden intensity drop after $\Delta t = 0$ point and its gradual recovery on a few hundreds of picoseconds. In order to quantify $\Delta I_{max,hkl} / I_{hkl}$ and τ_{hkl} of the time trace, the fit function (6.1) used for the fitting of the temporal trace of the direct beam is used. Here, $\Delta I_{max,hkl} / I_{hkl}$ and τ_{hkl} denote the maximum magnitude of the normalized relative intensity and recovery time constant, respectively, for each [hkl] diffraction spot.

The excitation fluence dependence on $\Delta I_{max,hkl} / I_{hkl}$ is summarized in Figure 6.1 (b). Two clear trends are identified. Firstly, with the increase of excitation fluence, $\Delta I_{max,hkl} / I_{hkl}$ increases for both of the [10] and [11] diffraction spots. This proportional relation between $\Delta I_{max,hkl} / I_{hkl}$ and fluence is in common for both of the diffracted and direct beam (Figure 6.4) cases, not enabling one to distinguish if this kinetic stems from the TEF effect or a structural change. Secondly, for the entire fluence range, $\Delta I_{max,hkl} / I_{hkl}$ of the [11] spot is larger than that of the [10] one. This observation is counter intuitive from the TEF effect. The two-dimensional Gaussian intensity profile of the excitation laser is expected to generate TEF of which the strength is the highest at the center of the

117

excitation laser-graphene interaction region and decreases in the direction toward the edge of the region. In this regard, if the TEF effect is the dominant factor of the kinetics, the diffraction intensity drop of the 1st order spot should be larger than or equal to that of the 2nd order one, opposite to the latter trend.

For a given laser-excited area (= $9.9*10^{-4}$ cm^2 FWHM, separately measured by a knife-edge technique) and excitation laser fluence, T_l of graphene can be estimated. In this estimation, the absorption efficiency of 2.3 % for monolayer graphene at 515 nm wavelength is assumed [111], and the specific heat of graphite, a constant (≈ 0.7 J $g^{-1} K^{-1}$) identical to that of monolayer graphene above 100 K, is quoted [129]. The calculated T_l corresponding to each fluence is displayed in the upper x-axis of Figure 6.6 (b), showing the T_l dependence on $\Delta I_{\max,hkl} / I_{hkl}$. The proportional relation between $\Delta I_{\max,hkl} / I_{hkl}$ and T_l can be explained by the Debye-Waller effect, introduced in section 4.1.5: the increased atomic displacement caused by a thermal motion at higher temperature results in a weaker diffraction spot intensity. The Debye-Waller effect also accounts for the order dependence of $\Delta I_{\max,hkl} / I_{hkl}$ on each calculated T_l: for a given crystal temperature, the higher order diffraction spot intensity drops more than that of the lower order one.

To quantitatively evaluate if the measured $\Delta I_{\max,hkl} / I_{hkl}$ follows the Debye-Waller theory, a parameter q relating the in-plane mean-square displacement of a carbon atom $<u(T)^2>$ to T_l is introduced:

$$<u(T)^2> = qT_l \tag{6.2}$$

In equation (6.2), a linearly proportional dependence of $<u(T)^2>$ on T_l is explicitly made, valid at high temperature limit [130], and for the graphene case, it is a fair assumption above 300 K [131]. Combining equation (6.2) into the Debye-Waller model (equation (4.15)) yields the following form of q:

$$q = \frac{-3\ln\left\{1 + \dfrac{\Delta I_{\max,hkl}(T_l)}{I_{hkl}(RT)}\right\}}{G_{hkl}^2(T_l - RT)} \tag{6.3}$$

where, RT, $I_{hkl}(RT)$, G_{hkl} denote room temperature (= 300 K), intensity of the $[hkl]$ spot at RT, and the reciprocal lattice vector for the $[hkl]$ plane, respectively. In deriving equation (6.3), the

assumption that $I_{hkl}(\Delta t < 0)$ is equal to $I_{hkl}(RT)$ is implicitly made. From the measured $\Delta I_{max,hkl} / I_{hkl}$, the calculated T_l, and the known values of G_{hkl} ($G_{10} = 2.948 \times 10^{-2} \, pm^{-1}$, $G_{11} = 5.106 \times 10^{-2} \, pm^{-1}$), q is evaluated. The full derivation of equation (6.3) is described in Appendix D.
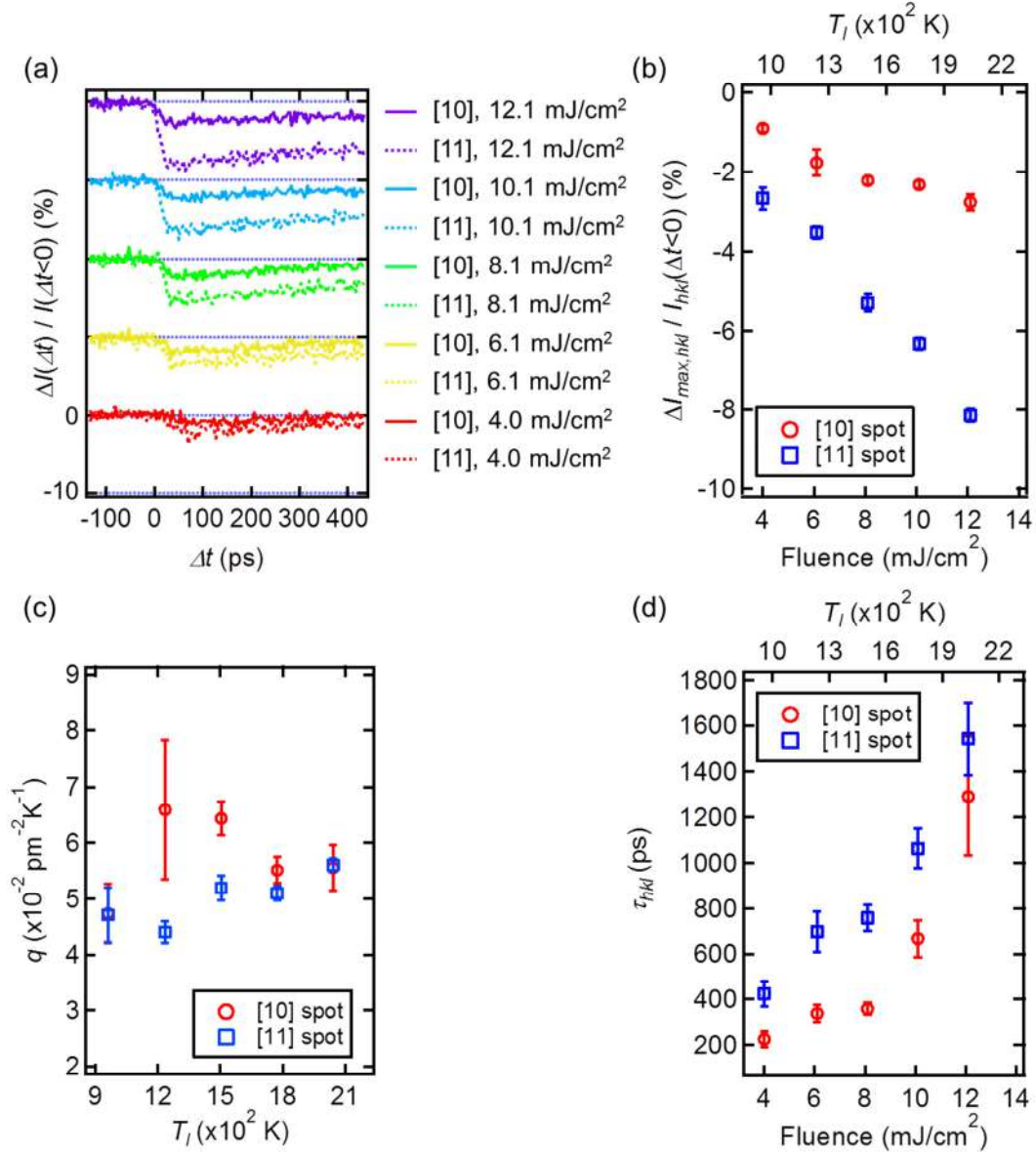
{Figure 6.6. Pump-probe kinetics of the diffracted beam at different excitation pulse fluences. (a) Temporal evolution of the diffracted beam intensity difference, normalized to the intensity at negative time delays ($\Delta I(\Delta t) = I(\Delta t < 0) - I(\Delta t)$). The solid and dotted lines indicate the [10] and [11] Bragg spots intensity trace, respectively. (b) Pulse fluence dependence on the maximum of the normalized intensity difference $\Delta I_{max,hkl} / I_{hkl}$ for each [hkl] diffraction spot. The upper x-axis denotes the calculated monolayer graphene temperature for the given excitation pulse fluence. (c) The

parameter q as a function of T_l, see the main text for the definition of q. (d) Pulse fluence dependence on the recovery time constant τ_{hkl}.}

Since q is independent of the diffraction spot order by definition, relying on the Debye-Waller model, the evaluated q should be equal for both of [10] and [11] spots. In contrast to this expectation, it is noticeable that q for [10] spot is larger than that for [11] one for the entire range of T_l, as shown in Figure 6.6 (c). The averaged one over the five q values evaluated at each T_l also indicates the larger value of $q = 5.77 \pm 0.54 (\times 10^{-2} pm^{-2} K^{-1})$ for the [10] spot than $q = 5.00 \pm 0.23 (\times 10^{-2} pm^{-2} K^{-1})$ for the [11] spot. One plausible explanation about the mismatch of q for the two different diffraction order spots is that the contribution of the TEF effect to the [10] spot intensity is greater than that to the [11] spot intensity. Indeed, the TEF profile resulted from the laser excitation was evaluated to have a steeper gradient than that of the laser intensity profile, extracted from the TEF induced angular deflection measurement with 6 keV electron beam in a transmission geometry [132]. This non-uniform field profile implies that the [10] spot intensity formed with a small scattering angle (= 7.4 °) is likely to be affected by TEF more, while the [11] spot formed with a large scattering angle (= 12.8 °) is less or not affected. As a result, the q value for the [10] spot is evaluated higher than the one resulted only from the thermally driven structural change, which could lead one to extract the wrong structure information from the lower order diffraction spot.

The fluence dependence on τ_{hkl} also supports the above scenario developed upon the intensity drop. As summarized in Figure 6.6 (d), τ_{hkl} for both of the [10] and [11] spots increases with the increase of fluence. This intensity recovery kinetic of the diffracted beam is directly in the opposite direction of the observed trend with the direct beam (Figure 6.4 (c)). Therefore, this global trend cannot be accounted for by the TEF effect exhibiting the inverse proportionality with respect to fluence. Instead, it is attributed to the increase of the lattice thermal conductivity of suspended graphene at high temperature [129] such that lattice cooling via phonon-phonon scattering is retarded more for higher T_l.

Also identified in Figure 6.6 (d) is the faster recovery of the [10] spot intensity than the [11] spot in the entire range of fluence. If the thermal relaxation is the only mechanism for the recovery kinetics, in theory, τ_{hkl} should not show the order dependence at a given fluence. In this regard, the different recovery constant depending on the diffraction spot order is a clear indication of the contribution of the TEF effect. The additional recovery mechanism induced by the TEF effect requires

summing up of the two recovery rates by the thermal relaxation and by the TEF effect. The resultant recovery rate (or equivalently the inverse of the recovery time) should be larger than the one driven only by a single mechanism. Given that the 1st order spot is more vulnerable to TEF than the 2nd order one, as expected, τ_{hkl} for the [10] spot is smaller than that for the [11] one.

Next, the pulse duration dependence of the TEF effect on the diffracted beam is investigated. In this measurement, the excitation laser fluence is fixed to 12.1 mJ/cm^2, corresponding to the highest T_l evaluated in the fluence dependence measurement, and the pulse duration is varied from 550 fs to 2.5 ps. Since excitation fluence is unchanged in this measurement, T_l of graphene is expected to be the same independent of the pulse durations, while T_e of graphene and Cu mesh grid is different depending on the pulse duration because of the electron-phonon thermal coupling. The temporal behavior of $\Delta I / I$ for both of the 1st and 2nd order spots measured with different pulse durations are displayed in Figure 6.7 (a). As summarized in Figure 6.7 (b), $\Delta I_{\max,hkl} / I_{hkl}$ for the [11] spot shows little variation, except the case of the 550 fs pulse duration, while that for the [10] spot changes rapidly in the entire pulse duration range. This observation, again, can be understood by the position-dependent TEF strength caused by the Gaussian excitation profile. A distinguishing intensity drop from both of the [10] and [11] spots are identified in the case of the 550 fs pulse duration, indicating that the TEF effect is large enough to give rise to the additional intensity drop from both spots in this high intensity laser excitation case. In contrast, in case of the 2.5 ps pulse duration, the excitation intensity is not sufficient for TEF to affect the intensity of the diffracted beams, identified from no intensity recovery from both spots within the time-window of this measurement ($\Delta t = 433$ ps) (Figure 6.7 (a)). This behavior can be understood by the lack of the TEF effect on the diffracted beams and by the increased lattice thermal conductivity at the high T_l.

The pulse duration dependence on τ_{hkl} is displayed in Figure 6.7 (d). For the [10] spot, τ_{hkl} increases with the increase of the pulse duration, which cannot be explained by the thermal relaxation between an elevated T_l and room temperature at the same fluence condition. Rather, this trend follows the pulse duration dependence on τ of the direct beam, to which only the TEF effect contributes (Figure 6.7 (c)). In contrast, for the [11] spot, τ_{hkl} reaches to a saturated value at the pulse duration of 1.55 ps, indicating that the TEF effect is minimal beyond this pulse duration at the given fluence for the 2nd order spot.

Referring to the time trace of $\Delta I / I$ obtained in the direct beam measurements (Figure 6.4

(a) and Figure 6.5 (a)), I determine the interaction of the emitted hot electron cloud with the probe electron beam is insignificant beyond Δt = 400 ps, driven via the charge recombination process. Based on the determined electron cloud lifetime, I interpret the measured $\Delta I / I$ of the diffraction spots after Δt = 400 ps as induced predominantly by the structural effect. Assuming the maximum rise of T_l of graphene is the same (in this case, calculated as ~2042 K), independent of the pulse duration at the given excitation fluence condition, my interpretation implies that the recovered intensity changes $\Delta I(\Delta t > 400\,ps) / I$ of the diffraction spots measured with the different pulse durations should be comparable each other. Interestingly, the measured intensity change at Δt equal to 400 ps $\Delta I(\Delta t = 400\,ps) / I$ shows clear pulse duration dependence (Figure 6.7 (c)). In particular, I note that $\Delta I(\Delta t = 400\,ps) / I$ s for the pulse durations from 550 fs to 2.0 ps are smaller than that of the 2.5 ps one showing the least contaminated diffraction spot intensity from the TEF effect in the present measurement set. This observation leads me to the following stepwise scenario: 1) the hot electron cloud is released from the sample, 2) due to the lack of the thermal carriers, T_l does not reach to a level at which it should be in the condition without the TEF effect for the same excitation fluence, 3) the decreased T_l gives rise to a smaller temperature gradient and a higher thermal conductivity both of which results in a decreased lattice temperature during thermalization.
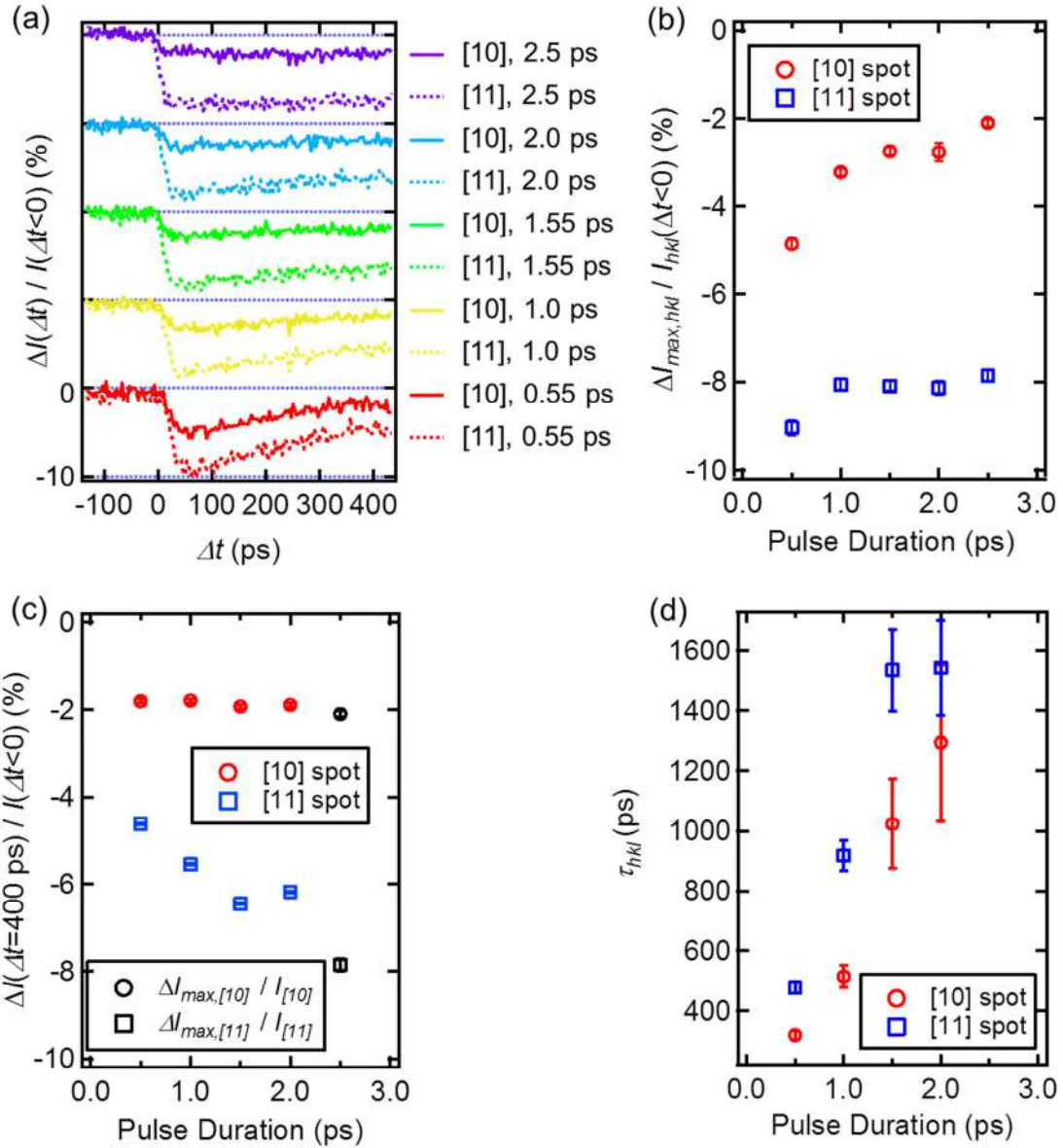
{Figure 6.7. Pump-probe kinetics of the diffracted beam at different excitation pulse duration. (a) Temporal evolution of the diffracted beam intensity difference, normalized to the intensity at negative time delays ($\Delta I(\Delta t) = I(\Delta t < 0) - I(\Delta t)$). The solid and dotted lines indicate the [10] and [11] Bragg spots intensity trace, respectively. (b) Pulse duration dependence on the maximum of the normalized intensity difference $\Delta I_{max,hkl} / I_{hkl}$ for each [hkl] diffraction spot. (c) Normalized intensity change at $\Delta I = 400\,ps$ as a function of pulse duration. The black opened circle and square indicate $\Delta I_{max,hkl} / I_{hkl}$ at the pulse duration of 2.5 ps for the [10] and the [11] spot, respectively. (d) Pulse duraton dependence on the recovery time constant τ_{hkl}.}

123

7. Ultrafast Low-Energy Streak Diffraction

7.1. Motivation: An alternative strategy – streaking

Many of chemical reactions occurring at a surface or interface of chemical species are irreversible processes, meaning that once the system is perturbed by an external trigger, it never goes back to its initial state. In order to capture the structural changes induced by these chemical reactions, as a result, a fresh sample area that can be assumed to have an identical initial sample state needs to be replenished to the pump and probe interaction region at every delay time point during the entire course of measurement. Considering a typical the pump-probe interaction area of 100 μm and a TEM grid size of 3 mm, for example, totally 300 time points can be sampled in principle in this way. Unfortunately, preparation of a freestanding thin sample (1 – 2 nm thick) with such an uniform large area, suited for transmission-mode low-energy electron diffraction is not trivial, which limits the types of samples that can be studied with low-energy electrons. In addition, in case of nanotip based electron sources, the typical number of electrons per bunch generated by a femtosecond laser trigger is less than 100. Given the fact that at least 10^6 incident electrons are required for a single reasonable quality diffraction image, it is unimaginable to study any irreversible chemical dynamics with this type of electron source and the conventional stroboscopic method.

As an alternative, ultrafast streak diffraction is an ideal single shot structure determination method to follow chemical reactions, particularly suited for low-energy electrons. This experimental technique enables to convert temporal information encoded in a single electron bunch into spatial information, allowing for transient structure retrieval from a single streak diffraction pattern. Because of the space-time correlation feature of this technique, the notorious $\Delta t = 0$ (the very initial time point when reaction starts) problem and the associated timing jitter issue can be avoided. Moreover, in streak diffraction, temporal resolution is mainly determined by the streak velocity of the streak camera, and not limited by space charge induced bunch broadening. Therefore, this technique can eliminate the necessity of nanotip source in time-resolved low-energy electron diffraction, advantageous in minimizing sample-to-source distance but suffering from low number of electrons, and allows for using a conventional large area photocathode that can produce 10^4 – 10^6 electrons per bunch. The streak velocity is a function of the streak camera geometry and the biasing voltage on the photoswitch for a given electron energy, as will be explained in the following sections, and in this thesis, it is demonstrated that subpicosecond resolution is feasible with this technique for 2.0 keV electrons, the world record in time-resolved low-energy electron diffraction, at the time of writing. Lastly, even concerning the reversible system, compared to the conventional stroboscopic method, the streaking

method is merited by the larger total number of the accumulated electrons for a given recording time of a single diffraction image due to the larger number of electrons per single bunch. This feat leads to the high signal-to-noise ratio (SNR) to make large image contrast with even better temporal resolution by this method.

7.2. Principle of streaking

Let us assume that the temporal profile, $\rho(t)$, of the electron bunch is composed of five discrete temporal slices in numerical order, and each slice has its one profile, $\rho(t_1)$, $\rho(t_2)...\rho(t_5)$, as depicted in Figure 7.1. We also assume a situation that both of the electron bunch and a pump pulse hit a diffraction sample exactly at t_0 in a synchronous way, and that the pump pulse duration is negligible compared to the electron bunch duration. Upon diffraction, the first temporal slice of the probe bunch captures the changing structures of the sample after excitation during the time from t_0 to t_1, and the second temporal does the same thing from t_1 to t_2, and so on. After the completion of the interaction between the electron bunch and the sample, the entire structural information captured during the time from t_0 to t_5 is contained in the single diffracted electron bunch composed of the five temporal slices. Without streaking, all the five temporal slices arrive at the same position on the screen, being recorded as a spot intensity profile of the time-dependent unstreaked diffraction, $u(x, y: t)$, where x and y are the transverse axes to define the spot position in space. The $u(x, y: t)$ consists of contribution of the structural information stamped at each time point in that the entire diffracted electron bunch is made of five different temporal slices. Considering the charge density of each slice, as a weighting factor, the contribution of each slice to $u(x, y: t)$ can be mathematically expressed as $\rho(t_k) \cdot u(x, y: t_k)$ (Figure 7.2).

In the streaking process, the diffracted bunch transits through a streaking region, typically formed just behind the sample, where a transient (time-varying) electric field is generated in a perpendicular direction (x- or y-axis direction) with respect to the bunch propagation direction (z-axis). By adjusting the bunch entrance timing with respect to the transient field, the maximum streak velocity is provided to the bunch, approximated by a linear field ramp. Then, as illustrated in Figure 7.3, each temporal slice of the bunch sees the different field strength inside the streak region and concomitantly gets deflected with different amount of angle. As a consequence, each slice arrives at a different location on the screen, forming a streak (elongated) diffraction spot resulting from the continuously overlapped temporal slices in one direction (streaking direction). This streaking process is equivalent to a conversion of the temporal information encoded in the diffracted bunch into the spatial information at the screen, providing the possibility to decode the structure dynamics contained in the single streak by a proper image analysis.
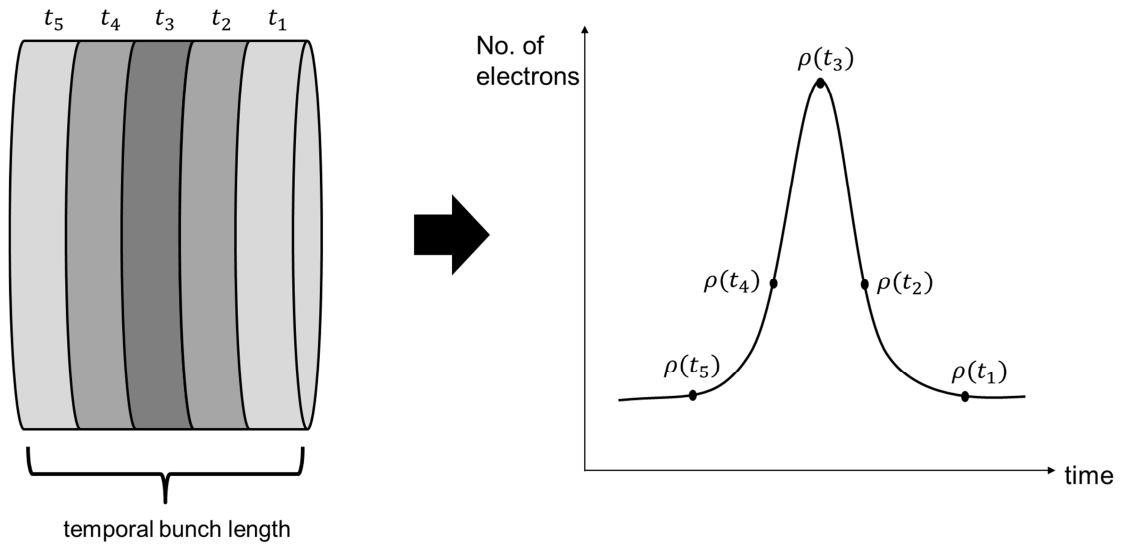
{Figure 7.1. Illustration of the temporal profile of electron bunch}
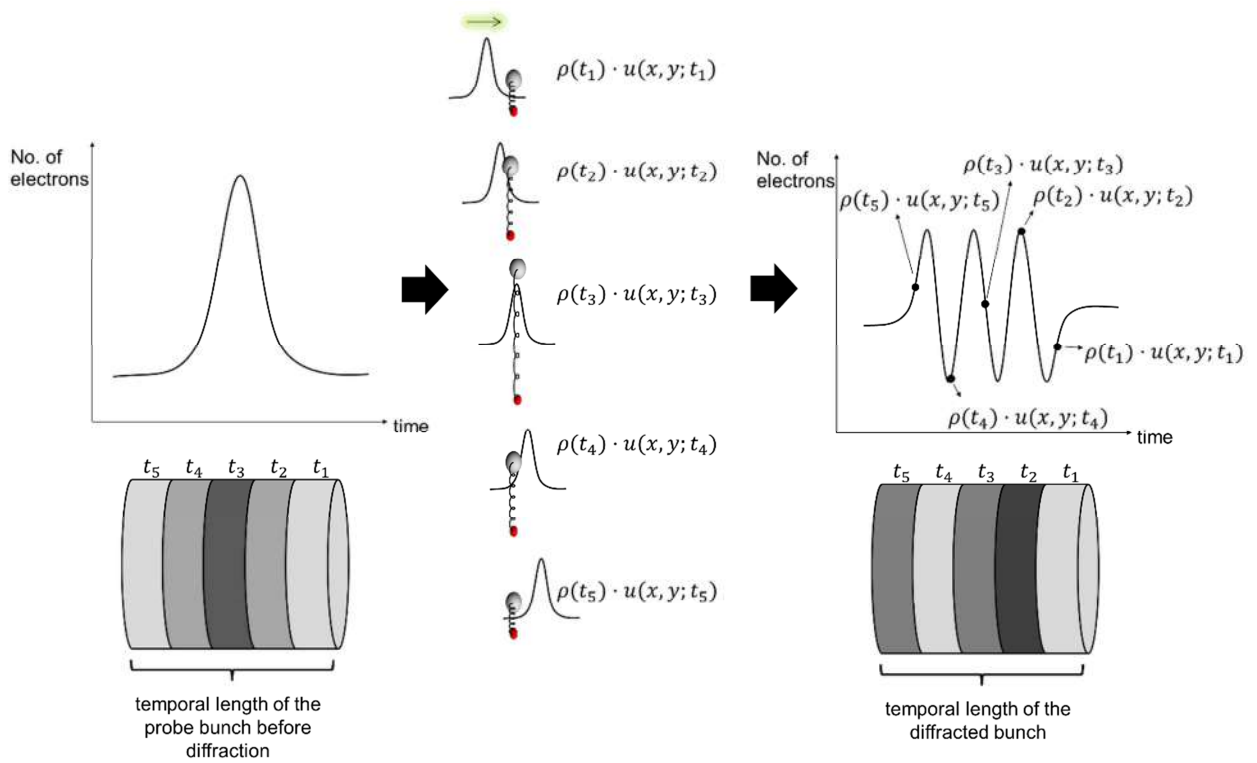
{Figure 7.2. Illustration of the temporal intensity profile change of the electron bunch after experiencing a diffraction sample with a structure change described by a diatomic molecule with a spring}

7.3. Streak camera design

The streak camera, the central unit of the streak diffraction, consists of two parallel streak plates and a photoswitch, and is placed behind the diffraction sample in perpendicular direction with respect to the

126

probe beam propagation direction. The transient electric field is generated at the gap between the two streak plates. In this regard, factors (field strength, frequency) affecting the field inside are governed by the geometrical parameters of the streak camera. In this chapter, these factors are discussed in detail.
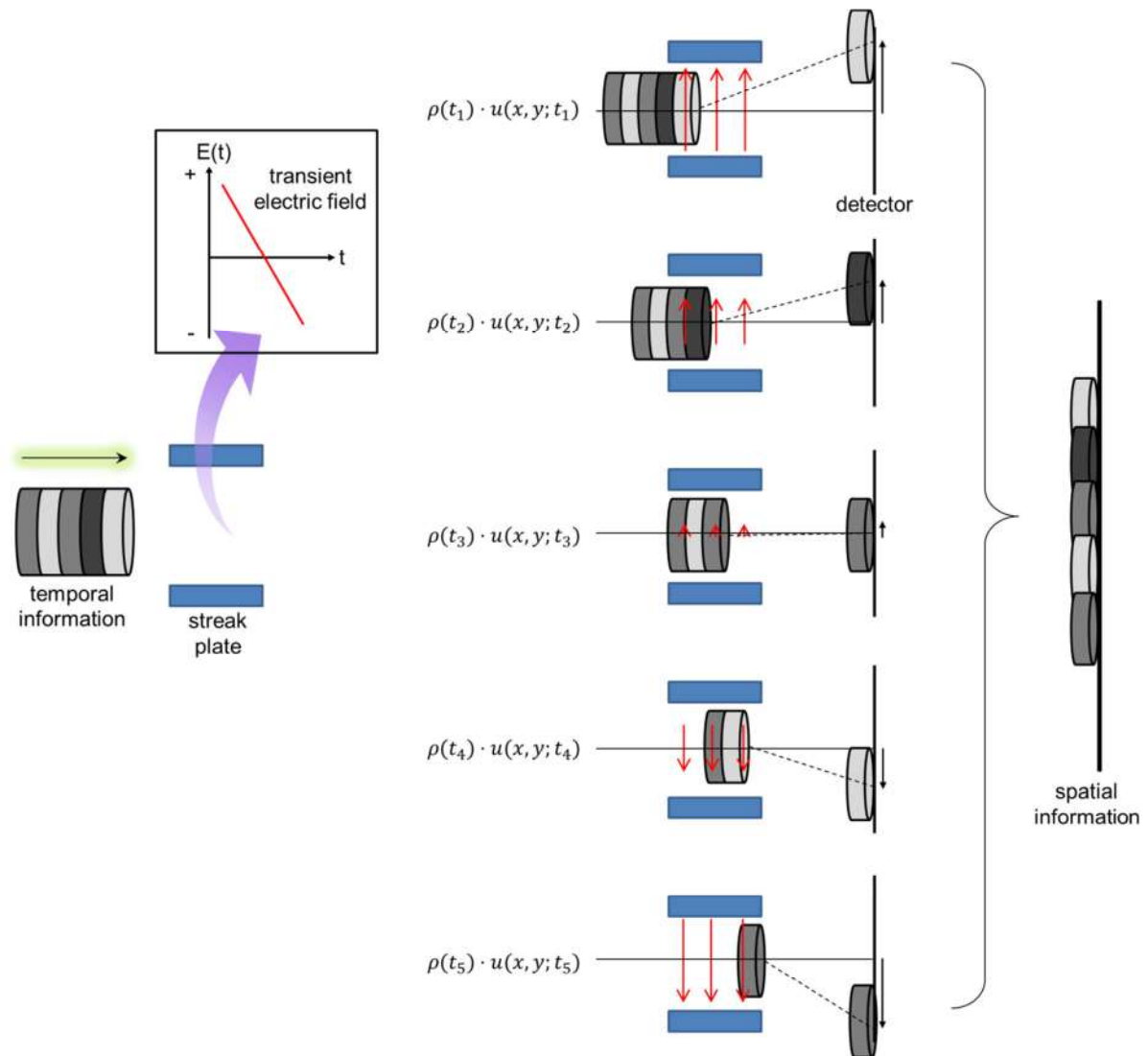
{Figure 7.3. Illustration of the streaking process. Each temporal element of the diffraction electron bunch gets deflected at a different location at the detector, resulting in a streak diffraction pattern.}

The basic idea to obtain the transient field at the streak plates is to use a damped harmonic oscillation field generated by a LCR electric circuit. As shown in the circuit diagram of the streak camera in Figure 7.4 (a), the parallel streak plates, photoswitch, and connection wires can be considered as equivalent as a capacitor with the intrinsic capacitance C, the resistor with the parasitic resistance, R_s, and the inductor with the parasitic inductance L, respectively. These circuit elements are mounted on a specially designed double-sided PCB (printed circuit board) where two high voltage and one ground electric contacts are also soldered, as shown in Figure 7.4 (b). The LCR circuit is

127

connected to the pulsed high voltage DC source through a decoupling resistor, R_d, in order to isolate the fast transient from the DC voltage during its operation.
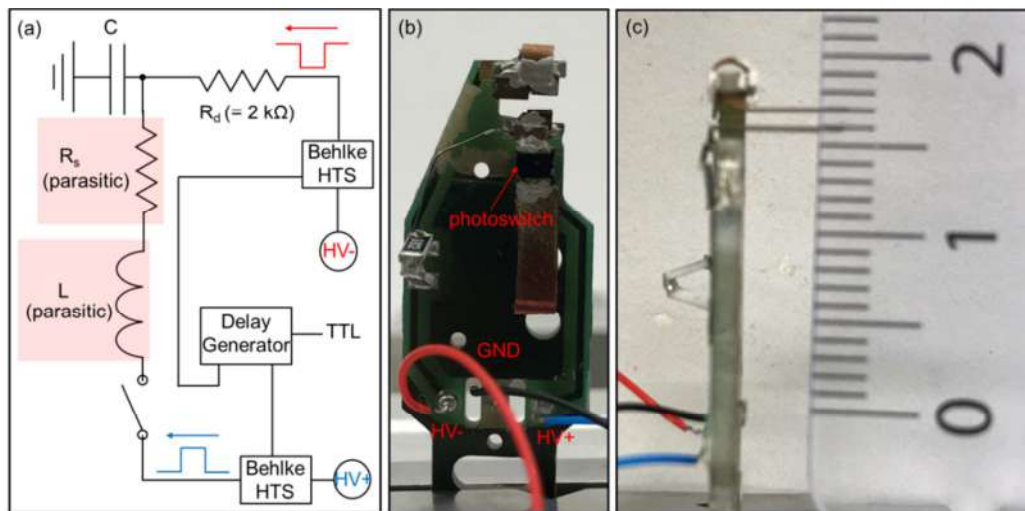
{Figure 7.4. (a) Circuit design of the streak camera. (b) PCB where the circuit elements are mounted. (c) image showing the streak plate gap distance}

The time-dependent electric field by a harmonic oscillation can be expressed as $E(t) = E_0 \cos(2\pi t/T_\omega)$, where, E_0 and T_ω are the field amplitude and oscillation period, respectively. The electron bunch, in principle, can see any field strength at the moment when it enters and exits the streak plates, but to obtain the maximum streaking for a given E_0, the ideal case is to use the full half swing of the oscillation as illustrated in Figure 7.5, resulting in the maximum difference of the field strength: the electron transit time through the streaking field, T, needs to match with half of T_ω. In this case, the streak velocity, v_s, is defined by the slope of the harmonic oscillation at the zero crossing, which is approximated as a liner field ramp.

What frequency of the harmonic streaking field is the most optimal for the purpose of capturing full chemical transient dynamics? When an electron bunch transits through the streak field, T is determined by the streak field length (in the propagation direction) and the speed of the electron v_z. In case of the streak field generated at the gap between two parallel streak plates, the streak field length is approximately equal to the plate length, l_p. Assuming T is equal to the $\frac{1}{2}T_\omega$ to achieve the maximum streaking, the required streaking field frequency, f, is given by $\frac{1}{2}\frac{v_z}{l_p}$. For the 2 keV electron bunch with the speed of $\sim 2.65\times10^7$ m/sec, f and T, required for the maximum streaking, are listed as a function of l_p in Table 7.1. Conclusively, this estimation of the required streak field

frequency indicates the following point: 1 to ~10 GHz is the right regime for the streak field frequency, considering the fact that the observable time window of the structural dynamics (few tens of ps) defined by the bunch length should be much shorter than T and T_ω. In case of this thesis, 1 mm of l_p is chosen, aiming for 2 keV electron bunch streaking in few tens of picosecond observable time window.
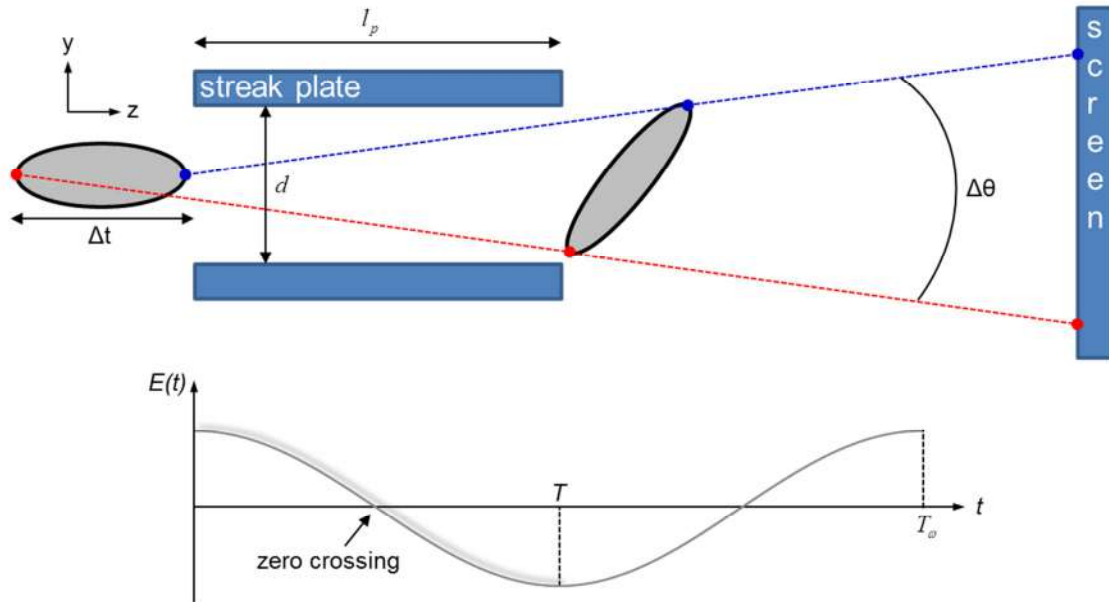
{Figure 7.5. Illustration of the harmonic oscillation inside the streak camera. The bunch propagation direction is assumed to z-axis, while the streaking direction is y-axis. The blue and red dot indicates the front and rear electron, respectively. l_p: streak plate width, d: streak plate separation, T: electron bunch transit time, T_ω : period of streak field oscillation, $\Delta\theta$: streak angle, Δt : bunch duration}

l_p	f	T
10 cm	132 MHz	3.78 ns
1 cm	1.32 GHz	378 ps
1 mm	13.2 GHz	37.8 ps
100 μm	132 GHz	3.78 ps
10 μm	1.32 THz	378 fs

129

{Table 7.1. Streak field frequency f and electron bunch transit time T at the streak plate with the plate width l_p for 2 keV electron}

The remaining task is to find an optimal range of the streak plate separation, d, which affects the maximum applicable streak field for a given streak plate voltage, ΔV, thereby determines the streak angle, $\Delta\theta$, and the temporal resolution, $\Delta\tau$. For a given v_z, the streak angle, $\Delta\theta$, is determined by the angular streak velocity, ω_s, and the electron bunch duration, Δt [133]:

$$\Delta\theta = \omega_s \cdot \Delta t \tag{7.1}$$

The ω_s is defined by $e\Delta E / \gamma m_e v_z$, where ΔE denotes the difference of the streak field when the electron bunch just enters and just exits the streak camera, and e, γ, and m_e denote elementary charge, Lorentz factor, and electron mass, respectively. The streak velocity, v_s, is defined by $\omega_s \cdot l_c$, where l_c denotes the camera length. Assuming $\Delta\tau$ in streaking experiment is determined by the finite pixel size of the electron detector, d_p, (the actual temporal resolution in the streak pattern data analysis is discussed in section 7.5, and reflecting the fact that the minimum streak angle is given by the ratio of d_p to l_c, the above equation (7.2) can be rearranged as:

$$d = \frac{l_c e \Delta V \Delta\tau}{d_p \gamma m_e v_z} \tag{7.2}$$

As shown in Table 7.2, basically as the smaller the d is, the better the temporal resolution can be achieved owing to the larger field strength. However, d is also limited by the scattering angle of the Bragg diffracted beams from a sample. In case of this thesis, $d = 1$ mm is chosen (together with $l_p = 1$ mm), as shown in Figure 7.4 (c), indicating that the maximum allowed scattering angle is 26.6° for this streak camera geometry.

$\Delta\tau$ (ps)	d (mm)
1	4.64
0.8	3.71
0.6	2.78

0.4	1.85
0.2	0.91
0.1	0.46

{Table 7.2. Required streak plate spacing, d, as a function of the aimed temporal resolution, for 2 keV electron. The actual mechanical parameters of the experimental setup (d_p = 50 μm, l_c = 35 mm) and the threshold voltage (ΔV = 1 kV) that the photoswitch can hold are reflected in the calculation. }

7.4. Fabrication and characterization of photoswitch

The entire fabrication process of the photoswitch, the central unit for the streak camera, is illustrated in Figure 7.6. A direct gap undoped semiconductor GaAs wafer with resistivity of 10^7 $\Omega \cdot cm$ and 500 μm thickness is chosen for the fast response of the switch on light. On top of the polished side of the wafer, about 1 μm thick photoresist is spin-coated. After a soft-backing step, the wafer is patterned by photolithography. 5 nm Ni layer for adhesion, 100 nm AuGe and 200 nm Au layers for biasing pad are deposited consecutively by electron-beam assisted evaporator. As a lift-off process, the metalized wafer is dipped into a removal solvent until the metal layers on the unpatterned region are completely peeled off as shown in Figure 7.7 (b). Subsequently, the wafer is annealed at 480 ℃ for 5 min in Ar environment in order to make an Ohmic contact between the semiconductor substrate and the metal pad, and finally diced into a single photoswitch as shown in Figure 7.7 (d).
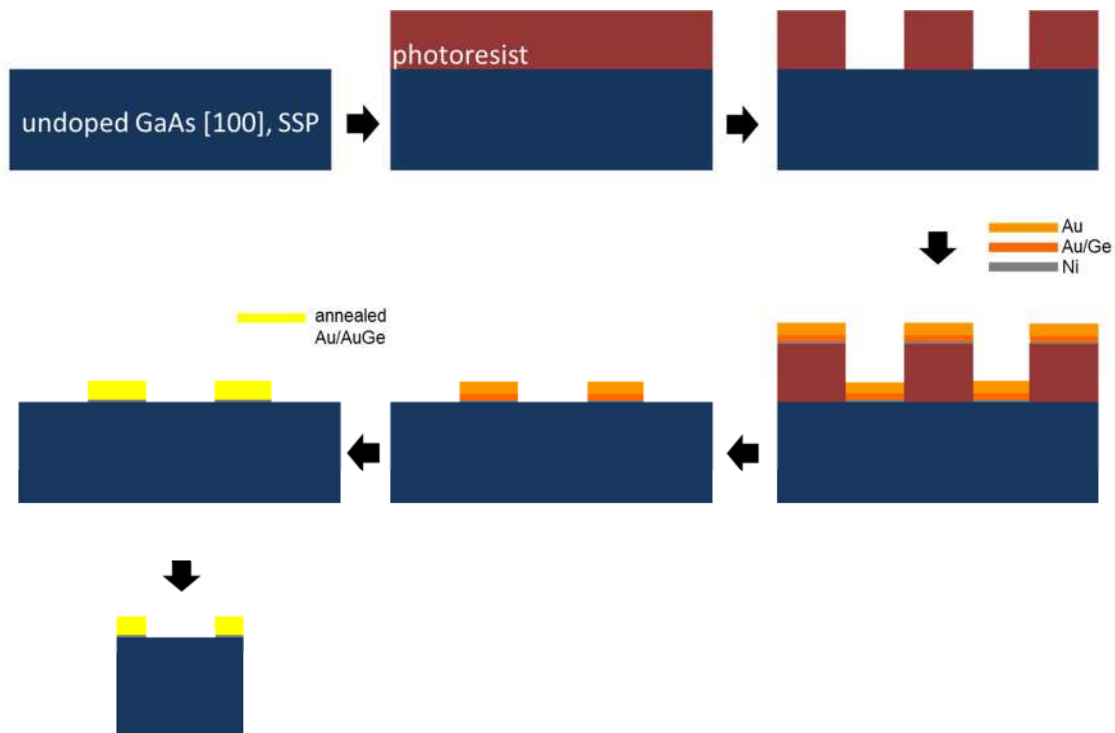
{Figure 7.6 Illustration of fabrication process of the photoswitch}
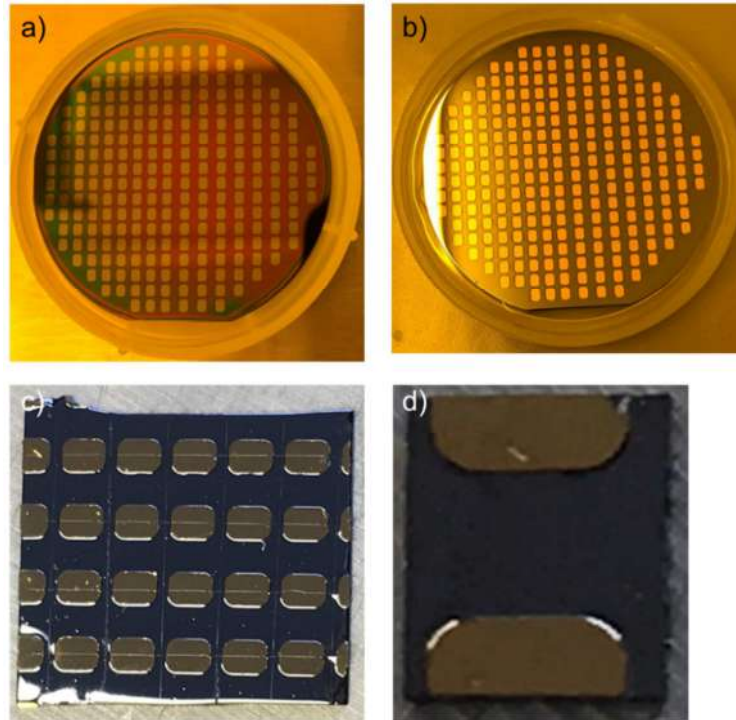
{Figure 7.7. (a) GaAs wafer after patterning and (b) metallization and liftoff process. (c) A piece of diced wafer after annealing. (d) single photoswitch cut by 2 mm by 2.5 mm}

The characterization on the response of the fabricated photoswitch on light is necessary for its use in the streak camera operation further. A simple test setup consisting of two electrical contacts for biasing (= 5 V) and sensing, respectively, and a decoupling resistor is used for the purpose as shown in Figure 7.8. Upon irradiating the triggering light (1 kHz) on the well-performing switch, signals with the voltage amplitude matched to the applied biasing voltage are detected with the same repetition rate of the trigger.
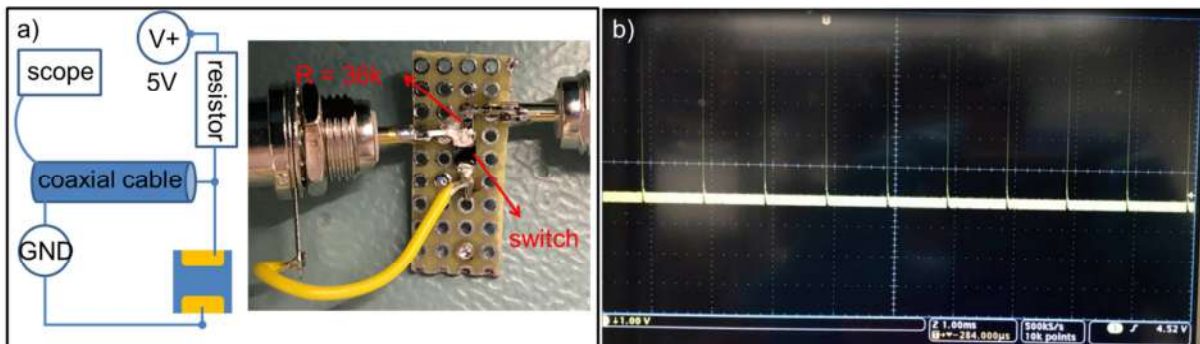
{Figure 7.8. (a) circuit diagram and image of the test setup for photoswitch performance characterization. (b) Scope image indicating the switch response on the triggering light}

7.5. Streak Pattern Analysis

Further to the section 7.2, defining y-axis as the streaking direction and y' as the displacement due to the deflection by streaking, and given by the fact that the streak diffraction pattern is made of continuously overlapped temporal slices at detector, the streak pattern intensity profile, $s(x, y)$, can be mathematically expressed as an integral form:

$$s(x, y) = \int_{-\infty}^{\infty} \rho(t) \cdot u(x, y - y')dt \qquad (7.3)$$

Note that the time-dependent change in position of the deflected slice is implicitly reflected through the relation, $y' = v_s \cdot t$, allowing for the exchange of the integral variable in equation (7.3) by y', yielding the following equation:

$$s(x, y) = \int_{-\infty}^{\infty} \rho(y') \cdot u(x, y - y')dy' \qquad (7.4)$$

In this thesis, for simplicity, one-dimensional streak pattern analysis (in the streaking direction) is only considered. This statement implies that the intensity profile of the streak diffraction spot can be binned along the x-axis direction, generating a one-dimensional convolution function:

$$s(y) = \int_{-\infty}^{\infty} \rho(y') \cdot u(y - y')dy' = \rho * u \qquad (7.5)$$

Since the electron beam spot intensity is recorded as a form of the pixel count on the detector, a discretized form of equation (7.5) is required for computation. As illustrated in Figure 7.9, the conceptually fragmented charges in each temporal slice, which arrives at the same detector pixel position, are accumulated, contributing to the pixel count of the particular pixel. Based on this concept, a single detector pixel count of the streak spot, $s(y_i)$, is mathematically expressed as a summation of the charge fragments:

$$s(y_i) = \sum_{k=1}^{i} \rho(y_k') \cdot u(y_{i-k+1} - y_k') \qquad (7.6)$$

where, i and k denote the index of the streak spot pixel and the temporal slice. For the entire streak spot intensity profile, equation (7.6) can be extended to a matrix equation:

$$\mathbf{s} = \mathbf{U}\mathbf{d} \qquad (7.7)$$

where, $\mathbf{s}$ and $\mathbf{d}$ are vectors constructed by $s(y_i)$ and $\rho(y_k')$ elements, respectively. For a given total number of the temporal slices, m, and that of fragments in each slice, n, the dimension of $\mathbf{s}$ and $\mathbf{d}$ are $[(m + n - 1) \times 1]$ and $[n \times 1]$, respectively. The $\mathbf{U}$ is $(m + n - 1)$-by-n matrix that

contains u elements:

$$
\begin{bmatrix}
u(y_1 - y_1') & 0 & 0 & 0 & \cdots & 0 \\
u(y_2 - y_1') & u(y_1 - y_2') & 0 & 0 & \cdots & 0 \\
u(y_3 - y_1') & u(y_2 - y_2') & u(y_1 - y_3') & 0 & \cdots & 0 \\
\vdots & u(y_3 - y_2') & u(y_2 - y_3') & u(y_1 - y_4') & \cdots & 0 \\
u(y_n - y_1') & \vdots & u(y_3 - y_3') & u(y_2 - y_4') & \cdots & 0 \\
0 & u(y_n - y_2') & \vdots & u(y_3 - y_4') & \cdots & 0 \\
0 & 0 & u(y_n - y_3') & \vdots & \cdots & 0 \\
0 & 0 & 0 & u(y_n - y_4') & \cdots & \vdots \\
\vdots & \vdots & \vdots & \vdots & \vdots & u(y_{n-1} - y_m') \\
0 & 0 & 0 & 0 & 0 & u(y_n - y_m')
\end{bmatrix}
$$

detector: $s(y_1)$, $s(y_2)$, $s(y_3)$, $s(y_4)$, $s(y_5)$, $s(y_6)$, $s(y_7)$, $s(y_8)$, $s(y_9)$

Red array:
$\rho(y_1') \cdot u(y_1 - y_1')$
$\rho(y_1') \cdot u(y_2 - y_1')$
$\rho(y_1') \cdot u(y_3 - y_1')$
$\rho(y_1') \cdot u(y_4 - y_1')$
$\rho(y_1') \cdot u(y_5 - y_1')$

Orange array:
$\rho(y_2') \cdot u(y_1 - y_2')$
$\rho(y_2') \cdot u(y_2 - y_2')$
$\rho(y_2') \cdot u(y_3 - y_2')$
$\rho(y_2') \cdot u(y_4 - y_2')$
$\rho(y_2') \cdot u(y_5 - y_2')$

Yellow array:
$\rho(y_3') \cdot u(y_1 - y_3')$
$\rho(y_3') \cdot u(y_2 - y_3')$
$\rho(y_3') \cdot u(y_3 - y_3')$
$\rho(y_3') \cdot u(y_4 - y_3')$
$\rho(y_3') \cdot u(y_5 - y_3')$

Green array:
$\rho(y_4') \cdot u(y_1 - y_4')$
$\rho(y_4') \cdot u(y_2 - y_4')$
$\rho(y_4') \cdot u(y_3 - y_4')$
$\rho(y_4') \cdot u(y_4 - y_4')$
$\rho(y_4') \cdot u(y_5 - y_4')$

Blue array:
$\rho(y_5') \cdot u(y_1 - y_5')$
$\rho(y_5') \cdot u(y_2 - y_5')$
$\rho(y_5') \cdot u(y_3 - y_5')$
$\rho(y_5') \cdot u(y_4 - y_5')$
$\rho(y_5') \cdot u(y_5 - y_5')$

streak plate

unstreaked bunch: $u(y_1)$, $u(y_2)$, $u(y_3)$, $u(y_4)$, $u(y_5)$

$s(y_1) = \rho(y_1') \cdot u(y_1 - y_1')$

$s(y_2) = \rho(y_1') \cdot u(y_2 - y_1') + \rho(y_2') \cdot u(y_1 - y_2')$

$s(y_3) = \rho(y_1') \cdot u(y_3 - y_1') + \rho(y_2') \cdot u(y_2 - y_2') + \rho(y_3') \cdot u(y_1 - y_3')$

$s(y_4) = \rho(y_1') \cdot u(y_4 - y_1') + \rho(y_2') \cdot u(y_3 - y_2') + \rho(y_3') \cdot u(y_2 - y_3') + \rho(y_4') \cdot u(y_1 - y_4')$

$s(y_5) = \rho(y_1') \cdot u(y_5 - y_1') + \rho(y_2') \cdot u(y_4 - y_2') + \rho(y_3') \cdot u(y_3 - y_3') + \rho(y_4') \cdot u(y_2 - y_4') + \rho(y_5') \cdot u(y_1 - y_5')$

$s(y_6) = \rho(y_2') \cdot u(y_5 - y_2') + \rho(y_3') \cdot u(y_4 - y_3') + \rho(y_4') \cdot u(y_3 - y_4') + \rho(y_5') \cdot u(y_2 - y_5')$

$s(y_7) = \rho(y_3') \cdot u(y_5 - y_3') + \rho(y_4') \cdot u(y_4 - y_4') + \rho(y_5') \cdot u(y_3 - y_5')$

$s(y_8) = \rho(y_4') \cdot u(y_5 - y_4') + \rho(y_5') \cdot u(y_4 - y_5')$

$s(y_9) = \rho(y_5') \cdot u(y_5 - y_5')$

135

{Figure 7.9 Conceptual illustration of one-dimensional streak spot formation at detector pixels. In this illustration, it is assumed that 1) the unstreaked spot is imaged on five pixels $(u(y_1), u(y_2), \cdots, u(y_5))$ along y-axis direction and that 2) the unstreaked bunch is composed of five temporal slices (red, orange, yellow, green, and blue columns) with the respective temporal bunch profile, $\rho(y_1'), \rho(y_2')$, $\cdots, \rho(y_5')$. The streak spot profile results from the overlapping of these five deflected slices in space after streaking, which arrives at different pixel locations of the detector. In this example, the resultant streak spot occupies nine detector pixels from $s(y_1)$ to $s(y_9)$, and each fragment of the respective five temporal slices arriving at the same detector pixel position contributes to the accumulation of pixel count at the particular pixel.}

It is intuitive from equation (7.7) that the temporal bunch profile, **d,** is the preliminary information required to extract the time-dependent unstreaked diffraction profile. Experimentally, it can be extracted by streaking static diffraction pattern or the direct beam. With the known **d** by the static measurement and the recorded **s**, the time-dependent diffraction pattern profile, u, is recovered via equation (7.7). Therefore, the rest of this chapter is focused on the computational strategy to extract **d** from the measured static streak spot profile.

In case of the static streak spot, upon the commutative property of convolution operator, the equation (7.5) can be rewritten as:

$$s(y) = \int_{-\infty}^{\infty} u(y') \cdot \rho(y - y')dy' = u * \rho \tag{7.8}$$

Similarly as the case of the time-dependent streak diffraction, the above equation is to be discretized, yielding a matrix equation:

$$\mathbf{s} = A\mathbf{d} \tag{7.9}$$

This equation is a form that the matrix U in equation (7.7) is only replaced by a new matrix A, which is given by

$$\mathbb{A} = \begin{bmatrix} u(y'_1) & 0 & 0 & 0 & \cdots & 0 \\ u(y'_2) & u(y'_1) & 0 & 0 & \cdots & 0 \\ u(y'_3) & u(y'_2) & u(y'_1) & 0 & \cdots & 0 \\ \vdots & u(y'_3) & u(y'_2) & u(y'_1) & \cdots & 0 \\ u(y'_n) & \vdots & u(y'_3) & u(y'_2) & \cdots & 0 \\ 0 & u(y'_n) & \vdots & u(y'_3) & \cdots & 0 \\ 0 & 0 & u(y'_n) & \vdots & \cdots & 0 \\ 0 & 0 & 0 & u(y'_n) & \cdots & \vdots \\ \vdots & \vdots & \vdots & \vdots & \vdots & u(y'_{n-1}) \\ 0 & 0 & 0 & 0 & 0 & u(y'_n) \end{bmatrix}$$

In general, for the given A and $\mathbf{s}$, the easiest way to solve $\mathbf{d}$, is to take the linear least square method that seeks to minimize the sum of square of the difference between the right- and left-hand side term:

$$\min \|\mathbf{Ad} - \mathbf{s}\|^2 \tag{7.10}$$

where, $\| \ \|$ denotes the two-dimensional Euclidean norm. However, solving equation (7.10) is to treat the inverse problem of the discrete linear system, which is typically ill-conditioned due to the absence of an unique solution of $\mathbf{d}$. In this ill-conditioned linear inverse problem, small changes in $s(y)$ and $u(y')$, caused by a measurement noise, gives rise to a large change in the solution $\mathbf{d}$, which is not true. In this regard, finding $\mathbf{d}$ only to minimize the cost function $\|\mathbf{Ad} - \mathbf{s}\|^2$ leads to overfitting in this linear inverse problem, and consequently, the fitted $\mathbf{d}$ does not capture the true charge density profile. To mitigate this numerical artifact in solving equation (7.10), a regularization step is required, which can be achieved by adding a penalty term:

$$\min_{\mathbf{d} \geq 0} \left\{ \|\mathbf{Ad} - \mathbf{s}\|^2 + \gamma \|\mathbf{d}\|^2 \right\} \tag{7.11}$$

where, γ denotes the Tikhonov regularization factor that controls the importance of the penalty term. The constraint, $\mathbf{d} \geq \mathbf{0}$, is introduced to reflect the non-negative charge density in the electron bunch profile. To solve equation (7.11), a useful constraint is imposed additionally: $\mathbf{d}$ is continuous. By setting the second constraint, equation (7.11) is transformed to a well-conditioned problem by applying the gradient descent method, and $\mathbf{d}$ is solved. The detailed mathematical derivation of the gradient descent method is described in Appendix E.

The RMS deviation (= α) of the electron beam spot profiles (shot-to-shot error) can provide the data fidelity to the measured streak and unstreak profiles, which plays an important role to determine the optimal value of γ in the regularization step. α can be typically calculated from multiple unstreaked or streaked images, and once α is obtained, the rest of the regularization process is iterative as illustrated in Figure 7.10. First, an arbitrary value of γ is set, yielding an intermediate solution $\mathbf{d}$ extracted from the deconvolution of streaked profile s with the unstreaked one u. Second, the data extraction error (= δ), evaluated from the RMS of ($\boxed{}\mathbf{d} - \mathbf{s}$) is compared to α. These two steps need to continue until an optimal γ is found such that δ is close to α. By this iterative process, the properly regularized final solution $\mathbf{d}$ is extracted with the data extraction uncertainty of δ. Given that $\mathbf{d}$ is the electron bunch profile, the bunch duration is determined by taking the line width of $\mathbf{d}$.

The last part is to discuss about the temporal resolution, Δτ, in the streak image analysis, especially for the case of electron bunch duration, τ, determination. There are several contributions to the estimation of temporal resolution, associated with computational or experimental errors. The first contribution is the impulse response, $\Delta\tau_{imp}$, of the streak camera. Deconvolution of the unstreaked profile with itself should generate ideally a delta function with a zero line width if γ= 0 (without regularization). However, as a nonzero value of γ is chosen during regularization, the deconvolved profile essentially has the line width with a certain value (= $\Delta\tau_{imp}$), a sort of computational error. The second contribution originates from deconvolution of the streak profile with the unstreaked one. Because the line width of the extracted $\mathbf{d}$ with regularization (γ> 0) is always longer than that of the unregularized one (γ= 0), the former is to be considered as the maximum bunch duration, τ_{max}, calculated by the deconvolution. The latter is denoted by τ_0. Given that the actual bunch length is ranged in between τ_{max} and τ_0, the difference of these two measures (= $\tau_{max} - \tau_0$) has to be admitted as the uncertainty in the determination of the bunch length, also a computational error. The last contribution is related with timing jitter, $\Delta\tau_{jitt}$, of the streak camera. The intensity fluctuation of the photoswitch triggering laser and shear-type misalignment of the streak plates are main sources of $\Delta\tau_{jitt}$. The contribution of this experimental error to temporal resolution is well described in Ref [133], and the typical value of it is less than 100 fs, negligible in the context of subpicosecond resolution in this thesis. Overall, taking into account those contributions, the temporal resolution is estimated by the following relation:

$$\Delta\tau = \Delta\tau_{imp} + (\tau_{max} - \tau_0) + \Delta\tau_{jitt} \qquad (7.12)$$

All the parameters used in equation (7.12) are summarized in Table 7.3.
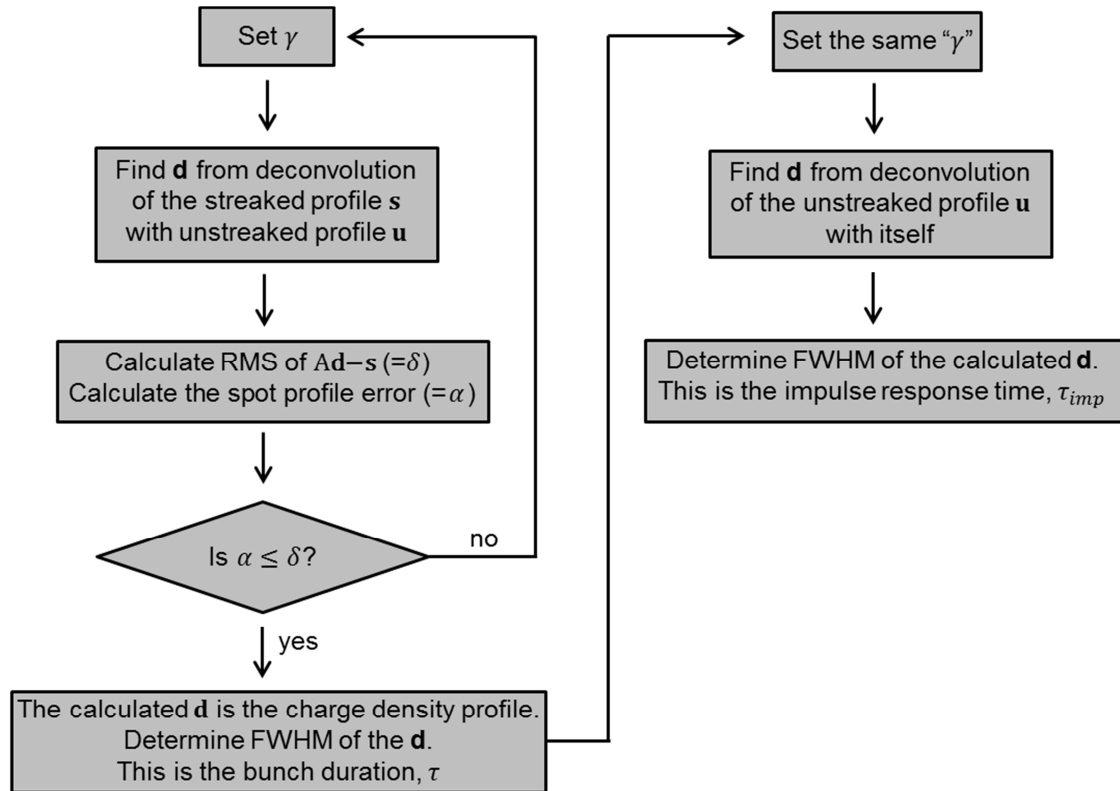
{Figure 7.10. Flowchart of the temporal bunch profile extraction from streak spot image}

parameter	description
τ_{max}	FWHM of the profile extracted from deconvolution of the streaked profile with the unstreaked one with regularization ($\gamma > 0$)
τ_0	FWHM of the profile extracted from deconvolution of the streaked profile with the unstreaked one without regularization ($\gamma = 0$)
$\Delta\tau_{imp}$	FWHM of the profile extracted from deconvolution of the unstreaked profile with itself with regularization ($\gamma > 0$)
$\Delta\tau_{jitt}$	all other measurement errors caused by, for example, timing jitter

{Table 7.3. Parameters necessary to estimate the temporal resolution of the streak camera}

7.6. Static streak diffraction

By exploiting the compact home-built streak camera described ealier in this Section, static streak diffraction is tested. For this test, a suspended graphene sample introduced in section 5.5.5, is placed in between the electron gun and the streak camera. Precise synchronization among the streak camera triggering optical pulse, photoinjection pulse, and high voltage electrical pulse applied to the GaAs photoswith is confirmed as described in section 7.4.
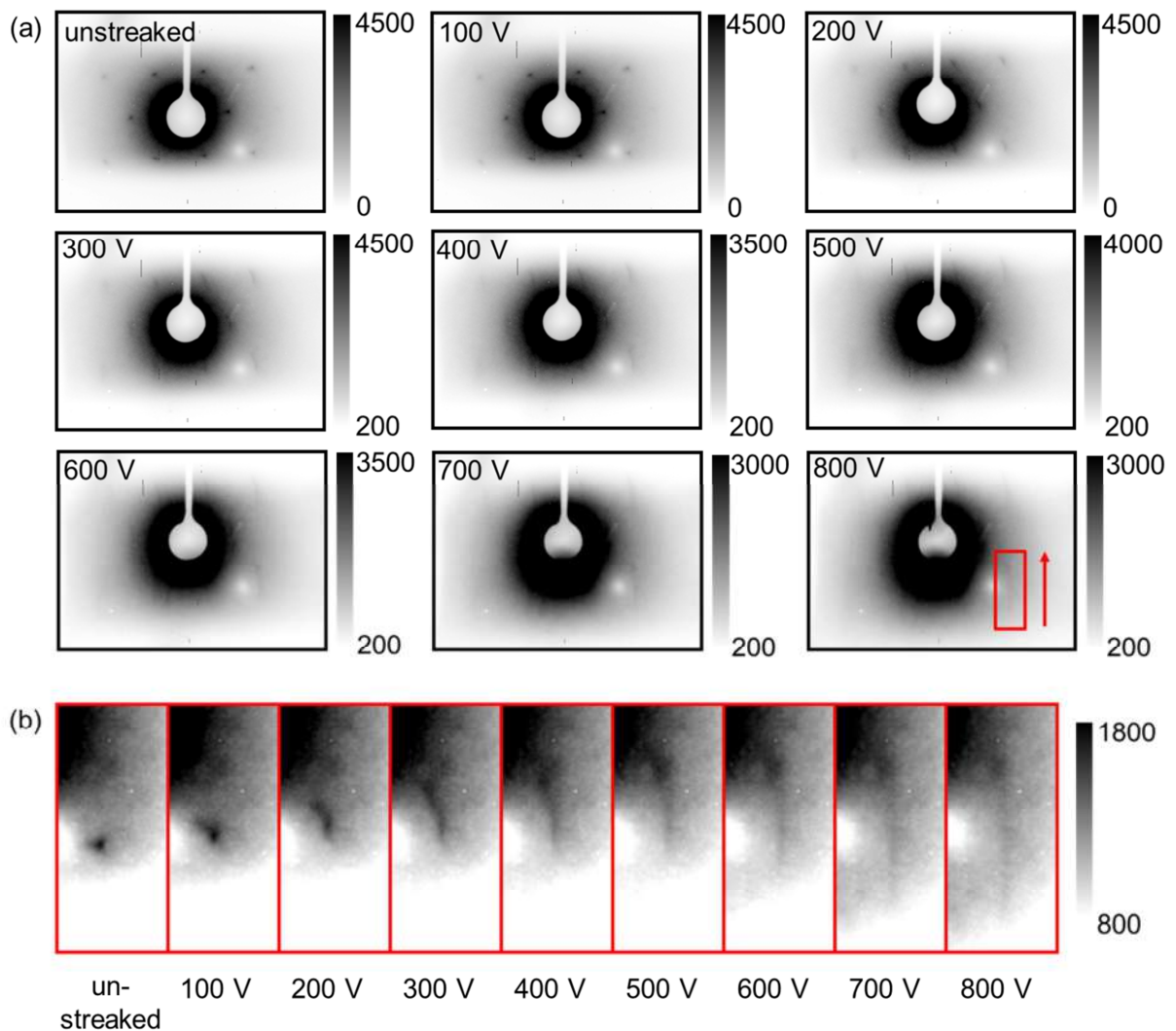
{Figure 7.11. (a) Static streak diffraction of graphene, imaged at different streak plate voltage from 0 (unstreaked) to 800 V. (b) A close-up image on the region of interest defined in the red box in the 800 V image in (a). The red arrow shown in (a) indicates the streak direction.}

The static graphene streak diffraction images as a function of the streak plate voltage are displayed in Figure 7.11. Given by the six-fold symmetry of graphene diffraction, the loss of the two 2nd order diffraction spots (6 and 12 o'clock direction) shown in the all images (Figure 7.11) implies the clipping of these two scattered beams by the upper and lower streak plates of the streak camera. This aperering effect can be avoided by simply increasing the streak plate separation in the further measurement at the expense of the maximum field strength decrease.
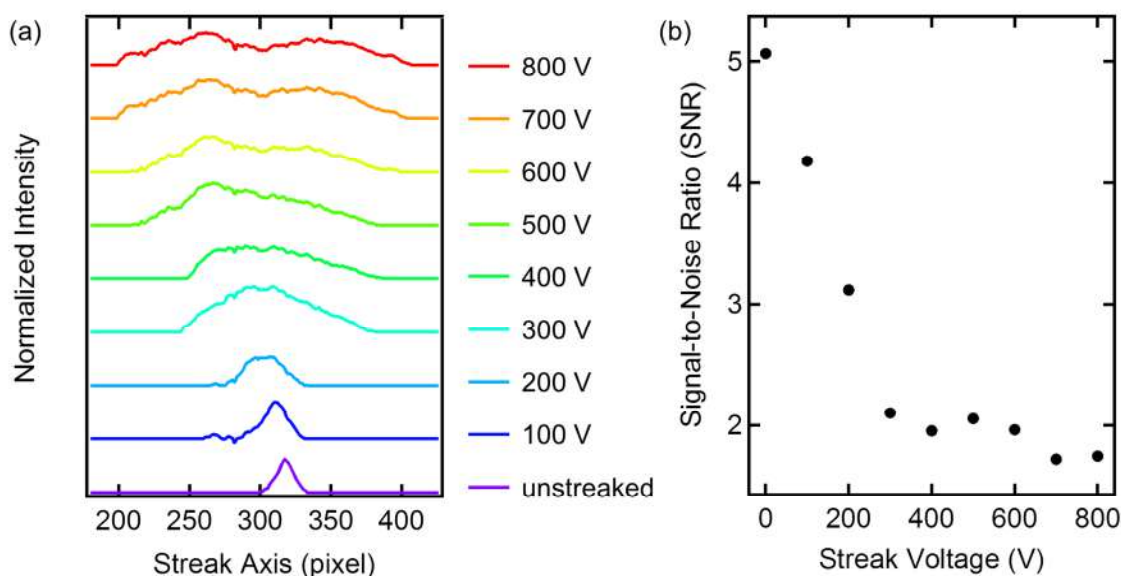
{Figure 7.12. (a) Line profiles of the streak diffraction spot defined the red box in Figure 7.11. (a). The linearly approximated background is subtracted from the raw data profile. (b) Signal-to-noise ratio (SNR) of the line profile as a function of streak voltage.}

From the streak plate voltage dependent diffraction images, it is identified that the diffraction spots are elongated in the streaking direction with the increase of streak plate voltage. For the quantitative analysis, one of the 2nd order spot is selected from the respective image as indicated in the red box in Figure 7.11 (a). By binning the pixel intensity in the perpendicular direction of the streaking axis in the region of interest, the line profile is obtained, as shown in Figure 7.11 (a). Clearly, the line width gradually increases as the streak voltage increases.

At the same time of the elongation, the diffraction spots are smeared out to the background that originates from many factors. One definie factor is the inelastic scattering from graphene, which can possibly be subtracted by a digital processing algorithm used in X-ray protein crystal community [134]. Alternatively, a simple energy filter [135] developed for low-energy electron microscopy can be implemented in the current diffraction beam line to physically remove the inelastic scattering. The camera noise following the Poisson distribution is an intrinsic background.

The signal-to-noise ratio (SNR) of the streak diffraction spot intensity is calculated. For this calculation, the signal and the noise are defined by the peak amplitude and the standard deviation of each integrated line profile in Figure 7.12 (a). As shown in Figure 7.12 (b), the SNR decreases with the increase of streak voltage, which can be understood by the fact that the total number of electrons accumulated to recorde the single streak diffraction image is the same, independent of the streak voltage condition.

7.7. Time-resolved streak diffraction

Some preliminary results of the time-resolved low-energy streak electron diffraction are present in Figure 7.12 (b). The conventional pump-probe unstreaked diffraction images are also displayed toghether Figure 7.12 (a)). All the displayed images in Figure 7.12 are the intensity difference map obtained by the subtraction of the pumped image from the unpumped one at a certain time delay Δt. For the comparison between the two methodes, two 2nd order diffraction spots (indicated by the red boxes in the images) are chosen from which the line profiles are extracted after pixel binning as similarly as done in the static streak diffraction case in section 7.6. This simple line profile comparison (Figure 7.7 (c) and (d)) already underlines the feasibility of the time-resolved streak diffraction with ultrafast low-energy electrons. A further deconvolution analysis to extract the electron density profile and to determine the temporal resolution is still ongoing.
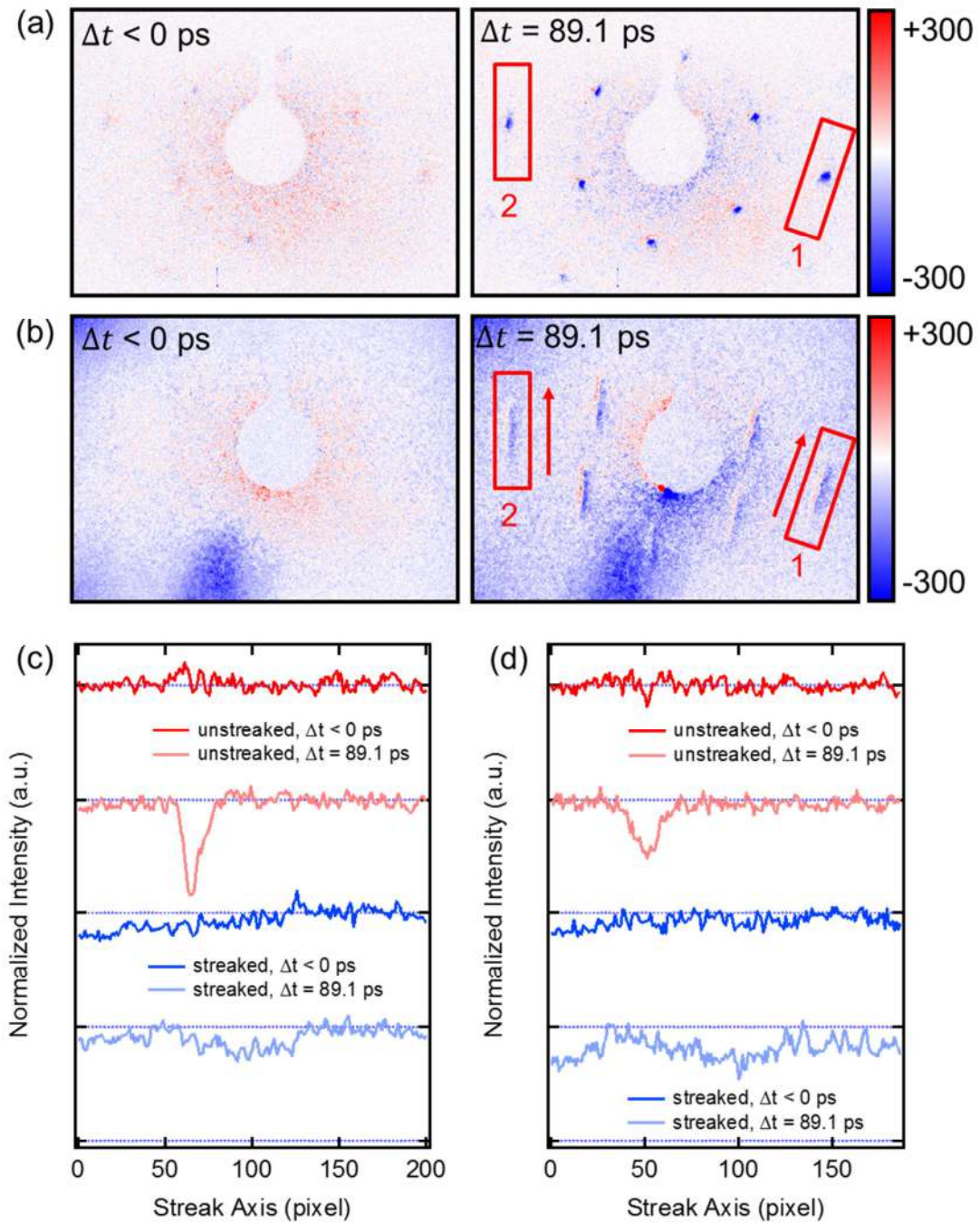
{Figure 7.13. (a) Intensity difference map of the conventional pump-probe low-energy diffraction. Left and right panels show the intensity map before and after $\Delta t = 0$, respectively. (b) Intensity difference map of the pump-probe low-energy streak diffraction. Line profiles extracted from the region-on-interest indicated by the red box 1 (c) and the box 2 (d) shown in each panel.}

143

8. Outlook

Further to the experimental and simulation results presented in the previouse Chapters, there exists plenty of room to improve the electron source and setup performance required for the investigation of new types of sample systems. The ideas are challenging but interesting and feasible.

First of all, the implementation of the photoswitch developed for the streak camera operation to the double-gate field emitter (Chapter 3) will allow the use of this device in an ultrafast mode. Because of the few micrometer sized extraction and collimation aperture size of the device in its current design, direct femtosecond laser illumination on the nanotip apex is quite challenging. Experimentally, multiphoton induced electron emission generated *not from* the nanotip apex *but from* aperture layers is observed with the direct excitation due to the possible imprecise alignment and a larger beam size. Instead of this method, femtosecond laser triggering of the photoswith electrically connected to either the gate or the emitter plate will provide a picosecond switching time of the gate-emitter potential on the device.

Second, visible or IR laser induced single photon photoemission triggering of the fiber-based photocathode (Chapter 3) will enable to use this source with less photodegradation. The so-called solarization effect of the fiber is more significant in UV regime than visible or IR such that the operation time and the generated electron beam current of the fiber photocathode are limited. Experimentally, the solarization effect can be clearly identified by measuring the output power of the fiber as a function of time at a fixed input laser power, as shown in Figure 8.1. After about 2 hours of the measurement, 20 – 40 % of the output power remains at a saturated power level, depending on the intial input power. Once the fiber is damaged, the output power cannot be recovered to the initial level, and the condition deteriorates. One possible solution for this issue is to exploit a thin film having a lower workfunction as the cathode layer on the fiber. LaB6 thin film is an ideal candidate for this purpose because of its workfunction ranged in 2.3 – 3.2 eV [136,137,138]. Alternatively, graphene coated Ni thin film is recently reported to have an ultralow workfunction of 1.1 eV [139]. In this case, Ni substrate provides free electrons to graphene to equilibrate the electron density between the graphene and Ni, increasing the density of states of graphene. As a result, the Fermi level of graphene increases, giving rise to the concomitant decrease of graphene workfunction. These two approaches enabling the visible or IR drivien fiber photocathode are currently under study.

Third, the electron bunch compressor concept [90] exploiting the GaAs photoswith can be implemented to the present low-energy electron gun, which will possibily reduce the bunch length upto one order of magnitude. By applying a transient electric field in parallel to the electron beam

propagation direction, a broadened electron bunch can be temporally focused at the diffraction target. The required electrical and mechanical components can be easily adapted to the current gun design, keeping the compact gun geometry. The implementation of the compressor will improve the temporal resolution of the conventional stroboscopic pump-probe diffraction with ultrafast low-energy electrons.
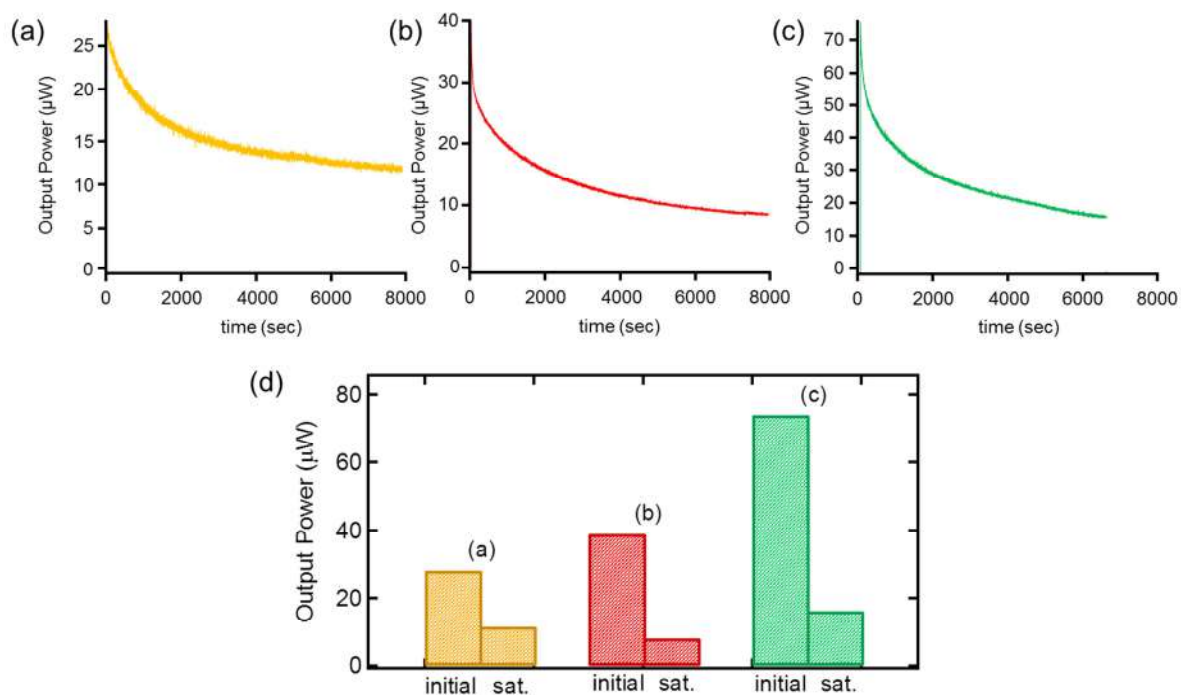
{Figure 8.1. Fiber Solarization. The output intensity of the fiber is measured as a function of time. The initial output power at 0 sec is 28 μW (a), 38.9 μW (b), and 74 μW (c), respectively. (d) The comparison of the initial and saturated output power for (a), (b), (c) cases, indicating a clear output power drop.}

On the setup development side, currently, the next generation time-resolved LEED setup in the normal-incidence backscattering geometry is under construction. The most critical challenge in this setup construction is the electron gun part. To avoid the shadowing of the backscattered beams by the electron gun while keeping the source-to-sample distance short to minimize the bunch broadening, the entire gun size is required to be small. The current electron gun design features an about 1.2 mm gun diameter including an electric field shilding cover, expected to generate a highly focused electron beam at the diffraction sample placed 2-3 mm from the gun exit. Since the conventional photocathode is planned to be used in the electron gun, the number of electrons per bunch is expected to reach maximally $10^5 - 10^6$, opening the possibility to investigate structure dynamics of irreversible systems with ultrafast low-energy elecrons.
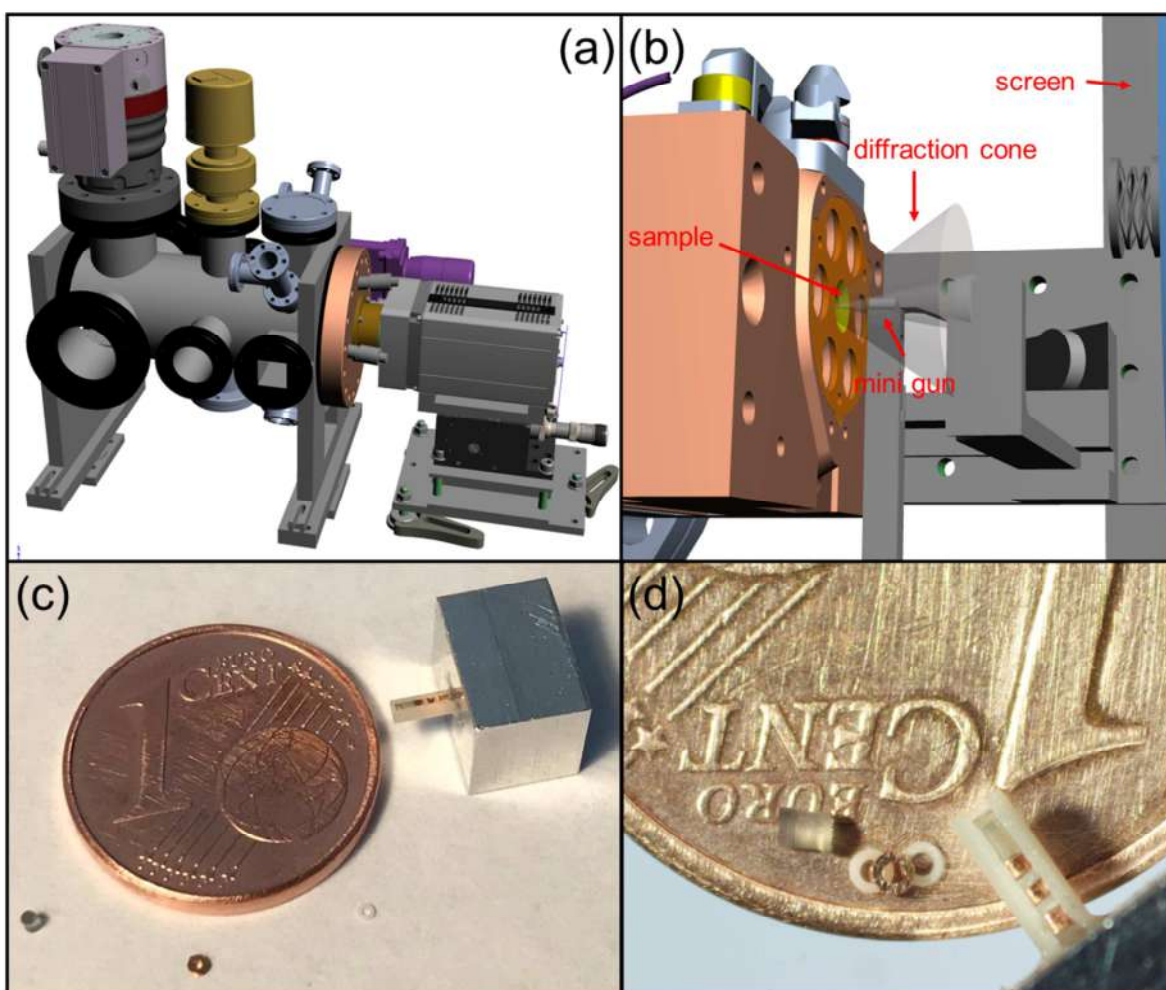
{Figure 8.2. The second time-resolved LEED setup in the normal-incidence backscattering gemoery. (a), (b) The CAD model of the entire setup. (c), (d) Miniaturized electron gun to be used in the setup.}

Apart from the technical side, some interesting heterogeneouse systems that require the surface-sensitivity of the structural probe are planned to be investigated with the current setup. One of the most interesting systems is the H_2O adsorbed TiO_2 surface, well-known for its photocatalytic ability in water splitting or hydrogen production [140]. Even though many works have been focused on what forms of water exist on the surface and what are the factors governing the adsorption behavior, the structural evolution of the adsorbate and the substrate after photoexciation is still questionable. The time-resolved LEED is an ideal tool for this study in that the setup can provide relavent spatial and temporal resolution. In addition, water-freestanding graphene combination is an interesting system to investigate. Monolayer freestanding graphene has attracted attention from electron microscopiest for the use of this material as a liquid cell window in a UHV environemennt, merited by the material's transperenet property with electrons. When graphene is in contact with the water layer, investigating the formation of thermal equilibrium between the two substrates, known for the highest (in plane) thermal conductivity and the largest heat capacity, respectively, and tracking the

146

following structure evolution in time will be interesting topic. Lastly, Van der Waals heterostructures is worthwhile to be mentioned. Many exotic behabior such as (electronic driven) phase transition and etc in the two-dimensional system can be monitored with ultrafast low-energy electrons.

The above problems to be addressed with the new electron source technology developed in this thesis cover such an impression of the great advance that will be forthcoming in catalysis, surface reaction dynamics, and nanoscale control of material properties. We now have a new pair of atomic glasses through which to see nature in action more clearly.

9. References

1   G.A. Somorjai and Y. Li, Proceedings of the National Academy of Sciences **108**(3), 917 (2011).

2   M. Boudart, Journal of molecular catalysis **30**(1-2), 27 (1985).

3   R.J.D. Miller, Science **343**(6175), 1108 (2014).

4   A.H. Zewail, Science **242**(4886), 1645 (1988).

5   T. Van Oudheusden, P. Pasmans, S. Van Der Geer, M. De Loos, M. Van Der Wiel, and O. Luiten, Physical review letters **105**(26), 264801 (2010).

6   B.J. Siwick, J.R. Dwyer, R.E. Jordan, and R.D. Miller, Journal of Applied Physics **92**(3), 1643 (2002).

7   I. Schapiro, M.N. Ryazantsev, L.M. Frutos, N. Ferré, R. Lindh, and M. Olivucci, Journal of the American Chemical Society **133**(10), 3354 (2011).

8   M.R. Otto, L. René de Cotret, M.J. Stern, and B.J. Siwick, Structural Dynamics **4**(5), 051101 (2017).

9   Y. Morimoto and P. Baum, Nature Physics **14**(3), 252 (2018).

10 S. Weathersby, G. Brown, M. Centurion, T. Chase, R. Coffee, J. Corbett, J. Eichner, J. Frisch, A. Fry, and M. Gühr, Review of Scientific Instruments **86**(7), 073702 (2015).

11 M. Krüger, M. Schenk, and P. Hommelhoff, Nature **475**(7354), 78 (2011).

12 S. Vogelgesang, G. Storeck, J. Horstmann, T. Diekmann, M. Sivis, S. Schramm, K. Rossnagel, S. Schäfer, and C. Ropers, Nature Physics **14**(2), 184 (2018).

13 S. Boutet, L. Lomb, G.J. Williams, T.R. Barends, A. Aquila, R.B. Doak, U. Weierstall, D.P. DePonte, J. Steinbrener, and R.L. Shoeman, Science **337**(6092), 362 (2012).

14 W. Qian, M. Scheinfein, and J. Spence, Journal of applied physics **73**(11), 7041 (1993).

15 J. Buon, 1992.

16 M. Hachmann,   (2012).

17 M. Reiser, *Theory and design of charged particle beams*. (John Wiley & Sons, 2008).

18 K. Floettmann, Physical Review Special Topics-Accelerators and Beams **6**(3), 034202 (2003).

19 P. Baum, Chemical Physics **423**, 55 (2013).

20 D. Ehberger, J. Hammer, M. Eisele, M. Krüger, J. Noe, A. Högele, and P. Hommelhoff, Physical review letters **114**(22), 227601 (2015).

21 C. Gerbig, A. Senftleben, S. Morgenstern, C. Sarpe, and T. Baumert, New Journal of Physics **17**(4), 043050 (2015).

22 J. Spence, U. Weierstall, and M. Howells, Ultramicroscopy **101**(2-4), 149 (2004).

23   D.H. Dowell and J.F. Schmerge, Physical Review Special Topics-Accelerators and Beams **12**(7), 074201 (2009).

24   G.N. Fursey, *Field emission in vacuum microelectronics*. (Springer Science & Business Media, 2007).

25   R.G. Forbes and J.H. Deane, Proceedings of the Royal Society A: Mathematical, Physical and Engineering Sciences **463**(2087), 2907 (2007).

26   R.G. Forbes, Journal of Vacuum Science & Technology B: Microelectronics and Nanometer Structures Processing, Measurement, and Phenomena **17**(2), 526 (1999).

27   R.G. Forbes, Applied Physics Letters **92**(19), 193105 (2008).

28   C. Lee, P.D. Kanungo, V. Guzenko, P. Hefenstein, R.D. Miller, and S. Tsujino, Journal of Vacuum Science & Technology B, Nanotechnology and Microelectronics: Materials, Processing, Measurement, and Phenomena **33**(3), 03C111 (2015).

29   W.E. Spicer and A. Herrera-Gomez, presented at the Photodetectors and Power Meters, 1993 (unpublished).

30   H.-W. Fink, Physica Scripta **38**(2), 260 (1988).

31   P. Hommelhoff, Y. Sortais, A. Aghajani-Talesh, and M.A. Kasevich, Physical review letters **96**(7), 077401 (2006).

32   C. Ropers, D. Solli, C. Schulz, C. Lienau, and T. Elsaesser, Physical review letters **98**(4), 043907 (2007).

33   S. Tsujino, P. Beaud, E. Kirk, T. Vogel, H. Sehr, J. Gobrecht, and A. Wrulich, Applied Physics Letters **92**(19), 193501 (2008).

34   A. Crewe, D. Eggenberger, J. Wall, and L. Welter, Review of Scientific Instruments **39**(4), 576 (1968).

35   H. Zhang, J. Tang, J. Yuan, Y. Yamauchi, T.T. Suzuki, N. Shinya, K. Nakajima, and L.-C. Qin, Nature nanotechnology **11**(3), 273 (2016).

36   G. Storeck, S. Vogelgesang, M. Sivis, S. Schäfer, and C. Ropers, Structural Dynamics **4**(4), 044024 (2017).

37   C. Spindt, C. Holland, A. Rosengreen, and I. Brodie, IEEE Transactions on Electron Devices **38**(10), 2355 (1991).

38   C. Spindt, C. Holland, A. Rosengreen, and I. Brodie, Journal of Vacuum Science & Technology B: Microelectronics and Nanometer Structures Processing, Measurement, and Phenomena **11**(2), 468 (1993).

39   P. Schwoebel, C. Spindt, and C. Holland, Journal of Vacuum Science & Technology B: Microelectronics and Nanometer Structures Processing, Measurement, and Phenomena **21**(1), 433 (2003).

40   C. Spindt, I. Brodie, L. Humphrey, and E. Westerberg, Journal of Applied Physics **47**(12), 5248 (1976).

41   C. Lee, S. Tsujino, and R.D. Miller, Applied Physics Letters **113**(1), 013505 (2018).

42   E. Kirk, S. Tsujino, T. Vogel, K. Jefimovs, J. Gobrecht, and A. Wrulich, Journal of Vacuum Science & Technology B: Microelectronics and Nanometer Structures Processing, Measurement, and Phenomena **27**(4), 1813 (2009).

43   P. Helfenstein, V. Guzenko, H.-W. Fink, and S. Tsujino, Journal of Applied Physics **113**(4), 043306 (2013).

44   W.P. Dyke and J. Trolan, Physical Review **89**(4), 799 (1953).

45   C. Brau, Nuclear Instruments and Methods in Physics Research Section A: Accelerators, Spectrometers, Detectors and Associated Equipment **407**(1-3), 1 (1998).

46   H. Yanagisawa, C. Hafner, P. Doná, M. Klöckner, D. Leuenberger, T. Greber, M. Hengsberger, and J. Osterwalder, Physical review letters **103**(25), 257603 (2009).

47   P. Helfenstein, A. Mustonen, T. Feurer, and S. Tsujino, Applied Physics Express **6**(11), 114301 (2013).

48   S. Tsujino, M. Paraliev, E. Kirk, T. Vogel, F. Le Pimpec, C. Gough, S. Ivkovic, and H.-H. Braun, Journal of Vacuum Science & Technology B, Nanotechnology and Microelectronics: Materials, Processing, Measurement, and Phenomena **29**(2), 02B117 (2011).

49   Y. Neo, M. Takeda, T. Soda, M. Nagao, T. Yoshida, S. Kanemaru, T. Sakai, K. Hagiwara, N. Saito, and T. Aoki, Journal of Vacuum Science & Technology B: Microelectronics and Nanometer Structures Processing, Measurement, and Phenomena **27**(2), 701 (2009).

50   C. Tang, M. Goldstein, T. Swyden, and J. Walsh, Nuclear Instruments and Methods in Physics Research Section A: Accelerators, Spectrometers, Detectors and Associated Equipment **358**(1-3), 7 (1995).

51   P. Helfenstein, K. Jefimovs, E. Kirk, C. Escher, H.-W. Fink, and S. Tsujino, Journal of Applied Physics **112**(9), 093307 (2012).

52   V.A. Guzenko, A. Mustonen, P. Helfenstein, E. Kirk, and S. Tsujino, Microelectronic engineering **111**, 114 (2013).

53   M. Dehler, A. Candel, and E. Gjonaj, Journal of Vacuum Science & Technology B: Microelectronics and Nanometer Structures Processing, Measurement, and Phenomena **24**(2), 892 (2006).

54   Y. Ding, A. Brachmann, F.-J. Decker, D. Dowell, P. Emma, J. Frisch, S. Gilevich, G. Hays, P. Hering, and Z. Huang, Physical review letters **102**(25), 254801 (2009).

55   A. Mustonen, V. Guzenko, C. Spreu, T. Feurer, and S. Tsujino, Nanotechnology **25**(8), 085203 (2014).

56   R. Henderson, Quarterly reviews of biophysics **28**(2), 171 (1995).

57   A.A. Ischenko, P.M. Weber, and R.D. Miller, Chemical reviews **117**(16), 11066 (2017).

58   Y. Fujiyoshi, Advances in biophysics **35**, 25 (1998).

59   J.C. Spence, *High-resolution electron microscopy*. (OUP Oxford, 2013).

60   J.W. Gadzuk and E. Plummer, Reviews of Modern Physics **45**(3), 487 (1973).

61   S. Tsujino, P.D. Kanungo, M. Monshipouri, C. Lee, and R.D. Miller, Nature communications **7**, 13976 (2016).

62   A. Feist, N. Bach, N.R. da Silva, T. Danz, M. Möller, K.E. Priebe, T. Domröse, J.G. Gatzmann, S. Rost, and J. Schauss, Ultramicroscopy **176**, 63 (2017).

63   A. Paarmann, M. Gulde, M. Müller, S. Schäfer, S. Schweda, M. Maiti, C. Xu, T. Hohage, F. Schenk, and C. Ropers, Journal of Applied Physics **112**(11), 113109 (2012).

64   M. Gulde, S. Schweda, G. Storeck, M. Maiti, H.K. Yu, A.M. Wodtke, S. Schäfer, and C. Ropers, Science **345**(6193), 200 (2014).

65   M. Müller, A. Paarmann, and R. Ernstorfer, Nature communications **5**, 5292 (2014).

66   T. Latychevskaia, F. Wicki, C. Escher, and H.-W. Fink, Ultramicroscopy **182**, 276 (2017).

67   S. Tsujino, Journal of Applied Physics **124**(4), 044304 (2018).

68   P. Helfenstein, E. Kirk, K. Jefimovs, T. Vogel, C. Escher, H.-W. Fink, and S. Tsujino, Applied Physics Letters **98**(6), 061502 (2011).

69   W.E. King, G.H. Campbell, A. Frank, B. Reed, J.F. Schmerge, B.J. Siwick, B.C. Stuart, and P.M. Weber, Journal of Applied Physics **97**(11), 8 (2005).

70   U.K. Genick, G.E. Borgstahl, K. Ng, Z. Ren, C. Pradervand, P.M. Burke, V. Šrajer, T.-Y. Teng, W. Schildkamp, and D.E. McRee, Science **275**(5305), 1471 (1997).

71   A. Aquila, M.S. Hunter, R.B. Doak, R.A. Kirian, P. Fromme, T.A. White, J. Andreasson, D. Arnlund, S. Bajt, and T.R. Barends, Optics express **20**(3), 2706 (2012).

72   J. Tenboer, S. Basu, N. Zatsepin, K. Pande, D. Milathianaki, M. Frank, M. Hunter, S. Boutet, G.J. Williams, and J.E. Koglin, Science **346**(6214), 1242 (2014).

73   S. Tsujino and M. Paraliev, Journal of Vacuum Science & Technology B, Nanotechnology and Microelectronics: Materials, Processing, Measurement, and Phenomena **32**(2), 02B103 (2014).

74   A. Mustonen, P. Beaud, E. Kirk, T. Feurer, and S. Tsujino, Applied physics letters **99**(10), 103504 (2011).

75   G.H. Kassier, K. Haupt, N. Erasmus, E. Rohwer, H. Von Bergmann, H. Schwoerer, S.M. Coelho, and F.D. Auret, Review of Scientific Instruments **81**(10), 105103 (2010).

76   J.R. Dwyer, R.E. Jordan, C.T. Hebeisen, M. Harb, R. Ernstorfer, T. Dartigalongue, and R. Dwayne Miller, Journal of Modern Optics **54**(7), 923 (2007).

77 C. Kealhofer, S. Lahme, T. Urban, and P. Baum, Ultramicroscopy **159**, 19 (2015).

78 R. Li, W. Huang, Y. Du, L. Yan, Q. Du, J. Shi, J. Hua, H. Chen, T. Du, and H. Xu, Review of Scientific Instruments **81**(3), 036110 (2010).

79 P. Musumeci, J. Moody, C. Scoby, M. Gutierrez, M. Westfall, and R. Li, Journal of Applied Physics **108**(11), 114513 (2010).

80 D. Zhang, A. Fallahi, M. Hemmer, X. Wu, M. Fakhari, Y. Hua, H. Cankaya, A.-L. Calendron, L.E. Zapata, and N.H. Matlis, Nature photonics **12**(6), 336 (2018).

81 C. Lee, G. Kassier, and R.D. Miller, Applied Physics Letters **113**(13), 133502 (2018).

82 J. Cao, Z. Hao, H. Park, C. Tao, D. Kau, and L. Blaszczyk, Applied physics letters **83**(5), 1044 (2003).

83 B.J. Siwick, J.R. Dwyer, R.E. Jordan, and R.D. Miller, Science **302**(5649), 1382 (2003).

84 R. Ernstorfer, M. Harb, C.T. Hebeisen, G. Sciaini, T. Dartigalongue, and R.D. Miller, Science **323**(5917), 1033 (2009).

85 G. Sciaini, M. Harb, S.G. Kruglik, T. Payer, C.T. Hebeisen, F.-J.M. zu Heringdorf, M. Yamaguchi, M. Horn-von Hoegen, R. Ernstorfer, and R.D. Miller, Nature **458**(7234), 56 (2009).

86 M. Eichberger, H. Schäfer, M. Krumova, M. Beyer, J. Demsar, H. Berger, G. Moriena, G. Sciaini, and R.D. Miller, Nature **468**(7325), 799 (2010).

87 M. Gao, C. Lu, H. Jean-Ruel, L.C. Liu, A. Marx, K. Onda, S.-y. Koshihara, Y. Nakano, X. Shao, and T. Hiramatsu, Nature **496**(7445), 343 (2013).

88 T. Ishikawa, S.A. Hayes, S. Keskin, G. Corthey, M. Hada, K. Pichugin, A. Marx, J. Hirscht, K. Shionuma, and K. Onda, Science **350**(6267), 1501 (2015).

89 T. Van Oudheusden, E. De Jong, S. Van der Geer, W.O. 't Root, O. Luiten, and B. Siwick, Journal of Applied Physics **102**(9), 093501 (2007).

90 G. Kassier, N. Erasmus, K. Haupt, I. Boshoff, R. Siegmund, S. Coelho, and H. Schwoerer, Applied Physics B **109**(2), 249 (2012).

91 D.S. Badali and R. Dwayne Miller, Structural Dynamics **4**(5), 054302 (2017).

92 C. Frischkorn and M. Wolf, Chemical reviews **106**(10), 4207 (2006).

93 M. Muller, A. Paarmann, and R. Ernstorfer, Nat Commun **5**, 5292 (2014).

94 M. Eichberger, N. Erasmus, K. Haupt, G. Kassier, A. von Flotow, J. Demsar, and H. Schwoerer, Applied physics letters **102**(12), 121106 (2013).

95 A. Căsăndruc, R. Bücker, G. Kassier, and R.D. Miller, Applied Physics Letters **109**(9), 091105 (2016).

96 http://www.cst.com.

97   M. van Mourik, W. Engelen, E. Vredenbregt, and O. Luiten, Structural Dynamics **1**(3), 034302 (2014).

98   http://www.desy.de/~mpyflo/.

99   B.E. Saleh and M.C. Teich, *Fundamentals of photonics*. (John Wiley & Sons, 2019).

100   E. Marcatili, The Bell System Technical Journal **56**(1), 49 (1977).

101   A. Janzen, B. Krenzer, O. Heinz, P. Zhou, D. Thien, A. Hanisch, F.-J. Meyer zu Heringdorf, D. Von Der Linde, and M. Horn von Hoegen, Review of scientific instruments **78**(1), 013906 (2007).

102   J. Williams, Journal of Physics B: Atomic and Molecular Physics **8**(13), 2191 (1975).

103   W.H. Bragg and W.L. Bragg, Proceedings of the Royal Society of London. Series A, Containing Papers of a Mathematical and Physical Character **88**(605), 428 (1913).

104   P. Ewald, Acta Crystallographica Section A: Crystal Physics, Diffraction, Theoretical and General Crystallography **25**(1), 103 (1969).

105   M.P. Seah and W. Dench, Surface and interface analysis **1**(1), 2 (1979).

106   J. Henk, in *Handbook of Thin Films* (Elsevier, 2002), pp. 479.

107   M. Aidelsburger, F.O. Kirchner, F. Krausz, and P. Baum, Proceedings of the National Academy of Sciences **107**(46), 19714 (2010).

108   S. Horiuchi, T. Gotou, M. Fujiwara, T. Asaka, T. Yokosawa, and Y. Matsui, Applied physics letters **84**(13), 2403 (2004).

109   J. Hu, G.M. Vanacore, A. Cepellotti, N. Marzari, and A.H. Zewail, Proceedings of the National Academy of Sciences **113**(43), E6555 (2016).

110   K.S. Novoselov, A.K. Geim, S.V. Morozov, D. Jiang, Y. Zhang, S.V. Dubonos, I.V. Grigorieva, and A.A. Firsov, Science **306**(5696), 666 (2004).

111   R.R. Nair, P. Blake, A.N. Grigorenko, K.S. Novoselov, T.J. Booth, T. Stauber, N.M. Peres, and A.K. Geim, Science **320**(5881), 1308 (2008).

112   D.M. Riffe, X. Wang, M.C. Downer, D. Fisher, T. Tajima, J. Erskine, and R. More, JOSA B **10**(8), 1424 (1993).

113   S. Anisimov, B. Kapeliovich, and T. Perelman, Zh. Eksp. Teor. Fiz **66**(2), 375 (1974).

114   H. Elsayed-Ali, T. Norris, M. Pessot, and G. Mourou, Physical Review Letters **58**(12), 1212 (1987).

115   W. Fann, R. Storz, H. Tom, and J. Bokor, Physical Review B **46**(20), 13592 (1992).

116   G. Eesley, Physical Review B **33**(4), 2144 (1986).

117   J. Fujimoto, J. Liu, E. Ippen, and N. Bloembergen, Physical Review Letters **53**(19), 1837 (1984).

118   R. Schoenlein, W. Lin, J. Fujimoto, and G. Eesley, Physical Review Letters **58**(16), 1680 (1987).

119   G. Farkas, Z. Naray, and P. Varga, Physics Letters A **24**(2), 134 (1967).

120   E. Logothetis and P. Hartman, Physical Review Letters **18**(15), 581 (1967).

121   G. Farkas, Z.G. Horváth, I. Kertész, and G. Kiss, Lettere Al Nuovo Cimento (1971–1985) **1**(8), 314 (1971).

122   G. Farkas, Z.G. Horváth, and I. Kertész, Physics Letters A **39**(3), 231 (1972).

123   J. Bechtel, W. Smith, and N. Bloembergen, Optics Communications **13**(1), 56 (1975).

124   M. Murnane, H. Kapteyn, and R. Falcone, Physical review letters **62**(2), 155 (1989).

125   H. Park and J.-M. Zuo, Applied Physics Letters **94**(25), 251103 (2009).

126   S. Schäfer, W. Liang, and A.H. Zewail, Chemical Physics Letters **493**(1-3), 11 (2010).

127   C.-Y. Ruan, V.A. Lobastov, F. Vigliotti, S. Chen, and A.H. Zewail, Science **304**(5667), 80 (2004).

128   D.-S. Yang and A.H. Zewail, Proceedings of the National Academy of Sciences **106**(11), 4122 (2009).

129   E. Pop, V. Varshney, and A.K. Roy, MRS bulletin **37**(12), 1273 (2012).

130   M. Fox,   (AAPT, 2002).

131   C.S. Allen, E. Liberti, J.S. Kim, Q. Xu, Y. Fan, K. He, A.W. Robertson, H.W. Zandbergen, J.H. Warner, and A.I. Kirkland, Journal of Applied Physics **118**(7), 074302 (2015).

132   D.S. Badali, Universität Hamburg Hamburg, 2016.

133   G.H. Kassier, Stellenbosch: University of Stellenbosch, 2010.

134   R. Fraser, T. Macrae, E. Suzuki, and P. Tulloch, Journal of Applied Crystallography **10**(1), 64 (1977).

135   R. Tromp, Y. Fujikawa, J. Hannon, A. Ellis, A. Berghaus, and O. Schaff, Journal of Physics: Condensed Matter **21**(31), 314007 (2009).

136   C. Oshima, S. Horiuchi, and S. Kawai, Japanese Journal of Applied Physics **13**(S1), 281 (1974).

137   L. Swanson, M. Gesley, and P. Davis, Surface Science **107**(1), 263 (1981).

138   H. Yamauchi, K. Takagi, I. Yuito, and U. Kawabe, Applied Physics Letters **29**(10), 638 (1976).

139   X. Shao, A. Srinivasan, W.K. Ang, and A. Khursheed, Nature communications **9**(1), 1288 (2018).

140   A.L. Linsebigler, G. Lu, and J.T. Yates Jr, Chemical reviews **95**(3), 735 (1995).
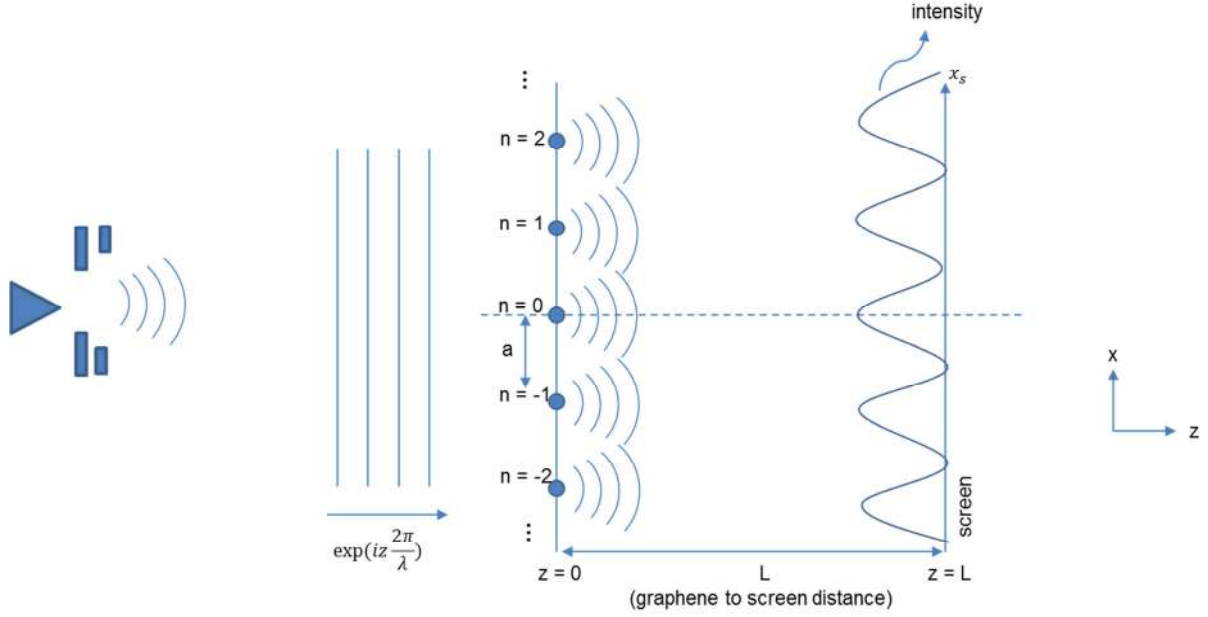
10. Appendices

Appendix A.
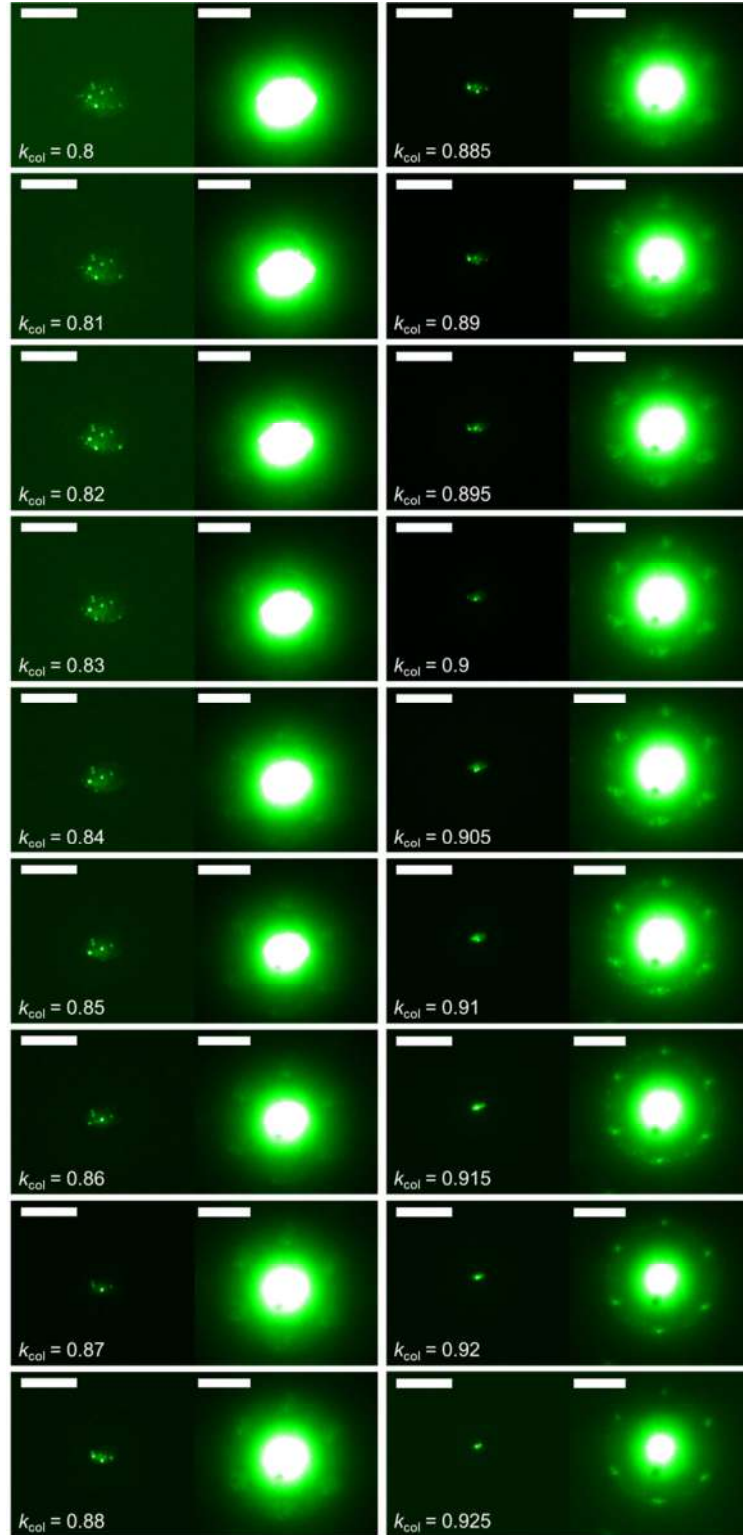
Display of direct beam and diffraction spot images in the range of k_{col} from 0.8 to 0.925.

Appendix B.

Derivation of transverse coherence length of collimated electron beam generated by double-gate nanotip field emitter from monolayer graphene diffraction image

I. perfect coherence case

We assume the incident electron beam on the graphene position (z=0) as the random summation of plane wave packets.

$$\Psi(z, x) = \exp(ikz)\sum_s \psi(x - x_s) \tag{B1}$$

nth carbon atom emits spherical wavefunction ψ_n

$$\psi_n = a_\theta(\theta)\frac{\exp(i|r - r_n|\frac{2\pi}{\lambda})}{|r - r_n|} \tag{B2}$$

where, $a_\theta(\theta)$ is the electron elastic scattering cross-section, $r_n = \begin{pmatrix} na \\ 0 \\ 0 \end{pmatrix}$, a is the graphene unit cell.

On the screen at $r_s = \begin{pmatrix} x_s \\ 0 \\ L \end{pmatrix}$, the total intensity is

$$S(x_s) = \left| \sum_{n=-\infty}^{+\infty} a_\theta \frac{\exp(i|r_s - r_n|\frac{2\pi}{\lambda})}{|r_s - r_n|} \right|^2 \tag{B3}$$

When $L \gg na$,

$$S(x_s) \cong \frac{1}{L^2} \left| \sum_{n=-\infty}^{+\infty} a_\theta(\theta) \exp(i|r_s - r_n|\frac{2\pi}{\lambda}) \right|^2 \tag{B4}$$

Simplification of $|r_s - r_n|$ part of the exponential term of equation B4 yields

$$|r_s - r_n| = \sqrt{L^2 + (x_s - na)^2} = \sqrt{L^2 + x_s^2 + (na)^2 - 2x_s na} = L(1 - \frac{nx_s a}{L^2})$$

Then, equation B4 can be further simplified.

$$S(x_s) \cong \frac{1}{L^2} \left| \sum_{n=-\infty}^{+\infty} a_\theta(\theta) \exp(i\frac{2\pi}{\lambda} L(1 - \frac{nx_s a}{L^2})) \right|^2$$

$$= \frac{1}{L^2} a_\theta^2(\theta) \left| \sum_{n=-\infty}^{+\infty} \exp(-i\frac{2\pi}{\lambda}\frac{nx_s a}{L}) \right|^2 \tag{B5}$$

II. Partial coherence case with finite coherence length x_c

We assume the incident electron beam on the graphene position (z=0) as the random summation of Gaussian wave packets with the rms transverse momentum of σ_p and corresponding rms transverse coherence length of x_c.

$$\psi_n \sim \int dp \exp(-\frac{p^2}{2\sigma_p^2}) \exp(\frac{ipx}{\hbar}) = const. \times \exp(-\frac{x^2}{2x_c^2}) \tag{B6}$$

Equation B5 and B6 will give the total intensity at the screen (z=L) in case of partial coherence. We take into account only the phase factor of the total intensity.
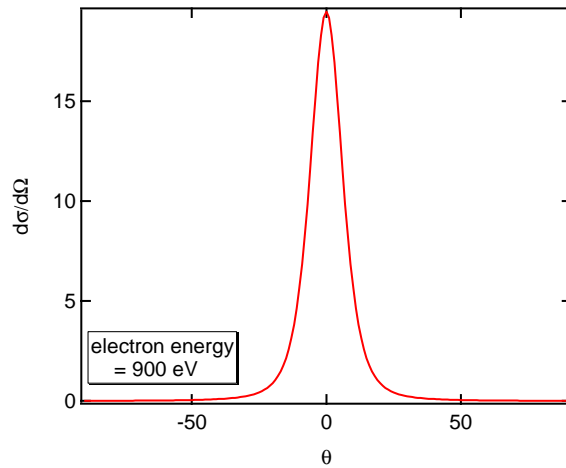
$$S(x_s, x_s) \sim a_\theta^2(\theta) \left| \sum_{n=-\infty}^{+\infty} \exp(-\frac{(na)^2}{2x_c^2}) \exp(-i\frac{2\pi}{\lambda}\frac{nx_s a}{L}) \right|^2 \tag{B7}$$

L = 1.5 cm

a = 0.2465 nm

$\lambda = 4.09 \times 10^{-11}$ m (=900 eV)

$a_\theta(\theta)$ data were obtained from NIST Standard Reference Database 64 (NIST Electron Elastic-Scattering Cross-Section, http://www.nist.gov/srd/nist64.cfm). The case that the electron beam energy is 900 eV is shown in graph B1.
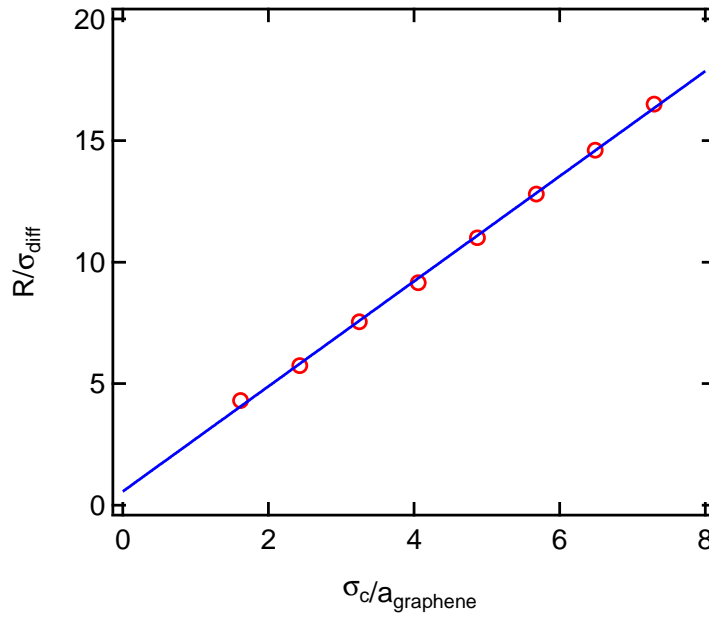

Graph B1

The calculation result of the total intensity, $S(x_s, x_c)$, with the considering of the electron elastic cross-section term, a_θ, is given in graph B2.

Graph B2

158
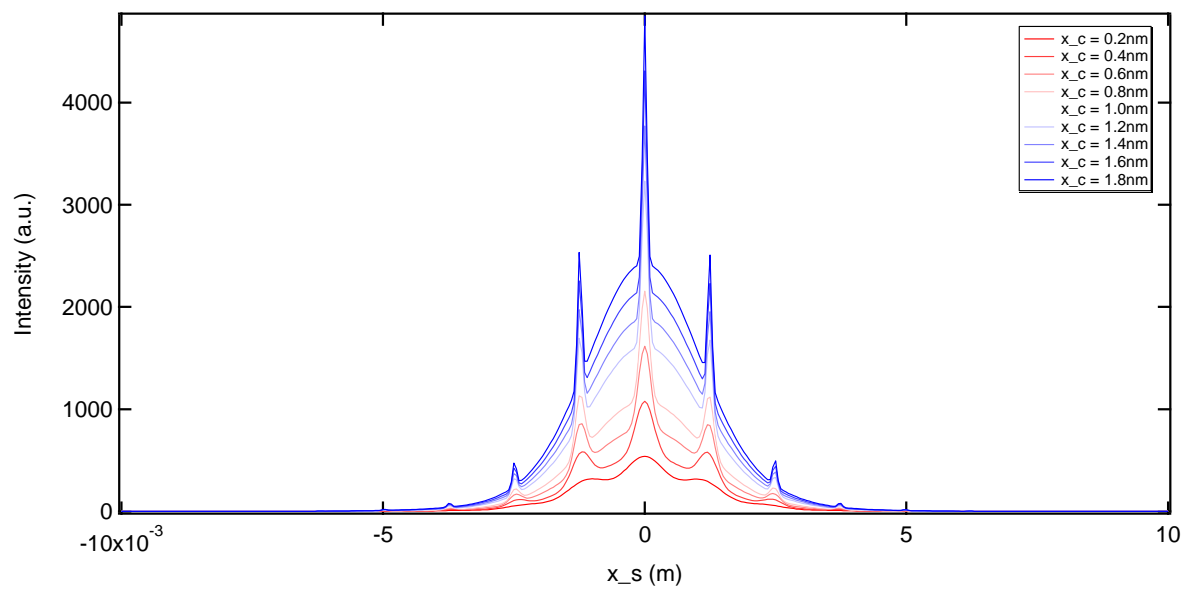
We define σ_{diff} as the RMS diffraction spot size at the screen, R as the distance from the beam center to the diffraction spot size. From graph B2, we can measure σ_{diff} and R, for each of x_c case. In the end, we can plot R/σ_{diff} vs x_c/a relationship, based on the measured data from graph B2, as shown in Graph B3 below.

Graph B3

In Graph B3, the blue curve is the linear fitting of the measured data. The fitting equation is y = 2.16x + 0.56723.

From the monolayer graphene diffraction image taken at k_{col} = 0.92, it is measured that σ_{diff} = 0.388 mm and R = 5.851 mm at the screen, respectively. The R/σ_{diff} is evaluated by 15.081. Inserting this value in the fitting equation results in ~ 1.6 nm of x_c.

Appendix C.

The electron elastic cross-section, $\sigma_{elastic}$, is defined by the total number of elastically scattered electrons per incident electron flux (number of electron/sec/cm^2). This quantity indicates statistical probability of the scattering event for a given diffraction sample or an atom, and can be expressed by the elastic scattering radius, r, through the following relation:

$$\sigma_{elastic} = \pi r^2 \tag{C1}$$

The r for electron-electron and electron-nucleus interaction, respectively, has a form described by the following:

$$r_{electron} = \frac{e}{V\theta} \tag{C2}$$

$$r_{nucleus} = \frac{Ze}{V\theta} \tag{C3}$$

where, e, V, Z, and θ refer to elementary charge, potential of the incident electron, atomic number, and scattering angle. Equations C1, C2, and C3 imply that, except hydrogen atom with $Z = 1$, elastic scattering cross section by nucleus-incident electron interaction, $\sigma_{nucleus}$, is always larger than that by the electron cloud-incident electron interaction, $\sigma_{electron}$. For example, in case of Au with $Z = 79$, $\sigma_{nucleus}$ is larger than $\sigma_{electron}$ by a factor of 6241 ($=72^2$) for a given incident electron energy.

Appendix D.

Upon the Debye-Waller theory, intensity of the Bragg diffraction spot of a $[hkl]$ plane is a function of the lattice temperature T_l .

$$I_{hkl}(T_l) = I_{hkl}(0) \cdot \exp\left\{-\frac{1}{3} < u(T_l)^2 > G_{hkl}^2\right\} \qquad (D1)$$

For the unpumped case (without optical excitation), we assume that T_l is equal to room temperature (RT). That is, $I_{hkl}(\Delta t < 0) = I_{hkl}(RT)$. Then, the spot intensity is expressed as

$$I_{hkl}(T_l = RT) = I_{hkl}(0) \cdot \exp\left\{-\frac{1}{3} < u(T_l = RT)^2 > G_{hkl}^2\right\} \qquad (D2)$$

Combining equation D1 and D2 yields the following:

$$\frac{I_{hkl}(T_l)}{I_{hkl}(T_l = RT)} = \exp\left\{-\frac{1}{3} G_{hkl}^2 (< u(T_l)^2 > - < u(T_l = RT)^2 >)\right\} \qquad (D3)$$

The above RT assumption also allows for converting the Δt dependence of the maximum absolute intensity change, mentioned in the main text, into the T_l dependence:

$$\Delta I_{max,hkl}(\Delta t) = I_{max,hkl} - I_{hkl}(\Delta t < 0) = I_{max,hkl}(T_l) - I_{hkl}(RT) = \Delta I_{max,hkl}(T_l) \qquad (D4)$$

Then, the normalized maximum intensity change extracted from the fitting curve (eqation 6.1) can be expressed with respect to T_l:

$$\frac{\Delta I_{max,hkl}(\Delta t)}{I_{hkl}(\Delta t < 0)} = \frac{I_{max,hkl}(\Delta t) - I_{hkl}(\Delta t < 0)}{I_{hkl}(\Delta t < 0)} = -1 + \frac{I_{max,hkl}(\Delta t)}{I_{hkl}(\Delta t < 0)} = -1 + \frac{I_{max,hkl}(T_i)}{I_{hkl}(T_i = RT)} = \frac{\Delta I_{max,hkl}(T)}{I_{hkl}(RT)}$$

$$= -1 + \exp\left\{-\frac{1}{3} G_{hkl}^2 (< u(T_i)^2 > - < u(RT)^2 >)\right\} \qquad (D5)$$

We assume that the in-plane mean-square displacement of a carbon atom is linearly proportional to T_l, introducing a parameter q :

$$< u(T_l)^2 >= q T_l \qquad (D6)$$

Equation D5 can be reformulated with respect to q :

$$\frac{\Delta I_{\max,hkl}(T_i)}{I_{hkl}(RT)} = -1 + \exp\left\{-\frac{1}{3}G_{hkl}^2 q(T_i - RT)\right\} \tag{D6}$$

Rearranging equation D6 with respect to q gives the following:

$$q = \frac{-3\ln\left\{1 + \frac{\Delta I_{\max,hkl}(T_l)}{I_{hkl}(RT)}\right\}}{G_{hkl}^2(T_l - RT)} \tag{D7}$$

Appendix E.

$$\min_{\mathbf{d}\geq 0}\left\{\|A\mathbf{d}-\mathbf{s}\|^2 - \gamma\|\mathbf{d}\|^2\right\} \qquad \text{(E1)}$$

The expression inside the argument of the mathematical statement E1 can be manipulated as follows:

$$\|A\mathbf{d}-\mathbf{s}\|^2 - \gamma\|\mathbf{d}\|^2$$
$$= (A\mathbf{d}-\mathbf{s})^T (A\mathbf{d}-\mathbf{s}) - \gamma\mathbf{d}^T\mathbf{d}I$$
$$= \mathbf{s}^T\mathbf{s} + \mathbf{d}^T A^T A\mathbf{d} - 2\mathbf{d}^T A^T\mathbf{s} + \gamma\mathbf{d}^T\mathbf{d}I$$
$$= \mathbf{s}^T\mathbf{s} + \mathbf{d}^T (A^T A + \gamma I)\mathbf{d} - 2\mathbf{d}^T A^T\mathbf{s}$$

In order to find the minimum, we take a derivative of the expression with respect to $\mathbf{d}$:

$$\nabla_{\mathbf{d}}\left\{\mathbf{s}^T\mathbf{s} + \mathbf{d}^T (A^T A + \gamma I)\mathbf{d} - 2\mathbf{d}^T A^T\mathbf{s}\right\}$$
$$= 2(A^T A + \gamma I)\mathbf{d} - 2A^T\mathbf{s}$$

Setting the above derivative equal to 0 and solving for $\mathbf{d}$ yields:

$$\mathbf{d} = (A^T A + \gamma I)^{-1} A^T\mathbf{s} \qquad \text{(E2)}$$

For a suitable choice of the regularization parameter, γ, equation E2 is always a well-conditioned problem.

Appendix F.

Below is a list of the hazardous substances used in this work. They are marked with the relevant pictograms, as well as the H (hazard) and P (precautionary) statements.

Substance	Pictogram	H-statmement	P-statement
Acetone		225, 319, 336	210, 305+351+338, 337+313, 403
Isopropyl alcohol		225, 319, 335	210, 233, 240, 241, 242, 243, 261, 264, 271, 280, 303+361+353, 305+351+338, 312, 337+313, 370+378, 403+233, 405, 501, 235
Ammonium fluoride		301+311+331	261, 264, 270, 271, 280, 301+310+330, 302+352+312, 304+340+311, 361+364, 403+233, 405, 501
Potassium hydroxide		302, 314, 402	260, 264, 270, 273, 280, 301+330+331, 303+361+353, 305+351+338, 310, 363, 405, 501
Phosphoric acid		314	260, 264, 280, 301+330+331, 303+361+353, 305+351+338, 310, 363, 405, 501
Nitric acid		290, 314	234, 260, 264, 280, 301+330+331, 303+361+353, 304+340, 305+351+338, 310, 363, 390, 405, 406, 501
Acetic acid		226, 314, 402	210, 233, 240, 241, 242, 243, 260, 264, 273, 280, 301+330+331, 303+361+353, 304+340, 305+351+338, 310, 363, 370+378, 403+235, 405, 501